

DOCTORAL THESIS

**Advanced homogenization techniques for
biomedical materials: complexity in geometry
and failure mechanisms**

submitted in satisfaction of the requirements for the degree of
Doctor of Science in Civil Engineering
of the TU Wien, Faculty of Civil Engineering

DISSERTATION

**Höhere Homogenisierungstheorie für Stoffe
aus der Biomedizin: komplexe Geometrien und
Versagensmechanismen**

ausgeführt zum Zwecke der Erlangung des akademischen Grades eines
Doktors der technischen Wissenschaften
eingereicht an der Technischen Universität Wien, Fakultät für Bauingenieurwesen

von

Dipl.-Ing. **Valentina Kumbolder**, BSc
Matr.Nr.: 01026112

Betreuer: Univ.Prof. Dipl.-Ing. Dr.techn. **Christian Hellmich**
Institut für Mechanik der Werkstoffe und Strukturen
Technische Universität Wien
Karlsplatz 13/202, 1040 Wien, Österreich

Gutachter: Prof. **Stéphane Avril**
Institut Mines Telecom
Mines Saint-Etienne, Université de Lyon, Université Jean Monnet
42023 Saint-Etienne, Frankreich

Gutachter: Univ. Prof. Dipl.-Ing. Dr. **Heinz Redl**
Experimentelle und Klinische Traumatologie (LBI Trauma)
Ludwig Boltzmann Institut
Donaueschingengasse 13, 1200 Wien, Österreich

Wien, im August 2020

FÜR JOSEF
- *in liebevoller Erinnerung* -

Danksagung

Die vorliegende Dissertation ist das Ergebnis meiner Arbeit am Institut für Mechanik der Werkstoffe und Strukturen (IMWS) im Rahmen des Doktoratskollegs Biointerface an der Technischen Universität Wien. Ich möchte an dieser Stelle allen Personen, die diese Dissertation ermöglicht haben, meinen herzlichen Dank aussprechen.

Allen voran gilt mein besonderer Dank meinem Betreuer Christian Hellmich, der mich mit seiner Begeisterung für die Wissenschaft und seinem immensen, interdisziplinären Wissen dazu inspiriert hat, meinen Weg vom Bauingenieurwesen in die Biomechanik einzuschlagen und mir die Möglichkeit einer Dissertation am IMWS geboten hat.

Ich möchte auch den großen Einfluss von Bernhard Pichler hervorheben, der durch sein außergewöhnliches Engagement in der Lehre, bereits im Rahmen meiner Bachelorarbeit meinen Kontakt zum IMWS hergestellt und mein Interesse an wissenschaftlichen Arbeiten geweckt hat. Mein Dank gilt außerdem Stefan Scheiner, der in der Abschlussphase meiner Dissertation mein Betreuerteam erweitert hat und bei der Finalisierung meiner Arbeit eine große Hilfe war.

Des Weiteren möchte ich auch meinen anderen Kollegen am IMWS, allen voran Patricia Hasslinger, Raphael Höller, Johannes Kalliauer und Robert Plachy meine große Dankbarkeit für die stets gute Zusammenarbeit und ihre uneingeschränkte Unterstützung in wissenschaftlichen sowie privaten Angelegenheiten aussprechen.

Mein besonderer Dank gilt auch Claire Morin, die während ihres Aufenthalts in Wien einen großen Beitrag zum Fortschritt meiner Dissertation geleistet hat, sowie Gabriele Ostrowski, Martina Pöll und Astrid Schuh, die mir bei jeglichen administrativen Fragen oder Problemen zur Seite gestanden sind.

Ich möchte mich außerdem für die Unterstützung durch das interdisziplinäre Doktoratskolleg Biointerface und die Finanzierung durch die Technische Universität Wien bedanken. Neben der Ermöglichung der Teilnahme an internationalen Konferenzen und des Austauschs mit Experten aus unterschiedlichsten Forschungsgebieten, möchte ich besonders das entstandene Biointerface Netzwerk, sowohl auf wissenschaftlicher als auch menschlicher Ebene hervorheben.

Mein größter Dank gilt schließlich meiner Familie und meinem Mann Nicholas. Ich kann nicht in Worte fassen, wie viel mir ihre Liebe und Unterstützung bedeutet und tagtäglich Kraft gibt.

Danke.



Die approbierte gedruckte Originalversion dieser Dissertation ist an der TU Wien Bibliothek verfügbar.
The approved original version of this doctoral thesis is available in print at TU Wien Bibliothek.

Kurzfassung

Beinahe jedes biologische Material, sei es natürlicher oder synthetischer Natur, weist im Allgemeinen eine große Anzahl von Heterogenitäten in seiner Mikrostruktur auf. Die vorliegende Arbeit basiert auf der Philosophie, dass das Verständnis und die Modellierung des mechanischen Verhaltens eines solchen heterogenen (Bio-)Materials die Kenntnis seiner zugrunde liegenden *mikroskopischen* Bestandteile und Mechanismen erfordert. Für den Übergang von dieser mikroskopischen Information zu dem *makroskopischen* Materialverhalten, wird das Konzept der Homogenisierung herangezogen. Um dabei komplexe Geometrien und Versagensmechanismen auf der Mikrostrukturebene zuverlässig mathematisch abbilden zu können, werden Methoden der Kontinuumsmikromechanik unter besonderer Berücksichtigung des „Prinzip der virtuellen Leistungen“ weiterentwickelt. Innerhalb dieses theoretischen Rahmens befasst sich die vorliegende Dissertation mit der Vorhersage mechanischer Eigenschaften, nämlich der elastischen Steifigkeit und der einaxialen Festigkeit, von drei grundlegend unterschiedlichen, jedoch trotzdem verbundenen, Materialien:

- Poröse polykristalline Mikrostrukturen, die für zahlreiche natürliche und künstliche Materialien charakteristisch sind, werden hinsichtlich ihrer Stabilität untersucht. Basierend auf einer Erweiterung der Transformationsfeldanalyse von Dvorak wird ihre einaxiale Festigkeit einerseits mithilfe eines neuartigen Ansatzes der Traglastanalyse und andererseits mithilfe einer vollständigen elastoplastischen Analyse bewertet, welche durch einen weiterentwickelten, iterativen Return-Mapping-Algorithmus ermöglicht wird.
- Knochen, welcher aus einem hierarchisch aufgebauten, heterogenen Gewebe besteht, wird auf seine Steifigkeit und einaxiale Druck- und Zugfestigkeit untersucht, indem die Eigenschaften und der Plastizitätsalgorithmus der Polykristalle in ein mehrskaliges elastoplastisches Kontinuumsmikromechanikmodell integriert werden. Dieses Multiskalenmodell erlaubt die Berücksichtigung spezifischer Knochenzusammensetzungen, während es auf davon unabhängigen Eigenschaften der drei Knochenhauptbestandteile basiert. Das Modell wird einer Bottom-up-Homogenisierung sowie einer vollständigen elastoplastischen Analyse unterzogen, um probenspezifische Steifigkeits- und Festigkeitswerte des kortikalen Knochens vorherzusagen. Die Validierung erfolgt durch experimentelle Ergebnisse von kortikalen Knochen verschiedener Spezies und anatomischer Stellen.
- Käfigartige Mikrogerüste, die mit Gewebezellen gefüllt sind, werden als Grundbausteine im Tissue Engineering verwendet. Um den Entwurfsprozess dieser, für die Knochengebezüchtung vorgesehenen Gerüste zu vereinfachen, untersucht die vorliegende Arbeit die Auswirkungen unterschiedlicher Gerüstmaterialien und Abmessungen auf die effektiven Eigenschaften verschiedener periodischer Gerüstpackungen. Unter Anwendung der Einheitszellenmethode, welche auf einer periodischen Homogenisierung von Finite-Elemente-Simulationen basiert, wird die elastische Steifigkeit vorhergesagt. Korrelationen zwischen den individuellen Eigenschaften des Einzelgerüsts und dem resultierenden Gesamtkonstrukt werden identifiziert und ermöglichen einen schnelleren Designprozess.

Abstract

Almost any biological material, whether natural or synthetic, generally has a large number of heterogeneities within its microstructure. The present thesis is built upon the philosophy that understanding and modeling the mechanical behavior of such a heterogeneous (bio)material at the *macroscopic* scale, requires the knowledge of its underlying *microscopic* constituents, interactions and mechanisms. For the transition between this microscopic information and the overall macroscopic material behavior, the concept of homogenization is the method of choice throughout the whole thesis. To computationally link the characteristic features of the different length scales, methods of continuum micromechanics, with particular emphasis on the “Principle of Virtual Power”, are adapted and further developed, so as to come up with a reliable mathematical representation of complex geometries and failure mechanisms of the microstructure. In this framework, the present thesis addresses the prediction of mechanical properties, i.e. elastic stiffness and uniaxial strength, of three fundamentally different biomedical materials, that are, however, strongly connected to each other:

- Porous polycrystal-type microstructures, which are characteristic for numerous natural and man-made materials are investigated in terms of their structural stability. Relying on an extension of Dvorak’s transformation field analysis, their uniaxial strength is assessed on the one hand by means of a novel yield design approach, and on the other hand by applying a full elastoplastic analysis enabled by an updated iterative return-mapping algorithm.
- Bone, a highly hierarchically organized material, is examined for its elastic stiffness and uniaxial compressive and tensile strength by integrating the properties of the in advance investigated porous polycrystals and the thereby developed plasticity algorithm in a multiscale elastoplastic continuum micromechanics model. This multiscale model allows to take into account sample-specific bone compositions, while being based on tissue- and composition-independent properties of bone’s three elementary constituents, i.e. collagen, mineral and water. The model is subjected to a bottom-up homogenization and a full elastoplastic analysis to predict sample-specific stiffness and strength values of cortical bone at different hierarchical levels. The predictions are validated by experimental results for cortical bone of different species and anatomical locations.
- Cage-like microscaffolds which are filled with tissue spheroids, are the basic building blocks used in the so-called third strategy of tissue engineering. To facilitate the design process of these scaffolds targeting their clinical application in bone tissue engineering, this work investigates the effects of varying scaffold-materials and dimensions on the overall effective properties of different periodic scaffold-packings. The unit cell method based on periodic homogenization by means of the Finite Element Method is used to predict the elastic stiffness of different scaffold packings with varying individual properties. Correlations between the single scaffold and the overall construct are identified and allow for a much faster scaffold-design process.

Contents

1	Introduction	1
1.1	Motivation and objective	1
1.2	Concept of Homogenization	2
1.2.1	Homogenization methods	3
1.2.2	Representative Volume Element	3
1.3	Mean-Field homogenization	4
1.3.1	Elastoplastic homogenization - Transformation field analysis	4
1.3.1.1	Fundamental equations of continuum micromechanics	5
1.3.2	Estimation of concentration and influence tensors	6
1.3.2.1	Mori-Tanaka scheme for a two-phase composite	8
1.3.2.2	Self-consistent scheme for a two-phase composite	9
1.3.2.3	Self-consistent scheme for a porous polycrystal	10
1.4	Periodic homogenization - Unit Cell Method	12
1.4.1	Periodic strain and stress fields	12
1.4.2	Displacement controlled method of macroscopic degrees of freedom	13
1.5	Outline of the thesis	15
2	Transformation field analysis-based yield design of porous polycrystals: theory and full elastoplastic validation	16
2.1	Introduction	17
2.2	Yield design for materials with continuous micro-heterogeneous plastic fields	18
2.2.1	Fundamentals of continuum micromechanics – representative volume element	18
2.2.2	Admissible microstresses and virtual microvelocity fields derived from transformation field analysis	20
2.3	Yield design for porous plastic polycrystals	21
2.3.1	RVE of a porous polycrystal	21
2.3.2	Discretization	22
2.3.3	Average rules and concentration-influence relations	22
2.3.4	Virtual microstrain field associated with plastic collapse - ultimate macroscopic load	23
2.4	Validation: full elastoplastic analysis	26
2.4.1	Elastoplastic state equations, upscaling of plastic strains, and non-associative flow rules	26
2.4.2	Algorithmic treatment I: general iteration strategy and discretized plastic flow rule	27
2.4.3	Algorithmic treatment II: series of stress states and return mapping	28
2.4.4	Numerical results	30
2.5	Discussion	32

3	Multiscale elastoplasticity: theory, algorithm, and application to bone	33
3.1	Introduction	34
3.2	Continuum micromechanics-based multiscale elastoplasticity	35
3.2.1	Fundamentals of continuum micromechanics	35
3.2.2	Single-scale up- and downscaling relations	36
3.2.3	Extension to multiscale scheme	37
3.2.4	Derivation of the multiscale influence tensor	38
3.3	Multiscale plasticity algorithm	40
3.3.1	Elastoplastic state equations and non-associative flow rules	40
3.3.2	General iteration strategy and discretized plastic flow rule	40
3.3.3	Series of stress states and return mapping	42
3.4	Application to bone tissue	44
3.4.1	Hierarchical organization and micromechanical representation	44
3.4.2	Plasticity of bone	47
3.4.3	Establishment of a micromechanical up- and downscaling scheme	47
3.4.3.1	Adaptation of micromechanical formulations to bone tissue	48
3.4.3.2	Downscaling from the macroscale to the plasticity-inducing material phases	51
3.4.3.3	Input quantities for homogenization scheme	53
3.4.3.4	Consideration of failure mechanisms	54
3.4.4	Algorithmic aspects	55
3.4.5	Experimental validation	57
3.4.5.1	Stiffness validation	57
3.4.5.2	Strength validation at the macroscopic scale	59
3.4.5.3	Strength validation at the extracellular scale	62
3.5	Discussion	63
3.5.1	Novel aspects concerning the micromechanical representation	63
3.5.2	Effects of the extracellular mass density and of the vascular porosity on bone strength	64
3.5.3	Comments on the employed iterative return-mapping algorithm	64
3.5.4	Sequence of plastic events	65
3.5.5	Concluding remarks	66
A	Appendix	68
A.1	Hill tensors	68
A.2	Concentration tensors	71
A.3	Influence tensors	72
A.4	Derivation of the multiscale influence tensors	74
A.5	Volume fractions of the extracellular space	76
A.6	Experimental stiffness data from literature	78
4	Finite Element-based periodic homogenization of cage-like microcaffolds for tissue engineering	81
4.1	Introduction	82
4.2	Microcaffolds	83
4.2.1	Lattice packing	83
4.3	Homogenization: Unit Cell method	85
4.3.1	Discrete beam problem	85
4.3.2	Principle of Virtual Power based homogenization	85

4.3.3	Unit effective strain	87
4.3.4	Periodic boundary conditions	88
4.3.4.1	Implementing the boundary conditions in Abaqus	88
4.4	Results	90
4.4.1	Densest packing: Effects of varying scaffold properties	90
4.4.2	Effects of varying packing configurations	91
4.4.3	Dimensional analysis	93
4.5	Conclusion and perspectives	95
B	Appendix	96
B.1	Truncated icosahedron	96
B.2	Lattice packings	97
B.2.1	Densest packing	97
B.2.2	Packing along the x_1, x_2, x_3 -axes	97
B.2.3	Packing along the x_1 - and x_3 -axis	98
B.3	Derivations	98
B.4	FE-simulation results	99
5	Conclusion	102
	Nomenclature	105
	Bibliography	111
	Curriculum Vitae	122

List of Figures

1.1	Scheme representing the three topics/materials, which are investigated within this thesis and their connection to each other	2
1.2	Continuum micromechanics concept	4
1.3	Overview of the continuum micromechanics transitions between the macro- and microscopic scale	6
1.4	Generalized matrix-inclusion problem with definition of shape and orientation of the inclusion	6
1.5	Mori-Tanaka-type RVE consisting of two phases: matrix and inclusion	8
1.6	Self-consistent RVE consisting of two phases embedded in an auxiliary matrix	9
1.7	Self-consistent RVE representing a porous polycrystal	10
1.8	Different possible choices of the unit cell for a periodic 2-dimensional structure with two vectors of translational invariance	12
1.9	Unit Cell with surface pairs	13
2.1	RVE representing a porous polycrystal	21
2.2	Modified Newton-Raphson iteration scheme	27
2.3	Principle of iterative return-mapping	28
2.4	Plasticity algorithm based macroscopic stress-strain relation in comparison with the limit analysis based ultimate loading for uniaxial compression, uniaxial tension and pure shear	31
2.5	Distribution of the norm of the microscopic ultimate stress in the mineral needles over the needle orientations under uniaxial compression, tension and pure shear	31
3.1	Multiscale homogenization scheme comprising two up-/downscaling paths	35
3.2	Modified Newton-Raphson iteration scheme used to determine the macroscopic strain corresponding to the applied macroscopic stress	41
3.3	Principle of iterative return-mapping considering a series of stress states and their corresponding flow directions being developed by a novel sequential one-step linearized backprojection process	42
3.4	Hierarchical organization of bone	45
3.5	Micromechanical representation of cortical bone by means of a multiscale homogenization scheme	46
3.6	Orientation of the solid needles by means of spherical coordinates and distributions of the Gaussian set of integration points	47
3.7	Downscaling paths to the extrafibrillar and intermolecular mineral needles	51
3.8	Comparison between model predictions and experiments of radial stiffness and axial stiffness at the extracellular scale	58
3.9	Comparison between model predictions and experiments of radial stiffness and axial stiffness at the extravascular scale	58

3.10	Comparison between model prediction and experimental data for the compressive strength of human femoral and tibial and bovine femoral and tibial cortical bone tissue	61
3.11	Comparison between model prediction and experimental data for the tensile strength of human femoral and tibial and bovine femoral and tibial cortical bone tissue	62
3.12	Effects of the extracellular mass density on the predicted cortical compressive strength and tensile strength; as well as constituents volume fractions	64
3.13	Comparison of iterative return-mapping principles	65
3.14	Distribution of the norm of the plastic strains in the mineral over the needle orientations in the extrafibrillar and intermolecular space at selected macroscopic stress levels under uniaxial compression	66
3.15	Distribution of the norm of the plastic strains in the mineral over the needle orientations in the extrafibrillar and intermolecular space at selected macroscopic stress levels under uniaxial tension	66
3.16	Contourplot of axial and radial cortical bone stiffness as a function of extracellular mass density and vascular porosity	67
3.17	Contourplot of compressive and tensile cortical bone strength as a function of extracellular mass density and vascular porosity	67
4.1	Truncated icosahedron shaped micro scaffold encapsulating a tissue spheroid	83
4.2	Three different lattice packings of truncated icosahedra	84
4.3	Unit cells of three different lattice packings	85
4.4	(a) human femoral bone; (b) macroscopic scale: defect in cortical bone filled with quasi-homogeneous scaffold spheroid material; (c) microscopic scale: discrete beam scaffold-structure filled with tissue spheroids; (d) unit cell representing the scaffold packing with forces acting at all beam-ends on the surface of the unit cell	86
4.5	Effective strain states applied to a unit cell	87
4.6	Periodic displacement boundary conditions	88
4.7	Master nodes for implementation of periodic boundary conditions	89
4.8	Effects of varying scaffold properties on the effective stiffness components of the densest scaffold packing	91
4.9	Effective stiffness components of varying scaffold packings with equal individual scaffold properties	92
4.10	Comparison of all 21 independent FE-based and power-law-predicted stiffness components for the 33 varying scaffold configurations of the densest packing	93
4.11	FE-based results of the radial and axial stiffness of the densest packing based on a constant Poisson's ratio and varying E , ℓ and d in dimensionless form fitted with power-law functions	94
4.12	Orientation of the truncated icosahedron in the x, y, z -coordinate system	96

List of Tables

2.1	Properties of solid and pore material phases of equine osteonal bone	26
2.2	Limit analysis based ultimate uniaxial micro- and macroscopic stress of equine osteonal bone under uniaxial loading	26
2.3	Plasticity algorithm based characteristic stress states of equine osteonal bone under uniaxial loading	31
3.1	Tissue-specific experimental composition values of cortical bone	59
3.2	Tissue-specific experimental uniaxial strength values	60
3.3	Tissue-specific extracellular mass density	60
3.4	Predicted and experimental stiffness and compressive strength values of ovine extracellular bone	63
3.5	Experimental characterization of various cortical bone samples - extracellular scale in radial direction	78
3.6	Experimental characterization of various cortical bone samples - extracellular scale in axial direction	79
3.7	Experimental characterization of equine cortical bone samples - extravascular scale	80
4.1	Three lattice packings of truncated icosahedra	84
4.2	Varying scaffold configurations used as input for finite element simulations of the densest packing	90
4.3	Effective stiffness components of varying scaffold packings with equal individual scaffold properties	92
4.4	Power-law function fitting parameters ϕ_1 , ϕ_2 and ϕ_3 for the 21 independent components of the homogenized stiffness tensor of the densest scaffold packing	94
4.5	Results of the finite element simulations for the 33 different densest packing configurations - Part 1	99
4.6	Results of the finite element simulations for the 33 different densest packing configurations - Part 2	100
4.7	Results of the finite element simulations for the 33 different densest packing configurations - Part 3	101



Die approbierte gedruckte Originalversion dieser Dissertation ist an der TU Wien Bibliothek verfügbar.
The approved original version of this doctoral thesis is available in print at TU Wien Bibliothek.

Chapter 1

Introduction

1.1 Motivation and objective

In recent years, it has become increasingly obvious that the mechanical properties of biological materials or systems are key determinants of their biological functioning. However, the fundamental principles behind these mechano-biological interactions are largely unknown. Being actually a traditional topic of biology, biophysics and biochemistry, more recently published research has shown the great potential of one of the oldest engineering disciplines, (civil) engineering mechanics, to further reveal the secrets still pertaining in the functioning of biomaterials.

Therefore, the present thesis aims at providing a portfolio of theoretical concepts and numerical models, using methods arising from the field of civil engineering, which would be needed for the prediction of the mechanical behavior of different complex biomedical materials. In detail, the present work examines three fundamentally different biological or biomedical materials, which are, nevertheless, strongly linked to each other as sketched in Figure 1.1 and pointed out in the following:

1. **Porous polycrystals** are made up of millions of individual needle-like platelets or sheets with random orientation and pore spaces in between (Parker 2001, Fritsch et al. 2006). Such polycrystalline microstructures are characteristic for numerous natural and synthetic materials such as bone, metals, ceramics, polymers and cementitious materials.
2. **Bone** fulfills an important role in the body of vertebrates, including provision of structure, protection of organs, locomotion and also production of blood cells. To serve all these mechanical, biological and chemical functions, bones have been optimized through evolutionary processes and undergo constant functional adaptation during lifetime. The result is a highly hierarchically organized heterogeneous microstructure, which exhibits some fundamental, species- and organ-independent, organizational patterns. One of these universal patterns, namely the arrangement of bone's fundamental component hydroxyapatite, corresponds to the structure of a *porous polycrystal* (Prostak & Lees 1996).
3. **Cage-like microscaffolds** filled with tissue spheroids are the basic building blocks of the so-called third strategy in tissue engineering (Ovsianikov et al. 2018). The implementation of this strategy is envisioned in bone tissue engineering. For successful clinical application, the mechanical properties of the scaffold-spheroid-conglomerate have to match those of the material it replaces, i.e. they have to be in the range of the stiffness of *bone*.

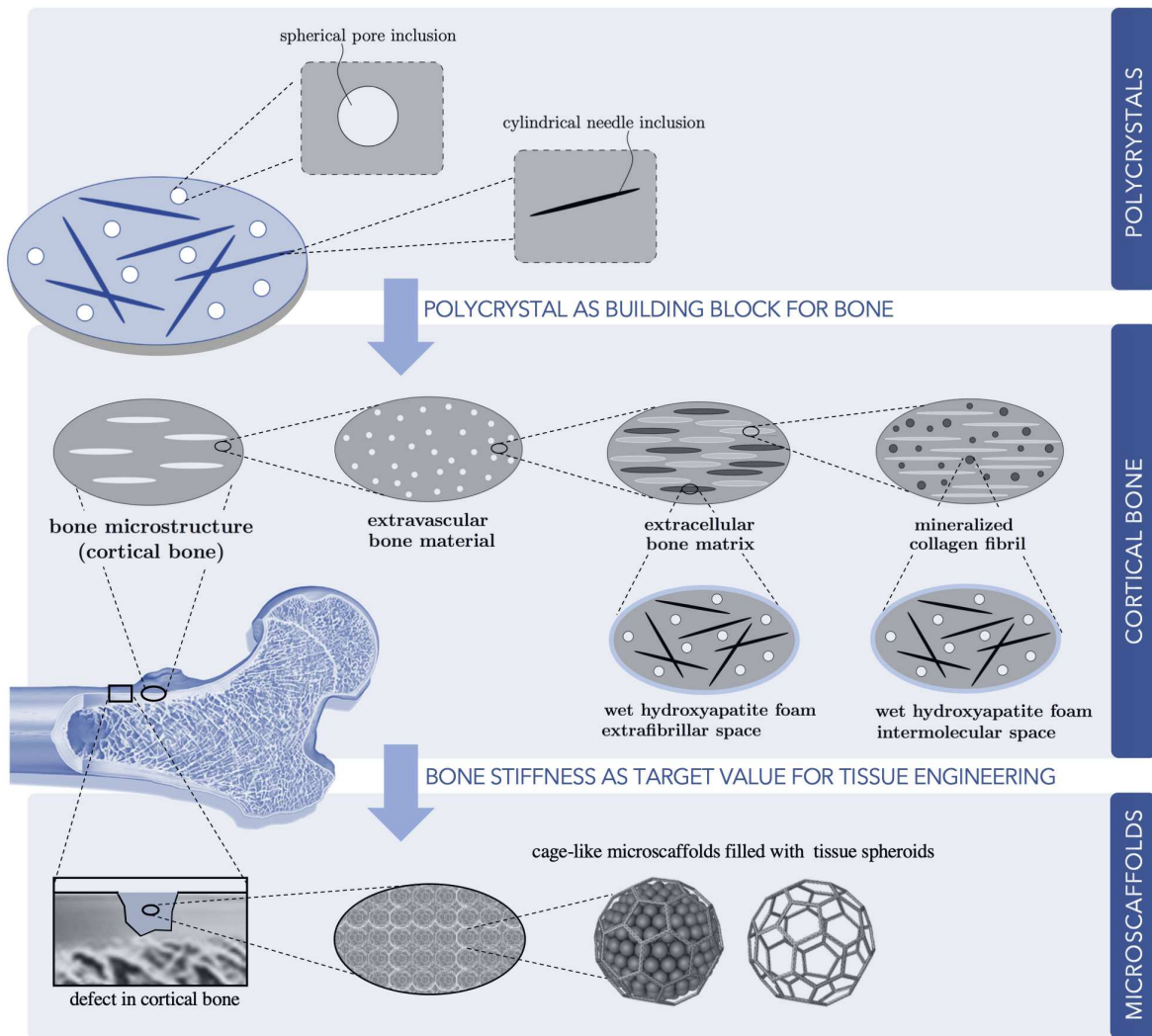


Fig. 1.1: Scheme representing the three topics/materials, which are investigated within this thesis and their connection to each other

1.2 Concept of Homogenization

Almost every biological material (and any other material in general) has a large number of heterogeneities within its microstructure, even if it appears to be homogeneous to the naked eye. These heterogeneities arise either due to the material being a manufactured mixture of at least two different constituents, a so-called composite material, or due to the type of structure itself, having for example cracks, pores, individual layers or fibers. In general, the microstructure of heterogeneous materials is very disordered and complex because the size, shape and distribution of the defects or different materials are random. Bone, bone biomaterials, tissues and polycrystals are typical examples of natural heterogeneous materials. In such materials, the mechanical properties are obviously inhomogeneously distributed over the body under consideration and per se no uniform set of material parameters can be used as basis for a structural analysis. However, describing explicitly all heterogeneities in the material and determining the point-specific set of mechanical properties often proves to be too costly

and sometimes simply impossible. To overcome this issue, the art lies in computationally finding a fictitious homogeneous material, which behaves globally in the same way as the micro-heterogeneous one. To this end, a macro-homogeneous material is derived by smearing the microscopic heterogeneities and defining so-called *effective* properties, that are independent of the location and take into account the heterogeneous microstructure in an averaged sense. This process is called homogenization.

1.2.1 Homogenization methods

Heterogeneities within a material can occur at very different length scales. While in some materials, the different constituents are visible to the naked eye (e.g. certain concretes), other materials have to be examined through a microscope (e.g. bone) or using an even higher resolution to reveal their heterogeneity. Consequently, homogenization may be applied at very different length scales ranging from atomic up to continuum scales. Identification of the microgeometry at all these different length scales tends to be of major importance and determines the macroscopic homogenized response. However, in general an exact analysis of the spatial variations of the microstructure is almost impossible. Therefore suitable approximations must be introduced, which can be split up into two major groups of homogenization methods:

- The first group comprises homogenization methods that describe the microstructure and interactions in a collective, averaged way, e.g. Mean-Field Approaches.
- The second group comprises homogenization methods that are based on studying a discrete approximation of the microstructures and its interactions, e.g. Periodic Microfield Approaches.

Regardless of the method and length scale, homogenization always aims at computing the effective behavior of a higher-scale-homogeneous but lower-scale-heterogeneous material based on the material properties and geometrical arrangement of its microscopic constituents. In order to reduce the computational costs of the homogenization process, not the entire structure may be taken into account, but only a partial volume that is representative of the whole material, a so-called Representative Volume Element.

1.2.2 Representative Volume Element

A Representative Volume Element (RVE) corresponds to a subvolume of the material, which has to fulfill the following requirements so that it can be regarded as representative for the whole material and allows a reasonable homogenization:

1. The heterogeneities must be statistically evenly distributed within the volume element.
2. A necessary (yet not sufficient) condition is that the characteristic length ℓ of the RVE must be considerably larger than the characteristic length of the inhomogeneities d , while being at the same time significantly smaller than the characteristic structural length \mathcal{L} of the loading or geometry of the whole structure. This so-called *separation-of-scales-requirement* mathematically reads as

$$d \ll \ell \ll \mathcal{L}. \quad (1.1)$$

While the left inequality sign typically refers to factors of 2 to 3 (Drugan & Willis 1996) in order to provide all necessary geometric information about the material's composition,

ℓ and \mathcal{L} need to be separated by a factor of 5 to 10 (Kohlhauser & Hellmich 2013) to allow the RVE to be considered as homogeneous from a macroscopic point of view.

1.3 Mean-Field homogenization

Mean-Field Approaches are a major modeling strategy in continuum micromechanics. They are a suitable homogenization method when dealing with materials with a random microstructure, which cannot be described in every single detail but rather in a statistical sense and for which it is possible to define a Representative Volume Element. The microstructure within such an RVE is in general too complex to be described in full detail. For this reason, idealized microgeometries are used by considering the material as a composition of clearly distinguishable, quasi-homogeneous subdomains, so-called *phases*, see Figure 1.2. The microfields within the constituents are approximated by their phase averages (or *means*), i.e. phase-wise uniform stress and strain fields are employed.

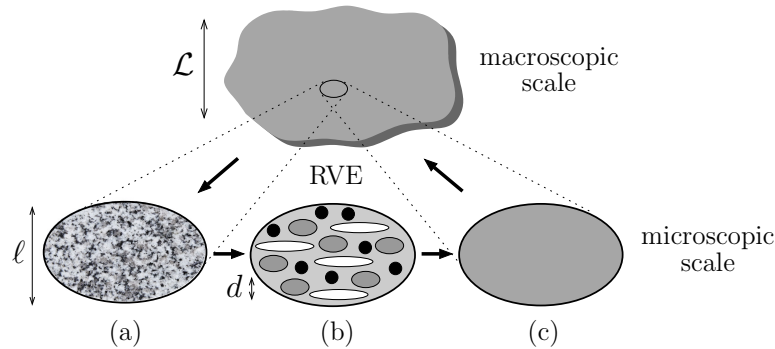


Fig. 1.2: *Continuum micromechanics concept: (a) heterogeneous microstructure; (b) introduction of homogeneous phases; (c) homogenized effective material*

The phase geometry is considered via statistical descriptors, such as volume fractions and phase topology. Therefore, the phases are assigned with specific material properties, some of which are quantitative (e.g. volume fractions and mechanical properties like stiffness or strength) and some of which are qualitative (e.g. characteristic shape and orientation). Each of the phases (labeled by r) fills a volume V_r within the RVE and the sum of all these partial volumes yields the total volume $V_{\text{RVE}} = \sum_r V_r$. The phases are characterized by a fourth-order stiffness tensor \mathbb{C}_r , their characteristic shape and volume fraction $f_r = V_r/V_{\text{RVE}}$, whereby $\sum_r f_r = 1$.

1.3.1 Elastoplastic homogenization - Transformation field analysis

While micromechanical homogenization theories have been highly successful in describing the response of elastic materials ever since the field of continuum micromechanics based homogenization emerged around 1960 (Hill 1963, Zaoui 2002), it took until the early 1990s, that Dvorak and coworkers proposed a fundamental approach to elastoplastic-homogenization theory. The classical *Transformation Field Analysis* of Dvorak (1992) enabled the homogenization of a nonlinear behavior of inhomogeneous materials with aligned phase inclusions of identical shape. Its extension of Pichler & Hellmich (2010) towards heterogeneous media

comprising inclusion phases with an arbitrary ellipsoidal shape and with arbitrary spatial orientation, provides the theoretical fundamentals for elastoplastic homogenization within this work.

1.3.1.1 Fundamental equations of continuum micromechanics

Considering an RVE that satisfies the separation of scales between the macroscopic scale “M” and the microscopic scale “ μ ” and that is build up by different phases r , which are exhibiting elastoplastic material behavior, continuum micromechanics defines the homogenization relations for the stress and strain fields as volume averages (Zaoui 2002), reading as

$$\boldsymbol{\Sigma} = \frac{1}{V_{\text{RVE}}} \int_{V_{\text{RVE}}} \boldsymbol{\sigma}(\mathbf{x}) dV = \langle \boldsymbol{\sigma} \rangle = \sum_r f_r \boldsymbol{\sigma}_r \quad (1.2)$$

$$\mathbf{E} = \frac{1}{V_{\text{RVE}}} \int_{V_{\text{RVE}}} \boldsymbol{\varepsilon}(\mathbf{x}) dV = \langle \boldsymbol{\varepsilon} \rangle = \sum_r f_r \boldsymbol{\varepsilon}_r, \quad (1.3)$$

whereby the macroscopic strain \mathbf{E} and macroscopic stress $\boldsymbol{\Sigma}$ characterize the mechanical state at the boundary of the RVE, and the microscopic strains $\boldsymbol{\varepsilon}_r$ and microscopic stresses $\boldsymbol{\sigma}_r$ denote the average strains and stresses in phase r . The microscopic stress $\boldsymbol{\sigma}_r$ and strain $\boldsymbol{\varepsilon}_r$ within the elastoplastic phase r are following the constitutive law

$$\boldsymbol{\sigma}_r = \mathbb{C}_r : (\boldsymbol{\varepsilon}_r - \boldsymbol{\varepsilon}_r^p), \quad (1.4)$$

with $\boldsymbol{\varepsilon}_r^p$ as the average plastic strain in phase r . The microscopic phase strains $\boldsymbol{\varepsilon}_r$ are multilinearly related to both, the macroscopic strains \mathbf{E} and the microscopic plastic strains $\boldsymbol{\varepsilon}_r^p$, through the so-called concentration-influence relation (Dvorak & Benveniste 1992, Pichler & Hellmich 2010)

$$\boldsymbol{\varepsilon}_r = \mathbb{A}_r : \mathbf{E} + \sum_s \mathbb{D}_{rs} : \boldsymbol{\varepsilon}_s^p, \quad (1.5)$$

with the fourth order concentration tensor \mathbb{A}_r , providing a multilinear relation between the macroscopic and the microscopic strain; and the fourth-order influence tensor \mathbb{D}_{rs} , expressing the effect of the plastic strain in phase s on the overall strain in phase r .

In case of plastic behavior in one of the phases within the RVE, hence non-zero microscopic plastic strains, the whole RVE exhibits plastic behavior leading to macroscopic plastic strains \mathbf{E}^p . The stress and strain average rules allow for the homogenization (or upscaling) of the known microscopic constitutive laws to the macroscopic level

$$\boldsymbol{\Sigma} = \mathbb{C}_{\text{hom}} : (\mathbf{E} - \mathbf{E}^p), \quad (1.6)$$

with \mathbb{C}_{hom} as the homogenized stiffness tensor of the RVE reading as

$$\mathbb{C}_{\text{hom}} = \sum_r f_r \mathbb{C}_r : \mathbb{A}_r \quad (1.7)$$

and with the macroscopic plastic strains \mathbf{E}^p accessed through Levin’s theorem (Levin 1967)

$$\mathbf{E}^p = \sum_r f_r \mathbb{C}_{\text{hom}}^{-1} : \mathbb{A}_r^T : \mathbb{C}_r : \boldsymbol{\varepsilon}_r^p. \quad (1.8)$$

A compilation of all these continuum micromechanics relations used to either up- or downscale mechanical properties of two successive scales by means of homogenization or concentration, also called localization, is shown in Figure 1.3.

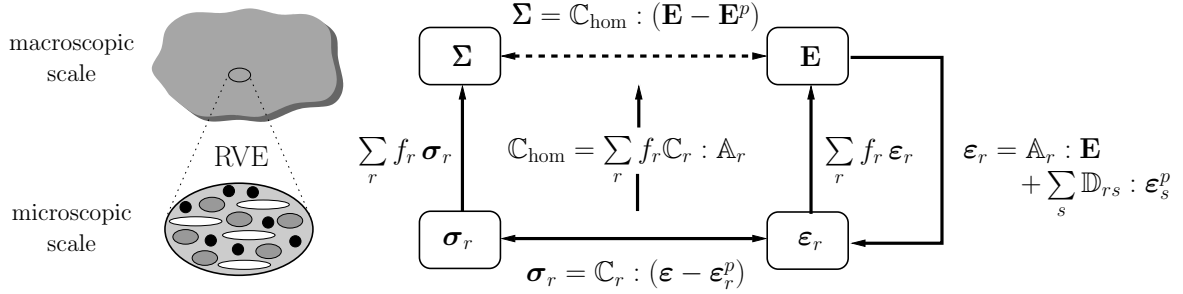


Fig. 1.3: Overview of the continuum micromechanics transitions between the macro- and microscopic scale

1.3.2 Estimation of concentration and influence tensors

For a realistic estimation of the concentration tensor \mathbb{A}_r , the so-called matrix inclusion problem according to Eshelby (1957) is utilized: This problem considers an ellipsoidal inclusion with stiffness \mathbb{C}_r being embedded in an infinite auxiliary matrix with stiffness \mathbb{C}^0 , see Figure 1.4. The choice of the latter allows to take into account the mechanical interaction between the material phases. While choosing $\mathbb{C}^0 = \mathbb{C}_m$ leads to the so-called Mori-Tanaka scheme, which is suitable for materials exhibiting a continuous matrix phase m surrounding all the other phases, the so-called self-consistent scheme considers the inclusions to be embedded in a fictitious matrix with no volume fraction, to which the stiffness properties homogenized over the whole RVE are assigned ($\mathbb{C}^0 = \mathbb{C}_{\text{hom}}$).

Regardless of the chosen scheme, the matrix is subjected to homogeneous strains \mathbf{E}^0 at its boundary being infinitely distant from the inclusion. Eshelby showed, that under these conditions, the strain state in an inclusion phase, $\boldsymbol{\varepsilon}_r$ is associated to the physical quantities of the matrix by means of

$$\boldsymbol{\varepsilon}_r = [\mathbb{I} + \mathbb{P}_r^0 : (\mathbb{C}_r - \mathbb{C}^0)]^{-1} : \mathbf{E}^0, \quad (1.9)$$

with \mathbb{I} as the fourth-order identity tensor and \mathbb{P}_r^0 as the fourth-order Hill tensor.

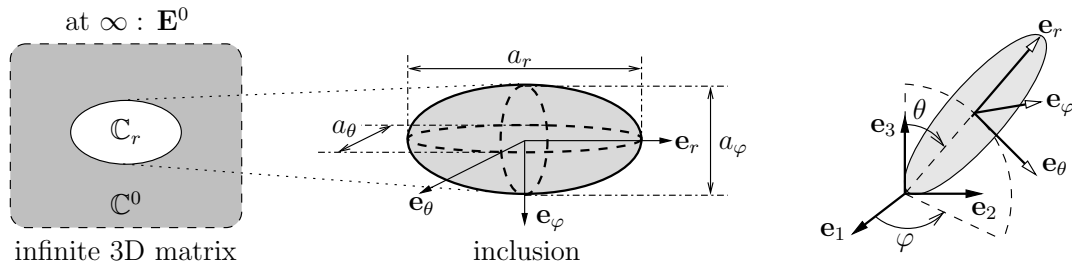


Fig. 1.4: Generalized matrix-inclusion problem with definition of shape (middle) and orientation (right) of the inclusion

The **Hill tensor** $\mathbb{P}_r^0 = \mathbb{P}_r^0(w, s, \theta, \varphi, \mathbb{C}^0)$ depends on the shape and orientation of the inclusion and the stiffness of the surrounding matrix. As shown in Figure 1.4, the orientation of the inclusion is defined by the two angles θ and φ and its shape is described by the aspect ratio $w = a_\theta/a_\varphi$ and the slenderness ratio $s = a_\theta/a_r$ (e.g. $w = 1, s = 0$ for a cylindrical inclusion and $w = 1, s = 0$ for a spherical inclusion). Analytical solutions for the Hill tensor exist only for simple matrix inclusion problems. The detailed Hill tensors for spherical inclusions in an isotropic matrix, cylindrical inclusions in an isotropic matrix and cylindrical inclusions in an transversely isotropic matrix are given in the Appendix A.

Continuing with the estimation of the strain concentration tensor, Eq. (1.9) is inserted into the strain average rule according to (1.3), to establish a link between the auxiliary strains \mathbf{E}^0 and the actual macroscopic strains \mathbf{E} , reading as

$$\mathbf{E} = \sum_r f_r [\mathbb{I} + \mathbb{P}_r^0 : (\mathbb{C}_r - \mathbb{C}^0)]^{-1} : \mathbf{E}^0. \quad (1.10)$$

Solving Eq. (1.10) for \mathbf{E}^0 , inserting the result in (1.9) and comparing the final expression to (1.5) for $\boldsymbol{\varepsilon}_s^p = 0$, allows to identify the strain concentration tensor as

$$\mathbb{A}_r = \mathbb{A}_r^\infty : \left\{ \sum_s f_s [\mathbb{I} + \mathbb{P}_s^0 : (\mathbb{C}_s - \mathbb{C}^0)]^{-1} \right\}^{-1}, \quad (1.11)$$

whereby

$$\mathbb{A}_r^\infty = [\mathbb{I} + \mathbb{P}_r^0 : (\mathbb{C}_r - \mathbb{C}^0)]^{-1}. \quad (1.12)$$

It is emphasized, that the thus derived expression for the strain concentration tensor \mathbb{A}_r does not change upon the presence of plastic stresses or strains ($\boldsymbol{\varepsilon}_s^p \neq 0$), as shown by Pichler & Hellmich (2010). Neither estimated homogenized stiffnesses nor Levin's theorem-predicted macrostresses are influenced by eigenstresses. However, to estimate the hence *additional effect of plastic strains* on the total microscopic phase strains, it is necessary to extend the classical matrix-inclusion problem by an auxiliary matrix eigenstress, which is a function of all phase eigenstresses and thereby accounts for eigenstress interactions as proposed by Pichler & Hellmich (2010). This extended eigenstressed matrix-inclusion problem allows to derive estimates for the strain influence tensor \mathbb{D}_{rs} . The mathematical definition of the influence tensor depends on the morphology of the respective RVE and is defined based on the phase concentration tensors. In the following, detailed expressions will be derived separately for three specified RVE compositions.

1.3.2.1 Mori-Tanaka scheme for a two-phase composite

We consider a Mori-Tanaka-type RVE consisting of two phases: one matrix phase (labeled by suffix m) and one inclusion phase (labeled by suffix i), see Figure 1.5. Both phases may be subjected to plastic strains, $\boldsymbol{\varepsilon}_i^p$ and $\boldsymbol{\varepsilon}_m^p$.

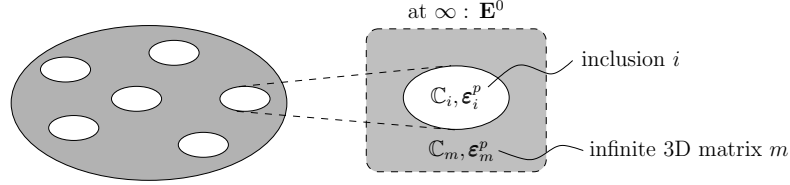


Fig. 1.5: Mori-Tanaka-type RVE consisting of two phases: matrix and inclusion

The concentration tensors read according to (1.11) as

$$\begin{aligned} \mathbb{A}_i &= \mathbb{A}_i^\infty : \{f_i \mathbb{A}_i^\infty + f_m \mathbb{A}_m^\infty\}^{-1}, \\ \mathbb{A}_m &= \mathbb{A}_m^\infty : \{f_i \mathbb{A}_i^\infty + f_m \mathbb{A}_m^\infty\}^{-1}, \end{aligned} \quad (1.13)$$

with

$$\begin{aligned} \mathbb{A}_i^\infty &= [\mathbb{I} + \mathbb{P}_i^0 : (\mathbb{C}_i - \mathbb{C}_m)]^{-1}, \\ \mathbb{A}_m^\infty &= \mathbb{I}. \end{aligned} \quad (1.14)$$

The microstrain in the matrix phase, $\boldsymbol{\varepsilon}_m$ and in the inclusion phase, $\boldsymbol{\varepsilon}_i$ are related to the macroscopic strain \mathbf{E} imposed on the RVE and the plastic strains inside the two phases according to (1.5) by

$$\begin{aligned} \boldsymbol{\varepsilon}_m &= \mathbb{A}_m : \mathbf{E} + \mathbb{D}_{mi} : \boldsymbol{\varepsilon}_i^p + \mathbb{D}_{mm} : \boldsymbol{\varepsilon}_m^p, \\ \boldsymbol{\varepsilon}_i &= \mathbb{A}_i : \mathbf{E} + \mathbb{D}_{ii} : \boldsymbol{\varepsilon}_i^p + \mathbb{D}_{im} : \boldsymbol{\varepsilon}_m^p. \end{aligned} \quad (1.15)$$

Following the derivation in Pichler & Hellmich (2010) for the extended matrix-inclusion problem and considering that, in the present case, the eigenstrain of the auxiliary matrix is equal to the eigenstrain of the matrix phase, delivers the phase strains as

$$\begin{aligned} \boldsymbol{\varepsilon}_m &= \mathbb{A}_m : (\mathbf{E} - f_i \mathbb{A}_i^\infty \mathbb{P}_i : (\mathbb{C}_i : \boldsymbol{\varepsilon}_i^p - \mathbb{C}_m : \boldsymbol{\varepsilon}_m^p)), \\ \boldsymbol{\varepsilon}_i &= \mathbb{A}_i : (\mathbf{E} - f_i \mathbb{A}_i^\infty \mathbb{P}_i : (\mathbb{C}_i : \boldsymbol{\varepsilon}_i^p - \mathbb{C}_m : \boldsymbol{\varepsilon}_m^p)) + \mathbb{A}_i^\infty \mathbb{P}_i : (\mathbb{C}_i : \boldsymbol{\varepsilon}_i^p - \mathbb{C}_m : \boldsymbol{\varepsilon}_m^p). \end{aligned} \quad (1.16)$$

By comparing both equations (1.15) and (1.16), the expressions of the influence tensors can be derived as

$$\begin{aligned} \mathbb{D}_{mi} &= -f_i \mathbb{A}_m : \mathbb{A}_i^\infty : \mathbb{P}_i : \mathbb{C}_i, \\ \mathbb{D}_{mm} &= f_i \mathbb{A}_m : \mathbb{A}_i^\infty : \mathbb{P}_i : \mathbb{C}_m, \\ \mathbb{D}_{ii} &= (\mathbb{I} - f_i \mathbb{A}_i) : \mathbb{A}_i^\infty : \mathbb{P}_i : \mathbb{C}_i, \\ \mathbb{D}_{im} &= (f_i \mathbb{A}_i - \mathbb{I}) : \mathbb{A}_i^\infty : \mathbb{P}_i : \mathbb{C}_m. \end{aligned} \quad (1.17)$$

1.3.2.2 Self-consistent scheme for a two-phase composite

We consider a self-consistent RVE with two differently shaped inclusion phases i and j embedded in an auxiliary matrix with stiffness of the RVE itself (\mathbf{C}_{hom}) and no volume fraction, see Figure 1.6. Both inclusion phases may be subjected to plastic strains, $\boldsymbol{\varepsilon}_i^p$ and $\boldsymbol{\varepsilon}_j^p$.

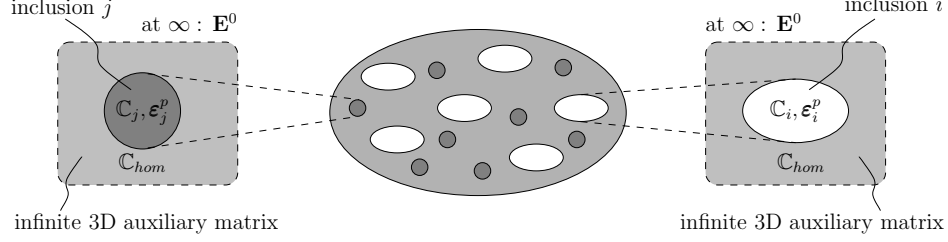


Fig. 1.6: Self-consistent RVE consisting of two phases embedded in an auxiliary matrix

The concentration tensors read according to (1.11) as

$$\begin{aligned} \mathbb{A}_i &= \mathbb{A}_i^\infty : \left\{ f_i \mathbb{A}_i^\infty + f_j \mathbb{A}_j^\infty \right\}^{-1} \\ \mathbb{A}_j &= \mathbb{A}_j^\infty : \left\{ f_i \mathbb{A}_i^\infty + f_j \mathbb{A}_j^\infty \right\}^{-1} \end{aligned} \quad (1.18)$$

with

$$\begin{aligned} \mathbb{A}_i^\infty &= [\mathbb{I} + \mathbb{P}_i : (\mathbf{C}_i - \mathbf{C}_{\text{hom}})]^{-1} \\ \mathbb{A}_j^\infty &= [\mathbb{I} + \mathbb{P}_j : (\mathbf{C}_j - \mathbf{C}_{\text{hom}})]^{-1} \end{aligned} \quad (1.19)$$

The microstrains in the two phases $\boldsymbol{\varepsilon}_i$ and $\boldsymbol{\varepsilon}_j$ are related to the macroscopic strain \mathbf{E} imposed on the RVE and the plastic strains inside the phases according to (1.5) by

$$\begin{aligned} \boldsymbol{\varepsilon}_i &= \mathbb{A}_i : \mathbf{E} + \mathbb{D}_{ii} : \boldsymbol{\varepsilon}_i^p + \mathbb{D}_{ij} : \boldsymbol{\varepsilon}_j^p \\ \boldsymbol{\varepsilon}_j &= \mathbb{A}_j : \mathbf{E} + \mathbb{D}_{ji} : \boldsymbol{\varepsilon}_i^p + \mathbb{D}_{jj} : \boldsymbol{\varepsilon}_j^p \end{aligned} \quad (1.20)$$

According to the matrix-inclusion problem extended with auxiliary matrix eigenstress, the influence tensors are defined as (Pichler & Hellmich 2010)

$$\begin{aligned} \mathbb{D}_{ij} &= \left\{ [\delta_{ij} \mathbb{I} - f_j \mathbb{A}_i] : \mathbb{A}_j^\infty : \mathbb{P}_j + \left[\mathbb{A}_i : \sum_k f_k \mathbb{A}_k^\infty : \mathbb{P}_k - \mathbb{A}_i^\infty : \mathbb{P}_i \right] \right. \\ &\quad \left. : \left[\sum_k f_k (\mathbf{C}_{\text{hom}} - \mathbf{C}_k) : \mathbb{A}_k^\infty : \mathbb{P}_k \right]^{-1} : f_j \left[(\mathbb{I} - \mathbb{A}_j)^T + (\mathbf{C}_{\text{hom}} - \mathbf{C}_j) : \mathbb{A}_j^\infty : \mathbb{P}_j \right] \right\} : \mathbf{C}_j \end{aligned} \quad (1.21)$$

In case the two inclusion phases exhibit the same shape, hence they are both associated with one and the same Hill tensor $\mathbb{P}_i = \mathbb{P}_j = \mathbb{P}$, the influence tensors (1.21) simplify to (Pichler & Hellmich 2010)

$$\begin{aligned} \mathbb{D}_{ii} &= [\mathbb{I} - f_i \mathbb{A}_i] : \mathbb{A}_i^\infty : \mathbb{P} : \mathbf{C}_i \\ \mathbb{D}_{ij} &= -\mathbb{A}_i : f_j \mathbb{A}_j^\infty : \mathbb{P} : \mathbf{C}_j \\ \mathbb{D}_{jj} &= [\mathbb{I} - f_j \mathbb{A}_j] : \mathbb{A}_j^\infty : \mathbb{P} : \mathbf{C}_j \\ \mathbb{D}_{ji} &= -\mathbb{A}_j : f_i \mathbb{A}_i^\infty : \mathbb{P} : \mathbf{C}_i \end{aligned} \quad (1.22)$$

1.3.2.3 Self-consistent scheme for a porous polycrystal

We consider a self-consistent RVE with inclusion phases embedded in an auxiliary matrix: a spherical-shaped pore phase p and infinitely many needle-shaped solid phases s , which are orientated in all space directions, each represented as a cylindrical inclusion, see Figure 1.7. The needles may be subjected to plastic strains and their orientation is defined through the vector \mathbf{e}_r , given as a function of the orthonormal base frame \mathbf{e}_1 , \mathbf{e}_2 and \mathbf{e}_3 and of the longitudinal and co-latitudinal angles φ and θ (see Figure 1.4)

$$\mathbf{e}_r = \sin \theta (\cos \varphi \mathbf{e}_1 + \sin \varphi \mathbf{e}_2) + \cos \theta \mathbf{e}_3 \quad (1.23)$$

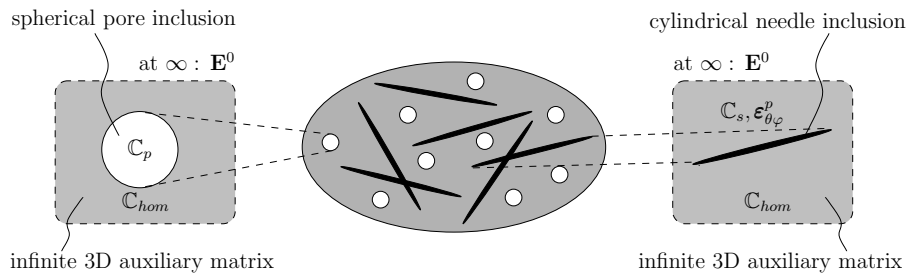


Fig. 1.7: Self-consistent RVE representing a porous polycrystal

The summation over all needle orientations, which is necessary to evaluate for example the strain and stress average rules or the concentration-influence relations, is done by integration over the angles $\varphi = \{0, \dots, \pi\}$ and $\theta = \{0, \dots, 2\pi\}$. For algorithmic treatment these integrals are approximated by weighted sums of the integrands being evaluated at a particular set \mathcal{G} of Gaussian points on the unit sphere, which are quantified in terms of the two angles $\{\theta_i, \varphi_i\}_{i \in \mathcal{G}}$ and their associated Gaussian weights ω_i . Accordingly, the integral over the unit sphere of an arbitrary function $a_{\theta\varphi}$ depending on θ and φ can be approximated through

$$\int_{\theta=0}^{\pi} \int_{\varphi=0}^{2\pi} a_{\theta\varphi} \frac{\sin \theta}{4\pi} d\theta d\varphi = \sum_{i \in \mathcal{G}} \omega_i a_{\theta\varphi}(\theta_i, \varphi_i) = \sum_{i \in \mathcal{G}} \omega_i a_i \quad (1.24)$$

Hence, the concentration tensors for the pore phase and the needle phase evaluated for a particular set of Gaussian points i , read according to (1.11) as (Morin et al. 2017)

$$\begin{aligned} \mathbb{A}_{s,i} &= \mathbb{A}_{s,i}^\infty : \left\{ f_p \mathbb{A}_p^\infty + f_s \sum_{j \in \mathcal{G}} \omega_j \mathbb{A}_{s,j}^\infty \right\}^{-1} \quad \forall i \in \mathcal{G} \\ \mathbb{A}_p &= \mathbb{A}_p^\infty : \left\{ f_p \mathbb{A}_p^\infty + f_s \sum_{j \in \mathcal{G}} \omega_j \mathbb{A}_{s,j}^\infty \right\}^{-1} \end{aligned} \quad (1.25)$$

with

$$\begin{aligned} \mathbb{A}_{s,i}^\infty &= [\mathbb{I} + \mathbb{P}_s(\theta_i, \varphi_i) : (\mathbb{C}_s - \mathbb{C}_{\text{hom}})]^{-1} \\ \mathbb{A}_p^\infty &= [\mathbb{I} + \mathbb{P}_p : (\mathbb{C}_p - \mathbb{C}_{\text{hom}})]^{-1} \end{aligned} \quad (1.26)$$

The microstrain in the phases $\boldsymbol{\varepsilon}_i$ and $\boldsymbol{\varepsilon}_p$ are related to the macroscopic strain imposed on the RVE and the plastic strain inside the solid needle phase according to (1.5) by

$$\begin{aligned}\boldsymbol{\varepsilon}_{s,i} &= \mathbb{A}_{s,i} : \mathbf{E} + \sum_{j \in \mathcal{G}} \omega_j \mathbb{D}_{ij} : \boldsymbol{\varepsilon}_{s,j}^p \quad \forall i \in \mathcal{G} \\ \boldsymbol{\varepsilon}_p &= \mathbb{A}_p : \mathbf{E} + \sum_{j \in \mathcal{G}} \omega_j \mathbb{D}_{pj} : \boldsymbol{\varepsilon}_{s,j}^p\end{aligned}\tag{1.27}$$

According to the matrix-inclusion problem extended with auxiliary matrix eigenstress and including the discretization over a set of Gaussian points, the influence tensors are defined as (Morin et al. 2017)

$$\begin{aligned}\mathbb{D}_{pj} &= \left\{ -\mathbb{A}_p : f_s \mathbb{A}_{s,j}^\infty : \mathbb{P}_s(\boldsymbol{\theta}_j, \boldsymbol{\varphi}_j) + \right. \\ &\quad \left[f_p \mathbb{A}_p : \mathbb{A}_p^\infty : \mathbb{P}_p + f_s \mathbb{A}_p : \sum_{k \in \mathcal{G}} \omega_k \mathbb{A}_{s,k}^\infty : \mathbb{P}_s(\boldsymbol{\theta}_k, \boldsymbol{\varphi}_k) - \mathbb{A}_p^\infty : \mathbb{P}_p \right] : \\ &\quad \left[f_p (\mathbb{C}_{\text{hom}} - \mathbb{C}_p) : \mathbb{A}_p^\infty : \mathbb{P}_p + f_s (\mathbb{C}_{\text{hom}} - \mathbb{C}_s) : \sum_{k \in \mathcal{G}} \omega_k \mathbb{A}_{s,k}^\infty : \mathbb{P}_s(\boldsymbol{\theta}_k, \boldsymbol{\varphi}_k) \right]^{-1} : \\ &\quad \left. f_s \left[(\mathbb{I} - \mathbb{A}_{s,j})^T + (\mathbb{C}_{\text{hom}} - \mathbb{C}_s) : \mathbb{A}_{s,j}^\infty : \mathbb{P}_s(\boldsymbol{\theta}_j, \boldsymbol{\varphi}_j) \right] \right\} : \mathbb{C}_s,\end{aligned}\tag{1.28}$$

$$\begin{aligned}\mathbb{D}_{ij} &= \left\{ [\delta_{ij} \omega_j^{-1} \mathbb{I} - \mathbb{A}_{s,i} : f_s] : \mathbb{A}_{s,j}^\infty : \mathbb{P}_s(\boldsymbol{\theta}_j, \boldsymbol{\varphi}_j) + \right. \\ &\quad \left[f_p \mathbb{A}_{s,i} : \mathbb{A}_p^\infty : \mathbb{P}_p + f_s \mathbb{A}_{s,i} : \sum_{k \in \mathcal{G}} \omega_k \mathbb{A}_{s,k}^\infty : \mathbb{P}_s(\boldsymbol{\theta}_k, \boldsymbol{\varphi}_k) - \mathbb{A}_{s,i}^\infty : \mathbb{P}_s(\boldsymbol{\theta}_i, \boldsymbol{\varphi}_i) \right] : \\ &\quad \left[f_p (\mathbb{C}_{\text{hom}} - \mathbb{C}_p) : \mathbb{A}_p^\infty : \mathbb{P}_p + f_s (\mathbb{C}_{\text{hom}} - \mathbb{C}_s) : \sum_{k \in \mathcal{G}} \omega_k \mathbb{A}_{s,k}^\infty : \mathbb{P}_s(\boldsymbol{\theta}_k, \boldsymbol{\varphi}_k) \right]^{-1} : \\ &\quad \left. f_s \left[(\mathbb{I} - \mathbb{A}_{s,j})^T + (\mathbb{C}_{\text{hom}} - \mathbb{C}_s) : \mathbb{A}_{s,j}^\infty : \mathbb{P}_s(\boldsymbol{\theta}_j, \boldsymbol{\varphi}_j) \right] \right\} : \mathbb{C}_s,\end{aligned}$$

1.4 Periodic homogenization - Unit Cell Method

The unit cell method is a homogenization method suitable when dealing with materials with a (nearly) periodic microstructure, be it a classical continuum or a highly cellular material where the volume fraction of the solid phase is very low compared to the void phase. Analogous to the Mean-field method, in the course of periodic homogenization, the effective properties are determined based on the study of an RVE, being in that case a so-called *unit cell*. This unit cell is a basic unit of the material, which defines by periodic repetition and translation the whole microstructure of the material. This periodic translation in a d -dimensional space must take place along a combination of integer multiples of the vectors \mathbf{w}_i , $i \in (1, d)$ of translational invariance of the microstructure. These vectors may (but don't have to) coincide with the unit cell spanning vectors. Generally, unit cells are non-unique, leading to a wide range of possible shapes for one and the same microstructure, see Figure 1.8. However, the resulting effective behavior should be independent of the chosen unit cell (Michel et al. 1999).

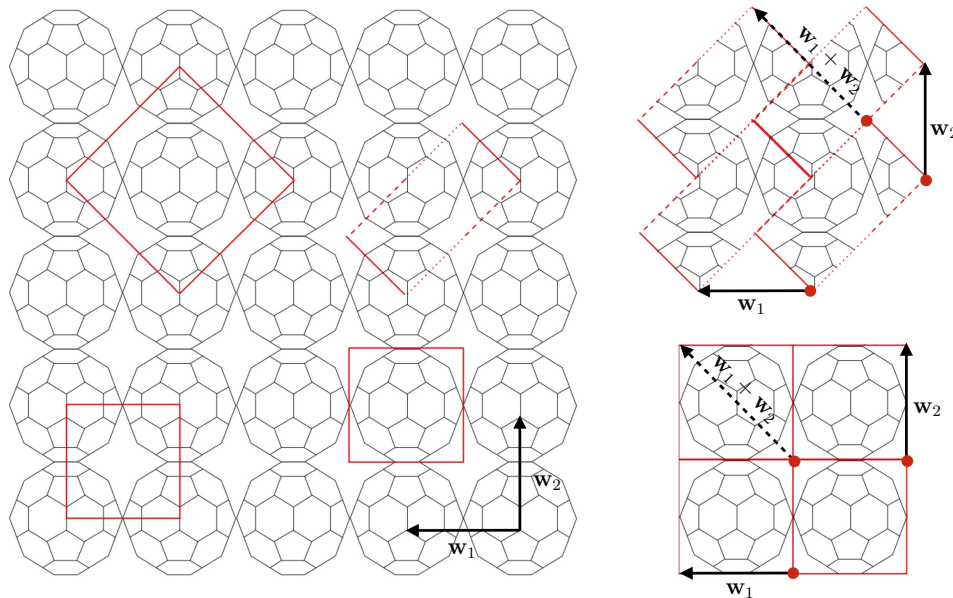


Fig. 1.8: *Different possible choices of the unit cell for a periodic 2-dimensional structure with two vectors of translational invariance*

1.4.1 Periodic strain and stress fields

If a periodic material is subjected to an affine displacement on its boundary, the resulting microscopic strain and stress fields conform themselves to the periodicity of the microstructure (Suquet 1985). The microscopic strain and stress fields are therefore periodic and can be determined on the level of a single unit cell. To ensure periodicity, the boundary of the unit cell S_{UC} is divided into surface pairs as shown in Figure 1.9, consisting of a positive part S_{UC}^{i+} and a negative part S_{UC}^{i-} with periodically corresponding nodes $\mathbf{x}^{i+} \in S_{UC}^{i+}$ and $\mathbf{x}^{i-} \in S_{UC}^{i-}$, being connected by the vectors \mathbf{w}_i of translational invariance of the microstructure.

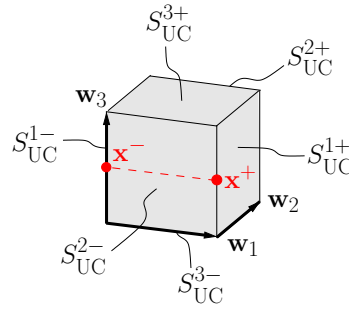


Fig. 1.9: Unit Cell with surface pairs

Periodic strain

The microscopic strain field $\boldsymbol{\varepsilon}(\mathbf{x})$ within the unit cell can be split into the overall (average) strain \mathbf{E} and an additional (fluctuation) field $\boldsymbol{\varepsilon}^*(\mathbf{x})$ accounting for the heterogeneities within the material

$$\boldsymbol{\varepsilon}(\mathbf{x}) = \mathbf{E} + \boldsymbol{\varepsilon}^*(\mathbf{x}). \quad (1.29)$$

Michel et al. (1999) proves, that the average of the fluctuation strain field vanishes on the unit cell, causing the average of the total strain to be equal the macroscopic strain

$$\frac{1}{V_{UC}} \int_{V_{UC}} \boldsymbol{\varepsilon}(\mathbf{x}) = \mathbf{E} \quad \text{and} \quad \frac{1}{V_{UC}} \int_{V_{UC}} \boldsymbol{\varepsilon}^*(\mathbf{x}) = 0. \quad (1.30)$$

Periodic stress

The microscopic stress field $\boldsymbol{\sigma}(\mathbf{x})$, in addition to being periodic, has to fulfill equilibrium inside the volume of the periodic medium as well as on its boundary. This conditions require the stress field to be divergence free and the traction vectors $\mathbf{T}(\mathbf{x}) = \boldsymbol{\sigma}(\mathbf{x}) \cdot \mathbf{n}(\mathbf{x})$ to be opposite on opposite points of boundary of the unit cell

$$\text{div } \boldsymbol{\sigma} = 0 \quad \text{and} \quad \mathbf{T}(\mathbf{x}^{i+}) = -\mathbf{T}(\mathbf{x}^{i-}), \quad (1.31)$$

whereby \mathbf{x}^{i+} and \mathbf{x}^{i-} are two periodically corresponding points of the microstructure on the surface of the unit cell.

1.4.2 Displacement controlled method of macroscopic degrees of freedom

Since the discrete structure within the unit cell is taken into account for the homogenization process, the microscopic geometry-specific behavior is often computed using a standard finite element based concept, the so-called concept of macroscopic degrees of freedom (concept of master nodes) as proposed by Michel et al. (1999). To this end a displacement controlled model may be chosen, where the unit cell is subjected to predefined effective strain states \mathbf{E} at the macroscopic scale, which provoke a locally changing but periodic response at the microscopic scale. The boundary conditions which have to be applied to the unit cell to

reproduce this state of periodicity and ensure equilibrium as well as a seamless tiling of space with the unit cell in both its undeformed and deformed configuration, read as

$$\left. \begin{aligned} \mathbf{u}(\mathbf{x}) &= \mathbf{E} \cdot \mathbf{x} + \mathbf{u}^*(\mathbf{x}) \\ \mathbf{u}^*(\mathbf{x}^{i+}) &= \mathbf{u}^*(\mathbf{x}^{i-}) \\ \mathbf{T}(\mathbf{x}^{i+}) &= -\mathbf{T}(\mathbf{x}^{i-}) \end{aligned} \right\} \forall \mathbf{x} \in S_{\text{UC}} \quad (1.32)$$

The displacement field $\mathbf{u}(\mathbf{x})$ is thereby split into the overall (average) displacement field $\mathbf{E} \cdot \mathbf{x}$ and an additional (fluctuation) field $\mathbf{u}^*(\mathbf{x})$, which accounts for the heterogeneities within the material and can be proved to be periodic up to a rigid body motion (Michel et al. 1999). Periodicity implies identical values for the displacement fluctuation field $\mathbf{u}^*(\mathbf{x}^{i+})$ and anti-periodic tractions $\mathbf{T}(\mathbf{x}^{i+})$ acting in two periodically corresponding points \mathbf{x}^{i+} and \mathbf{x}^{i-} of the microstructure.

An effective way to implement the periodic boundary conditions in FE-simulations is the introduction of additional arbitrarily chosen master nodes M_i (one for each surface pair of the unit cell). As described by Kästner et al. (2011), these master nodes are used to control the relative displacement of two opposite surfaces and are connected to the unit cell by enforcing constraint equations

$$\mathbf{u}(M_i) = \mathbf{u}(\mathbf{x}^{i+}) - \mathbf{u}(\mathbf{x}^{i-}) = \mathbf{E}^{kl} \cdot (\mathbf{x}^{i+} - \mathbf{x}^{i-}). \quad (1.33)$$

Once a suitable FE model has been defined and the boundary conditions have been applied, a three-dimensional unit cell must be subjected to six linearly independent effective strain states, to enable an access to the 36 independent components of the stiffness tensor. To actually compute this effective stiffness tensor of the heterogeneous material based on the results of the six FE-simulations, a physically meaningful criterion of equivalence has to be found to link the two successive scales. To this end, a powerful tool used in the further course of this work, is the principle of virtual power as proposed by Germain (1973), stating that the total power of all internal and external forces acting on an equilibrated system in virtual motion must be zero

$$\mathcal{P}^{int} + \mathcal{P}^{ext} = 0. \quad (1.34)$$

For a classical 3D continuum \mathcal{P}^{int} and \mathcal{P}^{ext} read as

$$\mathcal{P}^{int} = - \int_V \boldsymbol{\sigma}(\mathbf{x}) : \hat{\mathbf{d}}(\mathbf{x}) dV, \quad (1.35)$$

and

$$\mathcal{P}^{ext} = \int_V \mathbf{f}(\mathbf{x}) \cdot \hat{\mathbf{v}}(\mathbf{x}) dV + \int_S \mathbf{T}(\mathbf{n}, \mathbf{x}) \cdot \hat{\mathbf{v}}(\mathbf{x}) dA, \quad (1.36)$$

with \mathbf{x} denoting the the location vector of points throughout the continuum with volume V and surface S , $\hat{\mathbf{v}}(x)$ denoting an arbitrary continuous virtual velocity field, $\hat{\mathbf{d}}(\mathbf{x}) = \nabla \hat{\mathbf{v}}(x)$ denoting the virtual Eulerian strain rate tensor, $\mathbf{f}(\mathbf{x})$ and $\mathbf{T}(\mathbf{x}, \mathbf{n})$ denoting the volume and surface forces, and $\boldsymbol{\sigma}(\mathbf{x})$ denoting the stress tensor.

For a system of forces \mathbf{F}_i acting in points \mathbf{x}_i , \mathcal{P}^{ext} reads as

$$\mathcal{P}^{ext} = \sum_i \mathbf{F}_i(\mathbf{x}_i) \cdot \hat{\mathbf{v}}(\mathbf{x}_i). \quad (1.37)$$

1.5 Outline of the thesis

In the remainder of the present thesis, the different homogenization methods presented in **Chapter 1** are applied to three different biomedical materials in order to predict their effective mechanical behavior.

Chapter 2 deals with porous polycrystal-type microstructures. In this chapter, the structural stability of such porous polycrystals is assessed on the one hand by means of yield design, and on the other hand by applying a full elastoplastic analysis based on a novel iterative return-map algorithm. Both methods rely on an extension of Dvorak's transformation field analysis and are in the further course used to predict the mechanical behavior of cement lines in equine osteonal bone. The thereby gained results allow a comparison and validation of the two methods.

In **Chapter 3**, a theoretical framework for continuum micromechanics-based multiscale elastoplasticity is developed and applied to bone. The novel iterative return-map algorithm proposed in Chapter 2 is therefore integrated into a novel multiscale elastoplastic continuum micromechanics model for cortical bone to investigate the mechanical behavior of the hierarchically organized material. Bone exhibits species independent, "universal" organizational patterns, which we propose to represent in terms of a six-step micromechanical homogenization scheme. The model is based on tissue-independent mechanical properties of bone's three elementary constituents, mineral, collagen and water, while their volume fractions can be adapted according to sample-specific bone compositions in terms of porosity and extracellular mass density. The multiscale model is in the further course subjected to a full elastoplastic analysis to predict sample-specific stiffness and strength values of cortical bone and thereby aims at explaining the great variety in the mechanical properties of bone.

While Chapter 2 and 3 use a mean-field homogenization method, **Chapter 4** deals with homogenization of a periodic microstructure by applying the unit cell method. The examined biomedical material is furthermore not continuous at the microscopic scale but consists of a discrete arrangement of cylindrical beam elements. In detail, Chapter 4 deals with cage-like microscaffolds filled with tissue spheroids, which shall be used as building blocks in tissue engineering. In order to facilitate the design process of the scaffolds targeting their clinical application, this chapter investigates the effects of varying scaffold-materials and dimensions on the overall effective stiffness properties of different periodic scaffold-packings. We use the unit cell method based on periodic homogenization by means of the Finite Element Method and propose a transition from locally changing beam quantities to a fictitious homogenized continuum based on the principle of virtual power.

Finally, the thesis is concluded in **Chapter 5**.

Chapter 2

Transformation field analysis-based yield design of porous polycrystals: theory and full elastoplastic validation

Authored by Valentina Kumbolder & Christian Hellmich

Submitted to *International Journal of Plasticity*

Abstract: Plastic collapse of extended bodies or material microstructures is typically linked to failure mechanisms involving displacement discontinuities; and in the framework of limit analysis or yield design, the power of admissible stress states on corresponding virtual velocities gives access to upper bounds of collapse loads. We here extend this classical concept towards microstructures with non-localized plastic fields, namely to plastic polycrystals. At the limit state, the elastic portion of the overall strain rate vanishes, so that the concentration-influence relations of transformation field analysis, after setting equal the total and the plastic microscopic strain rates, give direct access to plastic collapse load-related macro-to-micro concentration relations, corresponding virtual velocity fields, and associated ultimate strength values for the homogenized porous polycrystals. The latter limit loads are impressively confirmed through the results of a full elastoplastic analysis. However, the novel yield design solution is over hundred times more efficient than a full elastoplastic analysis. For the latter, we introduce a new algorithm in which elastic trial stress states are step-wisely backprojected, along repeatedly updated plastic flow directions, onto the various yield surfaces associated with the solid plastic material phases.

Contribution: Christian Hellmich set up the overall research strategy and supervised the research progress as well as the finalization of the manuscript. Valentina Kumbolder conducted the derivation of the mathematical framework, developed the corresponding Matlab codes, improved and optimized the return-mapping algorithm, performed all computations and supported the making of the manuscript.

Keywords: yield design, micromechanics, porous polycrystals, concentration-influence relations, transformation field analysis, elastoplasticity, return map algorithm

2.1 Introduction

Yield design, also referred to as limit analysis, is a particularly efficient, yet reliable, method for assessing the stability of structures, from the strength characteristics of the materials building them up. Its origin may be traced back to the famous paper of Coulomb (1773); dealing with soil mechanics and structural engineering problems. The theoretical foundations of yield design theory, in terms of the principle of virtual power, were reviewed by Salençon (1990), thereby acknowledging the fundamental idea of Drucker & Prager (1952) to introduce quantities of the dimension “power” when discussing the limit state of rigid-perfectly plastic solids: Let external loads perform power on velocities which are compatible with typical failure patterns of the investigated structures. Then, the maximum power of admissible stresses on the aforementioned failure pattern velocities yields an upper bound for the maximum or limit load bearable by the investigated system.

Beyond soil mechanics and structural engineering problems, such as the failure of anisotropic plates (Corradi & Vena 2003, Capsoni et al. 2001), or the seismic retrofitting of masonry towers (Milani et al. 2018) yield design theory and limit analysis have had, during the last four decades, a major impact on inelastic material micromechanics. The most straightforward micromechanical application of yield design theory concerns the failure of material systems along pre-defined velocity discontinuities (“slip lines”), such as joints within rock masses (Maghous et al. 1998, Bekaert & Maghous 1996), or mortar joints within masonry (De Buhan & De Felice 1997, Milani et al. 2006, Tiberti & Milani 2020). The situation is more delicate when it comes to non-localized plastic fields within the material microstructures. Corresponding material theories have been developed along different conceptual lines, having all to do with the question of how to introduce appropriate power expressions for admissible microstresses and corresponding microvelocity fields representing characteristic microstructural failure patterns. The corresponding classical approach lets microstresses lying on failure surfaces perform power on suitably chosen “trial velocity fields”: For incompressible von Mises-type rigid-plastic hollow spheres or cylinders representing microstructures consisting of matrices and voids, Gurson (1977) proposed to estimate explicit forms of the trial fields from incompressible linear viscous fluid behavior, obeying an associative flow rule, in combination with homogeneous boundary conditions linking the microvelocity field to macroscopic strain rates. This key concept of the famous Gurson model has been extended along various lines: Well-established extensions concern anisotropic plastic behavior (Benzerga & Besson 2001, Keralavarma & Benzerga 2010), or plastic dilatancy (Guo et al. 2008), and more recent examples include amendments of Gurson’s microscopic power expression (Cazacu et al. 2013), as well as the investigation of matrices with a more complex plastic behavior, be they characterized by an elliptic yield criterion (Shen et al. 2012), by a Mohr-Coulomb criterion (Anoukou et al. 2016), or by general yield functions depending on three stress invariants (Brach et al. 2017, 2018). In order to deal with microstructures whose complexity lies beyond that of plastic matrices with voids, an alternative strategy to Gurson’s velocity fields has gained considerable popularity: Approximative strain fields and corresponding power expressions, called strain rate potentials, dissipation potentials or support functions, are homogenized by means of the modified secant method resting on mathematical solutions from elastic micromechanics applied to “equivalent linear composite” (Castaneda & Suquet 1997, Barthélémy & Dormieux 2004). This strategy has been applied for various microstructural morphologies, such as nanoporous materials with dominant surface/interface stress effects (Zhang, Wang & Chen 2010), or argillite where voids and mineral inclusions are present at different scales (Shen et al. 2013), or to granular materials with cohesive Mohr-Coulomb interfaces (He et al. 2013) with

a homogenized behavior reminiscent to that of the famous Cam Clay model (Bignonnet et al. 2016).

Despite of the aforementioned rich progress in the field, one may still remark that Gurson-type and modified secant-type model results do show some (often acceptable) deviations from the results of full elastoplastic simulations (Fritzen et al. 2012). This motivates re-consideration of the theoretical foundations of the aforementioned homogenization approaches set in the framework of yield design theory; in particular the adoption of rigid-viscous material models for the actually *elasto*-plastically behaving microstructures. It is in this spirit that we here propose an alternative to the void shape-specific construction of “trial velocity fields” or the morphology-specific construction of “equivalent composites”, so as to widen the applicability range of yield design strategies for microstructures with non-localized plastic phenomena. The key ingredient of our new strategy is an extension of Dvorak’s transformation field analysis (Dvorak 1992, Dvorak et al. 1994, Dvorak & Benveniste 1992, Pichler & Hellmich 2010, Dvorak 2013, Morin et al. 2017, Königsberger et al. 2020). Based on the extended use of Green’s functions, this type of micromechanical analysis provides so-called concentration-influence relations, which link, based on the elastic properties of the microstructural elements, fields of total microscopic strains to the total macroscopic strains and to fields of microscopic eigenstrains, i.e. to strains not linked to elastic deformations. In order to apply this general concept to yield design problems, the microscopic eigenstrains are specified to be plastic strains. Finally, adopting a classical reasoning of Drucker & Prager (1952), the plastic collapse is associated to a situation where the microscopic plastic strain rate is identical to the total microscopic strain rate.

Accordingly, the remainder of the present paper is organized as follows: We first review the micromechanics of eigenstressed microheterogeneous materials, and we use corresponding key results for constructing a virtual micro-velocity field associated with plastic failure of the microstructure (Section 2.2). We then determine the latter for a discretized RVE of a porous polycrystal and let them perform power on microstresses fulfilling a Mohr-Coulomb criterion to access the macroscopic ultimate load (Section 2.3). The results are validated by a full elastoplastic analysis in Section 2.4, for which we introduce a new algorithm with iterative updates of the plastic flow directions used for backprojection. Finally, the paper is concluded with a discussion in Section 2.5.

2.2 Yield design for materials with continuous micro-heterogeneous plastic fields

2.2.1 Fundamentals of continuum micromechanics – representative volume element

In continuum micromechanics (Zaoui 2002), a piece of material is considered to be homogeneous at the *macroscopic* scale, but heterogeneous when zooming into a lower - *microscopic* - scale. Accordingly, at the macroscopic scale, a piece of material is associated to a point, i.e. an indivisible or partless “chunk” (Rajagopal 2013), while, at the microscopic scale, the same piece of material is associated with a so-called Representative Volume Element (RVE). This different associations are relevant if the separation-of-scales-requirement is fulfilled. Mathematically, it reads as (Hashin 1983, Zaoui 2002)

$$d \ll \ell \ll \mathcal{L} \quad (2.1)$$

whereby the characteristic length ℓ of the RVE needs to exceed the characteristic size d of the inhomogeneities by a factor of typically 2 to 3 (Drugan & Willis 1996), while ℓ needs to be, typically by a factor of 5 to 10 (Kohlhauser & Hellmich 2013), separated from the structural length \mathcal{L} . The latter is given through the macroscopic strain field $\mathbf{E}(\mathbf{X})$, with \mathbf{E} as the macroscopic (linearized) strain associated with line elements of length ℓ , and \mathbf{X} as the macroscopic location vector, labeling positions in space up to resolution of ℓ . More precisely, Auriault et al. (2009) defined the structural length as

$$\mathcal{L} = \frac{\|\mathbf{E}\|}{\|\text{GRAD } \mathbf{E}\|} \quad (2.2)$$

with the macroscopic gradient $\text{GRAD}(\cdot) = \partial(\cdot)/\partial\mathbf{X}$. Macroscopic strains are homogeneous at the level of the RVEs; i.e. they do not depend on the microscopic location vectors \mathbf{x} labeling positions within the RVEs up to a resolution of d . Accordingly, microscopic displacements $\boldsymbol{\xi}$, which are associated to one and the same macroscopic strain tensor, are prescribed at the boundary ∂V_{RVE} of each RVE; this reads mathematically as (Hashin 1983, Zaoui 2002)

$$\forall \mathbf{x} \in \partial V_{\text{RVE}} : \quad \boldsymbol{\xi}(\mathbf{x}) = \mathbf{E} \cdot \mathbf{x} \quad (2.3)$$

Boundary conditions according to Eq. (2.3) imply the so-called strain average rule

$$\mathbf{E} = \frac{1}{V_{\text{RVE}}} \int_{V_{\text{RVE}}} \boldsymbol{\varepsilon}(\mathbf{x}) \, dV \quad (2.4)$$

with the linearized microscopic strain being defined as

$$\boldsymbol{\varepsilon}(\mathbf{x}) = \frac{1}{2} \left(\text{grad } \boldsymbol{\xi}(\mathbf{x}) + \text{grad}^T \boldsymbol{\xi}(\mathbf{x}) \right) = \nabla^S \boldsymbol{\xi} \quad (2.5)$$

with $\text{grad}(\cdot) = \partial(\cdot)/\partial\mathbf{x}$ as the microscopic gradient. Moreover, equilibrium of microscopic external volume forces \mathbf{f} as well as microscopic stresses $\boldsymbol{\sigma}$ is fulfilled in the sense of the Principle of the Virtual Power (PVP) (Germain 1973, Germain et al. 1983): The powers performed by these forces on any admissible microscopic virtual velocity field, $\hat{\mathbf{v}}(\mathbf{x})$ need to be zero. In accordance with Eq. (2.3), admissible virtual velocities need to vanish at the boundary of the RVE. For this situation, the PVP takes the following mathematical format,

$$\forall \hat{\mathbf{v}} : \quad \mathcal{P}_{\text{ext}} + \mathcal{P}_{\text{int}} = \int_{V_{\text{RVE}}} p_{\text{ext}}(\hat{\mathbf{v}}) + p_{\text{int}}(\hat{\mathbf{v}}) \, dV = \int_{V_{\text{RVE}}} \mathbf{f} \cdot \hat{\mathbf{v}} \, dV - \int_{V_{\text{RVE}}} \boldsymbol{\sigma} : \hat{\mathbf{d}} \, dV = 0 \quad (2.6)$$

whereby $\hat{\mathbf{d}} = \nabla^S \hat{\mathbf{v}}$ is the microscopic virtual Eulerian strain rate tensor, and p_{ext} and p_{int} are the power densities of the external and of the internal forces. Finally, homogenization is performed by requiring these power densities to be fully captured through the RVE-specific *macroscopic* virtual velocities $\hat{\mathbf{V}}$ and strain rates $\hat{\mathbf{D}}$, which do not depend on the microscopic location vector \mathbf{x} . Mathematically, this reads as (Königsberger et al. 2020)

$$p_{\text{int}} = -\frac{1}{V_{\text{RVE}}} \int_{V_{\text{RVE}}} \boldsymbol{\sigma}(\mathbf{x}) : \hat{\mathbf{D}} \, dV = -\boldsymbol{\Sigma} : \hat{\mathbf{D}} \quad (2.7)$$

$$p_{\text{ext}} = \frac{1}{V_{\text{RVE}}} \int_{V_{\text{RVE}}} \mathbf{f}(\mathbf{x}) : \hat{\mathbf{V}} \, dV = \mathbf{F} : \hat{\mathbf{V}} \quad (2.8)$$

with the RVE-specific macroscopic stresses Σ and macroscopic volume force \mathbf{F} . Eq. (2.7) and (2.8) obviously induce averaging rules for stresses and volume forces, reading as

$$\Sigma = \frac{1}{V_{\text{RVE}}} \int_{V_{\text{RVE}}} \boldsymbol{\sigma}(\mathbf{x}) \, dV \quad (2.9)$$

$$\mathbf{F} = \frac{1}{V_{\text{RVE}}} \int_{V_{\text{RVE}}} \mathbf{f}(\mathbf{x}) \, dV \quad (2.10)$$

2.2.2 Admissible microstresses and virtual microvelocity fields derived from transformation field analysis

The local bearing capacity of the microstructure within the RVE is associated with the microscopic stresses fulfilling a strength criterion in the form

$$\boldsymbol{\sigma} \in \mathcal{G}(\mathbf{x}) \leftrightarrow \mathfrak{F}(\boldsymbol{\sigma}, \mathbf{x}) \leq 0 \quad \forall \mathbf{x} \in V_{\text{RVE}} \quad (2.11)$$

with the domain of admissible microstress states \mathcal{G} , defined by means of the microscopic yield function \mathfrak{F} . This domain of admissible microstresses, together with the principle of virtual power, allows for the derivation of the kinematic approach of yield design theory (Salençon 1990). The derivation comprises the following steps: First, we identify the RVE-specific power of external forces from Eq. (2.6) and (2.7) as

$$\mathcal{P}_{\text{ext}} + \mathcal{P}_{\text{int}} = 0 \quad \Rightarrow \quad \mathcal{P}_{\text{ext}} = -\mathcal{P}_{\text{int}} = \Sigma : \hat{\mathbf{D}} V_{\text{RVE}} \quad (2.12)$$

Then, we replace the integrand occurring in the power of internal forces by $\boldsymbol{\pi}$ -functions obeying the following supremum characteristics

$$\boldsymbol{\pi}(\mathbf{x}, \hat{\mathbf{d}}(\mathbf{x})) = \text{Sup} \{ \boldsymbol{\sigma}(\mathbf{x}) : \hat{\mathbf{d}}(\mathbf{x}) \mid \boldsymbol{\sigma} \in \mathcal{G} \} \quad (2.13)$$

yielding, together with Eq. (2.6) and (2.12), the following inequality

$$\Sigma : \hat{\mathbf{D}} \leq \frac{1}{V_{\text{RVE}}} \int_{V_{\text{RVE}}} \boldsymbol{\pi}(\mathbf{x}, \hat{\mathbf{d}}(\mathbf{x})) \, dV \quad (2.14)$$

Hence, integrals over the $\boldsymbol{\pi}$ -functions (“admissible microscopic stresses performing powers on suitably chosen virtual microstrain rates”) give upper bounds for “macroscopic loads” Σ .

The more realistic the chosen virtual microvelocity fields, the closer the upper bounds for the bearable load approach the *actually bearable* ultimate (or limit) load. Aiming at a particularly realistic representation of micro-plastic failure mechanisms within the RVE, we resort to the transformation field analysis (Dvorak 1992, Dvorak et al. 1994, Dvorak & Benveniste 1992, Pichler & Hellmich 2010, Morin et al. 2017, Königsberger et al. 2020), as it provides generally valid relations between microscopic eigenstrains, such as *plastic strains*, microscopic (total) strains, and macroscopic strains. Accordingly, the microscopic strains depend multilinearly on both the macroscopic strains \mathbf{E} and on the microscopic plastic (eigen-)strains $\boldsymbol{\varepsilon}^p$,

$$\boldsymbol{\varepsilon}(\mathbf{x}) = \mathbb{A}(\mathbf{x}) : \mathbf{E} + \int_{V_{\text{RVE}}} \mathbb{D}(\mathbf{x}, \mathbf{x}') : \boldsymbol{\varepsilon}^p(\mathbf{x}') \, dV(\mathbf{x}') \quad (2.15)$$

with the fourth-order strain concentration or downscaling tensor field \mathbb{A} and the influence tensor field \mathbb{D} quantifying the effect of microscopic plastic strains at location \mathbf{x}' on the microscopic (total) strains at location \mathbf{x} . Moreover, we consider the limit case of collapse (Drucker & Prager 1952), where the plastic strain rate becomes identical to the total strain rate, $\dot{\boldsymbol{\varepsilon}}^p = \dot{\boldsymbol{\varepsilon}}$, and we choose, under these conditions, the temporal derivatives of the strain measures appearing in Eq.(2.15) as virtual strain rates, i.e. $\hat{\mathbf{D}} = \dot{\mathbf{E}}$ and $\hat{\mathbf{d}} = \dot{\boldsymbol{\varepsilon}}$. Then, Eq. (2.15) readily yields

$$\mathbb{A}(\mathbf{x}) : \hat{\mathbf{D}} + \int_{V_{\text{RVE}}} (\mathbb{D}(\mathbf{x}, \mathbf{x}') - \mathbb{I}\delta(\mathbf{x} - \mathbf{x}')) : \hat{\mathbf{d}}(\mathbf{x}') dV(\mathbf{x}') = 0 \quad (2.16)$$

with the Dirac delta distribution δ , the integration over which yields one, and the value of which is zero everywhere except for the point 0, where this value becomes infinite. Eq. (2.16) is a Fredholm integral equation of the first kind. Its solution $\hat{\mathbf{d}}(\mathbf{x})$ can be formally given as

$$\hat{\mathbf{d}}(\mathbf{x}) = \mathbb{A}^{\text{PC}}(\mathbf{x}) : \hat{\mathbf{D}} \quad (2.17)$$

with the plastic collapse-related strain rate downscaling tensor \mathbb{A}^{PC} . The actual determination of the latter rests on an appropriate solution scheme, as given in more detail in Section 2.3. Insertion of Eq. (2.17) into Eq. (2.14) yields an upper bound for the ultimate macroscopic stress which can be sustained by the investigated RVE; namely

$$\boldsymbol{\Sigma}^{\text{ult}} \leq \frac{1}{V_{\text{RVE}}} \int_{V_{\text{RVE}}} \text{Sup} \{ \boldsymbol{\sigma} : \mathbb{A}^{\text{PC}} \mid \boldsymbol{\sigma} \in \mathcal{G}(\mathbf{x}) \} dV(\mathbf{x}) \quad (2.18)$$

2.3 Yield design for porous plastic polycrystals

2.3.1 RVE of a porous polycrystal

The microstructure within an RVE is in general too complex to be described in complete detail and is therefore reasonably defined as a composition of quasi-homogeneous subdomains, so-called phases. These phases have known quantitative and qualitative properties (such as volume fractions f , characteristic shapes and mechanical properties). In the present contribution, we consider an RVE which hosts a spherically shaped pore phase p (of vanishing stiffness and vanishing strength; hence $\mathbb{C}_p = \boldsymbol{\sigma}_p = 0$) with volume fraction f_p , as well as infinitely many needle-shaped solid phases filling altogether volume fraction f_s ; accordingly $f_p + f_s = 1$, see Figure 2.1. The solid needle-shaped phases are oriented in all space directions indicated by Euler angles (φ, θ) , and they exhibit a stiffness \mathbb{C}_s and phase-specific plastic strains $\boldsymbol{\varepsilon}^p(\varphi, \theta)$.

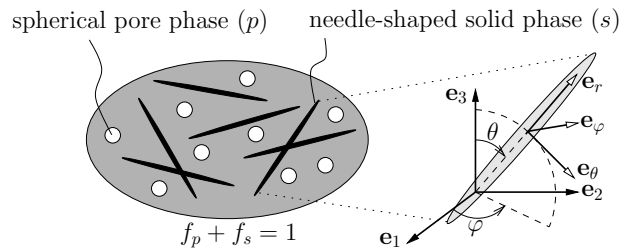


Fig. 2.1: RVE representing a porous polycrystal

2.3.2 Discretization

The infinitely many solid phases oriented in all space directions are discretized through a particular set \mathcal{G} of Gaussian points on the unit sphere, being quantified in terms of the two angles $\{\theta_i, \varphi_i\}_{i \in \mathcal{G}}$ and their associated Gaussian weights ω_i . We here employ a discretization set \mathcal{G} of $N_i = 120$ integration points achieved by the centroids and areas of triangles meshing the unit sphere as described in Badel & Leblond (2004). Accordingly, the integral over the unit sphere, of an arbitrary function a depending on θ and φ can be approximated through

$$\int_{\theta=0}^{\pi} \int_{\varphi=0}^{2\pi} a(\theta, \varphi) \frac{\sin \theta}{4\pi} d\theta d\varphi = \sum_{i \in \mathcal{G}} \omega_i a(\theta_i, \varphi_i) = \sum_{i \in \mathcal{G}} \omega_i a_i \quad (2.19)$$

2.3.3 Average rules and concentration-influence relations

For the phases given in Figure 2.1 and after discretization according to Eq. (2.19), the average rules (2.4) and (2.9) can be recast in the format

$$\begin{aligned} \boldsymbol{\Sigma} &= f_s \sum_{i \in \mathcal{G}} \omega_i \boldsymbol{\sigma}_{s,i} \\ \mathbf{E} &= f_p \boldsymbol{\varepsilon}_p + f_s \sum_{i \in \mathcal{G}} \omega_i \boldsymbol{\varepsilon}_{s,i} \end{aligned} \quad (2.20)$$

with $\boldsymbol{\varepsilon}_p$ being the average strain within the pore phases, and with $\boldsymbol{\sigma}_{s,i}$ and $\boldsymbol{\varepsilon}_{s,i}$ being the average stresses and strains in the i -th solid phase. The discretized counterpart to the concentration-influence relations (2.15) read as

$$\begin{aligned} \forall i \in \mathcal{G} : \quad \boldsymbol{\varepsilon}_{s,i} &= \mathbb{A}_{s,i} : \mathbf{E} + \sum_{j \in \mathcal{G}} \omega_j \mathbb{D}_{ij} : \boldsymbol{\varepsilon}_{s,j}^p \\ \boldsymbol{\varepsilon}_p &= \mathbb{A}_p : \mathbf{E} + \sum_{j \in \mathcal{G}} \omega_j \mathbb{D}_{pj} : \boldsymbol{\varepsilon}_{s,j}^p \end{aligned} \quad (2.21)$$

with \mathbb{A}_p as the concentration (or downscaling) tensor associated with the pore phase, with \mathbb{D}_{pj} as the influence tensor quantifying the effect of plastic strains in the j -th solid phase on the strains in the pore phase, with $\mathbb{A}_{s,i}$ as the concentration (or downscaling) tensor associated with the i -th solid phase and with \mathbb{D}_{ij} as the influence tensor quantifying the effect of plastic strains in phase j on the total strains in phase i . The concentration and influence tensors can be determined from eigenstressed matrix-inclusion problems of the Eshelby-laws type (Eshelby 1957, Laws 1977, Zaoui 2002, Pichler & Hellmich 2010, Dvorak 2013); and for the chosen set \mathcal{G} of Gaussian points used for the discretization of a porous polycrystal, they read as (Morin et al. 2017)

$$\mathbb{A}_{s,i} = \mathbb{A}_{s,i}^\infty : \left\{ f_p \mathbb{A}_p^\infty + f_s \sum_{j \in \mathcal{G}} \omega_j \mathbb{A}_{s,j}^\infty \right\}^{-1} \quad (2.22)$$

$$\mathbb{A}_p = \mathbb{A}_p^\infty : \left\{ f_p \mathbb{A}_p^\infty + f_s \sum_{j \in \mathcal{G}} \omega_j \mathbb{A}_{s,j}^\infty \right\}^{-1} \quad (2.23)$$

$$\begin{aligned} \mathbb{D}_{pj} = & \left\{ -\mathbb{A}_p : f_s \mathbb{A}_{s,j}^\infty : \mathbb{P}_s(\theta_j, \varphi_j) + \right. & (2.24) \\ & \left[f_p \mathbb{A}_p : \mathbb{A}_p^\infty : \mathbb{P}_p + f_s \mathbb{A}_p : \sum_{k \in \mathcal{G}} \omega_k \mathbb{A}_{s,k}^\infty : \mathbb{P}_s(\theta_k, \varphi_k) - \mathbb{A}_p^\infty : \mathbb{P}_p \right] : \\ & \left[f_p \mathbb{C}_{\text{hom}} : \mathbb{A}_p^\infty : \mathbb{P}_p + f_s (\mathbb{C}_{\text{hom}} - \mathbb{C}_s) : \sum_{k \in \mathcal{G}} \omega_k \mathbb{A}_{s,k}^\infty : \mathbb{P}_s(\theta_k, \varphi_k) \right]^{-1} : \\ & \left. f_s \left[(\mathbb{I} - \mathbb{A}_{s,j})^\text{T} + (\mathbb{C}_{\text{hom}} - \mathbb{C}_s) : \mathbb{A}_{s,j}^\infty : \mathbb{P}_s(\theta_j, \varphi_j) \right] \right\} : \mathbb{C}_s \end{aligned}$$

$$\begin{aligned} \mathbb{D}_{ij} = & \left\{ [\delta_{ij} \omega_j^{-1} \mathbb{I} - \mathbb{A}_{s,i} : f_s] : \mathbb{A}_{s,j}^\infty : \mathbb{P}_s(\theta_j, \varphi_j) + \right. & (2.25) \\ & \left[f_p \mathbb{A}_{s,i} : \mathbb{A}_p^\infty : \mathbb{P}_p + f_s \mathbb{A}_{s,i} : \sum_{k \in \mathcal{G}} \omega_k \mathbb{A}_{s,k}^\infty : \mathbb{P}_s(\theta_k, \varphi_k) - \mathbb{A}_{s,i}^\infty : \mathbb{P}_s(\theta_i, \varphi_i) \right] : \\ & \left[f_p \mathbb{C}_{\text{hom}} : \mathbb{A}_p^\infty : \mathbb{P}_p + f_s (\mathbb{C}_{\text{hom}} - \mathbb{C}_s) : \sum_{k \in \mathcal{G}} \omega_k \mathbb{A}_{s,k}^\infty : \mathbb{P}_s(\theta_k, \varphi_k) \right]^{-1} : \\ & \left. f_s \left[(\mathbb{I} - \mathbb{A}_{s,j})^\text{T} + (\mathbb{C}_{\text{hom}} - \mathbb{C}_s) : \mathbb{A}_{s,j}^\infty : \mathbb{P}_s(\theta_j, \varphi_j) \right] \right\} : \mathbb{C}_s \end{aligned}$$

In Eqs. (2.22)-(2.25), the following notations are used: \mathbb{I} is the fourth-order identity tensor, and \mathbb{P}_s is the fourth-order Hill tensor depending on the shape of the solid inclusion s and on the stiffness of the surrounding matrix, which - in the present case of a self-consistent scheme which is appropriate for polycrystal modeling - is identical to the (homogenized) stiffness of the porous polycrystal, \mathbb{C}_{hom} . The latter obeys the classical stiffness homogenization rule reading as (Zaoui 2002, Fritsch et al. 2006)

$$\mathbb{C}_{\text{hom}} = f_s \sum_{i \in \mathcal{G}} \omega_i \mathbb{C}_s : \mathbb{A}_{s,i} \quad (2.26)$$

$\mathbb{A}_{s,i}^\infty$ and \mathbb{A}_p^∞ are tensors associated with the auxiliary matrix-inclusion problems used for the derivation of Eq. (2.22)-(2.25). They read as (Pichler & Hellmich 2010)

$$\begin{aligned} \mathbb{A}_{s,i}^\infty &= [\mathbb{I} + \mathbb{P}_s(\theta_i, \varphi_i) : (\mathbb{C}_s - \mathbb{C}_{\text{hom}})]^{-1} \\ \mathbb{A}_p^\infty &= [\mathbb{I} - \mathbb{P}_p : \mathbb{C}_{\text{hom}}]^{-1} \end{aligned} \quad (2.27)$$

2.3.4 Virtual microstrain field associated with plastic collapse - ultimate macroscopic load

Our starting point is the derivative of the concentration-influence relation (2.21)₁ with respect to time

$$\forall i \in \mathcal{G} : \quad \dot{\epsilon}_{s,i} = \mathbb{A}_{s,i} : \dot{\mathbf{E}} + \sum_{j \in \mathcal{G}} \omega_j \mathbb{D}_{ij} : \dot{\epsilon}_{s,j}^p \quad (2.28)$$

As explained in Section 2.2.2, plastic collapse is associated with purely plastic strain evolution, so that the rate of the microscopic total strains becomes identical to the rate of plastic strains,

$$\forall i \in \mathcal{G} : \quad \dot{\epsilon}_{s,i} = \dot{\epsilon}_{s,i}^p \quad (2.29)$$

Combination of Eqs. (2.29) and (2.28) yields

$$\forall i \in \mathcal{G} : \quad \dot{\epsilon}_{s,i} = \mathbb{A}_{s,i} : \dot{\mathbf{E}} + \sum_{j \in \mathcal{G}} \omega_j \mathbb{D}_{ij} : \dot{\epsilon}_{s,j} \Leftrightarrow \mathbb{A}_{s,i} : \dot{\mathbf{E}} = \sum_{j \in \mathcal{G}} (\delta_{ij} \mathbb{I} - \omega_j \mathbb{D}_{ij}) : \dot{\epsilon}_{s,j} \quad (2.30)$$

The set of linear equations arising from evaluation of Eq. (2.30) for $\forall i \in \mathcal{G}$ can be written in matrix-vector notation as

$$\underbrace{\begin{bmatrix} \mathcal{M}_{\mathbb{A}_{s,1}} \\ \mathcal{M}_{\mathbb{A}_{s,2}} \\ \vdots \\ \mathcal{M}_{\mathbb{A}_{s,i}} \end{bmatrix}}_{\mathcal{A}[(6N_i) \times 6]} \cdot \underbrace{\begin{bmatrix} \mathcal{V}_{\dot{\mathbf{E}}} \end{bmatrix}}_{[6 \times 1]} = \underbrace{\begin{bmatrix} \mathcal{M}_{\mathbb{I}} - \omega_1 \mathcal{M}_{\mathbb{D}_{11}} & -\omega_2 \mathcal{M}_{\mathbb{D}_{12}} & \cdot & \cdot & \cdot & -\omega_i \mathcal{M}_{\mathbb{D}_{1i}} \\ \omega_1 \mathcal{M}_{\mathbb{D}_{21}} & \mathcal{M}_{\mathbb{I}} - \omega_2 \mathcal{M}_{\mathbb{D}_{22}} & \cdot & \cdot & \cdot & -\omega_i \mathcal{M}_{\mathbb{D}_{2i}} \\ \cdot & \cdot & \cdot & \cdot & \cdot & \cdot \\ \cdot & \cdot & \cdot & \cdot & \cdot & \cdot \\ \cdot & \cdot & \cdot & \cdot & \cdot & \cdot \\ \omega_1 \mathcal{M}_{\mathbb{D}_{i1}} & \omega_2 \mathcal{M}_{\mathbb{D}_{i2}} & \cdot & \cdot & \cdot & \mathcal{M}_{\mathbb{I}} - \omega_i \mathcal{M}_{\mathbb{D}_{ii}} \end{bmatrix}}_{\mathcal{D}[(6N_i) \times (6N_i)]} \cdot \underbrace{\begin{bmatrix} \mathcal{V}_{\dot{\epsilon}_{s,1}} \\ \mathcal{V}_{\dot{\epsilon}_{s,2}} \\ \cdot \\ \cdot \\ \cdot \\ \mathcal{V}_{\dot{\epsilon}_{s,i}} \end{bmatrix}}_{\mathcal{E}[(6N_i) \times 1]} \quad (2.31)$$

whereby $\mathcal{V}_{\mathbf{T}}$ is the Kelvin-Mandel vector representation of the second-order tensor \mathbf{T} (see e.g. Eq. (1) of Mandel (1965); or Eq. (45) of Walpole (1984); or Eq. (2a) of Cowin (2003)); and $\mathcal{M}_{\mathbb{T}}$ is the Kelvin-Mandel matrix representation of the fourth-order tensor \mathbb{T} , see e.g. Eq. (45) of Walpole (1984), or Eq. (2a) of Cowin (2003). These matrices and vectors are assembled to larger matrices \mathcal{A} , \mathcal{D} , and \mathcal{E} , the dimension of which is indicated in Eq. (2.31) by $[m \times n]$, with m as the number of rows and n as the number of columns.

Solving (2.31) for the vector of microstrain rates, \mathcal{E} , yields

$$\mathcal{E} = \mathcal{D}^{-1} \mathcal{A} \cdot \mathcal{V}_{\dot{\mathbf{E}}} \quad (2.32)$$

The vector of phase-specific microstrain rates follows from

$$\mathcal{V}_{\dot{\epsilon}_{s,i}} = \mathcal{M}_{\mathbb{A}_i^{\text{PC}}} \cdot \mathcal{V}_{\dot{\mathbf{E}}} \quad (2.33)$$

with the phase-specific submatrices $\mathcal{M}_{\mathbb{A}_i^{\text{PC}}}$ being submatrices of $(\mathcal{D}^{-1} \mathcal{A})$, according to the rule

$$\mathcal{M}_{\mathbb{A}_i^{\text{PC}}} = (\mathcal{D}^{-1} \mathcal{A})[6(i-1)+1, 6(i-1)+2, 6(i-1)+3, 6(i-1)+4, 6(i-1)+5, 6i; 1, 2, 3, 4, 5, 6] \quad (2.34)$$

whereby $\mathcal{M}[m_1, m_2, \dots, m_r; n_1, n_2, \dots, n_s]$ denotes a submatrix of \mathcal{M} , this submatrix comprising the rows $\{m_1, m_2, \dots, m_r\}$ and the columns $\{n_1, n_2, \dots, n_s\}$. Identifying the solid phase-specific virtual microstrain rates as $\hat{\mathbf{d}}_{s,i} = \dot{\epsilon}_{s,i}^p$ and the macroscopic virtual strain rates as $\hat{\mathbf{D}} = \dot{\mathbf{E}}$ while considering (2.32) yields a discretized form of the plastic collapse-related concentration relation (2.17), reading as

$$\hat{\mathbf{d}}_{s,i} = \mathbb{A}_i^{\text{PC}} : \hat{\mathbf{D}} \quad (2.35)$$

Discretization of the upper bound equation (2.18) for an RVE of a porous polycrystal with weak pores ($\sigma_p = 0$) yields

$$\Sigma^{\text{ult}} \leq f_s \sum_i \omega_i \text{Sup} \{ \sigma : \mathbb{A}_i^{\text{PC}} | \sigma \in \mathcal{G}_{s,i} \} \quad (2.36)$$

with $\mathcal{G}_{s,i}$ being the space of admissible microstresses in the solid phase i .

A particularly interesting case can be derived from Eq. (2.36) when introducing *identical* admissible microstress spaces for all solid phases, and considering identical ultimate stress states σ^{ult} in all these solid phases. Then Eq. (2.36) reduces to

$$\Sigma^{\text{ult}} \leq f_s \sigma^{\text{ult}} : \sum_i \omega_i \mathbb{A}_i^{\text{PC}} \quad (2.37)$$

Evaluating the weighted sum over the plastic collapse-related strain rate concentration tensors yields the remarkable result

$$\sum_i \omega_i \mathbb{A}_i^{\text{PC}} = \mathbb{I} \quad (2.38)$$

Hence,

$$\Sigma^{\text{ult}} \leq f_s \sigma^{\text{ult}} \quad (2.39)$$

On the other hand, the static approach of yield design (Salençon 1990) identifies loads associated to admissible stresses which are in equilibrium, as lower bounds to the ultimate load. In the case of an RVE, equilibrium is associated with the stress average rule (2.20)₁, so that we obtain for a porous polycrystal with a weak pore phase that

$$\Sigma = f_s \sigma^{\text{ult}} \leq \Sigma^{\text{ult}} \quad (2.40)$$

Simultaneous validity of Eqs. (2.39) and (2.40) yields the *exact expression* for the ultimate load of the considered porous polycrystal system as

$$\Sigma^{\text{ult}} = f_s \sigma^{\text{ult}} \quad (2.41)$$

As an application, we consider ultimate microstresses associated with a multisurface Mohr-Coulomb criterion written in terms of principal stresses

$$\begin{aligned} \mathfrak{F}_s^{(1)}(\sigma_{s,i}) &= \beta \cdot \sigma_{s,i,I} - \sigma_{s,i,III} - \sigma_s^{\text{yield}} \leq 0 \\ \mathfrak{F}_s^{(2)}(\sigma_{s,i}) &= \beta \cdot \sigma_{s,i,II} - \sigma_{s,i,III} - \sigma_s^{\text{yield}} \leq 0 \\ \mathfrak{F}_s^{(3)}(\sigma_{s,i}) &= \beta \cdot \sigma_{s,i,I} - \sigma_{s,i,II} - \sigma_s^{\text{yield}} \leq 0 \end{aligned} \quad (2.42)$$

with $\sigma_{s,i,I} \geq \sigma_{s,i,II} \geq \sigma_{s,i,III}$ as the principal values of the stress tensor $\sigma_{s,i}$, β as the friction parameter and σ_s^{yield} as the yield strength of the solid phases. Eqs. (2.41) and (2.42) readily yield the macroscopic stresses under uniaxial compression, uniaxial tension, and pure shear as

$$\text{compression: } \Sigma^{\text{ult,c}} = -f_s \sigma_s^{\text{yield}} (\mathbf{e}_u \otimes \mathbf{e}_u) \quad (2.43)$$

$$\text{tension: } \Sigma^{\text{ult,t}} = f_s \frac{\sigma_s^{\text{yield}}}{\beta} (\mathbf{e}_u \otimes \mathbf{e}_u) \quad (2.44)$$

$$\text{shear: } \Sigma^{\text{ult,sh}} = f_s \frac{\sigma_s^{\text{yield}}}{\beta + 1} (\mathbf{e}_u \otimes \mathbf{e}_v) \quad (2.45)$$

whereby the uniaxial loading is applied in \mathbf{e}_u -direction in case of compression and tension, or in the \mathbf{e}_u - \mathbf{e}_v -plane in case of shear.

Concerning an application to a real-life problem, porous hydroxyapatite polycrystals in equine osteonal bone are characterized by the properties summarized in Table 2.1; see Morin et al. (2017) for experimental details. The corresponding ultimate stress states are collected in Table 2.2. They will be validated by a full elastoplastic analysis, as described next.

Tab. 2.1: *Properties of solid and pore material phases of equine osteonal bone*

Property	solid hydroxyapatite	weak pores
Volume fractions	$f_s = 0.68$	$f_p = 0.32$
Bulk modulus	$k_s = 82.6$ GPa	$k_p = 0$ GPa
Shear modulus	$\mu_s = 44.69$ GPa	$\mu_p = 0$ GPa
Yield strength	$\sigma_s^{\text{yield}} = 570$ MPa	
Friction parameter	$\beta = 12$	

Tab. 2.2: *Limit analysis based ultimate uniaxial micro- and macroscopic stress of equine osteonal bone under uniaxial loading*

	Compression	Tension	Shear
σ^{ult} [MPa]	-570.0	47.5	43.8
Σ^{ult} [MPa]	-387.4	32.3	29.8

2.4 Validation: full elastoplastic analysis

2.4.1 Elastoplastic state equations, upscaling of plastic strains, and non-associative flow rules

A full elastoplastic analysis requires introduction of stress-strain relations, both at the microscopic level of the solid phases

$$\boldsymbol{\sigma}_{s,i} = \mathbb{C}_s : (\boldsymbol{\varepsilon}_{s,i} - \boldsymbol{\varepsilon}_{s,i}^p) \quad (2.46)$$

and at the macroscopic level of the porous polycrystal

$$\boldsymbol{\Sigma} = \mathbb{C}_{\text{hom}} : (\mathbf{E} - \mathbf{E}^p) \quad (2.47)$$

whereby the macroscopic plastic strain, \mathbf{E}^p , follows from Levin's theorem (Levin 1967, Morin et al. 2017)

$$\mathbf{E}^p = f_s \sum_{i \in \mathcal{G}} \omega_i \mathbb{C}_{\text{hom}}^{-1} : \mathbb{A}_{s,i}^T : \mathbb{C}_s : \boldsymbol{\varepsilon}_{s,i}^p \quad (2.48)$$

Moreover, the multisurface Mohr-Coulomb criterion (2.42) is complemented by a non-associative flow rule of the Koiter type (Koiter 1953), reading as (Morin et al. 2017)

$$\forall i \in \mathcal{G} : \quad \dot{\boldsymbol{\varepsilon}}_{s,i}^p = \sum_{\alpha=1}^3 \dot{\lambda}_i^{(\alpha)} \frac{\partial \mathfrak{G}_s^{(\alpha)}}{\partial \boldsymbol{\sigma}_{s,i}} (\boldsymbol{\sigma}_{s,i}), \quad (2.49)$$

Eq. (2.49) governs the evolution of the plastic strains, according to the Melan-Kuhn-Tucker conditions (Simo & Hughes 1998, Melan 1938)

$$\forall \alpha \in \{1,2,3\} \quad \dot{\lambda}_i^{(\alpha)} \geq 0, \quad \mathfrak{F}_s^{(\alpha)}(\boldsymbol{\sigma}_{s,i}) \leq 0 \quad \text{and} \quad \dot{\lambda}_i^{(\alpha)} \times \mathfrak{F}_s^{(\alpha)}(\boldsymbol{\sigma}_{s,i}) = 0 \quad (2.50)$$

with associated plastic multipliers $\dot{\lambda}_i^{(\alpha)}$, governing the magnitude of the plastic strain rate. The three plastic potential functions occurring in Eq. (2.49) read in terms of principal stresses as

$$\begin{aligned}\mathfrak{G}_s^{(1)}(\boldsymbol{\sigma}_{s,i}) &= \sigma_{s,i,I} - \sigma_{s,i,III} \\ \mathfrak{G}_s^{(2)}(\boldsymbol{\sigma}_{s,i}) &= \sigma_{s,i,II} - \sigma_{s,i,III} \\ \mathfrak{G}_s^{(3)}(\boldsymbol{\sigma}_{s,i}) &= \sigma_{s,i,I} - \sigma_{s,i,II}\end{aligned}\quad (2.51)$$

2.4.2 Algorithmic treatment I: general iteration strategy and discretized plastic flow rule

In order to solve the equations (2.19) to (2.27) and (2.46) to (2.51), we largely follow the algorithmic strategy described in Morin et al. (2017), prescribing a series of macroscopic stress states $\boldsymbol{\Sigma}^n$, $n = \{1, \dots, N_n\}$, each one being associated with the end of load step n ; and respective macroscopic stress increments $\Delta\boldsymbol{\Sigma}^n = \boldsymbol{\Sigma}^n - \boldsymbol{\Sigma}^{n-1}$. The non-linear stress-strain behavior at the macroscopic level of the entire RVE requires an iterative scheme for the determination of corresponding macroscopic strain states \mathbf{E}^n . As in Morin et al. (2017), we employ a modified Newton-Raphson scheme comprising N_r iteration steps, each of them being indicated by index r , with the corresponding residual stress increment being denoted by $\mathbf{R}^{n,r}$, see Figure 2.2.

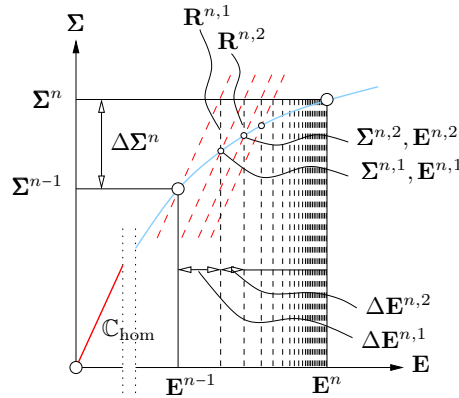


Fig. 2.2: Modified Newton-Raphson iteration scheme

At all incremental steps n and iteration steps r , it is mandatory to fulfill the requirement

$$\boldsymbol{\sigma}_{s,i}^{n,r} = \mathbb{C}_s : \left(\mathbb{A}_{s,i} : \mathbf{E}^{n,r} + \sum_{j \in \mathcal{G}} (\omega_j \mathbb{D}_{ij} - \delta_{ij} \mathbb{I}) : \boldsymbol{\epsilon}_{s,j}^{p,n,r} \right) \quad (2.52)$$

Eq. (2.52) arises from a combination of the concentration-influence relations (2.21) with the microscopic constitutive law, i.e. the state equation (2.46). Then, the key algorithmic task lies in computing, from the known values of state variables associated with load step n and iteration step r , $\mathbf{E}^{n,r}$ and $\boldsymbol{\epsilon}_{s,i}^{p,n,r}$ (with $\mathbf{E}^{p,n,r}$ readily following from (2.48)), the corresponding values for step $(r+1)$. Therefore, the flow rule needs to be discretized: Traditionally, forward or backward Euler schemes are employed for integrating the evolution equation (2.49), see e.g. Simo & Hughes (1998), Morin et al. (2017); meaning that the flow direction $\partial \mathfrak{G}_s^{(\alpha)} / \partial \boldsymbol{\sigma}_{s,i}$ is evaluated either at the beginning or at the end of the load step under investigation. We

here implement an alternative strategy: For any iteration step $(r + 1)$ of any load step n , we consider a series of N_k stress states $\sigma_{s,i}^{n,r+1,k}$, $k \in \{1, \dots, N_k\}$, converging, according to a stress backprojection process explained further below, towards $\sigma_{s,i}^{n,r+1}$, see Figure 2.3. The corresponding discretization of Eq. (2.49) reads as

$$\Delta \epsilon_{s,i}^{p,n,r+1} = \epsilon_{s,i}^{p,n,r+1} - \epsilon_{s,i}^{p,n,r} = \sum_{\alpha=1}^{N_{\text{Fact},i}^{n,r+1}} \sum_{k=1}^{N_k} \Delta \lambda_i^{(\alpha),n,r+1,k} \frac{\partial \mathfrak{G}_s^{(\alpha)}}{\partial \sigma_{s,i}} (\sigma_{s,i}^{n,r+1,k}) \quad (2.53)$$

with $N_{\text{Fact},i}^{n,r+1}$ as the number of active yield surfaces of solid phase i at load step n and iteration step $r + 1$, i.e. those yield surfaces with the associated plastic multipliers being non-zero. Finally, the plastic strain increments associated with the entire load step n read as

$$\Delta \epsilon_{s,i}^{p,n} = \sum_{r=1}^{N_r} \Delta \epsilon_{s,i}^{p,n,r} \quad (2.54)$$

2.4.3 Algorithmic treatment II: series of stress states and return mapping

Insertion of Eq. (2.53) into Eq. (2.52) yields

$$\begin{aligned} \sigma_{s,i}^{n,r+1} = \mathbb{C}_s : & \left[\mathbb{A}_{s,i} : \mathbf{E}^{n,r+1} + \sum_{j \in \mathcal{G}} (\omega_j \mathbb{D}_{ij} - \delta_{ij} \mathbb{I}) \right. \\ & \left. : \left(\epsilon_{s,i}^{p,n,r} + \sum_{k=1}^{N_k} \sum_{\alpha=1}^{N_{\text{Fact},j}^{n,r+1}} \Delta \lambda_j^{(\alpha),n,r+1,k} \frac{\partial \mathfrak{G}_s^{(\alpha)}}{\partial \sigma_{s,j}} (\sigma_{s,j}^{n,r+1,k}) \right) \right] \end{aligned} \quad (2.55)$$

Based on Eq. (2.55), the N_k plastic multipliers $\Delta \lambda_i^{(\alpha),n,r+1,k}$, $k = \{1, \dots, N_k\}$ associated to phase i , are determined in a sequential way, with corresponding stress states $\sigma_{s,i}^{n,r+1,k}$, $k = \{1, \dots, N_k\}$.

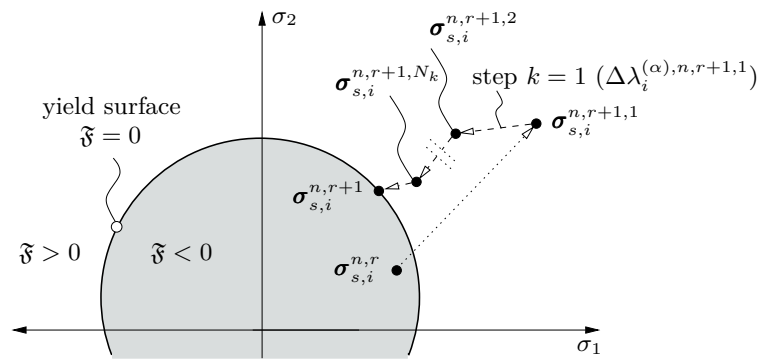


Fig. 2.3: Principle of iterative return-mapping

The first member of this stress series, $\sigma_{s,i}^{n,r+1,1}$, is inspired by the concept of elastic trial stress states (Simo & Taylor 1985) and follows from the assumption of no plastic events during iteration step $(r + 1)$, so that corresponding specification of Eq. (2.55) readily yields

$$\sigma_{s,i}^{n,r+1,1} = \mathbb{C}_s : \left(\mathbb{A}_{s,i} : \mathbf{E}^{n,r+1} + \sum_{j \in \mathcal{G}} (\omega_j \mathbb{D}_{ij} - \delta_{ij} \mathbb{I}) : \epsilon_{s,j}^{p,n,r} \right) \quad (2.56)$$

This microscopic stress state is then inserted into the multisurface yield criterion (2.42), yielding

$$\forall i \in \mathcal{G}, \forall \alpha \in \{1, 2, 3\} \quad \mathfrak{F}_{s,i}^{(\alpha),n,r+1,1} = \mathfrak{F}_s^{(\alpha)}(\boldsymbol{\sigma}_{s,i}^{n,r+1,1}) \quad (2.57)$$

The values for the yield function retrieved from Eq. (2.57) allow us to discriminate between plasticizing and purely elastic solid (needle-shaped) phases:

- Negative values $\mathfrak{F}_{s,i}^{(\alpha),n,r+1,1} \leq 0$ for all three yield surfaces associated to solid phase i indicate that the corresponding solid phase behaves purely elastic during iteration step $(r + 1)$.
- A positive value $\mathfrak{F}_{s,i}^{(\alpha),n,r+1,1} > 0$ for at least one yield surface associated to solid phase i violates Eq. (2.50), which means that the corresponding solid phase does not behave purely elastic, but exhibits plastic behavior during iteration step $(r + 1)$. The set of plasticizing solid phases $\mathcal{G}_{\text{plast}}^{n,r+1}$ (comprising $N_{\text{plast}}^{n,r+1} \in [0, 120]$ elements) is defined by all solid phases having at least one positive yield criterion during step $(r + 1)$. Each of these solid phases is associated to a number of active yield surfaces $N_{\text{Fact},i}^{n,r+1} \in \{1, 2, 3\}$.

Having identified the set of plasticizing solid phases, the next members of the stress series, $\boldsymbol{\sigma}_{s,i}^{n,r+1,k}$, $k \geq 2$, follow as

$$\begin{aligned} \boldsymbol{\sigma}_{s,i}^{n,r+1,k} = \mathbb{C}_s : & \left[\mathbb{A}_{s,i} : \mathbf{E}^{n,r+1} + \sum_{j \in \mathcal{G}_{\text{plast}}^{n,r+1}} (\omega_j \mathbb{D}_{ij} - \delta_{ij} \mathbb{I}) \right. \\ & \left. : \left(\boldsymbol{\varepsilon}^{p,n+1,r} + \sum_{l=1}^{k-1} \sum_{\alpha=1}^{N_{\text{Fact},j}^{n,r+1}} \Delta \lambda_j^{(\alpha),n,r+1,l} \frac{\partial \mathfrak{G}_s^{(\alpha)}}{\partial \boldsymbol{\sigma}_{s,j}}(\boldsymbol{\sigma}_{s,j}^{n,r+1,l}) \right) \right] \end{aligned} \quad (2.58)$$

Eq. (2.58) is used for the determination of the plastic multipliers associated with backprojection step $(k - 1)$. Therefore, Eq. (2.58) is regarded as a function with unknown variables $\Delta \lambda_j^{(\alpha),n,r+1,k-1}$, $\forall j \in \mathcal{G}_{\text{plast}}^{n,r+1}$ and $\forall \alpha \in \{1, \dots, N_{\text{Fact},j}^{n,r+1}\}$. Insertion of this function into the yield function $\mathfrak{F}_s^{(\alpha)}$ according to (2.42) makes the latter to depend on $\Delta \lambda_j^{(\alpha),n,r+1,k-1}$, $\forall j \in \mathcal{G}_{\text{plast}}^{n,r+1}$ and $\forall \alpha \in \{1, \dots, N_{\text{Fact},j}^{n,r+1}\}$, as well:

$$\begin{aligned} \mathfrak{F}_{s,i}^{(\alpha),n,r+1,k} = \mathfrak{F}_s^{(\alpha)} \left(\boldsymbol{\sigma}_{s,i}^{n,r+1,k} \left(\Delta \lambda_1^{(1)n,r+1,k-1}, \dots, \Delta \lambda_1^{(N_{\text{Fact},1}^{n,r+1})n,r+1,k-1}, \dots \right. \right. \\ \dots, \Delta \lambda_j^{(1)n,r+1,k-1}, \dots, \Delta \lambda_j^{(N_{\text{Fact},j}^{n,r+1})n,r+1,k-1}, \dots \\ \left. \left. \dots, \Delta \lambda_{N_{\text{plast}}^{n,r+1}}^{(1)n,r+1,k-1}, \dots, \Delta \lambda_{N_{\text{plast}}^{n,r+1}}^{(N_{\text{Fact},N_{\text{plast}}^{n,r+1}})^{n,r+1,k-1}} \right) \right) \end{aligned} \quad (2.59)$$

We then project the stress state “towards” the yield surface, by requiring the linearization of Eq. (2.59) for each plasticizing solid phase and each corresponding active yield surface to be zero, according to

$$\begin{aligned}
& \forall i \in \mathcal{G}_{\text{plast}}^{n,r+1}, \forall \alpha \in \{1, \dots, N_{\text{Fact},i}^{n,r+1}\} : \\
& \mathfrak{F}_s^{(\alpha)} \left(\boldsymbol{\sigma}_{s,i}^{n,r+1,k} \left(\Delta \lambda_l^{(\gamma),n,r+1,k-1} = 0, \forall \{l, \gamma\} \right) \right) \\
& + \sum_{j \in \mathcal{G}_{\text{plast}}^{n,r+1}} \sum_{\beta=1}^{N_{\text{Fact},j}} \frac{\partial \mathfrak{F}_s^{(\alpha)}}{\partial \boldsymbol{\sigma}_{s,i}} \left(\boldsymbol{\sigma}_{s,i}^{n,r+1,k} \left(\Delta \lambda_l^{(\gamma),n,r+1,k-1} = 0, \forall \{l, \gamma\} \right) \right) \\
& \quad : \frac{\partial \boldsymbol{\sigma}_{s,i}^{n,r+1,k}}{\partial (\Delta \lambda_j^{(\beta),n,r+1,k-1})} \Delta \lambda_j^{(\beta),n,r+1,k-1} = 0
\end{aligned} \tag{2.60}$$

whereby

$$\begin{aligned}
& \frac{\partial \mathfrak{F}_s^{(\alpha)}}{\partial \boldsymbol{\sigma}_{s,i}} \left(\boldsymbol{\sigma}_{s,i}^{n,r+1,k} \left(\Delta \lambda_l^{(\gamma),n,r+1,k-1} = 0, \forall \{l, \gamma\} \right) \right) : \frac{\partial \boldsymbol{\sigma}_{s,i}^{n,r+1,k}}{\partial (\Delta \lambda_j^{(\beta),n,r+1,k-1})} \\
& = \frac{\partial \mathfrak{F}_s^{(\alpha)}}{\partial \boldsymbol{\sigma}_{s,i}} \left(\boldsymbol{\sigma}_{s,i}^{n,r+1,k-1} \right) : \left(\omega_j \mathbb{D}_{ij} - \delta_{ij} \mathbb{I} \right) : \frac{\partial \mathfrak{G}_s^{(\beta)}}{\partial \boldsymbol{\sigma}_{s,j}} \left(\boldsymbol{\sigma}_{s,j}^{n,r+1,k-1} \right)
\end{aligned} \tag{2.61}$$

Eq. (2.60) yields a linear system of equations for the unknowns $\Delta \lambda_j^{(\alpha),n,r+1,k-1}$, $\forall j \in \mathcal{G}_{\text{plast}}^{n,r+1}$ and $\forall \alpha \in \{1, \dots, N_{\text{Fact},j}^{n,r+1}\}$ which finally allow to compute the k -th member of the stress series according to Eq. (2.58). The series of stress states is expanded according to Eqs. (2.58)-(2.61), until the stress state derived at the end of step N_k , $\boldsymbol{\sigma}_{s,i}^{n,r+1,N_k+1}$, is sufficiently fulfilling the Melan-Kuhn-Tucker conditions, i.e.

$$\forall i \in \mathcal{G}_{\text{plast}}^{n,r+1}, \forall \alpha \in \{1, \dots, N_{\text{Fact},i}^{n,r+1}\} : \quad \|\mathfrak{F}_s^{(\alpha)} \left(\boldsymbol{\sigma}_{s,i}^{n,r+1,N_k+1} \right)\| < \text{TOL} \tag{2.62}$$

with a prescribed tolerance value TOL.

2.4.4 Numerical results

Macroscopic stress-strain relations for the porous polycrystal defined in Table 2.1 under uniaxial tension and compression, as well as under pure shear, are depicted in Figure 2.4. The ultimate macroscopic stress states obtained from the yield analysis are perfectly confirmed. Obviously, the more expensive elastoplastic analysis provides additional information, such as the heterogeneous distribution of microstress states, as depicted for the ultimate loads in Figure 2.5 or the macroscopic stress-strain states, where three characteristic loading points can be distinguished: (i) the yield point Σ^{yield} , characterized by the start of the nonlinear behavior due to the first solid phase getting plastic; (ii) the stress state Σ^{plastic} , at which all solid phases exhibit plastic behavior; and (iii) the ultimate stress Σ^{ult} , characterized by a plateau in the stress-strain curve, see Table 2.3 for a collection of the respective stress values. While the ultimate stress is reached immediately after all solid phases are plasticizing in tensile and shear loading, there is an additional hardening effect taking place during compression. Regardless of this eventual hardening effect, the limit analysis based ultimate stress states, see Table 2.2, are able to perfectly predict the elastoplastic analysis based values for all three loading conditions, see Figure 2.4. Furthermore the computed shear strength value of 29.8 MPa agrees

very well with the mean experimental value of 30.7 MPa given by Bigley et al. (2006) for debond shear strength of cement lines derived by push-out tests on osteonal bone.

Tab. 2.3: *Plasticity algorithm based characteristic stress states of equine osteonal bone under uniaxial loading*

	Compression	Tension	Shear
Σ^{yield} [MPa]	-130.1	19.7	17.5
Σ^{plastic} [MPa]	-321.1	32.1	29.7
Σ^{ult} [MPa]	-388.1	32.3	29.8

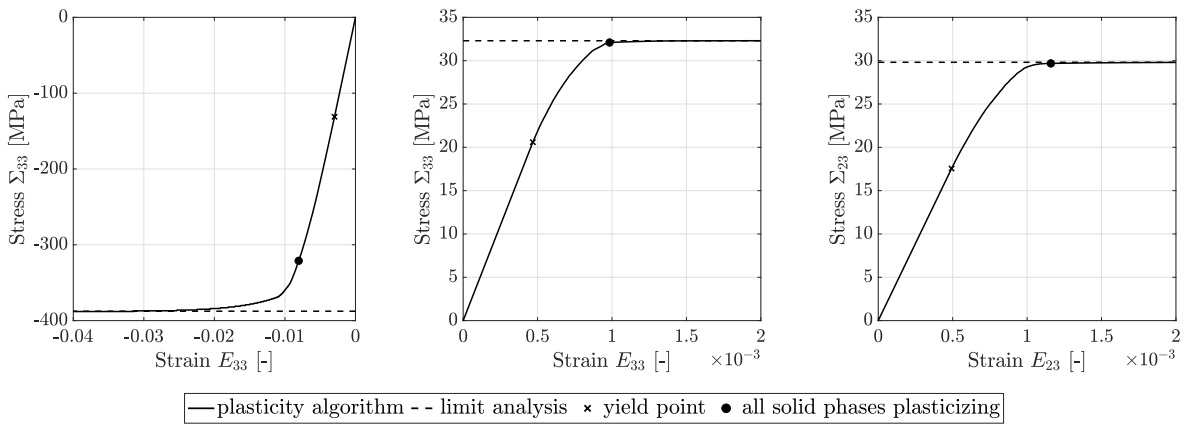


Fig. 2.4: *Plasticity algorithm based macroscopic stress-strain relation in comparison with the limit analysis based ultimate loading for uniaxial compression (left); uniaxial tension (middle); pure shear (right)*

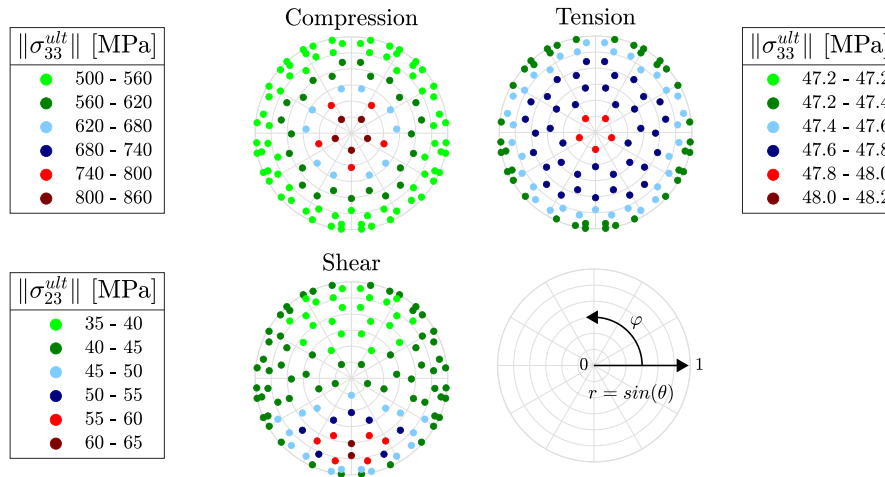


Fig. 2.5: *Distribution of the norm of the microscopic ultimate stress in the mineral needles over the needle orientations under uniaxial compression, tension and pure shear*

2.5 Discussion

A new yield design concept has been developed which gives direct access to the plastic collapse-related limit loads of microstructures exhibiting non-localized plastic microstrain fields. Instead of introducing more and more refined “trial velocity fields” derived from hollow sphere and hollow cylinder solutions, as is traditionally done in the context of Gurson-type plasticity models (Nahshon & Hutchinson 2008, Guo et al. 2008, Dormieux & Kondo 2010), the plastic flow fields were derived from combining Dvorak’s transformation field analysis (Dvorak 1992, Dvorak et al. 1994, Dvorak & Benveniste 1992, Pichler & Hellmich 2010, Dvorak 2013, Morin et al. 2017, Königsberger et al. 2020) with the plastic load concept of Drucker & Prager (1952). The latter identifies plastic and total microstrain rates occurring with plastic collapse, and this identification allows for simplification of the concentration-influence relations for eigenstressed representative volume elements (linking macroscopic strains, total microscopic strains and microscopic eigenstrains representing plastic deformations), giving rise to plastic collapse-specific strain rate concentration relations. The latter link macroscopic strain rates to a new type of “trial velocity field”. Remarkably, these new plastic velocity fields, when applied to porous polycrystals, deliver the *exact* solution of yield design problem, where the upper bound (“kinematic approach”) and the lower bound (“static approach”) turn out to be actually *identical*.

From a practical viewpoint, our new concept allows for reducing the computational cost needed for the determination of plastic collapse loads by a factor of one hundred, when compared to state-of-the-art elastoplastic homogenization approaches (Vena et al. 2008, Zeng et al. 2014, Morin et al. 2017). On the other hand, the present contribution has also advanced the state of the art concerning full elastoplastic micromechanics, through a novel return mapping scheme with sequences of iteratively updated plastic flow directions.

The application range and the adaptability of the novel method appears as very broad: The present contribution covered, as a first application example, the failure of cement lines in bone, considering its porous polycrystalline structure with many elongated crystal phases. As concerns more “monolithic” microstructures with pronounced matrix-inclusion morphologies and strongly inhomogeneous stress and strain fields in such matrices, it may be beneficial to resort to the approach of “non-uniform transformation field analysis” (Michel & Suquet 2003) so as to arrive at an interesting complement to the model developments described in Section 2.3. This would further widen the applicability of the presented strategy: Follow-up developments may concern any plastically active hierarchical material system which can reasonably be represented by concentration and influence tensors derived from an appropriate suite of eigenstressed matrix-inclusion problems; such as bone (Fritsch, Hellmich & Dormieux 2009), wood (Hofstetter et al. 2008, Füssl et al. 2017) or geomaterials (Shen et al. 2013, 2020).

Chapter 3

Multiscale elastoplasticity: theory, algorithm, and application to bone

Authored by Valentina Kumbolder, Claire Morin, Stefan Scheiner & Christian Hellmich

Prepared for submission to *Journal of the Mechanics and Physics of Solids*

Abstract: A considerable amount of engineering materials are hierarchically organized. On the macroscopic observation scale, such materials appear to be homogeneous, whereas zooming into the material's microstructure reveals heterogeneities, which govern the higher-scale physical properties of the material. As concerns the mechanical properties of hierarchically organized materials, multiscale models have been developed, in many cases focusing thereby on the elastic regime. However, it is evident that also the macroscopic *plastic behavior* of materials is induced by the plastic behavior of the corresponding microstructural organizational units. In this paper, we present a theoretical framework for continuum micromechanics-based multiscale elastoplasticity, applicable to any hierarchically organized material featuring distinctively separated observation scales. For that purpose, we introduce novel multiscale concentration-influence relations, which allow for directly linking the microscopic total strains at any observation scale to the macroscopic strain and the *plasticity-inducing* microscopic plastic strains. Numerically evaluating this scheme has required to also develop a novel multiscale iterative return mapping algorithm. We demonstrate the application of the latter by example of a material which has been studied by means of multiscale homogenization schemes extensively in the past, namely bone tissue. This way, the novel multiscale elastoplasticity model could be experimentally validated, showing both the potentials and limitations of the the model. It turns out that compressive tests can be reproduced by our model at a very high accuracy, while the errors between model predictions and experimental results are larger for tensile tests, suggesting that additional mechanisms should be taken into account in the future.

Contribution: Christian Hellmich set up the overall research strategy and supervised the research progress. Valentina Kumbolder extended the Matlab code with an optimized return-mapping algorithm, ran simulations, documented the results, carried out model validation, and wrote the first draft of the manuscript. Claire Morin provided codes and supported the development of an improved micromechanical representation of bone and the corresponding model implementation. Stefan Scheiner supported the finalization of the manuscript.

Keywords: multiscale micromechanics, transformation field analysis, elastoplasticity, return-mapping algorithm, bone, stiffness, strength

3.1 Introduction

In material mechanics, two fundamental regimes of material behavior are distinguished (Salençon 2012). Within the elastic regime, the stresses acting onto the material induce reversible deformations. Hence, after removal of the loading, the material returns to its initial, undeformed configuration. For most materials, the elastic regime is well-defined and mathematically describable through explicit constitutive laws. However, once the loading exceeds some kind of elastic limit, the plastic regime is entered, where deformations become irreversible. Then, in order to take into account that the respective material responds elastically (up to the elastic limit) *and* plastically (beyond the elastic limit), the aforementioned constitutive laws must be extended by suitably accounting for the related additional effects (Simo & Hughes 1998, de Souza Neto et al. 2011).

Typically, inelastic material behavior is mathematically considered based on rate-type constitutive equations (Simo & Taylor 1985, Lubarda 2001), requiring for numerical reasons some sort of implicit or explicit integration algorithms (Ortiz & Popov 1985, Ortiz & Simo 1986, Runesson et al. 1988). In this context, so-called elastic predictor-plastic corrector schemes have become a classical solution strategy, being actually an umbrella term for various types of algorithms, see de Souza Neto et al. (2011), Borja (2013) or Scalet & Auricchio (2018) for an overview of the pertinent literature. While a remarkable extent of sophistication has been reached in this major field of mechanics, the underlying techniques have been originally developed for homogeneous materials. Owing to the circumstance that many engineering materials are in fact heterogeneous or follow even some kind of organizational hierarchy, considerable efforts have been undertaken to make the fundamental laws describing elastoplastic material behavior applicable to such hierarchical materials. Examples include asymptotic expansion approaches for materials with periodic microstructures (Ghosh et al. 1996, Kalamkarov et al. 2009, Bensoussan et al. 1978), utilization of numerical (mostly Finite Element method-based) approaches (Matsui et al. 2004, Zhang, Wu & Fu 2010), and even molecular dynamics-based computational approaches (Yang et al. 2013).

One further modeling concept utilized for studying elastoplastically behaving materials, which has also proven to be exceptionally well suited for investigating hierarchically organized materials is continuum micromechanics (Zaoui 2002, Hill 1965), see Morin et al. (2017) for a brief literature survey on that matter. Remarkably, Morin et al. (2017) widened the state of the art in the field concerning one important aspect, namely by extending the famous influence tensor concept pioneered by Dvorak and colleagues (Dvorak 1992, Dvorak & Benveniste 1992, Dvorak et al. 1994) to infinitely many, mutually interacting needle-shaped phases oriented arbitrarily in all space directions. This way, a new modeling option for upscaling the elastoplastic behavior of polycrystals was obtained, overcoming thereby the deficits of traditional micromechanics-based elastoplasticity models (i.e., the overestimation of the material stiffness). Despite the strengths of the model proposed by Morin et al. (2017) (including computational efficiency and conceptual advantages), it lacks reliability when applied in a multiscale scheme, comprising at least two up- and downscaling steps. The work presented in this paper ties in with Morin et al. (2017), by presenting a rigorous multiscale elastoplasticity model applicable to any hierarchically organized material fulfilling the separation of scales-requirement (Zaoui 2002).

This paper is organized as follows: First, the conceptual basis is elaborated, comprising a brief summary of the very basics of continuum micromechanics (see Section 3.2.1), and the development of multiscale elastoplasticity within the framework of continuum micromechanics (see Sections 3.2.2 to 3.2.4). Solving the derived equations required the concurrent development

of a multiscale plasticity algorithm, described in Section 3.3. In order to demonstrate the potentials and limitations of our new modeling approach, the theoretical concept presented in Section 3.2 and 3.3 is then applied to a specific hierarchically organized material, namely to bone tissue (see Section 3.4). The paper is concluded by discussing the obtained results, the observed shortcomings, as well as perspectives for future research directions (see Section 3.5).

3.2 Continuum micromechanics-based multiscale elastoplasticity

3.2.1 Fundamentals of continuum micromechanics

Following the seminal works in this field (Hill 1963, 1965, Suquet 1997, Zaoui 2002), it is assumed within the framework of continuum micromechanics that a material is homogeneous at the macroscopic scale but heterogeneous at the microscopic scale. Such material is defined on a so-called representative volume element (RVE), with characteristic length ℓ . An RVE must be chosen so as to fulfill separation of scales. Hence, on the one hand, the characteristic length of the micro-heterogeneities within the RVE, d , must be considerably smaller than ℓ , $d \ll \ell$. On the other hand, the RVE must also fulfill $\ell \ll \{\mathcal{L}, \mathcal{P}\}$, with \mathcal{L} being the characteristic length of the geometry of a structure made of the material defined on the RVE, and with \mathcal{P} being the characteristic length of the loading acting onto this structure.

If single phases exhibit a heterogeneous microstructure themselves, multiscale micromechanical representations of a material can be established, which need to obey a correspondingly adapted separation of scales-requirement, reading as

$$d_v \ll \ell_v \leq d_{v-1} \ll \ell_{v-1} \leq \dots \leq d_2 \ll \ell_2 \leq d_1 \ll \ell_1 \ll \{\mathcal{L}, \mathcal{P}\}. \quad (3.1)$$

This applies also to the situation where a material possesses more than just one up- and down-scaling path π , see Figure 3.1 for an exemplary micromechanical representation of a material with $\pi = 2$. Clearly, this material would need to fulfill two separation of scales-requirements,

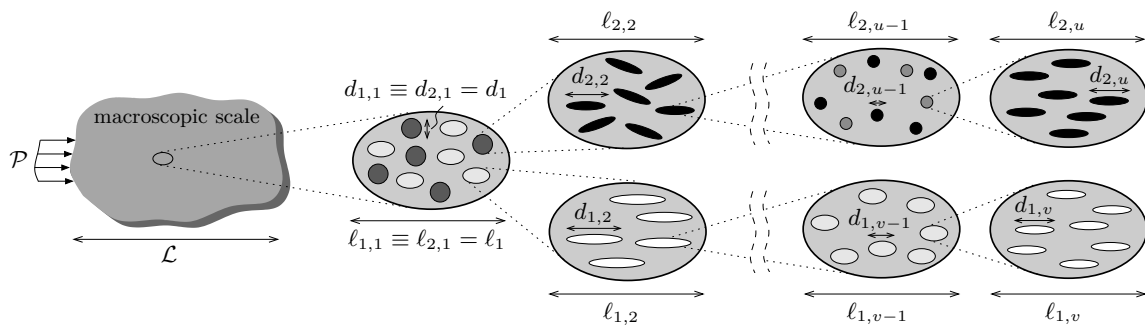


Fig. 3.1: Multiscale homogenization scheme comprising two up-/downscaling paths, both of which obey separation of scales according to Eq.(3.1)

namely $d_{1,v} \ll \ell_{1,v} \leq d_{1,v-1} \ll \ell_{1,v-1} \leq \dots \leq d_{1,2} \ll \ell_{1,2} \leq d_{1,1} \ll \ell_{1,1} \ll \{\mathcal{L}, \mathcal{P}\}$ and $d_{2,u} \ll \ell_{2,u} \leq d_{2,u-1} \ll \ell_{2,u-1} \leq \dots \leq d_{2,2} \ll \ell_{2,2} \leq d_{2,1} \ll \ell_{2,1} \ll \{\mathcal{L}, \mathcal{P}\}$, whereby $d_{1,1} \equiv d_{2,1} = d_1$ and $\ell_{1,1} \equiv \ell_{2,1} = \ell_1$. Furthermore, this scheme could be straightforwardly extended to more complicated branchings of the micromechanical representation (if necessary), merely requiring a correspondingly refined notation. As concerns the extent of scale separation,

in quantitative terms, Drugan & Willis (1996) revealed that a factor of 2 to 3 between the characteristic lengths of the RVEs and of the respective micro-heterogeneities is sufficient, whereas it has turned that $\{\mathcal{L}, \mathcal{P}\}$ and $\ell_{1,i}$ must be separated from each other by a factor of at least 5 (Kohlhauser & Hellmich 2013). Since the microstructure within one RVE is usually too complicated to be described in minute detail, quasi-homogeneous subdomains, called material phases, are introduced. Those material phases exhibit volume fractions, characteristic shapes and interactions between each other, as well as properties describing their physical behavior. Continuum micromechanics provides mathematical tools to process this information in such a way that up- and downscaling relations can be derived describing the material's behavior on all involved length scales, see the following sections as well as, e.g., (Zaoui 2002, Dormieux & Ulm 2007, Vass et al. 2018).

3.2.2 Single-scale up- and downscaling relations

Let us start with considering an RVE which exhibits characteristic lengths satisfying the conditions formulated in Section 3.2.1. Assuming furthermore that the microscopic stress field across the RVE is in equilibrium and that the corresponding strain field is geometrically compatible, the macroscopic stress $\boldsymbol{\Sigma}$ and the macroscopic strain \mathbf{E} to which this RVE is subjected follow from the volume averages of the respective microscopic quantities (Zaoui 2002),

$$\boldsymbol{\sigma} = \frac{1}{V_{\text{RVE}}} \int_{V_{\text{RVE}}} \boldsymbol{\sigma}(\mathbf{x}) \, dV = \sum_r f_r \boldsymbol{\sigma}_r, \quad (3.2)$$

$$\mathbf{E} = \frac{1}{V_{\text{RVE}}} \int_{V_{\text{RVE}}} \boldsymbol{\varepsilon}(\mathbf{x}) \, dV = \sum_r f_r \boldsymbol{\varepsilon}_r. \quad (3.3)$$

In Eqs. (3.2) and (3.3), \mathbf{x} is the position vector, $\boldsymbol{\sigma}(\mathbf{x})$ and $\boldsymbol{\varepsilon}(\mathbf{x})$ are the microscopic stress and strain fields, V_{RVE} is the volume of the considered RVE, f_r are the volume fractions of the material phases, while $\boldsymbol{\sigma}_r$ and $\boldsymbol{\varepsilon}_r$ are the material phase-specific stress and strain tensors. Within elastoplastic material phases, the constitutive law, relating stresses and strains, reads as

$$\boldsymbol{\sigma}_r = \mathbb{C}_r : (\boldsymbol{\varepsilon}_r - \boldsymbol{\varepsilon}_r^{\text{p}}), \quad (3.4)$$

with $\boldsymbol{\varepsilon}_r^{\text{p}}$ as the average plastic strain in phase r , and with \mathbb{C}_r as the (fourth-order) stiffness tensor quantifying the elastic behavior of phase r . Taking into account the so-called concentration-influence relations (Dvorak & Benveniste 1992, Pichler & Hellmich 2010), a relation between the microscopic total phase strains $\boldsymbol{\varepsilon}_r$, the microscopic plastic phase strains $\boldsymbol{\varepsilon}_r^{\text{p}}$, and the macroscopic strains \mathbf{E} follows:

$$\boldsymbol{\varepsilon}_r = \mathbb{A}_r : \mathbf{E} + \sum_s \mathbb{D}_{rs} : \boldsymbol{\varepsilon}_s^{\text{p}}, \quad (3.5)$$

with the (fourth-order) concentration tensor \mathbb{A}_r , relating $\boldsymbol{\varepsilon}_r$ and \mathbf{E} in multilinear fashion, and with \mathbb{D}_{rs} as (fourth-order) influence tensor, expressing the effect of the plastic strain in phase s on the overall strain in phase r . Note that \mathbb{A}_r follows from Eshelby's famous matrix-inclusion problem (Eshelby 1957), reading as

$$\mathbb{A}_r = [\mathbb{I} + \mathbb{P}_r^0 : (\mathbb{C}_r - \mathbb{C}_0)]^{-1} : \left\{ \sum_s f_s [\mathbb{I} + \mathbb{P}_s^0 : (\mathbb{C}_s - \mathbb{C}_0)]^{-1} \right\}^{-1}, \quad (3.6)$$

with \mathbb{I} as the fourth-order identity tensor, and \mathbb{P}_r^0 as the fourth-order Hill tensor, taking into account the shape of the inclusion r and the stiffness of the surrounding matrix \mathbb{C}_0 , see (Zaoui 2002) for details. The mathematical definition of the influence tensor depends on the morphology of the respective RVE and is defined based on the phase concentration tensors (Pichler & Hellmich 2010, Morin et al. 2017). On the macroscopic level, the constitutive law analogous to Eq. (3.4) reads as

$$\boldsymbol{\Sigma} = \mathbb{C}_{\text{hom}} : (\mathbf{E} - \mathbf{E}^{\text{P}}), \quad (3.7)$$

with \mathbb{C}_{hom} as the homogenized stiffness tensor of the RVE reading as (Zaoui 2002)

$$\mathbb{C}_{\text{hom}} = \sum_r f_r \mathbb{C}_r : \mathbb{A}_r. \quad (3.8)$$

The macroscopic plastic strains \mathbf{E}^{P} are derived based on Levin's theorem (Levin 1967), yielding

$$\mathbf{E}^{\text{P}} = \sum_r f_r \mathbb{C}_{\text{hom}}^{-1} : \mathbb{A}_r^{\text{T}} : \mathbb{C}_r : \boldsymbol{\varepsilon}_r^{\text{P}}. \quad (3.9)$$

3.2.3 Extension to multiscale scheme

Let us now consider the case of a material organized across several orders of magnitude, even comprising more than two up- and downscaling paths, as illustrated in Figure 3.1. Then, Eq. (3.5) needs to be extended accordingly, yielding

$$\boldsymbol{\varepsilon}_r^{\pi,i} = \mathbb{A}_r^{\pi,i} : \boldsymbol{\varepsilon}^{\pi,i-1} + \sum_s \mathbb{D}_{rs}^{\pi,i} : \boldsymbol{\varepsilon}_s^{\text{P};\pi,i}. \quad (3.10)$$

In Eq. (3.10), $\boldsymbol{\varepsilon}_r^{\pi,i}$ denotes the elastic strain tensor of phase r within RVE i along path π , $\mathbb{A}_r^{\pi,i}$ is the related concentration tensor, $\mathbb{D}_{r,s}^{\pi,i}$ the influence tensor quantifying the influence of plastic strain $\boldsymbol{\varepsilon}_s^{\text{P};\pi,i}$ on $\boldsymbol{\varepsilon}_r^{\pi,i}$. Strain tensor $\boldsymbol{\varepsilon}^{\pi,i-1}$ represents the volume average over all material phases constituting RVE i of path π , $\boldsymbol{\varepsilon}^{\pi,i-1} = \sum_s f_s^{\pi,i} \boldsymbol{\varepsilon}_s^{\pi,i}$, $f_s^{\pi,i}$ being the volume fractions of phases s within RVE i of path π . Obviously, evaluating $\boldsymbol{\varepsilon}^{\pi,i-1}$ for $i = 1$ yields $\boldsymbol{\varepsilon}^{\pi,0}$, which is identical to the macroscopic strain tensor \mathbf{E} .

Formulating Eq. (3.10) for all hierarchical levels of a multiscale up-and downscaling scheme along path π allows for expressing the strain tensor in phase r of RVE v (which may or may not be the lowest level) of path π as follows:

$$\begin{aligned} \boldsymbol{\varepsilon}_r^{\pi,v} &= \mathbb{A}_r^{\pi,v} : \mathbb{A}_{r_{\pi,v}}^{\pi,v-1} : \dots : \mathbb{A}_{r_{\pi,3}}^{\pi,2} : \mathbb{A}_{r_{\pi,2}}^{\pi,1} : \mathbf{E} \\ &+ \mathbb{A}_r^{\pi,v} : \mathbb{A}_{r_{\pi,v}}^{\pi,v-1} : \dots : \mathbb{A}_{r_{\pi,3}}^{\pi,2} : \sum_{s \in \mu^{\pi,1}} \mathbb{D}_{r_{\pi,2}s}^{\pi,1} : \boldsymbol{\varepsilon}_s^{\text{P};\pi,1} \\ &+ \mathbb{A}_r^{\pi,v} : \mathbb{A}_{r_{\pi,v}}^{\pi,v-1} : \dots : \mathbb{A}_{r_{\pi,4}}^{\pi,3} : \sum_{s \in \mu^{\pi,2}} \mathbb{D}_{r_{\pi,3}s}^{\pi,2} : \boldsymbol{\varepsilon}_s^{\text{P};\pi,2} \\ &\vdots \\ &+ \mathbb{A}_r^{\pi,v} : \sum_{s \in \mu^{\pi,v-1}} \mathbb{D}_{r_{\pi,v}s}^{\pi,v-1} : \boldsymbol{\varepsilon}_s^{\text{P};\pi,v-1} \\ &+ \sum_{s \in \mu^{\pi,v}} \mathbb{D}_{rs}^{\pi,v} : \boldsymbol{\varepsilon}_s^{\text{P};\pi,v}, \end{aligned} \quad (3.11)$$

where $\mu^{\pi,i}$ describes the set of all phases r situated within RVE i and $\mathbb{A}_{r_{\pi,i+1}}^{\pi,i}$ indicates the concentration tensor used to downscale the macroscopic strain imposed on RVE i of path π to its phase $r_{\pi,i+1}$, which hosts RVE $i+1$.

Eq. (3.11) expresses that the total strain in phase r is only governed by both the macroscopic strain \mathbf{E} and by phase-specific plastic strains occurring within all phases of all RVEs which are part of downscaling path π . Striving for a more concise format of Eq. (3.11), we introduce the new operator $\overset{e}{\prod}$, which is defined analogously to the conventional product operator but considering tensor contractions instead of scalar multiplications; namely in the following way:

$$\overset{e(-)}{\prod}_{i=a} \mathbb{A}_i = \begin{cases} \mathbb{I} & \text{if } a < e \\ \mathbb{A}_a : \mathbb{A}_{a-1} : \dots : \mathbb{A}_{e+1} : \mathbb{A}_e & \text{if } a \geq e \end{cases} \quad (3.12)$$

and

$$\overset{e(+)}{\prod}_{i=a} \mathbb{A}_i = \begin{cases} \mathbb{A}_a : \mathbb{A}_{a+1} : \dots : \mathbb{A}_{e-1} : \mathbb{A}_e & \text{if } a \leq e \\ \mathbb{I} & \text{if } a > e \end{cases} \quad (3.13)$$

Applying this new formalism to Eq. (3.11) allows for reducing it to

$$\boldsymbol{\varepsilon}_r^{\pi,v} = \overset{1(-)}{\prod}_{i=v} \mathbb{A}_{r_{\pi,i+1}}^{\pi,i} : \mathbf{E} + \sum_{j=1}^n \left(\overset{j+1(-)}{\prod}_{i=v} \mathbb{A}_{r_{\pi,i+1}}^{\pi,i} : \sum_{s \in \mu^{\pi,j}} \mathbb{D}_{r_{\pi,j+1}s}^{\pi,j} : \boldsymbol{\varepsilon}_s^{\text{P};\pi,j} \right), \quad (3.14)$$

whereby $r_{\pi,v+1} \equiv r$. For computational reasons, it makes sense to express the multiscale concentration-influence relation given by Eqs. (3.11) and (3.14), respectively, in terms of the phases from which the plastic behavior originates. This would allow for linking all independent plasticity variables to each other. To that end, Levin's theorem according to Eq. (3.9) is applied to express all the plastic strains arising in RVEs higher than level v as a function of their plasticity-inducing phases only yielding eventually the following expression:

$$\boldsymbol{\varepsilon}_r^{\pi,v} = \overset{1(-)}{\prod}_{i=v} \mathbb{A}_{r_{\pi,i+1}}^{\pi,i} : \mathbf{E} + \sum_{\rho} \mathbb{M}_{r\rho}^{\pi,v-\tau,u} : \boldsymbol{\varepsilon}_{\rho}^{\text{P};\tau,u}, \quad (3.15)$$

whereby the multiscale influence tensor $\mathbb{M}_{r\rho}^{\pi,v-\tau,u}$ unites the multiscale effect of the plastic strain of the plasticity-inducing phase ρ situated within RVE u of path τ on the total strain of phase r situated within RVE v of path π .

3.2.4 Derivation of the multiscale influence tensor

Considering a v -step up-/downscaling path π within an arbitrary multiscale homogenization scheme, allows to identify only the direct path from level v to the macroscopic scale, as being composed by the phases $r, r_{\pi,v}, r_{\pi,v-1}, \dots, r_{\pi,3}$ and $r_{\pi,2}$. All these phases may be accompanied by other neighboring phases within their respective RVEs. However, without knowing the actual composition of the homogenization scheme it is impossible to state whether these neighboring phases are plasticity-inducing ones or are described by a branching downscaling path themselves. Consequently, all phases that are not part of the direct downscaling path π cannot be expressed in terms of their plasticity-inducing phases. Nevertheless, the plastic

strains of the phases being part of path π can be linked to the plastic strains arising at the lowest level v of path π and the possible neighboring plastic strains only, reading as

$$\begin{aligned}
\boldsymbol{\varepsilon}_{r_{\pi,a+1}}^{\text{p},\pi,a} &= \prod_{i=a+1}^{v-1(+)} \left(f_{r_{\pi,i+1}}^{\pi,i} (\mathbb{C}_{\text{hom}}^{\pi,i})^{-1} : (\mathbb{A}_{r_{\pi,i+1}}^{\pi,i})^{\text{T}} : \mathbb{C}_{r_{\pi,i+1}}^{\pi,i} \right) \\
&: \sum_{r \in \mu^{\pi,v}} \left(f_r^{\pi,v} (\mathbb{C}_{\text{hom}}^{\pi,v})^{-1} : (\mathbb{A}_r^{\pi,v})^{\text{T}} : \mathbb{C}_r^{\pi,v} : \boldsymbol{\varepsilon}_r^{\text{p},\pi,v} \right) \\
&+ \sum_{j=a+1}^{v-1} \left[\prod_{i=a+1}^{j-1(+)} \left(f_{r_{\pi,i+1}}^{\pi,i} (\mathbb{C}_{\text{hom}}^{\pi,i})^{-1} : (\mathbb{A}_{r_{\pi,i+1}}^{\pi,i})^{\text{T}} : \mathbb{C}_{r_{\pi,i+1}}^{\pi,i} \right) \right. \\
&: \left. \sum_{r \in \mu^{\pi,j}/r_{\pi,j+1}} \left(f_r^{\pi,j} (\mathbb{C}_{\text{hom}}^{\pi,j})^{-1} : (\mathbb{A}_r^{\pi,j})^{\text{T}} : \mathbb{C}_r^{\pi,j} : \boldsymbol{\varepsilon}_r^{\text{p},\pi,j} \right) \right],
\end{aligned} \tag{3.16}$$

if $1 \leq a \leq v - 2$, and as

$$\boldsymbol{\varepsilon}_{r_{\pi,a+1}}^{\text{p},\pi,a} = \sum_{r \in \mu^{\pi,v}} \left(f_r^{\pi,v} (\mathbb{C}_{\text{hom}}^{\pi,v})^{-1} : (\mathbb{A}_r^{\pi,v})^{\text{T}} : \mathbb{C}_r^{\pi,v} : \boldsymbol{\varepsilon}_r^{\text{p},\pi,v} \right), \tag{3.17}$$

if $a = v - 1$. If we now consider one of the plastic strains $\boldsymbol{\varepsilon}_r^{\text{p},\pi,v}$ within level v to be a plasticity-inducing one $r = \rho$, evaluating and inserting Eq. (3.16) and (3.17) for all RVEs higher than level v (i.e. $1 \leq a \leq v - 1$) into the multiscale concentration influence relation (3.14) and comparing the result to Eq. (3.15) allows to identify the multiscale influence tensor $\mathbb{M}_{r\rho}^{\pi,v-\pi,v}$ linking phase r to the plasticity-inducing phase ρ residing within one and the same RVE v of path π , as

$$\begin{aligned}
\mathbb{M}_{r\rho}^{\pi,v-\pi,v} &= \sum_{j=1}^{v-1} \left(\prod_{i=v}^{j+1(-)} \mathbb{A}_{r_{\pi,i+1}}^{\pi,i} : \mathbb{D}_{r_{\pi,j+1}r_{\pi,j+1}}^{\pi,j} : \prod_{i=j+1}^{v-1(+)} \left(f_{r_{\pi,i+1}}^{\pi,i} (\mathbb{C}_{\text{hom}}^{\pi,i})^{-1} : (\mathbb{A}_{r_{\pi,i+1}}^{\pi,i})^{\text{T}} : \mathbb{C}_{r_{\pi,i+1}}^{\pi,i} \right) \right) \\
&: \left(f_{\rho}^{\pi,v} (\mathbb{C}_{\text{hom}}^{\pi,v})^{-1} : (\mathbb{A}_{\rho}^{\pi,v})^{\text{T}} : \mathbb{C}_{\rho}^{\pi,v} \right) + \mathbb{D}_{r\rho}^{\pi,v}.
\end{aligned} \tag{3.18}$$

The multiscale influence tensor $\mathbb{M}_{r\rho}^{\pi,v-\tau,u}$, linking phase r situated within RVE v of path π to a plasticity-originating phase ρ residing within a different RVE u of path τ is composed following the same principle. However, the complete expression can only be derived based on the actual composition of the multiscale homogenization scheme, since the number of terms depend on the (in general unknown) level at which path τ splits up from path π . In any case, however, it includes at least the following term

$$\begin{aligned}
\mathbb{M}_{r\rho}^{\pi,v-\tau,u} &= \prod_{i=v}^{2(-)} \mathbb{A}_{r_{\pi,i+1}}^{\pi,i} : \mathbb{D}_{r_{\pi,2r_{\tau,2}}^{\pi,1}}^{\pi,1} : \prod_{i=2}^{u-1(+)} \left(f_{r_{\tau,i+1}}^{\tau,i} (\mathbb{C}_{\text{hom}}^{\tau,i})^{-1} : (\mathbb{A}_{r_{\tau,i+1}}^{\tau,i})^{\text{T}} : \mathbb{C}_{r_{\tau,i+1}}^{\tau,i} \right) \\
&: \left(f_{\rho}^{\tau,u} (\mathbb{C}_{\text{hom}}^{\tau,u})^{-1} : (\mathbb{A}_{\rho}^{\tau,u})^{\text{T}} : \mathbb{C}_{\rho}^{\tau,u} \right) + \dots
\end{aligned} \tag{3.19}$$

3.3 Multiscale plasticity algorithm

3.3.1 Elastoplastic state equations and non-associative flow rules

A full elastoplastic analysis requires introduction of stress-strain relations, both at the microscopic levels of the elastoplastic phases

$$\boldsymbol{\sigma}_r = \mathbb{C}_r : (\boldsymbol{\varepsilon}_r - \boldsymbol{\varepsilon}_r^p), \quad (3.20)$$

and at the macroscopic level

$$\boldsymbol{\Sigma} = \mathbb{C}_{\text{hom}} : (\mathbf{E} - \mathbf{E}^p). \quad (3.21)$$

Moreover, the plasticity-inducing phases are assigned with a non-associated multisurface Mohr-Coulomb criterion

$$\begin{aligned} \mathfrak{F}_s^{(1)}(\boldsymbol{\sigma}_r) &= \beta \cdot \sigma_{r,I} - \sigma_{r,III} - \sigma_r^{\text{yield}} \leq 0, \\ \mathfrak{F}_s^{(2)}(\boldsymbol{\sigma}_r) &= \beta \cdot \sigma_{r,II} - \sigma_{r,III} - \sigma_r^{\text{yield}} \leq 0, \\ \mathfrak{F}_s^{(3)}(\boldsymbol{\sigma}_r) &= \beta \cdot \sigma_{r,I} - \sigma_{r,II} - \sigma_r^{\text{yield}} \leq 0, \end{aligned} \quad (3.22)$$

and three plastic potential functions

$$\begin{aligned} \mathfrak{G}_r^{(1)}(\boldsymbol{\sigma}_r) &= \sigma_{r,I} - \sigma_{r,III}, \\ \mathfrak{G}_r^{(2)}(\boldsymbol{\sigma}_r) &= \sigma_{r,II} - \sigma_{r,III}, \\ \mathfrak{G}_r^{(3)}(\boldsymbol{\sigma}_r) &= \sigma_{r,I} - \sigma_{r,II}, \end{aligned} \quad (3.23)$$

with $\sigma_{r,I} \geq \sigma_{r,II} \geq \sigma_{r,III}$ as principal stresses associated to $\boldsymbol{\sigma}_r$, β as the friction parameter, and σ_r^{yield} as the yield strength of the respective phase. The multi-surface criterion is complemented by a non-associative flow rule of the Koiter type (Koiter 1953), reading as (Morin et al. 2017)

$$\forall i \in \mathcal{G} : \quad \dot{\boldsymbol{\varepsilon}}_r^p = \sum_{\alpha=1}^3 \dot{\lambda}_r^{(\alpha)} \frac{\partial \mathfrak{G}_r^{(\alpha)}}{\partial \boldsymbol{\sigma}_r}(\boldsymbol{\sigma}_r), \quad (3.24)$$

with associated plastic multipliers $\dot{\lambda}_r^{(\alpha)}$, governing the magnitude of the plastic strain rate $\dot{\boldsymbol{\varepsilon}}_r^p$ of phase r . Equation (3.24) governs the evolution of the plastic strains, according to the Melan-Kuhn-Tucker conditions (Simo & Hughes 1998, Melan 1938)

$$\forall \alpha \in \{1,2,3\} \quad \dot{\lambda}_i^{(\alpha)} \geq 0, \quad \mathfrak{F}_r^{(\alpha)}(\boldsymbol{\sigma}_r) \leq 0, \quad \text{and} \quad \dot{\lambda}_r^{(\alpha)} \times \mathfrak{F}_r^{(\alpha)}(\boldsymbol{\sigma}_r) = 0. \quad (3.25)$$

3.3.2 General iteration strategy and discretized plastic flow rule

Inspired by the standard procedure in computational elastoplasticity, loading is applied in an incremental manner: We largely follow the algorithmic strategy described in Morin et al. (2017), prescribing a series of macroscopic stress states $\boldsymbol{\Sigma}^n$, $n = \{1, \dots, N_n\}$, each one being associated with the end of load step n ; with respective macroscopic load increments $\Delta \boldsymbol{\Sigma}^n = \boldsymbol{\Sigma}^n - \boldsymbol{\Sigma}^{n-1}$. The non-linear stress-strain behavior furthermore requires an iterative scheme for the determination of corresponding macroscopic strain states \mathbf{E}^n . We employ a modified Newton-Raphson scheme with each of the N_{τ} iteration steps being indicated by index τ and residual stress increments being denoted by $\mathbf{R}^{n,\tau}$, see Figure 3.2.

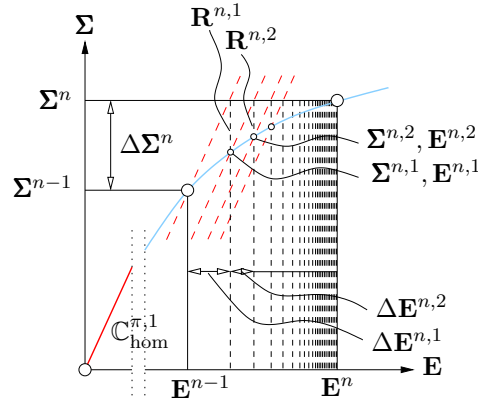


Fig. 3.2: Modified Newton-Raphson iteration scheme used to determine the macroscopic strain \mathbf{E}^n corresponding to the applied macroscopic stress Σ^n by iteratively adding strain increments $\Delta \mathbf{E}^{n,\tau}$

The key algorithmic task lies in computing, from the known values of state variables associated with load step n and iteration step τ , $\mathbf{E}^{n,\tau}$, $\mathbf{E}^{p,n,\tau}$ and $\boldsymbol{\varepsilon}_{s,i}^{p,n,\tau}$, the corresponding values for step $(\tau + 1)$. The challenge thereby lies in determining the unknown plastic events. These plastic events stem from phases which are a basic component of the material and exhibit (elasto)plastic material behavior, so-called plasticity-inducing phases. To avoid the necessity of continuous up- and downscaling of variables between the different levels during the determination of plastic events, it is convenient to derive a relation that summarizes all these processes and *independent* plasticity-variables in a *single multiscale equation* for each plasticity-inducing phase. To this end, the multiscale concentration-influence relation given by Eq. (3.15) allows to express the microscopic constitutive law of a plasticity-inducing phase r within RVE v of path π as a function of the applied macroscopic strain and the originating plastic strains of any downscaling path only, which has to be fulfilled for all incremental steps n and iteration steps r :

$$\boldsymbol{\sigma}_{r^{\pi,v}}^{n,\tau} = \mathbb{C}_r^{\pi,v} : \left[\prod_{i=v}^{1(-)} \mathbb{A}_{r^{\pi,i+1}}^{\pi,i} : \mathbf{E}^{n,\tau} + \sum_{\rho} (\mathbb{M}_{r^{\rho}}^{\pi,v-\tau,u} - \delta_{r\rho} \mathbb{I}) : \boldsymbol{\varepsilon}_{\rho^{\tau,u}}^{p;n,\tau} \right]. \quad (3.26)$$

Note that, for the sake of keeping the notation as clear and understandable as possible, we slightly change the notation of time depended variables, i.e. stresses and strains, as compared to Section 3.2. In detail, all indices related to the definition of the considered material phase and RVE are now included in the subscript, while all indices related to implementation of the algorithm are included in the superscript. Consequently, stresses denoted as $\boldsymbol{\sigma}_r^{\pi,v}$ in Section 3.2, are now denoted as $\boldsymbol{\sigma}_{r^{\pi,v}}$.

To get access to the evolution of plastic strains, the flow rule needs to be discretized: Traditionally, forward or backward Euler schemes are employed for integrating the evolution equation (3.24), see e.g. Simo & Hughes (1998), Morin et al. (2017); meaning that the flow direction $\partial \mathcal{G}_r^{(\alpha)} / \partial \boldsymbol{\sigma}_r$ is evaluated either at the beginning or at the end of the load step under investigation. We here implement an alternative strategy: For any iteration step $(\tau + 1)$ of any load step n , we consider a series of N_k stress states $\boldsymbol{\sigma}_r^{n,\tau+1,k}$, $k \in \{1, \dots, N_k\}$, converging,

according to a stress back-projection process explained further below, towards $\boldsymbol{\sigma}_r^{n,\tau+1}$, see Figure 2.3. The corresponding discretization of Eq. (3.24) reads as

$$\Delta \boldsymbol{\varepsilon}_{r^{\pi,v}}^{p,n,\tau+1} = \boldsymbol{\varepsilon}_{r^{\pi,v}}^{p,n,\tau+1} - \boldsymbol{\varepsilon}_{r^{\pi,v}}^{p,n,\tau} = \sum_{\alpha=1}^{N_{\text{Fact},i}^{n,\tau+1}} \sum_{k=1}^{N_k} \Delta \lambda_{r^{\pi,v}}^{(\alpha),n,\tau+1,k} \frac{\partial \mathfrak{G}_r^{(\alpha)}}{\partial \boldsymbol{\sigma}_r}(\boldsymbol{\sigma}_{r^{\pi,v}}^{n,\tau+1,k}), \quad (3.27)$$

with $N_{\text{Fact},i}^{n,\tau+1}$ as the active yield surfaces of solid phase i at load step n and iteration step $\tau + 1$, i.e. those yield surfaces with the associated plastic multipliers being non-zero. Finally, the plastic strain increments associated with the entire load step n read as

$$\Delta \boldsymbol{\varepsilon}_r^{p,n} = \sum_{\tau=1}^{N_r} \Delta \boldsymbol{\varepsilon}_r^{p,n,\tau}. \quad (3.28)$$

3.3.3 Series of stress states and return mapping

Insertion of Eq. (3.27) into Eq. (3.26) yields

$$\boldsymbol{\sigma}_{r^{\pi,v}}^{n,\tau+1} = \mathbb{C}_r^{\pi,v} : \left[\prod_{i=v}^{1(-)} \mathbb{A}_{r^{\pi,i+1}}^{\pi,i} : \mathbf{E}^{n,\tau+1} + \sum_{\rho} (\mathbb{M}_{r\rho}^{\pi,v-\tau,u} - \delta_{r\rho} \mathbb{I}) : \left(\boldsymbol{\varepsilon}_{\rho^{\tau,u}}^{p;n,\tau} + \sum_{k=1}^{N_k} \sum_{\alpha=1}^{N_{\text{Fact},i}^{n,\tau+1}} \Delta \lambda_{\rho^{\tau,u}}^{(\alpha),n,\tau+1,k} \frac{\partial \mathfrak{G}_\rho^{(\alpha)}}{\partial \boldsymbol{\sigma}_\rho}(\boldsymbol{\sigma}_{\rho^{\tau,u}}^{n,\tau+1,k}) \right) \right]. \quad (3.29)$$

The N_k plastic multipliers $\Delta \lambda_r^{(\alpha),n,\tau+1,k}$, $k = \{1, \dots, N_k\}$, associated to phase r , are determined in a sequential way, with corresponding stress states $\boldsymbol{\sigma}_r^{n,\tau+1,k}$, $k = \{1, \dots, N_k\}$, see Figure 3.3.

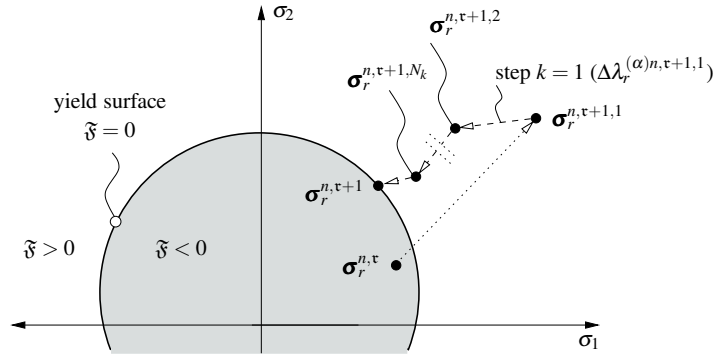


Fig. 3.3: Principle of iterative return-mapping considering a series of stress states and their corresponding flow directions being developed by a novel sequential one-step linearized backprojection process

The definition of the first member of this stress series, $\boldsymbol{\sigma}_{s,i}^{n,r+1,1}$, is inspired by the concept of elastic trial stress states (Simo & Hughes 1998) and follows from the assumption of no plastic events, so that

$$\boldsymbol{\sigma}_{r^{\pi,v}}^{n,\tau+1,1} = \mathbb{C}_r^{\pi,v} : \left[\prod_{i=v}^{1(-)} \mathbb{A}_{r^{\pi,i+1}}^{\pi,i} : \mathbf{E}^{n,\tau+1} + \sum_{\rho} (\mathbb{M}_{r\rho}^{\pi,v-\tau,u} - \delta_{r\rho} \mathbb{I}) : \boldsymbol{\varepsilon}_{\rho^{\tau,u}}^{p;n,\tau} \right]. \quad (3.30)$$

This microscopic stress state allows for discriminating between plasticizing and purely elastic phases by inserting (3.30), into the multisurface yield criterion for the respective phase given by Eq. (3.22):

$$\forall i \in \mathcal{G}, \forall \alpha \in \{1, 2, 3\} \quad \mathfrak{F}_r^{(\alpha), n, \tau+1, 1} = \mathfrak{F}_r^{(\alpha)}(\boldsymbol{\sigma}_r^{n, \tau+1, 1}). \quad (3.31)$$

Thereby, the following aspects are important to note:

- Negative values $\mathfrak{F}_r^{(\alpha), n, \tau+1, 1} \leq 0$ for all yield surfaces associated to the phase r , ensure that the corresponding phase behaves purely elastic during residual step $\tau + 1$.
- A positive value $\mathfrak{F}_r^{(\alpha), n, \tau+1, 1} > 0$ for at least one yield surface associated to the phase r , violates Eq. (3.25), which means that the corresponding phase does not behave purely elastic but exhibits plastic behavior during the residual step $\tau + 1$. The set of plasticizing phases $\mathcal{G}_{\text{plast}}^{n, \tau+1}$ (comprising $N_{\text{plast}}^{n, \tau+1}$ elements) is defined by all phases having at least one positive yield criterion during residual step $\tau + 1$. Each of this phases is associated to a number of active yield surfaces $N_{\text{Fact}, \tau}^{n, \tau+1} \in \{1, 2, 3\}$.

Having identified the set of plasticizing phases, the next members of the stress series, $\boldsymbol{\sigma}_r^{n, \tau+1, k}$, $k \geq 2$, follow as

$$\begin{aligned} \boldsymbol{\sigma}_{r, \pi, v}^{n, \tau+1, k} = \mathbb{C}_r^{\pi, v} : & \left[\prod_{i=v}^{1(-)} \mathbb{A}_{r, \pi, i+1}^{\pi, i} : \mathbf{E}^{n, \tau+1} + \sum_{\rho \in \mathcal{G}_{\text{plast}}^{n, \tau+1}} (\mathbb{M}_{r\rho}^{\pi, v-\tau, u} - \delta_{r\rho} \mathbb{I}) \right. \\ & \left. : \left(\boldsymbol{\epsilon}_{\rho^{\tau, u}}^{p; n, \tau} + \sum_{l=1}^{k-1} \sum_{\alpha=1}^3 \Delta \lambda_{\rho^{\tau, u}}^{(\alpha), n, \tau+1, l} \frac{\partial \mathfrak{G}_{\rho}^{(\alpha)}}{\partial \boldsymbol{\sigma}_{\rho}}(\boldsymbol{\sigma}_{\rho^{\tau, u}}^{n, \tau+1, l}) \right) \right]. \end{aligned} \quad (3.32)$$

Eq. (3.32) can also be written as

$$\begin{aligned} \boldsymbol{\sigma}_{r, \pi, v}^{n, \tau+1, k} = \boldsymbol{\sigma}_{r, \pi, v}^{n, \tau+1, k-1} + \mathbb{C}_r^{\pi, v} : & \left[\sum_{\rho \in \mathcal{G}_{\text{plast}}^{n, \tau+1}} (\mathbb{M}_{r\rho}^{\pi, v-\tau, u} - \delta_{r\rho} \mathbb{I}) \right. \\ & \left. : \sum_{\alpha=1}^3 \Delta \lambda_{\rho^{\tau, u}}^{(\alpha), n, \tau+1, k-1} \frac{\partial \mathfrak{G}_{\rho}^{(\alpha)}}{\partial \boldsymbol{\sigma}_{\rho}}(\boldsymbol{\sigma}_{\rho^{\tau, u}}^{n, \tau+1, k-1}) \right]. \end{aligned} \quad (3.33)$$

with $\boldsymbol{\sigma}_{r, \pi, v}^{n, \tau+1, k-1}$ summing up the previous return steps $l \in \{1, \dots, k-1\}$. Eq. (3.32) is used for the determination of the plastic multipliers associated with back-projection step $(k-1)$. Therefore, Eq. (3.32) is regarded as a function with unknown variables $\Delta \lambda_{\rho}^{(\alpha), n, \tau+1, k-1}$, $\forall \rho \in \mathcal{G}_{\text{plast}}^{n, \tau+1}$ and $\forall \alpha \in \{1, \dots, N_{\text{Fact}, \rho}^{n, \tau+1}\}$. Insertion of this function into the yield function $\mathfrak{F}_r^{(\alpha)}$ according to Eq. (3.22) makes the latter to depend on $\Delta \lambda_{\rho}^{(\alpha), n, \tau+1, k-1}$, $\forall \rho \in \mathcal{G}_{\text{plast}}^{n, \tau+1}$ and $\forall \alpha \in \{1, \dots, N_{\text{Fact}, \rho}^{n, \tau+1}\}$, as well:

$$\begin{aligned} \mathfrak{F}_r^{(\alpha), n, \tau+1, k} = \mathfrak{F}_r^{(\alpha)} \left(\boldsymbol{\sigma}_{r, \pi, v}^{n, \tau+1, k} \left(\Delta \lambda_1^{(1), n, \tau+1, k-1}, \dots, \Delta \lambda_1^{(N_{\text{Fact}, 1}^{n, \tau+1}), n, \tau+1, k-1}, \dots \right. \right. \\ \left. \left. \dots, \Delta \lambda_j^{(1), n, \tau+1, k-1}, \dots, \Delta \lambda_j^{(N_{\text{Fact}, j}^{n, \tau+1}), n, \tau+1, k-1}, \dots \right. \right. \\ \left. \left. \dots, \Delta \lambda_{N_{\text{plast}}^{n, \tau+1}}^{(1), n, \tau+1, k-1}, \dots, \Delta \lambda_{N_{\text{plast}}^{n, \tau+1}}^{(N_{\text{Fact}, N_{\text{plast}}^{n, \tau+1}}), n, \tau+1, k-1} \right) \right). \end{aligned} \quad (3.34)$$

We then project the stress state “towards” the yield surface, by requiring the linearization of Eq. (3.34) for each actually plasticizing plasticity-inducing phase and each corresponding active yield surface to be zero, according to

$$\begin{aligned}
& \forall i \in \mathcal{G}_{\text{plast}}^{n,\tau+1}, \forall \alpha \in \{1, \dots, N_{\text{Fact},i}^{n,\tau+1}\} : \\
& \mathfrak{F}_r^{(\alpha)} \left(\boldsymbol{\sigma}_{r^{\pi,v}}^{n,\tau+1,k} \left(\Delta \lambda_l^{(\gamma),n,\tau+1,k-1} = 0, \forall \{l, \gamma\} \right) \right) \\
& + \sum_{\rho \in \mathcal{G}_{\text{plast}}^{n,\tau+1}} \sum_{\beta=1}^{N_{\text{Fact},\rho}} \frac{\partial \mathfrak{F}_r^{(\alpha)}}{\partial \boldsymbol{\sigma}_r} \left(\boldsymbol{\sigma}_{r^{\pi,v}}^{n,\tau+1,k} \left(\Delta \lambda_l^{(\gamma),n,\tau+1,k-1} = 0, \forall \{l, \gamma\} \right) \right) \\
& \quad : \frac{\partial \boldsymbol{\sigma}_{r^{\pi,v}}^{n,\tau+1,k}}{\partial (\Delta \lambda_{\rho^{\tau,u}}^{(\beta),n,\tau+1,k-1})} \Delta \lambda_{\rho^{\tau,u}}^{(\beta),n,\tau+1,k-1} = 0,
\end{aligned} \tag{3.35}$$

whereby

$$\begin{aligned}
& \frac{\partial \mathfrak{F}_r^{(\alpha)}}{\partial \boldsymbol{\sigma}_r} \left(\boldsymbol{\sigma}_{r^{\pi,v}}^{n,\tau+1,k} \left(\Delta \lambda_l^{(\gamma),n,\tau+1,k-1} = 0, \forall \{l, \gamma\} \right) \right) : \frac{\partial \boldsymbol{\sigma}_{r^{\pi,v}}^{n,\tau+1,k}}{\partial (\Delta \lambda_{\rho^{\tau,u}}^{(\beta),n,\tau+1,k-1})} = \\
& \frac{\partial \mathfrak{F}_r^{(\alpha)}}{\partial \boldsymbol{\sigma}_r} \left(\boldsymbol{\sigma}_{r^{\pi,v}}^{n,\tau+1,k-1} \right) : (\mathbb{M}_{r\rho}^{\pi,v-\tau,u} - \delta_{r\rho} \mathbb{I}) : \frac{\partial \mathfrak{G}_\rho^{(\beta)}}{\partial \boldsymbol{\sigma}_\rho} \left(\boldsymbol{\sigma}_{\rho^{\tau,u}}^{n,\tau+1,k-1} \right).
\end{aligned} \tag{3.36}$$

Eq. (3.35) yields a linear system of equations for the unknowns $\Delta \lambda_\rho^{(\alpha),n,\tau+1,k-1}$, $\forall \rho \in \mathcal{G}_{\text{plast}}^{n,\tau+1}$ and $\forall \alpha \in \{1, \dots, N_{\text{Fact},\rho}^{n,\tau+1}\}$, which finally allow to compute the k -th member of the stress series according to Eq. (3.32). The series of stress states is further extended following Eqs. (3.32)-(3.36), until the stress state derived at the end of step N_k , $\boldsymbol{\sigma}_{r^{\pi,v}}^{n,\tau+1,N_k+1}$, is sufficiently fulfilling the Melan-Kuhn-Tucker conditions, i.e.

$$\forall r \in \mathcal{G}_{\text{plast}}^{n,\tau+1}, \forall \alpha \in \{1, \dots, N_{\text{Fact},r}^{n,\tau+1}\} : \quad \|\mathfrak{F}_r^{(\alpha)} \left(\boldsymbol{\sigma}_{r^{\pi,v}}^{n,\tau+1,N_k+1} \right)\| < \text{TOL}, \tag{3.37}$$

with a prescribed tolerance value TOL.

3.4 Application to bone tissue

3.4.1 Hierarchical organization and micromechanical representation

Bone tissue is a prime example for hierarchically organized materials, exhibiting several *universal* levels (Katz et al. 1984), see Figure 3.4:

- At the **macroscopic level**, see Figure 3.4(a), **cortical** (or compact) bone, which is the hard outer surface of bone, forms a protective layer around its internal cavity or filling with **trabecular** (or spongy) bone, which forms an open cell porous network.
- At the **microscopic level**, cortical bone includes structural subunits called **osteon**, see Figure 3.4(c), whereas trabecular bone is built up by individual beam, strut, or rod elements (so-called **trabeculae**), see Figure 3.4(b). Both cortical and trabecular bone exhibit a complex network of canals and pores. In particular, **vascular pores** form a tree-type branching network and host blood vessels, lymphatic vessels and cells.

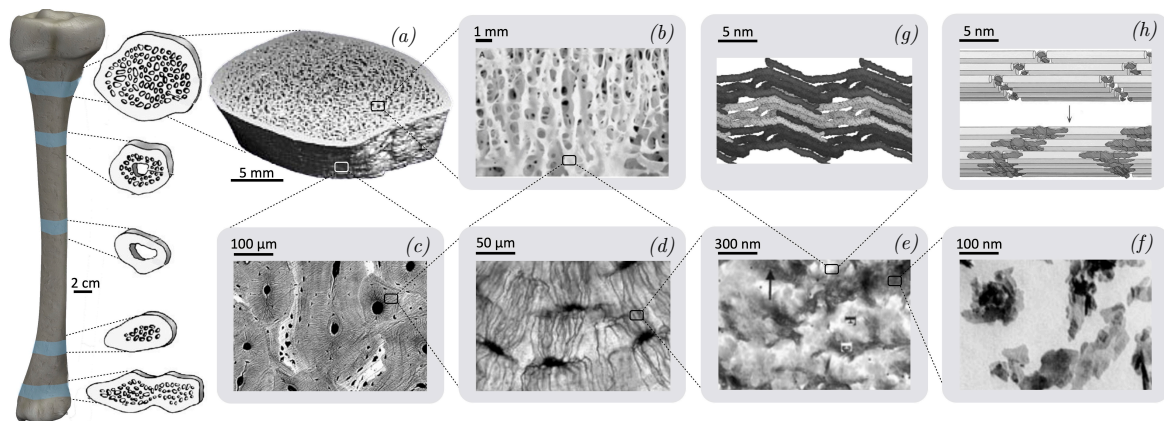


Fig. 3.4: Hierarchical organization of bone: (a) 3D reconstructed HR-pQCT image of a tibia with trabecular and cortical compartments (Liu et al. 2012); (b) spongy, trabecular bone inside a vertebral bone (Einhorn 2003); (c) osteonal cortical bone, acquired by SEM by Hang & Barber (2011); (d) osteocytic lacunae (brightfield light microscopy image taken by Tim Arnett); (e) ultrastructure (Prostak & Lees 1996); (f) hydroxyapatite crystals, obtained by means of SEM (Weiner & Wagner 1998); (g) wet collagen, electron density map (Orgel et al. 2006); (h) mineralization of collagen molecules starting in the gap zones and spreading into the intermolecular spaces, schematic illustration by Landis & Jacquet (2013)

While the branches running parallel to the bone axis are called Haversian canals, the connecting branches in between are referred to as Volkmann canals. Vascular porosity in cortical bone ranges from 2% to 8% for healthy bone up to 35% in case of disease (Fritsch & Hellmich 2007). In trabecular bone, vascular porosity reaches values of 50% up to 90% (Buckwalter et al. 1995). Furthermore, the vascular pores are connected to cave-like single **lacunae pores**, see the black dots in Figures 3.4(c), via much smaller channels called **canaliculi**, see Figure 3.4(d). The lacunar and canalicular porosities have a much smaller fluctuation range than the vascular porosity and are assumed to be in the range of 1.3% and 0.7% as reported by Schneider et al. (2007, 2011).

- At the so-called **ultrastructural level**, the material building up both osteons and trabeculae is characterized by **collagen-rich** and **collagen-free** domains, see the light and dark areas in Figure 3.4(e). Commonly, these domains are referred to as fibrils and extrafibrillar space (Prostak & Lees 1996).
- At the **molecular level**, shown in Figures 3.4(f) and (g), the elementary constituents of bone can be identified, namely (i) hydroxyapatite (HA) in form of plate-shaped mineral crystals; (ii) slender, helically wound collagen molecules being self-assembled in staggered organizational schemes (so-called fibrils), which themselves covalently bond to bigger units referred to as fibers; (iii) different non-collagenous organic components, such as lipids or proteins; and (iv) water

Obeying the separation of scales-principle introduced in Section 3.2.1 allows for deducing a micromechanical representation of bone tissue, considering the above-sketched hierarchical organization of bone tissue. Building on an earlier micromechanical model (Fritsch, Hellmich & Dormieux 2009), we here propose the following updated multiscale material model of bone tissue, as depicted in Figure 3.5:

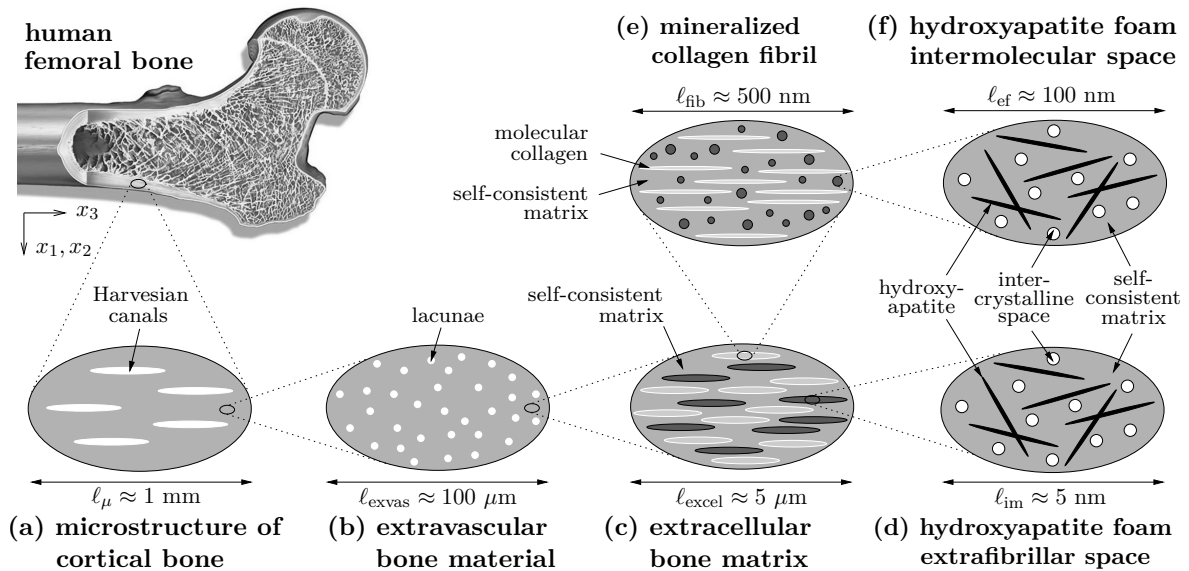


Fig. 3.5: *Micromechanical representation of cortical bone by means of a multiscale homogenization scheme (permission for bone image reproduction by courtesy of Pieter Keulen (2015))*

- The RVE of **bone microstructure**, indicated by suffix “ μ ”, exhibits a characteristic length of several millimeters and is composed of cylindrical vascular pores (indicated by suffix “vas”) embedded in a matrix of extravascular bone material, see Figure 3.5(a).
- The RVE of **extravascular bone material**, indicated by suffix “exvas”, exhibits a characteristic length of several hundred micrometers and is composed of spherical lacunae pores (labeled by suffix “lac”) in an extracellular matrix, see Figure 3.5(b).
- The RVE of **extracellular bone matrix**, the so-called ultrastructure indicated by suffix “excel”, exhibits a characteristic length of several micrometers and is composed of cylindrical, mineralized fibrils and a cylindrical phase of hydroxyapatite foam - the extrafibrillar space, see Figure 3.5(c).
- The RVE of **mineralized collagen fibril**, the so-called fibrillar space, indicated by suffix “fib”, exhibits a characteristic length of several hundred nanometers and is composed of a cylindrical molecular collagen phase and a spherical hydroxyapatite foam phase, see Figure 3.5(e).
- The RVE of the **extrafibrillar space**, indicated by suffix “ef”, has a characteristic length of around hundred nanometer and is composed of infinitely many cylindrical shaped hydroxyapatite needles orientated in all space directions (labeled by suffix “HA”) and spherical water-filled pores in-between, the so-called intercrystalline space (labeled by suffix “ic”), see Figure 3.5(d).

- The RVE of the **intermolecular space**, indicated by suffix “im”, exhibits a characteristic length of a few nanometers and is composed of consisting of infinitely many cylindrical shaped hydroxyapatite needles orientated in all space directions (labeled by suffix “HA”) and spherical water-filled pores in-between, the so-called intercrystalline space (labeled by suffix “ic”), see Figure 3.5(f).

3.4.2 Plasticity of bone

While the strength of bone materials is often related to the strength properties of collagen, or hydroxyapatite, or the interfaces between these constituents, more recent works indicate the great role of water for the failure properties of bone (Bhowmik et al. 2007, 2009, Wilson et al. 2006, Zahn & Hochrein 2003, Zahn et al. 2007). Following this theory, Fritsch, Hellmich & Dormieux (2009) presented a new proposition for bone failure based on layered water-induced ductile sliding of minerals. In detail, the mineral crystals are assumed not to break or detach once a critical stress threshold is reached, but to maintain the loads accumulated up to the elastic limit by starting to glide upon each other. In order to cast this vision of an elastoplastic interface behavior between hydrated hydroxyapatite crystals into a mathematical form, the findings of Fritsch, Dormieux, Hellmich & Sanahuja (2009) allow to mimic the effect of microinterface behavior of elongated 1D particles on the overall macroscopic material by equivalent bulk failure properties of the elongated phases. Therefore, elastoplastic material behavior is assigned to the needles and a continuum micromechanics theory for elastoplasticity is deemed suitable to explain the mechanical behavior of bone.

3.4.3 Establishment of a micromechanical up- and downscaling scheme

Based on the fundamental concepts presented in Section 3.2, the micromechanical representation of bone proposed in Section 3.4.1, and on the definition of hydroxyapatite as the plasticity-inducing material phase presented in Section 3.4.2, we establish in the following the respective mathematical framework for downscaling of stresses and strains from the macroscale to the lower-scale constituents, and for upscaling the stiffness from the lower-scale constituents to the macroscale. Thereby, we focus on the fundamental equations and on the novel aspects, and refer to previous works for (otherwise repetitive) details.

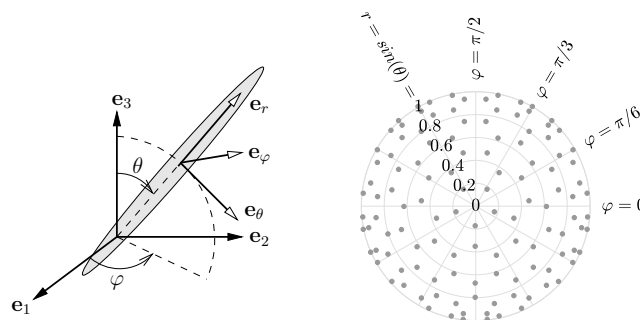


Fig. 3.6: Orientation of the solid needles by means of spherical coordinates (left); Projection of the Gaussian set of 120 integration points on the unit sphere onto a plane parallel to the base vectors e_1 and e_2 (right)

For algorithmic reasons, the infinitely many needle orientations in the intermolecular and extrafibrillar RVE are spatially discretized by a particular set \mathcal{G} of Gaussian points on the

unit sphere, which are quantified in terms of the two angles $\{\theta_i, \varphi_i\}_{i \in \mathcal{G}}$ and their associated Gaussian weights ω_i . In detail, we employ a discretization set \mathcal{G} of 120 integration points representing the centroids and areas of triangles meshing the unit sphere as described by Badel & Leblond (2004), see Figure 3.6.

3.4.3.1 Adaptation of micromechanical formulations to bone tissue

Homogenization over the intermolecular space

Specializing Eq. (3.8) according to the morphology of the RVE of intermolecular space, see Figure 3.5(f), while also taking into account the discretization of the needle directions shown in Figure 3.6, yields the homogenized stiffness tensor of intermolecular space, \mathbb{C}_{im} , reading as

$$\mathbb{C}_{\text{im}} = f_{\text{HA}}^{\text{im}} \mathbb{C}_{\text{HA}} : \sum_{i \in \mathcal{G}} \omega_i \mathbb{A}_{\text{HA},i} + f_{\text{ic}}^{\text{im}} \mathbb{C}_{\text{ic}} : \mathbb{A}_{\text{ic}}, \quad (3.38)$$

where the hydroxyapatite and intercrystalline phases are quantified in terms of their volume fractions $f_{\text{HA}}^{\text{im}}$ and $f_{\text{ic}}^{\text{im}}$, and feature stiffness tensors \mathbb{C}_{HA} and \mathbb{C}_{ic} . The concentration tensors $\mathbb{A}_{\text{HA},i}$ and \mathbb{A}_{ic} relate the macroscopic strain of the RVE, $\boldsymbol{\varepsilon}_{\text{im}}$ to the respective microscopic strains in the hydroxyapatite phase i and intercrystalline phase, $\boldsymbol{\varepsilon}_{\text{imHA},i}$ and $\boldsymbol{\varepsilon}_{\text{im-ic}}$, in terms of concentration-influence relations derived by specialization of Eq. (3.5),

$$\boldsymbol{\varepsilon}_{\text{imHA},i} = \mathbb{A}_{\text{HA},i} : \boldsymbol{\varepsilon}_{\text{im}} + \sum_{j \in \mathcal{G}} \omega_j \mathbb{D}_{\text{HA},ij} : \boldsymbol{\varepsilon}_{\text{imHA},j}^{\text{p}}, \quad (3.39)$$

$$\boldsymbol{\varepsilon}_{\text{im-ic}} = \mathbb{A}_{\text{ic}} : \boldsymbol{\varepsilon}_{\text{im}} + \sum_{j \in \mathcal{G}} \omega_j \mathbb{D}_{\text{ic},j} : \boldsymbol{\varepsilon}_{\text{imHA},j}^{\text{p}}. \quad (3.40)$$

The influence tensors $\mathbb{D}_{\text{HA},ij}$ and $\mathbb{D}_{\text{ic},j}$ thereby describe the effect of the plastic strain in the intermolecular hydroxyapatite phase j , $\boldsymbol{\varepsilon}_{\text{imHA},j}^{\text{p}}$ on the respective total strain in the hydroxyapatite phase i and intercrystalline space. Furthermore, the homogenized plastic strain of the intermolecular space $\boldsymbol{\varepsilon}_{\text{im}}^{\text{p}}$ reads, according to Levin's theorem, see Eq. (3.9), as

$$\boldsymbol{\varepsilon}_{\text{im}}^{\text{p}} = f_{\text{HA}}^{\text{im}} \mathbb{C}_{\text{im}}^{-1} : \sum_{i \in \mathcal{G}} \omega_i \mathbb{A}_{\text{HA},i}^{\text{T}} : \mathbb{C}_{\text{HA}} : \boldsymbol{\varepsilon}_{\text{imHA},i}^{\text{p}}. \quad (3.41)$$

The concentration and influence tensors occurring in Eq. (3.38)-(3.41) are defined in the Appendix A.2 and A.3.

Homogenization over the extrafibrillar space

Specializing Eq. (3.8) according to the morphology of the RVE of extrafibrillar space, see Figure 3.5(d), while also taking into account the discretization of the needle directions shown in Figure 3.6, yields the homogenized stiffness tensor of extrafibrillar space, \mathbb{C}_{ef} , reading as

$$\mathbb{C}_{\text{ef}} = f_{\text{HA}}^{\text{ef}} \mathbb{C}_{\text{HA}} : \sum_{i \in \mathcal{G}} \omega_i \mathbb{A}_{\text{HA},i} + f_{\text{ic}}^{\text{ef}} \mathbb{C}_{\text{ic}} : \mathbb{A}_{\text{ic}}, \quad (3.42)$$

where the hydroxyapatite and intercrystalline phases are quantified in terms of their volume fractions $f_{\text{HA}}^{\text{ef}}$ and $f_{\text{ic}}^{\text{ef}}$, and feature stiffness tensors \mathbb{C}_{HA} and \mathbb{C}_{ic} . The concentration tensors $\mathbb{A}_{\text{HA},i}$ and \mathbb{A}_{ic} relate the macroscopic strain of the RVE, $\boldsymbol{\varepsilon}_{\text{ef}}$ to the respective microscopic

strains in the hydroxyapatite phase i and intercrystalline phase, $\boldsymbol{\varepsilon}_{\text{effHA},i}$ and $\boldsymbol{\varepsilon}_{\text{ef-ic}}$, in terms of concentration-influence relations derived by specialization of Eq. (3.5),

$$\boldsymbol{\varepsilon}_{\text{effHA},i} = \mathbb{A}_{\text{HA},i} : \boldsymbol{\varepsilon}_{\text{ef}} + \sum_{j \in \mathcal{G}} \omega_j \mathbb{D}_{\text{HA},ij} : \boldsymbol{\varepsilon}_{\text{effHA},j}^{\text{p}}, \quad (3.43)$$

$$\boldsymbol{\varepsilon}_{\text{ef-ic}} = \mathbb{A}_{\text{ic}} : \boldsymbol{\varepsilon}_{\text{ef}} + \sum_{j \in \mathcal{G}} \omega_j \mathbb{D}_{\text{ic},j} : \boldsymbol{\varepsilon}_{\text{effHA},j}^{\text{p}}. \quad (3.44)$$

The influence tensors $\mathbb{D}_{\text{HA},ij}$ and $\mathbb{D}_{\text{ic},j}$ thereby describe the effect of the plastic strain in the extrafibrillar hydroxyapatite phase j , $\boldsymbol{\varepsilon}_{\text{effHA},j}^{\text{p}}$ on the respective total strain in the hydroxyapatite phase i and intercrystalline space. Furthermore, the homogenized plastic strain of the extrafibrillar space $\boldsymbol{\varepsilon}_{\text{ef}}^{\text{p}}$ reads, according to Levin's theorem, see Eq. (3.9), as

$$\boldsymbol{\varepsilon}_{\text{ef}}^{\text{p}} = f_{\text{HA}}^{\text{ef}} \mathbb{C}_{\text{ef}}^{-1} : \sum_{i \in \mathcal{G}} \omega_i \mathbb{A}_{\text{HA},i}^{\text{T}} : \mathbb{C}_{\text{HA}} : \boldsymbol{\varepsilon}_{\text{effHA},i}^{\text{p}}. \quad (3.45)$$

The concentration and influence tensors occurring in Eq. (3.42)-(3.45) are defined in the Appendix A.2 and A.3.

Homogenization over the mineralized collagen fibril

Specializing Eq. (3.8) according to the morphology of the RVE of the mineralized collagen fibril, see Figure 3.5(e), yields the homogenized stiffness tensor of the mineralized collagen fibril, \mathbb{C}_{fib} , reading as

$$\mathbb{C}_{\text{fib}} = f_{\text{im}}^{\text{fib}} \mathbb{C}_{\text{im}} : \mathbb{A}_{\text{im}} + f_{\text{col}}^{\text{fib}} \mathbb{C}_{\text{col}} : \mathbb{A}_{\text{col}}, \quad (3.46)$$

where the intermolecular and collagen phases are quantified in terms of their volume fractions $f_{\text{im}}^{\text{fib}}$ and $f_{\text{col}}^{\text{fib}}$, and feature stiffness tensors \mathbb{C}_{im} and \mathbb{C}_{col} . The concentration tensors \mathbb{A}_{im} and \mathbb{A}_{col} relate the macroscopic strain of the RVE, $\boldsymbol{\varepsilon}_{\text{fib}}$ to the respective microscopic strains in the intermolecular and collagen phase, $\boldsymbol{\varepsilon}_{\text{im}}$ and $\boldsymbol{\varepsilon}_{\text{col}}$, in terms of concentration-influence relations derived by specialization of Eq. (3.5),

$$\boldsymbol{\varepsilon}_{\text{im}} = \mathbb{A}_{\text{im}} : \boldsymbol{\varepsilon}_{\text{fib}} + \mathbb{D}_{\text{im}} : \boldsymbol{\varepsilon}_{\text{im}}^{\text{p}}, \quad (3.47)$$

$$\boldsymbol{\varepsilon}_{\text{col}} = \mathbb{A}_{\text{col}} : \boldsymbol{\varepsilon}_{\text{fib}} + \mathbb{D}_{\text{col}} : \boldsymbol{\varepsilon}_{\text{im}}^{\text{p}}. \quad (3.48)$$

The influence tensors \mathbb{D}_{im} and \mathbb{D}_{col} thereby describe the effect of the plastic strain in the intermolecular space, $\boldsymbol{\varepsilon}_{\text{im}}^{\text{p}}$ on the respective total strain in the intermolecular and collagen phase. Furthermore, the homogenized plastic strain of the mineralized collagen fibril $\boldsymbol{\varepsilon}_{\text{fib}}^{\text{p}}$ reads, according to Levin's theorem, see Eq. (3.9), as

$$\boldsymbol{\varepsilon}_{\text{fib}}^{\text{p}} = f_{\text{im}}^{\text{fib}} \mathbb{C}_{\text{fib}}^{-1} : \mathbb{A}_{\text{im}}^{\text{T}} : \mathbb{C}_{\text{im}} : \boldsymbol{\varepsilon}_{\text{im}}^{\text{p}}. \quad (3.49)$$

The concentration and influence tensors occurring in Eq. (3.46)-(3.49) are defined in the Appendix A.2 and A.3.

Homogenization over the extracellular bone matrix

Specializing Eq. (3.8) according to the morphology of the RVE of the extracellular bone matrix, see Figure 3.5(c), yields the homogenized stiffness tensor of the extracellular bone matrix, $\mathbb{C}_{\text{excel}}$, reading as

$$\mathbb{C}_{\text{excel}} = f_{\text{ef}}^{\text{excel}} \mathbb{C}_{\text{ef}} : \mathbb{A}_{\text{ef}} + f_{\text{fib}}^{\text{excel}} \mathbb{C}_{\text{fib}} : \mathbb{A}_{\text{fib}}, \quad (3.50)$$

where the extrafibrillar and fibrillar space are quantified in terms of their volume fractions $f_{\text{ef}}^{\text{excel}}$ and $f_{\text{fib}}^{\text{excel}}$, and feature stiffness tensors \mathbb{C}_{ef} and \mathbb{C}_{fib} . The concentration tensors \mathbb{A}_{ef} and \mathbb{A}_{fib} relate the macroscopic strain of the RVE, $\boldsymbol{\varepsilon}_{\text{excel}}$ to the respective microscopic strains in the extrafibrillar and fibrillar space, $\boldsymbol{\varepsilon}_{\text{ef}}$ and $\boldsymbol{\varepsilon}_{\text{fib}}$, in terms of concentration-influence relations derived by specialization of Eq. (3.5),

$$\boldsymbol{\varepsilon}_{\text{ef}} = \mathbb{A}_{\text{ef}} : \boldsymbol{\varepsilon}_{\text{excel}} + \mathbb{D}_{\text{ef,ef}} : \boldsymbol{\varepsilon}_{\text{ef}}^{\text{p}} + \mathbb{D}_{\text{ef,fib}} : \boldsymbol{\varepsilon}_{\text{fib}}^{\text{p}}, \quad (3.51)$$

$$\boldsymbol{\varepsilon}_{\text{fib}} = \mathbb{A}_{\text{fib}} : \boldsymbol{\varepsilon}_{\text{excel}} + \mathbb{D}_{\text{fib,ef}} : \boldsymbol{\varepsilon}_{\text{ef}}^{\text{p}} + \mathbb{D}_{\text{fib,fib}} : \boldsymbol{\varepsilon}_{\text{fib}}^{\text{p}}. \quad (3.52)$$

The influence tensors $\mathbb{D}_{\text{ef,ef}}$, $\mathbb{D}_{\text{ef,fib}}$, $\mathbb{D}_{\text{fib,ef}}$ and $\mathbb{D}_{\text{fib,fib}}$ thereby describe the effect of the plastic strains in the extrafibrillar and fibrillar space, $\boldsymbol{\varepsilon}_{\text{ef}}^{\text{p}}$ and $\boldsymbol{\varepsilon}_{\text{fib}}^{\text{p}}$, on the total strain in the extrafibrillar and fibrillar space, respectively. Furthermore, the homogenized plastic strain of the extracellular bone matrix $\boldsymbol{\varepsilon}_{\text{excel}}^{\text{p}}$ reads, according to Levin's theorem, see Eq. (3.9), as

$$\boldsymbol{\varepsilon}_{\text{excel}}^{\text{p}} = f_{\text{ef}}^{\text{excel}} \mathbb{C}_{\text{excel}}^{-1} : \mathbb{A}_{\text{ef}}^{\text{T}} : \mathbb{C}_{\text{ef}} : \boldsymbol{\varepsilon}_{\text{ef}}^{\text{p}} + f_{\text{fib}}^{\text{excel}} \mathbb{C}_{\text{excel}}^{-1} : \mathbb{A}_{\text{fib}}^{\text{T}} : \mathbb{C}_{\text{fib}} : \boldsymbol{\varepsilon}_{\text{fib}}^{\text{p}}. \quad (3.53)$$

The concentration and influence tensors occurring in Eq. (3.50)-(3.53) are defined in the Appendix A.2 and A.3.

Homogenization over the extravascular bone material

Specializing Eq. (3.8) according to the morphology of the RVE of the extravascular bone material, see Figure 3.5(b), yields the homogenized stiffness tensor of the extravascular bone material, $\mathbb{C}_{\text{exvas}}$, reading as

$$\mathbb{C}_{\text{exvas}} = f_{\text{excel}}^{\text{exvas}} \mathbb{C}_{\text{excel}} : \mathbb{A}_{\text{excel}} + f_{\text{lac+can}}^{\text{exvas}} \mathbb{C}_{\text{lac}} : \mathbb{A}_{\text{lac}}, \quad (3.54)$$

where the extracellular matrix and the lacunae pores are quantified in terms of their volume fractions $f_{\text{excel}}^{\text{exvas}}$ and $f_{\text{lac+can}}^{\text{exvas}}$, and feature stiffness tensors $\mathbb{C}_{\text{excel}}$ and \mathbb{C}_{lac} . The concentration tensors $\mathbb{A}_{\text{excel}}$ and \mathbb{A}_{lac} relate the macroscopic strain of the RVE, $\boldsymbol{\varepsilon}_{\text{exvas}}$ to the respective microscopic strains in the extracellular matrix and lacunae pores, $\boldsymbol{\varepsilon}_{\text{excel}}$ and $\boldsymbol{\varepsilon}_{\text{lac}}$, in terms of concentration-influence relations derived by specialization of Eq. (3.5),

$$\boldsymbol{\varepsilon}_{\text{excel}} = \mathbb{A}_{\text{excel}} : \boldsymbol{\varepsilon}_{\text{exvas}} + \mathbb{D}_{\text{excel}} : \boldsymbol{\varepsilon}_{\text{excel}}^{\text{p}}, \quad (3.55)$$

$$\boldsymbol{\varepsilon}_{\text{lac}} = \mathbb{A}_{\text{lac}} : \boldsymbol{\varepsilon}_{\text{exvas}} + \mathbb{D}_{\text{lac}} : \boldsymbol{\varepsilon}_{\text{excel}}^{\text{p}}. \quad (3.56)$$

The influence tensors $\mathbb{D}_{\text{excel}}$ and \mathbb{D}_{lac} thereby describe the effect of the plastic strains in the extracellular matrix, $\boldsymbol{\varepsilon}_{\text{excel}}^{\text{p}}$, on the respective total strain in the extracellular matrix and lacunae pores. Furthermore, the homogenized plastic strain of the extravascular bone material $\boldsymbol{\varepsilon}_{\text{exvas}}^{\text{p}}$ reads, according to Levin's theorem, see Eq. (3.9), as

$$\boldsymbol{\varepsilon}_{\text{exvas}}^{\text{p}} = f_{\text{excel}}^{\text{exvas}} \mathbb{C}_{\text{exvas}}^{-1} : \mathbb{A}_{\text{excel}}^{\text{T}} : \mathbb{C}_{\text{excel}} : \boldsymbol{\varepsilon}_{\text{excel}}^{\text{p}}. \quad (3.57)$$

The concentration and influence tensors occurring in Eq. (3.54)-(3.57) are defined in the Appendix A.2 and A.3.

Homogenization over the bone microstructure

Specializing Eq. (3.8) according to the morphology of the RVE of the bone microstructure, see Figure 3.5(a), yields the homogenized stiffness tensor of the bone microstructure, \mathbb{C}_μ , reading as

$$\mathbb{C}_\mu = f_{\text{exvas}}^\mu \mathbb{C}_{\text{exvas}} : \mathbb{A}_{\text{exvas}} + f_{\text{vas}}^\mu \mathbb{C}_{\text{vas}} : \mathbb{A}_{\text{vas}}, \quad (3.58)$$

where the extravascular matrix and vascular pores are quantified in terms of their volume fractions f_{exvas}^μ and f_{vas}^μ , and feature stiffness tensors $\mathbb{C}_{\text{exvas}}$ and \mathbb{C}_{vas} . The concentration tensors $\mathbb{A}_{\text{exvas}}$ and \mathbb{A}_{vas} relate the macroscopic strain of the RVE, \mathbf{E} to the respective microscopic strains in the extravascular matrix and vascular pore, $\boldsymbol{\varepsilon}_{\text{exvas}}$ and $\boldsymbol{\varepsilon}_{\text{vas}}$, in terms of concentration-influence relations derived by specialization of Eq. (3.5),

$$\boldsymbol{\varepsilon}_{\text{exvas}} = \mathbb{A}_{\text{exvas}} : \mathbf{E} + \mathbb{D}_{\text{exvas}} : \boldsymbol{\varepsilon}_{\text{exvas}}^{\text{P}}, \quad (3.59)$$

$$\boldsymbol{\varepsilon}_{\text{vas}} = \mathbb{A}_{\text{vas}} : \mathbf{E} + \mathbb{D}_{\text{vas}} : \boldsymbol{\varepsilon}_{\text{exvas}}^{\text{P}}. \quad (3.60)$$

The influence tensors $\mathbb{D}_{\text{exvas}}$ and \mathbb{D}_{vas} thereby describe the effect of the plastic strains in the extravascular matrix, $\boldsymbol{\varepsilon}_{\text{exvas}}^{\text{P}}$, on the respective total strain in the extravascular matrix and vascular pores. Furthermore, the homogenized plastic strain of the bone microstructure \mathbf{E}^{P} reads, according to Levin's theorem, see Eq. (3.9), as

$$\mathbf{E}^{\text{P}} = f_{\text{exvas}}^\mu \mathbb{C}_\mu^{-1} : \mathbb{A}_{\text{exvas}}^{\text{T}} : \mathbb{C}_{\text{exvas}} : \boldsymbol{\varepsilon}_{\text{exvas}}^{\text{P}}. \quad (3.61)$$

The concentration and influence tensors occurring in Eq. (3.58)-(3.61) are defined in the Appendix A.2 and A.3.

3.4.3.2 Downscaling from the macroscale to the plasticity-inducing material phases

Figure 3.7 shows visually the downscaling paths from the macroscopic scale to the plasticity-inducing hydroxyapatite needles, which are residing both within the extrafibrillar and intermolecular space. Mathematically, these downscaling paths are reflected in the following way:

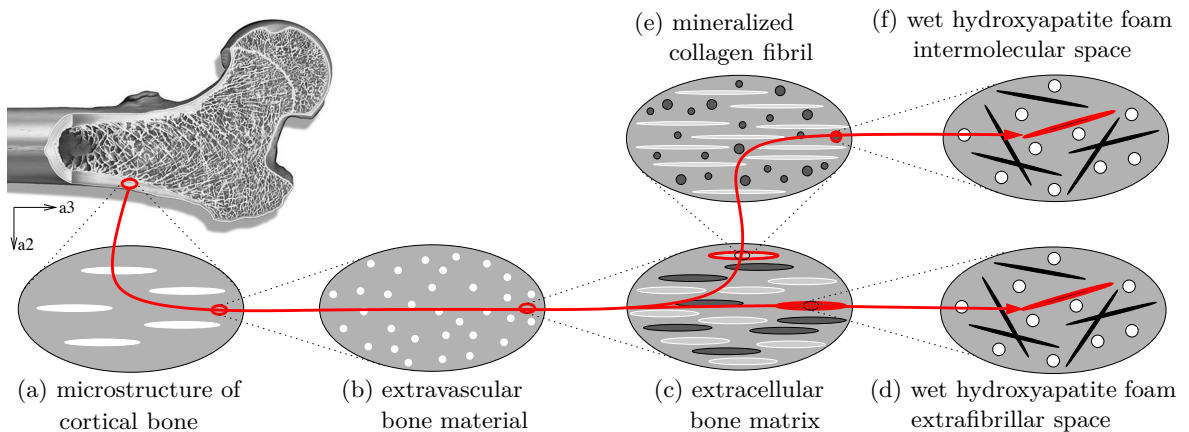


Fig. 3.7: Downscaling paths to the extrafibrillar and intermolecular mineral needles

According to the multiscale concept presented in Section 3.4.2, a multiscale concentration-influence relation for a transition from the macro-scale to the hydroxyapatite needles situated

within the lowest scale of the two downscaling paths of the multiscale bone model can be derived by specialization of Eq. (3.15), reading for the extrafibrillar mineral as

$$\boldsymbol{\varepsilon}_{\text{efHA},i} = \mathbb{A}_{\text{HA},i} : \mathbb{A}_{\text{ef}} : \mathbb{A}_{\text{excel}} : \mathbb{A}_{\text{exvas}} : \mathbf{E} + \sum_{j \in \mathcal{G}} \mathbb{M}_{ij}^{\text{ef-ef}} : \boldsymbol{\varepsilon}_{\text{efHA},j}^{\text{P}} + \mathbb{M}_{ij}^{\text{ef-im}} : \boldsymbol{\varepsilon}_{\text{imHA},j}^{\text{P}}, \quad (3.62)$$

and for the intermolecular mineral as

$$\boldsymbol{\varepsilon}_{\text{imHA},i} = \mathbb{A}_{\text{HA},i} : \mathbb{A}_{\text{im}} : \mathbb{A}_{\text{fib}} : \mathbb{A}_{\text{excel}} : \mathbb{A}_{\text{exvas}} : \mathbf{E} + \sum_{j \in \mathcal{G}} \mathbb{M}_{ij}^{\text{im-ef}} : \boldsymbol{\varepsilon}_{\text{efHA},j}^{\text{P}} + \mathbb{M}_{ij}^{\text{im-im}} : \boldsymbol{\varepsilon}_{\text{imHA},j}^{\text{P}}. \quad (3.63)$$

The multiscale influence tensors $\mathbb{M}_{ij}^{\text{ef-ef}}$ and $\mathbb{M}_{ij}^{\text{im-im}}$ describing the multiscale effect of the plastic strain in the needle j on the total strain in needle i , both situated within the same RVE (namely either the extrafibrillar or intermolecular space), read according to Eq. (3.18) as

$$\begin{aligned} \mathbb{M}_{ij}^{\text{ef-ef}} &= \mathbb{A}_{\text{HA},i} : \mathbb{A}_{\text{ef}} : \mathbb{A}_{\text{excel}} : \mathbb{D}_{\text{exvas}} : f_{\text{excel}}^{\text{exvas}} \mathbb{C}_{\text{exvas}}^{-1} : \mathbb{A}_{\text{excel}}^{\text{T}} : f_{\text{ef}}^{\text{excel}} \mathbb{A}_{\text{ef}}^{\text{T}} : f_{\text{HA}}^{\text{ef}} \omega_j \mathbb{A}_{\text{HA},j}^{\text{T}} : \mathbb{C}_{\text{HA}} \\ &+ \mathbb{A}_{\text{HA},i} : \mathbb{A}_{\text{ef}} : \mathbb{D}_{\text{excel}} : f_{\text{ef}}^{\text{excel}} \mathbb{C}_{\text{excel}}^{-1} : \mathbb{A}_{\text{ef}}^{\text{T}} : f_{\text{HA}}^{\text{ef}} \omega_j \mathbb{A}_{\text{HA},j}^{\text{T}} : \mathbb{C}_{\text{HA}} \\ &+ \mathbb{A}_{\text{HA},i} : \mathbb{D}_{\text{ef-ef}} : f_{\text{HA}}^{\text{ef}} \mathbb{C}_{\text{ef}}^{-1} : \omega_j \mathbb{A}_{\text{HA},j}^{\text{T}} : \mathbb{C}_{\text{HA}} \\ &+ \omega_j \mathbb{D}_{\text{HA},ij}, \end{aligned} \quad (3.64)$$

$$\begin{aligned} \mathbb{M}_{ij}^{\text{im-im}} &= \mathbb{A}_{\text{HA},i} : \mathbb{A}_{\text{im}} : \mathbb{A}_{\text{fib}} : \mathbb{A}_{\text{excel}} : \mathbb{D}_{\text{exvas}} : f_{\text{excel}}^{\text{exvas}} \mathbb{C}_{\text{exvas}}^{-1} : \mathbb{A}_{\text{excel}}^{\text{T}} : f_{\text{fib}}^{\text{excel}} \mathbb{A}_{\text{fib}}^{\text{T}} : f_{\text{im}}^{\text{fib}} \mathbb{A}_{\text{im}}^{\text{T}} \\ &: f_{\text{HA}}^{\text{im}} \omega_j \mathbb{A}_{\text{HA},j}^{\text{T}} : \mathbb{C}_{\text{HA}} \\ &+ \mathbb{A}_{\text{HA},i} : \mathbb{A}_{\text{im}} : \mathbb{A}_{\text{fib}} : \mathbb{D}_{\text{excel}} : f_{\text{fib}}^{\text{excel}} \mathbb{C}_{\text{excel}}^{-1} : \mathbb{A}_{\text{fib}}^{\text{T}} : f_{\text{im}}^{\text{fib}} \mathbb{A}_{\text{im}}^{\text{T}} : f_{\text{HA}}^{\text{im}} \omega_j \mathbb{A}_{\text{HA},j}^{\text{T}} : \mathbb{C}_{\text{HA}} \\ &+ \mathbb{A}_{\text{HA},i} : \mathbb{A}_{\text{im}} : \mathbb{D}_{\text{fib-fib}} : f_{\text{im}}^{\text{fib}} \mathbb{C}_{\text{fib}}^{-1} : \mathbb{A}_{\text{im}}^{\text{T}} : f_{\text{HA}}^{\text{im}} \omega_j \mathbb{A}_{\text{HA},j}^{\text{T}} : \mathbb{C}_{\text{HA}} \\ &+ \mathbb{A}_{\text{HA},i} : \mathbb{D}_{\text{im}} : f_{\text{HA}}^{\text{im}} \mathbb{C}_{\text{im}}^{-1} : \omega_j \mathbb{A}_{\text{HA},j}^{\text{T}} : \mathbb{C}_{\text{HA}} \\ &+ \omega_j \mathbb{D}_{\text{HA},ij}. \end{aligned} \quad (3.65)$$

The multiscale influence tensors $\mathbb{M}_{ij}^{\text{ef-im}}$ and $\mathbb{M}_{ij}^{\text{im-ef}}$ describing the multiscale effects of the plastic strain in the needle j on the total strain in needle i , situated within *different* RVEs, read according to Eq. (3.19) as

$$\begin{aligned} \mathbb{M}_{ij}^{\text{ef-im}} &= \mathbb{A}_{\text{HA},i} : \mathbb{A}_{\text{ef}} : \mathbb{A}_{\text{excel}} : \mathbb{D}_{\text{exvas}} : f_{\text{excel}}^{\text{exvas}} \mathbb{C}_{\text{exvas}}^{-1} : \mathbb{A}_{\text{excel}}^{\text{T}} : f_{\text{fib}}^{\text{excel}} \mathbb{A}_{\text{fib}}^{\text{T}} : f_{\text{im}}^{\text{fib}} \mathbb{A}_{\text{im}}^{\text{T}} \\ &: f_{\text{HA}}^{\text{im}} \omega_j \mathbb{A}_{\text{HA},j}^{\text{T}} : \mathbb{C}_{\text{HA}} \\ &+ \mathbb{A}_{\text{HA},i} : \mathbb{A}_{\text{ef}} : \mathbb{D}_{\text{excel}} : f_{\text{fib}}^{\text{excel}} \mathbb{C}_{\text{excel}}^{-1} : \mathbb{A}_{\text{fib}}^{\text{T}} : f_{\text{im}}^{\text{fib}} \mathbb{A}_{\text{im}}^{\text{T}} : f_{\text{HA}}^{\text{im}} \omega_j \mathbb{A}_{\text{HA},j}^{\text{T}} : \mathbb{C}_{\text{HA}} \\ &+ \mathbb{A}_{\text{HA},i} : \mathbb{D}_{\text{ef-fib}} : f_{\text{im}}^{\text{fib}} \mathbb{C}_{\text{fib}}^{-1} : \mathbb{A}_{\text{im}}^{\text{T}} : f_{\text{HA}}^{\text{im}} \omega_j \mathbb{A}_{\text{HA},j}^{\text{T}} : \mathbb{C}_{\text{HA}}, \end{aligned} \quad (3.66)$$

$$\begin{aligned} \mathbb{M}_{ij}^{\text{im-ef}} &= \mathbb{A}_{\text{HA},i} : \mathbb{A}_{\text{im}} : \mathbb{A}_{\text{fib}} : \mathbb{A}_{\text{excel}} : \mathbb{D}_{\text{exvas}} : f_{\text{excel}}^{\text{exvas}} \mathbb{C}_{\text{exvas}}^{-1} : \mathbb{A}_{\text{excel}}^{\text{T}} : f_{\text{ef}}^{\text{excel}} \mathbb{A}_{\text{ef}}^{\text{T}} \\ &: f_{\text{HA}}^{\text{ef}} \omega_j \mathbb{A}_{\text{HA},j}^{\text{T}} : \mathbb{C}_{\text{HA}} \\ &+ \mathbb{A}_{\text{HA},i} : \mathbb{A}_{\text{im}} : \mathbb{A}_{\text{fib}} : \mathbb{D}_{\text{excel}} : f_{\text{ef}}^{\text{excel}} \mathbb{C}_{\text{excel}}^{-1} : \mathbb{A}_{\text{ef}}^{\text{T}} : f_{\text{HA}}^{\text{ef}} \omega_j \mathbb{A}_{\text{HA},j}^{\text{T}} : \mathbb{C}_{\text{HA}} \\ &+ \mathbb{A}_{\text{HA},i} : \mathbb{A}_{\text{im}} : \mathbb{D}_{\text{fib-ef}} : f_{\text{HA}}^{\text{ef}} \mathbb{C}_{\text{ef}}^{-1} : \omega_j \mathbb{A}_{\text{HA},j}^{\text{T}} : \mathbb{C}_{\text{HA}}, \end{aligned} \quad (3.67)$$

see Appendix A.4 for details.

3.4.3.3 Input quantities for homogenization scheme

Following the proposition for bone failure as described in Section 3.4.2, the hydroxyapatite needles are the sole source of plasticity within the multiscale model and feature an elastic-perfectly plastic behavior, mathematically reading as

$$\boldsymbol{\sigma}_{\text{HA},i} = \mathbb{C}_{\text{HA}} : (\boldsymbol{\varepsilon}_{\text{HA},i} - \boldsymbol{\varepsilon}_{\text{HA},i}^{\text{p}}), \quad (3.68)$$

with \mathbb{C}_{HA} as the fourth-order stiffness tensor of hydroxyapatite and subscript i indicating the stress and strain in the hydroxyapatite needle with the orientation angles $\{\theta_i, \varphi_i\}_{i \in \mathcal{G}}$. The elastic properties of hydroxyapatite were determined by ultrasonic measurements by Katz & Ukraincik (1971) and are defined as

$$\mathbb{C}_{\text{HA}} = 3k_{\text{HA}}\mathbb{I}^{\text{vol}} + 2\mu_{\text{HA}}\mathbb{I}^{\text{dev}}, \quad (3.69)$$

with $k_{\text{HA}} = 82.6$ GPa and $\mu_{\text{HA}} = 44.9$ GPa as the bulk and shear moduli of hydroxyapatite, \mathbb{I}^{vol} as the volumetric part of the identity tensor \mathbb{I} with components $I_{ijkl}^{\text{vol}} = \frac{1}{3}\delta_{ij}\delta_{kl}$, and \mathbb{I}^{dev} as the deviatoric part of the identity tensor defined by $\mathbb{I}^{\text{dev}} = \mathbb{I} - \mathbb{I}^{\text{vol}}$.

The pore phases within the multiscale model, i.e. the Harvesian canals, the lacunar pores and the intercrystalline space, exhibit linear elastic material behavior in order to keep the mathematical descriptions as concise as possible

$$\boldsymbol{\sigma}_{\text{pore}} = \mathbb{C}_{\text{pore}} : \boldsymbol{\varepsilon}_{\text{pore}} \quad \text{with} \quad \text{pore} \in \{\text{vas}, \text{lac}, \text{ic}\}, \quad (3.70)$$

with \mathbb{C}_{pore} as the fourth-order stiffness tensor of the corresponding pore phase. The elastic properties of the lacunar pores and the intercrystalline space, both hosting water with mechanically insignificant amounts of non-collagenous matter are defined as

$$\mathbb{C}_{\text{lac}} = \mathbb{C}_{\text{ic}} = \mathbb{C}_{\text{H}_2\text{O}} = 3k_{\text{H}_2\text{O}}\mathbb{I}^{\text{vol}} + 2\mu_{\text{H}_2\text{O}}\mathbb{I}^{\text{dev}}, \quad (3.71)$$

whereby $k_{\text{H}_2\text{O}} = 2.3$ GPa and $\mu_{\text{H}_2\text{O}} = 0$ GPa, are the standard bulk and shear moduli of water. In case of drained conditions, the stiffness tensor of the the vascular pore phase is equal to zero $\mathbb{C}_{\text{vas}} = 0$.

The collagen is considered to exhibit a linear elastic material behavior,

$$\boldsymbol{\sigma}_{\text{col}} = \mathbb{C}_{\text{col}} : \boldsymbol{\varepsilon}_{\text{col}}, \quad (3.72)$$

with \mathbb{C}_{col} as the fourth-order stiffness tensor of molecular collagen obtained from experiments: The axial Young's modulus of dry collagen was determined as $E_{\parallel\text{dry}} = 2.9$ GPa by Sasaki & Odajima (1996)). However, the authors did not account for the water-filled intermolecular space, which makes up 12% even in fully dehydrated collagen (Lees & Heeley 1981). Considering the RVE shown in Figure 3.5(e) with 12% waterfilled intermolecular space allows to back-calculate the Young's modulus of molecular collagen, reading as $E_{\text{col}} = 3.58$ GPa, and a Poisson's ratio of $\nu_{\text{col}} = 0.33$.

The volume fractions of all the components within the hierarchical levels of bone can be accessed through the so-called *universal composition rules* of bone (Vass et al. 2018) based on the extracellular mass density ρ^{excel} , and known vascular, lacunar and canalicular porosities of a bone sample, $f_{\text{por}}^{\mu} = f_{\text{vas}}^{\mu} + f_{\text{lac}}^{\mu} + f_{\text{can}}^{\mu}$. The extracellular mass density can either serve as input value itself, or the macroscopic mass density of a millimeter-sized bone sample ρ^{μ} is transformed to the extracellular level, see Appendix A.5. Knowing a sample-specific

extracellular mass density, the universal composition rule for mineral and collagen dosages in extracellular bone (Vass et al. 2018) gives access to the volume fractions of the constituents in the extracellular RVE, namely mineral, organic and water content, ($f_{\text{HA}}^{\text{excel}}$, $f_{\text{col}}^{\text{excel}} = 0.9 \cdot f_{\text{org}}^{\text{excel}}$ and $f_{\text{H}_2\text{O}}^{\text{excel}}$). Then, these constituents volume fractions can be transformed into phase volume fractions of the extracellular RVE (namely extrafibrillar and fibrillar space with $f_{\text{ef}}^{\text{fib}}$ and $f_{\text{im}}^{\text{fib}}$) using the universal composition rule for tissue evolution during mineralization as proposed by Morin & Hellmich (2013). Hellmich & Ulm (2003) found out that the mineral distribution in extracellular bone follows another universal rule: The average mineral concentration in the extrafibrillar space equals that in the extracollageneous space. This rule allows for quantification of the volume fractions in the extrafibrillar space as

$$f_{\text{HA}}^{\text{ef}} = \frac{f_{\text{HA}}^{\text{excel}}}{1 - f_{\text{col}}^{\text{excel}}} \quad \text{and} \quad f_{\text{ic}}^{\text{ef}} = 1 - f_{\text{HA}}^{\text{ef}}, \quad (3.73)$$

and in the fibrillar space as

$$f_{\text{col}}^{\text{fib}} = \frac{f_{\text{col}}^{\text{excel}}}{f_{\text{fib}}^{\text{excel}}} \quad \text{and} \quad f_{\text{im}}^{\text{fib}} = 1 - f_{\text{col}}^{\text{fib}}. \quad (3.74)$$

The volume fractions of the constituents in the hydroxyapatite foam making up the intermolecular space are equal to those making up the extrafibrillar space given the fact of the equal mineral distribution and the same composition of the two RVEs,

$$f_{\text{HA}}^{\text{im}} = f_{\text{HA}}^{\text{ef}} \quad \text{and} \quad f_{\text{ic}}^{\text{im}} = f_{\text{ic}}^{\text{ef}}. \quad (3.75)$$

3.4.3.4 Consideration of failure mechanisms

As argued in Section 3.4.2, the role of water in the failure mechanism of bone is considered in terms of sliding mimicked by plastic behavior of the mineral needles. Consequently, bone strength can be linked to failure of the other two remaining elementary constituents of bone, namely collagen and hydroxyapatite. As for collagen, following the experimental evidence (Gentleman et al. 2003) that it exhibits a quasi-brittle failure characteristic under tension caused by failure of the crosslinks between the single collagen molecules, a Rankine failure criterion is assigned to this material phase, reading as

$$\tilde{\mathfrak{F}}_{\text{col}}(\boldsymbol{\sigma}_{\text{col}}) = |\mathbf{e}_3 \cdot \boldsymbol{\sigma}_{\text{col}} \cdot \mathbf{e}_3| - \sigma_{\text{col}}^{\text{ult}} \leq 0, \quad (3.76)$$

whereby the direction \mathbf{e}_3 coincides with the orientation direction of the collagen molecules (see Figure 3.5). Given the absence of direct measurements on collagen molecules, the tensile strength $\sigma_{\text{col}}^{\text{ult}}$ is assessed using a top-down approach, which allows to quantify constants of material constituents, which are nowadays not accessible by direct material testing. In detail, results from experiments carried out on rat tail tendon – a tissue consisting almost exclusively of collagen, in combination with a two-scale homogenization scheme for the tendon derived by demineralization of the relevant two scales of the six-step bone model, i.e. the RVEs of Figure 3.5(c) and 3.5(e), give access to the properties of the collagen itself. Thereby the volume-fractions within the two-scale homogenization scheme are depending on the hydration state of the tendon, characterized by the water-to-organic mass ratio \mathcal{R} . Under wet conditions the rat tail tendon exhibits a hydration ratio around $\mathcal{R} = 1.8$ (Meek et al. 1991) and a strength of 106.1 MPa (Gentleman et al. 2003). Using this information together with the

volume fractions derived in Morin et al. (2013) the two-scale scheme allows for downscaling the macroscopic strength of rat tail tendon to the level of collagen, resulting in a tensile strength of collagen of $\sigma_{\text{col}}^{\text{ult}} = 356.5$ MPa.

Since the plasticity of the hydroxyapatite needles mimics the interface effect of mutual gliding upon each other, failure of the whole hydroxyapatite phase is assumed upon full plastification, hence a fully unfolded sliding mechanism in all directions

$$\forall i \in \mathcal{G} : \mathfrak{F}_{\text{HA}}(\boldsymbol{\sigma}_{\text{HA},i}) = 0. \quad (3.77)$$

To this end, a non-associated multisurface Mohr-Coulomb criterion, comprising three yield functions according to Eq. (3.22) and three plastic potential functions according to Eq. (3.23), is assigned to the needle shaped hydroxyapatite.

The friction parameter and the yield strength are defined as $\beta = 12$ and $\sigma_{\text{HA}}^{\text{yield}} = 570$ MPa (Morin et al. 2017).

Finally, we want to stress that the macroscopic failure processes are traced back to the failure criteria that are defined for the two load-bearing constituents at the microscopic scales. By linking the different scales to each other, the homogenization approach integrates the microscopic failure criteria into a multiscale model and thereby allows to identify the overall material strength. We consider the macroscopic, cortical bone strength to be reached, once all load-bearing constituents, which are relevant for the given load case, fail. In detail, since the collagen is generally assumed to contribute to tensile loading only, the compressive strength of bone is reached as soon as all hydroxyapatite needles of the Gaussian orientation set \mathcal{G} are plasticizing according to criterion (3.77). On the contrary, the bone failure criterion for tension is linked to the failure of both, hydroxyapatite as well as collagen, which occurs once the equal sign holds in Eqs. (3.76) and (3.77). Therefore, the failure criterion for cortical bone under uniaxial compression, $\mathfrak{F}_{\text{bone}}(\Sigma_{33} < 0)$, reads as

$$\forall i \in \mathcal{G} : \mathfrak{F}_{\text{HA}}^{(1)}(\boldsymbol{\sigma}_{\text{HA},i}) = 0, \quad (3.78)$$

whereas the failure criterion for cortical bone under uniaxial tension, $\mathfrak{F}_{\text{bone}}(\Sigma_{33} > 0)$, reads as

$$\mathfrak{F}_{\text{col}}(\boldsymbol{\sigma}_{\text{col}}) = 0 \quad \text{and} \quad \forall i \in \mathcal{G} : \mathfrak{F}_{\text{HA}}^{(1)}(\boldsymbol{\sigma}_{\text{HA},i}) = 0. \quad (3.79)$$

3.4.4 Algorithmic aspects

Numerical evaluation of the multiscale up- and downscaling scheme established in section 3.4.3 requires respective application of the multiscale plasticity algorithm described in Section 3.3. As argued in Section 3.4.2 and taken into account in Eqs. (3.39)-(3.41), (3.43)-(3.45) and (3.68), the hydroxyapatite phases have been identified as plasticity-inducing material phases. Inserting the multiscale concentration-influence relations Eq. (3.62) and (3.63) into the local constitutive law of the mineral needles (3.68), yields the respective microscopic stresses within the plasticity-inducing phases as a function of the macroscopic strains \mathbf{E} and microscopic plasticity-inducing strains only, which has to be fulfilled for all incremental steps n and iteration steps τ , reading for the extrafibrillar mineral as

$$\begin{aligned} \boldsymbol{\sigma}_{\text{efHA},i}^{n,\tau} = \mathbb{C}_{\text{HA}} : & \left[\mathbb{A}_{\text{HA},i} : \mathbb{A}_{\text{ef}} : \mathbb{A}_{\text{excel}} : \mathbb{A}_{\text{exvas}} : \mathbf{E}^{n,\tau} \right. \\ & \left. + \sum_{j \in \mathcal{G}} \left(\mathbb{M}_{ij}^{\text{ef-ef}} - \delta_{ij} \mathbb{I} \right) : \boldsymbol{\varepsilon}_{\text{efHA},j}^{\text{p};n,\tau} + \mathbb{M}_{ij}^{\text{ef-im}} : \boldsymbol{\varepsilon}_{\text{imHA},j}^{\text{p};n,\tau} \right], \end{aligned} \quad (3.80)$$

and for the intermolecular mineral as

$$\begin{aligned} \boldsymbol{\sigma}_{\text{imHA},i}^{n,\tau} = \mathbb{C}_{\text{HA}} : & \left[\mathbb{A}_{\text{HA},i} : \mathbb{A}_{\text{im}} : \mathbb{A}_{\text{fib}} : \mathbb{A}_{\text{excel}} : \mathbb{A}_{\text{exas}} : \mathbf{E}^{n,\tau} \right. \\ & \left. + \sum_{j \in \mathcal{G}} \mathbb{M}_{ij}^{\text{im-ef}} : \boldsymbol{\varepsilon}_{\text{efHA},j}^{p;n,\tau} + \left(\mathbb{M}_{ij}^{\text{im-im}} - \delta_{ij} \mathbb{I} \right) : \boldsymbol{\varepsilon}_{\text{imHA},j}^{p;n,\tau} \right]. \end{aligned} \quad (3.81)$$

The key algorithmic task lies in computing, from the known values of state variables associated with load step n and iteration step τ , the corresponding values for step $(\tau + 1)$. The therefore introduced series of N_k stress states for any iteration step $(\tau + 1)$ of any load step n , is composed by the first member, $\boldsymbol{\sigma}^{n,\tau+1,1}$, used to identify the set of plasticizing needles within the extrafibrillar and intermolecular space, $\mathcal{G}_{\text{plast,ef}}^{n,\tau+1}$ and $\mathcal{G}_{\text{plast,im}}^{n,\tau+1}$ during step $\tau + 1$, reading as

$$\begin{aligned} \boldsymbol{\sigma}_{\text{efHA},i}^{n,\tau+1,1} = \mathbb{C}_{\text{HA}} : & \left[\mathbb{A}_{\text{HA},i} : \mathbb{A}_{\text{ef}} : \mathbb{A}_{\text{excel}} : \mathbb{A}_{\text{exas}} : \mathbf{E}^{n,\tau+1} \right. \\ & \left. + \sum_{j \in \mathcal{G}} \left(\mathbb{M}_{ij}^{\text{ef-ef}} - \delta_{ij} \mathbb{I} \right) : \boldsymbol{\varepsilon}_{\text{efHA},j}^{p;n,\tau} + \mathbb{M}_{ij}^{\text{ef-im}} : \boldsymbol{\varepsilon}_{\text{imHA},j}^{p;n,\tau} \right], \end{aligned} \quad (3.82)$$

and

$$\begin{aligned} \boldsymbol{\sigma}_{\text{imHA},i}^{n,\tau+1,1} = \mathbb{C}_{\text{HA}} : & \left[\mathbb{A}_{\text{HA},i} : \mathbb{A}_{\text{im}} : \mathbb{A}_{\text{fib}} : \mathbb{A}_{\text{excel}} : \mathbb{A}_{\text{exas}} : \mathbf{E}^{n,\tau+1} \right. \\ & \left. + \sum_{j \in \mathcal{G}} \mathbb{M}_{ij}^{\text{im-ef}} : \boldsymbol{\varepsilon}_{\text{efHA},j}^{p;n,\tau} + \left(\mathbb{M}_{ij}^{\text{im-im}} - \delta_{ij} \mathbb{I} \right) : \boldsymbol{\varepsilon}_{\text{imHA},j}^{p;n,\tau} \right], \end{aligned} \quad (3.83)$$

and the further members reading as

$$\begin{aligned} \boldsymbol{\sigma}_{\text{efHA},i}^{n,\tau+1,k+1} = \boldsymbol{\sigma}_{\text{efHA},i}^{n,\tau+1,k} \\ + \mathbb{C}_{\text{HA}} : & \left[\sum_{j \in \mathcal{G}_{\text{plast,ef}}^{n,\tau+1}} \sum_{\alpha=1}^{N_{\text{Fact},j}^{n,\tau+1}} \left(\mathbb{M}_{ij}^{\text{ef-ef}} - \delta_{ij} \mathbb{I} \right) : \Delta \lambda_{\text{ef},j}^{(\alpha),n,\tau+1,k} \frac{\partial \mathfrak{G}_{\text{HA}}^{(\alpha)}}{\partial \boldsymbol{\sigma}_j} \left(\boldsymbol{\sigma}_{\text{efHA},j}^{n,\tau+1,k} \right) \right. \\ & \left. + \sum_{j \in \mathcal{G}_{\text{plast,im}}^{n,\tau+1}} \sum_{\alpha=1}^{N_{\text{Fact},j}^{n,\tau+1}} \mathbb{M}_{ij}^{\text{ef-im}} : \Delta \lambda_{\text{im},j}^{(\alpha),n,\tau+1,k} \frac{\partial \mathfrak{G}_{\text{HA}}^{(\beta)}}{\partial \boldsymbol{\sigma}_j} \left(\boldsymbol{\sigma}_{\text{imHA},j}^{n,\tau+1,k} \right) \right] \stackrel{!}{=} 0, \end{aligned} \quad (3.84)$$

and

$$\begin{aligned} \boldsymbol{\sigma}_{\text{imHA},i}^{n,\tau+1,k+1} = \boldsymbol{\sigma}_{\text{imHA},i}^{n,\tau+1,k} \\ + \mathbb{C}_{\text{HA}} : & \left[\sum_{j \in \mathcal{G}_{\text{plast,ef}}^{n,\tau+1}} \sum_{\alpha=1}^{N_{\text{Fact},j}^{n,\tau+1}} \mathbb{M}_{ij}^{\text{im-ef}} : \Delta \lambda_{\text{ef},j}^{(\alpha),n,\tau+1,k} \frac{\partial \mathfrak{G}_{\text{HA}}^{(\alpha)}}{\partial \boldsymbol{\sigma}_j} \left(\boldsymbol{\sigma}_{\text{efHA},j}^{n,\tau+1,k} \right) \right. \\ & \left. + \sum_{j \in \mathcal{G}_{\text{plast,im}}^{n,\tau+1}} \sum_{\alpha=1}^{N_{\text{Fact},j}^{n,\tau+1}} \left(\mathbb{M}_{ij}^{\text{im-im}} - \delta_{ij} \mathbb{I} \right) : \Delta \lambda_{\text{im},j}^{(\alpha),n,\tau+1,k} \frac{\partial \mathfrak{G}_{\text{HA}}^{(\alpha)}}{\partial \boldsymbol{\sigma}_j} \left(\boldsymbol{\sigma}_{\text{imHA},j}^{n,\tau+1,k} \right) \right] \stackrel{!}{=} 0. \end{aligned} \quad (3.85)$$

The respective plastic multipliers $\Delta \lambda_j^{(\alpha),n,\tau+1,k}$ are derived according to Eqs. (3.34)-(3.36). Once the stresses of all plasticizing needles returns to the yield-surface at the end of step N_k

according to Eq. (2.62), the back-projection process is completed, giving access to the actual stress state at the end of the step $\tau + 1$, reading as

$$\begin{aligned} \boldsymbol{\sigma}_{\text{effHA},i}^{n,\tau+1} = \mathbb{C}_{\text{HA}} : & \left[\mathbb{A}_{\text{HA},i} : \mathbb{A}_{\text{ef}} : \mathbb{A}_{\text{excel}} : \mathbb{A}_{\text{exvas}} : \mathbf{E}^{n,\tau+1} \right. \\ & + \sum_{j \in \mathcal{G}_{\text{plast,ef}}^{n,\tau+1}} \left(\mathbb{M}_{ij}^{\text{ef-ef}} - \delta_{ij} \mathbb{I} \right) : \left(\boldsymbol{\varepsilon}_{\text{effHA},j}^{\text{p};n,\tau} + \sum_{k=1}^{N_k} \sum_{\alpha=1}^{N_{\text{Fact},j}^{n,\tau+1}} \Delta \lambda_{\text{ef},j}^{(\alpha),n,\tau+1,k} \frac{\partial \mathfrak{G}_{\text{HA}}^{(\alpha)}}{\partial \boldsymbol{\sigma}_j} \left(\boldsymbol{\sigma}_{\text{effHA},j}^{n,\tau+1,k} \right) \right) \\ & \left. + \sum_{j \in \mathcal{G}_{\text{plast,im}}^{n,\tau+1}} \mathbb{M}_{ij}^{\text{ef-im}} : \left(\boldsymbol{\varepsilon}_{\text{imHA},j}^{\text{p};n,\tau} + \sum_{k=1}^{N_k} \sum_{\alpha=1}^{N_{\text{Fact},j}^{n,\tau+1}} \Delta \lambda_{\text{im},j}^{(\alpha),n,\tau+1,k} \frac{\partial \mathfrak{G}_{\text{HA}}^{(\beta)}}{\partial \boldsymbol{\sigma}_j} \left(\boldsymbol{\sigma}_{\text{imHA},j}^{n,\tau+1,k} \right) \right) \right] \stackrel{!}{=} 0, \end{aligned} \quad (3.86)$$

and

$$\begin{aligned} \boldsymbol{\sigma}_{\text{imHA},i}^{n,\tau+1} = \mathbb{C}_{\text{HA}} : & \left[\mathbb{A}_{\text{HA},i} : \mathbb{A}_{\text{im}} : \mathbb{A}_{\text{fib}} : \mathbb{A}_{\text{excel}} : \mathbb{A}_{\text{exvas}} : \mathbf{E}^{n,\tau+1} \right. \\ & + \sum_{j \in \mathcal{G}_{\text{plast,ef}}^{n,\tau+1}} \mathbb{M}_{ij}^{\text{im-ef}} : \left(\boldsymbol{\varepsilon}_{\text{effHA},j}^{\text{p};n,\tau} + \sum_{k=1}^{N_k} \sum_{\alpha=1}^{N_{\text{Fact},j}^{n,\tau+1}} \Delta \lambda_{\text{ef},j}^{(\alpha),n,\tau+1,k} \frac{\partial \mathfrak{G}_{\text{HA}}^{(\alpha)}}{\partial \boldsymbol{\sigma}_j} \left(\boldsymbol{\sigma}_{\text{effHA},j}^{n,\tau+1,k} \right) \right) \\ & \left. + \sum_{j \in \mathcal{G}_{\text{plast,im}}^{n,\tau+1}} \left(\mathbb{M}_{ij}^{\text{im-im}} - \delta_{ij} \mathbb{I} \right) : \left(\boldsymbol{\varepsilon}_{\text{imHA},j}^{\text{p};n,\tau} + \sum_{k=1}^{N_k} \sum_{\alpha=1}^{N_{\text{Fact},j}^{n,\tau+1}} \Delta \lambda_{\text{im},j}^{(\alpha),n,\tau+1,k} \frac{\partial \mathfrak{G}_{\text{HA}}^{(\beta)}}{\partial \boldsymbol{\sigma}_j} \left(\boldsymbol{\sigma}_{\text{imHA},j}^{n,\tau+1,k} \right) \right) \right] \stackrel{!}{=} 0. \end{aligned} \quad (3.87)$$

These stress states are subsequently upscaled to all hierarchical levels. By first upscaling the resulting plastic strains within the mineral needles according to Eq. (3.27) using Levin's theorem, see Eqs. (3.41), (3.49), (3.45), (3.53), (3.57) and (3.61), afterwards computing the total strains using the concentration-influence relations, see Eqs. (3.59), (3.55), (3.52), (3.51), (3.43), (3.47), (3.48) and (3.39) and finally evaluating all the stresses by inserting the strains in the respective constitutive laws, the stress-strain state in all hierarchical levels at the end of step $\tau + 1$ is derived.

3.4.5 Experimental validation

This section is devoted to presenting comparisons of stiffnesses and strengths provided in experimental studies on cortical bone extracted from a large variety of different anatomical locations and different species to corresponding model predictions.

3.4.5.1 Stiffness validation

As for the stiffness, we have considered the experimental data provided in Tables 3.5, 3.6 and 3.7 in Appendix A.6. Based on the compositional rules described in Vass et al. (2018), the macroscopic mass densities ρ^μ gave access to the corresponding extracellular mass densities ρ^{excel} , based on a typical microstructural porosity of $f_{\text{vas}}^\mu = 3\%$ and $f_{\text{lac+can}}^\mu = 2\%$, see also Appendix A.5. Furthermore, the aforementioned compositional rules also allow for computation of the volume fractions on the lower-scale RVEs, allowing for stiffness upscaling,

according to Eqs. (3.38), (3.46), (3.42), (3.50), (3.54) and (3.58). At the extracellular scale, the model predictions are compared to ultrasonic tests performed on cortical bone samples of bovine, human, elephant, deer and cod tissues (Lees et al. 1979, 1983, 1996), see Appendix A.6. The good agreement between prediction and experiments is underlined by relative errors E amounting to $E = 6.85 \pm 7.16\%$ for the radial normal stiffness, and to $E = 10.37 \pm 6.60\%$ for the axial normal stiffness components for the different bone tissues, see Figure 3.8.

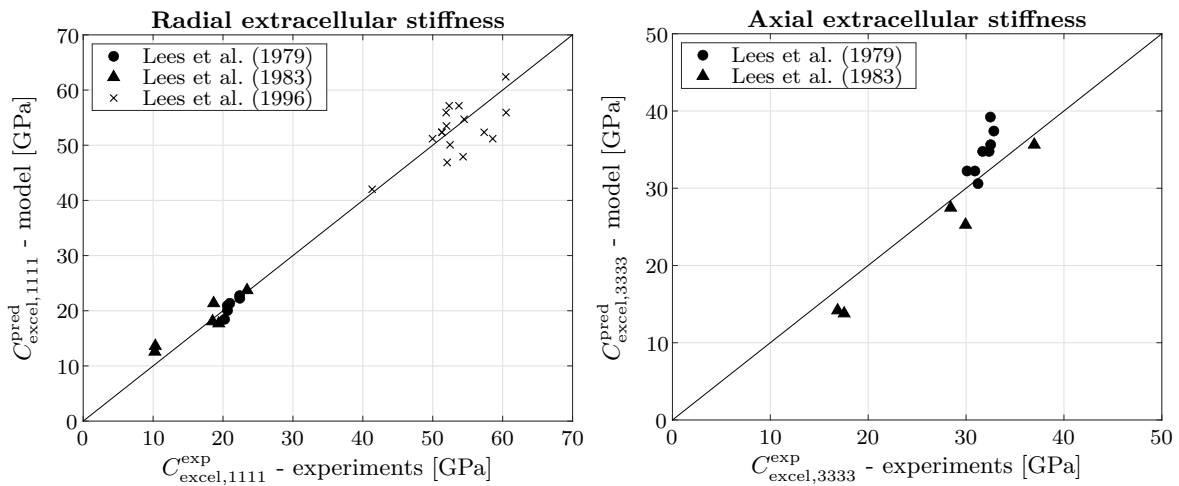


Fig. 3.8: Comparison between model predictions and experiments of radial stiffness $C_{excel,1111}$ (left) and axial stiffness $C_{excel,3333}$ (right) at the extracellular scale

At the extravascular scale, we compare the micromechanical elasticity predictions to an ultrasonic test carried out by McCarthy et al. (1990) on equine bones, see Appendix A.6. The good agreement between prediction and experiments is underlined by relative errors $E = 12.24 \pm 6.58\%$ for the radial normal stiffness, and $E = 9.90 \pm 6.83\%$ for the axial normal stiffness components for the different bone tissues, see Figure 3.9.

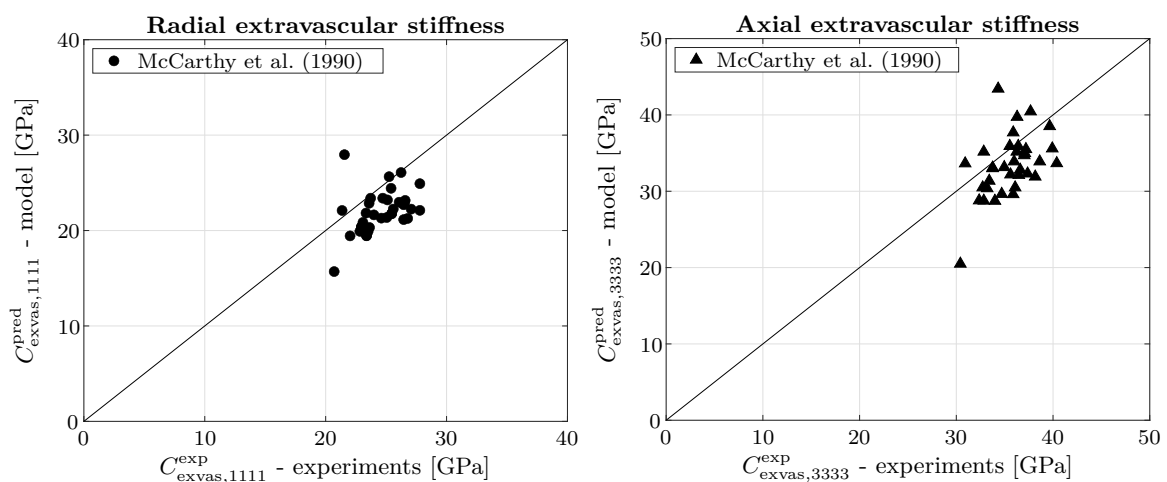


Fig. 3.9: Comparison between model predictions and experiments of radial stiffness $C_{exvas,1111}$ (left) and axial stiffness $C_{exvas,3333}$ (right) at the extravascular scale

3.4.5.2 Strength validation at the macroscopic scale

At the macroscopic scale, model validation is performed based on experimental data obtained from cortical bone extracted from the human femur, the human tibia, the bovine femur, and the bovine tibia. For these tissues, literature provides varying mass densities ρ^μ and vascular porosities f_{vas}^μ as well as varying uniaxial strength values. In order to find statistically relevant input values for our model, we subjected the data found in literature to a statistical analysis, described in the following. Based on the experimental mean values \bar{x} and standard deviations s (see Table 3.1 for experimental composition values and Table 3.2 for experimental strength values) a statistical sample is upscaled to a corresponding statistical population. This is done by considering a two-sided confidence interval for the population's mean value μ and an upper bound for the population's standard deviation σ ,

$$\bar{x} - \frac{s t_{n_s-1, 1-\alpha/2}}{\sqrt{n_s}} \leq \mu \leq \bar{x} + \frac{s t_{n_s-1, 1-\alpha/2}}{\sqrt{n_s}} \quad \text{and} \quad \sigma \leq \sqrt{\frac{(n_s - 1)s^2}{\chi_{n_s-1, \alpha}^2}} = \sigma_{\text{upp}}, \quad (3.88)$$

whereby n_s is the size of the sample, $t_{n_s-1, 1-\alpha/2}$ denotes the t-value that cuts an area equal to $1 - \alpha/2$ of the Student's t distribution with $n_s - 1$ degrees of freedom and $\chi_{n_s-1, \alpha}^2$ denotes the χ^2 -value that cuts an area equal to α of the chi-squared distribution with $n_s - 1$ degrees of freedom. α describes the significance level which is equal to 5% for a 95% confidence interval. In the next step, the above parameters $\mu = \bar{x}$ and $\sigma = \sigma_{\text{upp}}$ are used to randomly generate a statistical population with the size $n_p = 1000n_s$. Combination of all populations arising from different experiments on the *same tissue* gives access to one tissue-specific mean value and standard deviation (see bold values in Table 3.1 and 3.2).

In the next step, a random mass density from the tissue-specific population is combined with a random vascular porosity from the tissue-specific range (see Table 3.1) to compute the extracellular mass density, see Eq. (3.121) in the Appendix A.5. Repetition of this process gives access to the mean value and the standard deviation of the tissue-specific extracellular mass density (see Table 3.3).

Tab. 3.1: *Tissue-specific experimental composition values of cortical bone*

Tissue	Mass density ρ^μ		Vascular porosity f_{vas}^μ	
	n_s	mean \pm std.dev. [g/cm ³]	min - max [%]	
Human femur	8	1.96 \pm 0.04 (Lees et al. 1983)		
	8	1.93 \pm 0.06 (Lees et al. 1983)		
		1.95 \pm 0.09	2.0-8.0	(Vass et al. 2018)
Human tibia.	11	2.00 \pm 0.03 (Seifert et al. 2015)		
		2.00 \pm 0.04	3.1-5.6	(Seifert et al. 2015)
Bovine femur	19	1.99 \pm 0.10 (Zelaya-Lainez 2016)		
		1.99 \pm 0.14	2.5-4.6	(Zelaya-Lainez 2016)
Bovine tibia	22	2.04 \pm 0.04 (Lees et al. 1979)		
	8	2.06 \pm 0.02 (Lees et al. 1983)		
	8	2.07 \pm 0.03 (Lees et al. 1983)		
		2.05 \pm 0.05	2.0-8.0	(Vass et al. 2018)

Tab. 3.2: *Tissue-specific experimental uniaxial strength values (only test series with at least five specimens were taken into account)*

Tissue	Literature	compressive strength [MPa]			tensile strength [MPa]		
		n	age	mean \pm std	n	age	mean \pm std
Human femur	Burststein et al. (1976)	5	60-69	179 \pm 14.9	5	20-29	140 \pm 10.0
		6	50-59	131 \pm 12.6	8	60-69	129 \pm 6.4
		7	70-79	129 \pm 5.5	7	70-79	129 \pm 5.5
	Cezayirlioglu et al. (1985)	8	50-59	205 \pm 12.6	18	50-59	136 \pm 8.7
		11	70-79	206 \pm 13.4	19	70-79	133 \pm 7.5
		6	31	203 \pm 27.6	5	31	132 \pm 12.8
	Reilly et al. (1974)	8	61	191 \pm 10.7	11	61	121 \pm 4.6
		6	62	186 \pm 14.9	6	62	127 \pm 6.8
		6	69	189 \pm 10.9	7	69	127 \pm 6.8
		7	59	205 \pm 6.7	7	59	132 \pm 15.7
		6	45	212 \pm 6.2	6	45	146 \pm 10.7
		5	55	196 \pm 22.2	5	72	128 \pm 4.0
		6	72	192 \pm 16.9	5	47	127 \pm 12.0
		6	47	188 \pm 18.5	5	71	120 \pm 10.4
		7	21	206 \pm 10.0	5	20	122 \pm 19.9
		7	31	133 \pm 14.9	5	23	133 \pm 22.4
		5	23	133 \pm 22.4	5	23	133 \pm 22.4
mean \pm std		197.7 \pm 31.9			130.8 \pm 23.2		
Human tibia	Burststein et al. (1976)	6	50-59	164 \pm 9.4	6	50-59	164 \pm 9.4
		9	60-69	147 \pm 9.2	9	60-69	147 \pm 9.2
	Cezayirlioglu et al. (1985)	9	30-39	213 \pm 10.1	13	30-39	158 \pm 8.5
		12	60-69	192 \pm 6.9	18	60-69	154 \pm 8.7
mean \pm std		201.0 \pm 22.4			155.0 \pm 20.9		
Bovine femur	Cezayirlioglu et al. (1985)	25		217 \pm 26.8	27		162 \pm 14.2
		7		240 \pm 30.1	8		129 \pm 16.5
		10		214 \pm 10.4			
	Walsh & Guzelsu (1994)				26		111 \pm 14.5
					20		99 \pm 19.3
					35		125 \pm 34.1
					9		107 \pm 20.0
					15		115 \pm 26.0
					13		87 \pm 13.0
					10		112 \pm 20.0
mean \pm std		220.1 \pm 51.9			121.8 \pm 46.5		
Bovine tibia	Reilly et al. (1974)	8		228 \pm 31.3	7		152 \pm 16.5
	mean \pm std	228.0 \pm 56.3			152.0 \pm 31.6		

Tab. 3.3: *Tissue-specific extracellular mass density*

Tissue	Extracellular mass density ρ^{excl} mean \pm std.dev. [g/cm ³]
Human femur	2.01 \pm 0.10
Human tibia	2.06 \pm 0.04
Bovine femur	2.05 \pm 0.15
Bovine tibia	2.13 \pm 0.06

The experimentally based tissue-specific ranges of ρ^{excel} are translated into corresponding ranges of constituent volume fractions across all considered RVEs, see Section 3.4.3.3 for details. Entering those ranges into the full elastoplastic algorithm described in Sections 3.3 and 3.4.4 allows to compute corresponding tissue-specific ranges of the compressive tensile and compressive strengths, see Figures 3.10 and 3.11.

As for the compressive strength, it turns out that the agreement between experimental results and model predictions is exceptionally good for the human tibia (with the model covering the whole experimental range), while it not as good but still satisfying for the human femur. A similar picture emerges for the bovine tissues. For the bovine tibia, again a remarkable agreement between experimental data and model predictions is observed (while the experimental range is not fully covered), whereas this agreement is not as good but still satisfying for the bovine femur.

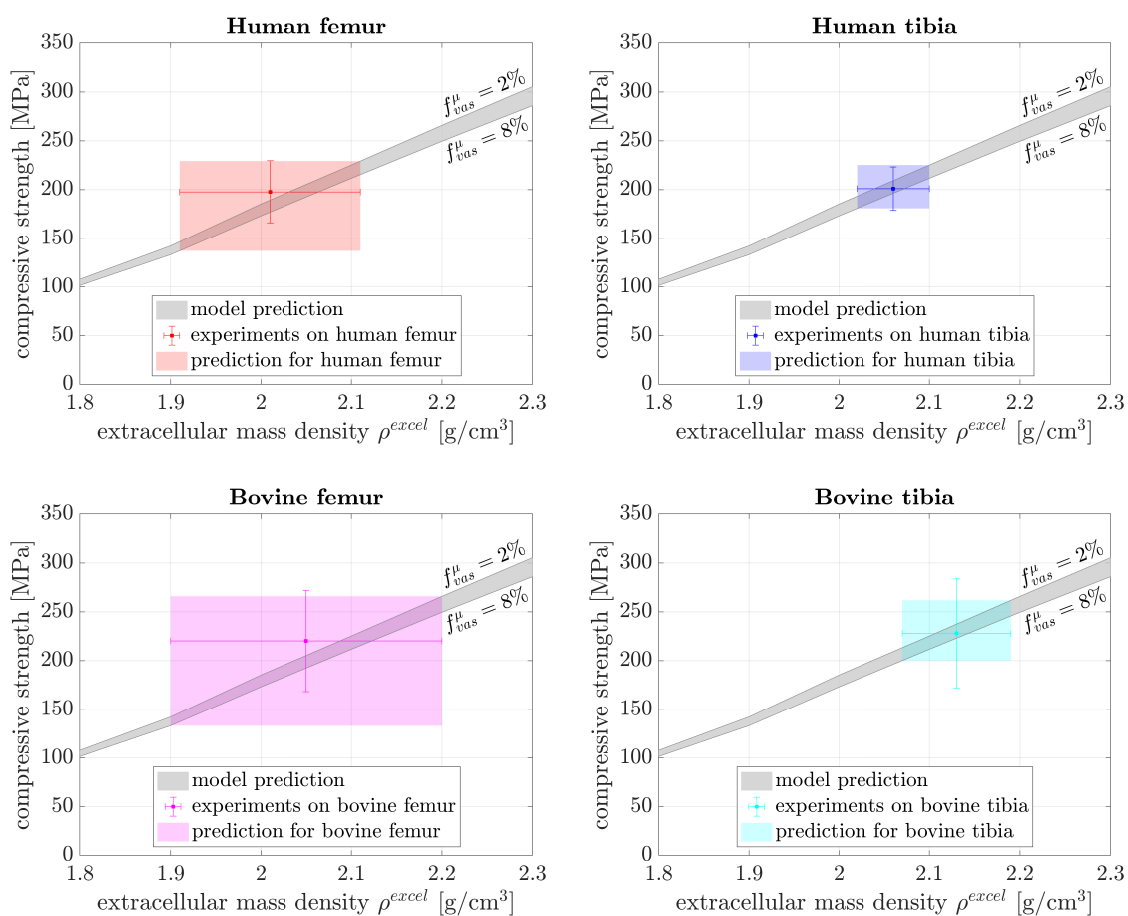


Fig. 3.10: Comparison between model prediction and experimental data for the compressive strength $\Sigma_{33}^{ult,c}$ of human femoral and tibial and bovine femoral and tibial cortical bone tissue

For tensile loading the predicted strength ranges are evenly distributed around the experimental mean value for human and bovine femur (see Figure 3.11). However, the model is not able to cover the entire experimentally determined strength ranges, and underestimates the experimental data for the tibia samples by $\approx 20\%$, suggesting that the proposed model may miss some additional hardening effect in the collagen.

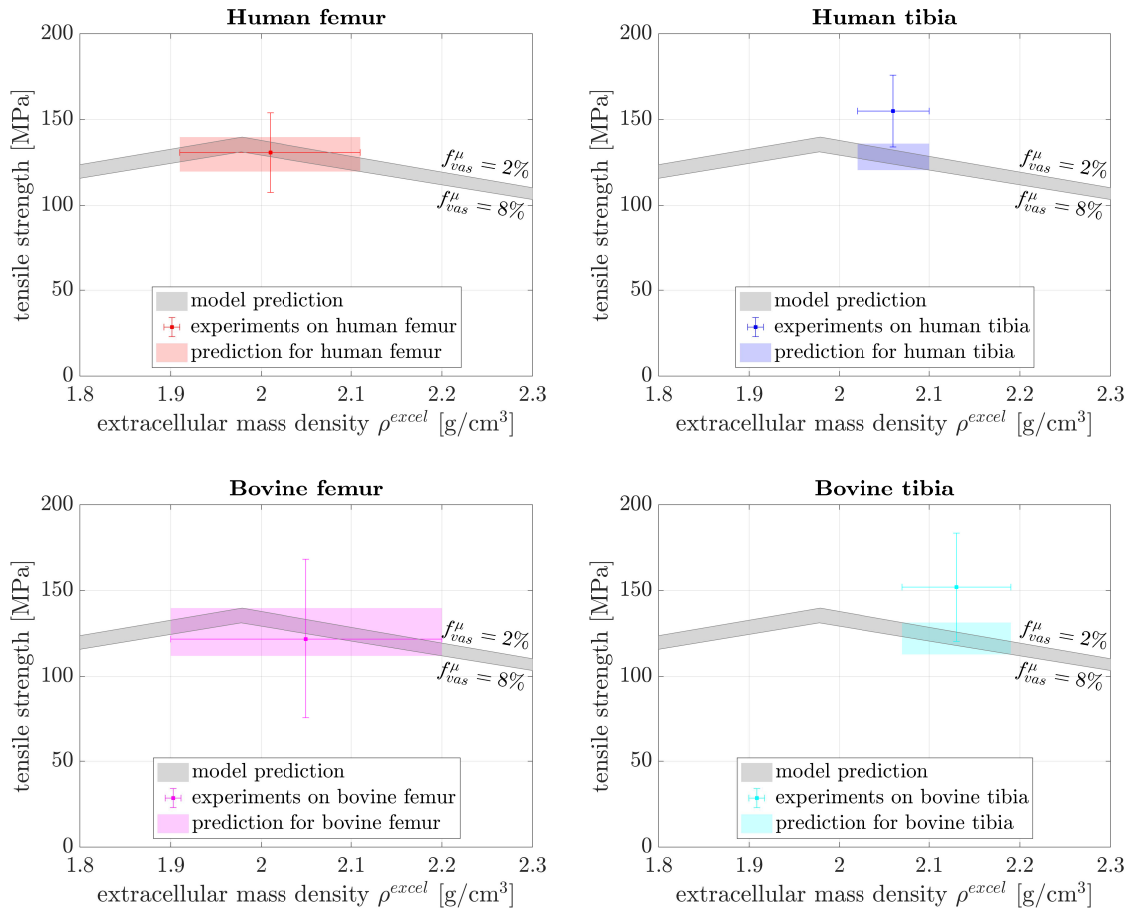


Fig. 3.11: Comparison between model prediction and experimental data for the tensile strength $\Sigma_{33}^{ult,t}$ of human femoral and tibial and bovine femoral and tibial cortical bone tissue

3.4.5.3 Strength validation at the extracellular scale

At the extracellular scale, we compare the compressive strength prediction from our model to experimental results from micropillar compression tests performed on hydrated ovine bone (Schwiedrzik et al. 2017). The elastic moduli of the respective bone have been determined based on nanoindentations in wet and dry conditions (Schwiedrzik et al. 2014) and serve as input value for our model. In this context, only the lower four levels of the multiscale-model are considered in the algorithm and the load is applied at the extracellular scale. This way, an extracellular mass density of $\rho^{excel} = 1.99 \text{ g/cm}^3$ is obtained, inducing a stiffness of extracellular tissue quantified by the following stiffness tensor:

$$\mathbb{C}_{excel} = \begin{bmatrix} 18.02 & 7.05 & 6.91 & 0 & 0 & 0 \\ 7.05 & 18.02 & 6.91 & 0 & 0 & 0 \\ 6.91 & 6.91 & 25.89 & 0 & 0 & 0 \\ 0 & 0 & 0 & 12.54 & 0 & 0 \\ 0 & 0 & 0 & 0 & 12.54 & 0 \\ 0 & 0 & 0 & 0 & 0 & 10.96 \end{bmatrix} \text{ GPa} \quad (3.89)$$

On this basis, the compressive strength of extracellular bone matrix was computed, yielding a model prediction of $\sigma_{33}^{\text{ult,excel}} = 190$ MPa. This is in very good agreement with the corresponding experimental value provided in Schwiedrzik et al. (2014), i.e. $\sigma_{33}^{\text{ult,excel}} = 180$ MPa. Hence, the model overestimates the mean value of the experimental results by only 5%.

Tab. 3.4: Predicted and experimental stiffness and compressive strength values of ovine extracellular bone

		Experimental values (Schwiedrzik et al. 2017)	Model prediction (with $\rho^{\text{excel}} = 1.99$ g/cm ³)
E_{11}^{excel}	[GPa]	14.5 ± 1.6	14.5
E_{33}^{excel}	[GPa]	22.8 ± 1.6	22.1
$\sigma_{33}^{\text{ult,excel}}$	[GPa]	0.18 ± 0.021	0.19

3.5 Discussion

3.5.1 Novel aspects concerning the micromechanical representation

The multiscale homogenization scheme of bone proposed in this paper includes an important adaption as compared to the micromechanical representation by Fritsch, Hellmich & Dormieux (2009). While in the latter work, the RVE of extracellular bone matrix was considered to be a matrix-inclusion composite, we here define it with two mutually interacting material phases, see Figure 3.5(c). This way, we take into account the fact that the collagen-rich and collagen-free areas in the bone ultrastructure, see the dark- and light-shaded areas in Figure 3.4(e), are in direct interaction with each other, while no surrounding matrix-phase can be identified. Furthermore, the fibrillar downscaling path has been substantially revised in our new formulation. It is widely accepted, that mineralization during bone formation starts in the gap zones between the molecules (Hodge & Petruska 1963, Landis et al. 1993). However, as the fibrils mature, further the whole collagen molecules become coated with mineral plates, see Figure 3.4(h) and Landis et al. (1993), Alexander et al. (2012), Landis & Jacquet (2013) for more details. In order to take into account that the mineral is therefore mainly but not exclusively found in the gap zones but also in the space between the collagen molecules (intermolecular space), we adapted the micromechanical representation of the mineralized collagen fibrils as follows: While Fritsch, Hellmich & Dormieux (2009) envisioned the collagen fibrils on the first scale as a network composed of a wet collagen and hydroxyapatite, the updated representation considers the collagen fibril as a network of a molecular collagen accompanied by intermolecular space. The latter was introduced by Fritsch, Hellmich & Dormieux (2009) only on the second scale, describing the wet collagen as a matrix consisting of collagen molecules hosting the intermolecular space in terms of cylindrical pores. Consequently, the model of Fritsch, Hellmich & Dormieux (2009) could not account for mineral in the intermolecular space. In our updated representation, the intermolecular space is described as a network of cylindrical mineral needles and waterfilled intercrystalline pores. On this basis, the new model is able to assign the same characteristic cylindrical shape to both occurrences of pure hydroxyapatite, in contrast to the different characterization of the mineral in terms of shape and material behavior by Fritsch, Hellmich & Dormieux (2009). Plasticity therefore arises within the extrafibrillar and intermolecular space in the proposed model.

3.5.2 Effects of the extracellular mass density and of the vascular porosity on bone strength

As basis for commenting on the influences of the extracellular mass density, ρ^{excel} , and of the vascular porosity, f_{vas}^{μ} , on the macroscopic strength of cortical bone, we have computed the latter for $f_{\text{vas}}^{\mu} = 0.02$, $f_{\text{vas}}^{\mu} = 0.05$ and $f_{\text{vas}}^{\mu} = 0.08$, considering thereby that ρ^{excel} ranges from 1.2 g/cm^3 (femur and humerus of albino rats (Hammett 1925)) to 2.4 g/cm^3 (otic bones of fin whale (Lees et al. 1996)), see Figure 3.12. Furthermore, Figure 3.12 contains also a plot showing how the volume fractions of the mineral, organic and water content, $f_{\text{HA}}^{\text{excel}}$, $f_{\text{org}}^{\text{excel}}$, and $f_{\text{H}_2\text{O}}^{\text{excel}}$ are related to ρ^{excel} , considering thereby the universal composition rules of bone tissue considered in this paper, see Vass et al. (2018) and Appendix A.5 for details.

While, in Figure 3.12 the tensile strength over the extracellular mass density shows the same characteristic features as the organic content-curve (linear dependency and maximum at $\rho^{\text{excel}} = 1.978 \text{ g/cm}^3$), the compressive strength increases with increasing mineral content. However, the features of the strength- and mineral content-curves differ in terms of their characteristic points and sort of dependency. Furthermore, there is no significant change of the compressive strength at the critical threshold of the content-curve ($\rho^{\text{excel}} = 1.978 \text{ g/cm}^3$), whereas the compressive strength plots change from non-linear to linear at around $\rho^{\text{excel}} = 1.8 \text{ g/cm}^3$. An explanation for this behavior could be that the water content exceeds the amount of both collagen and mineral in the extracellular matrix once the extracellular mass density falls below $\rho^{\text{excel}} = 1.8 \text{ g/cm}^3$. The assumption that this point represents a critical threshold of strength prediction, is also supported by the proposed model and algorithm being unable to predict a tensile strength for a bone below this mass-density limit.

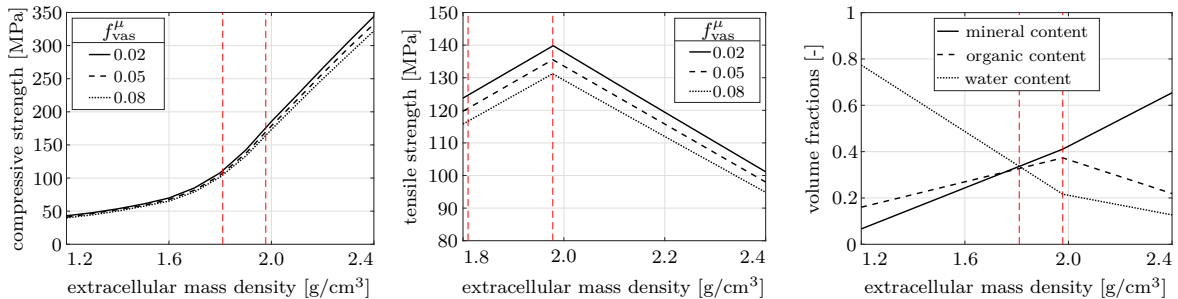


Fig. 3.12: Effects of the extracellular mass density ρ^{excel} on the predicted cortical compressive strength $\Sigma_{33}^{\text{ult},c}$ (left) and tensile strength $\Sigma_{33}^{\text{ult},t}$ (middle); as well as constituents volume fractions $f_{\text{HA}}^{\text{excel}}$, $f_{\text{org}}^{\text{excel}}$, and $f_{\text{H}_2\text{O}}^{\text{excel}}$ (right) (critical thresholds marked with red dashed lines)

3.5.3 Comments on the employed iterative return-mapping algorithm

The computation of the non-associated elastoplastic behavior in the mineral needles and the subsequent multiscale-upscaling of the elastoplastic constitutive relations from the mineral phase to the macroscopic scale of cortical bone is performed by a novel adaptation of the well-known return-mapping algorithm originating from the nonlinear elastoplastic Finite Element analysis (Simo & Hughes 1998), based on an incremental load apposition. We largely follow the algorithmic strategy described in Morin et al. (2017), where the micromechanical concentration-influence relations are employed to access the plastic behavior. Furthermore all

stress states in all (active) mineral phases are back-projected simultaneously onto the plastic yield surfaces. While the used plastic yield and potential functions, see Eqs. (3.22) and (3.23) appear as linear in the principal stress state, the corresponding principal stress directions do change during the back-projection steps, which renders the problem as a fully non-linear one that needs to be solved in an iterative manner. To this end, Morin et al. (2017) proposed a backward Euler scheme where they perform an iterative back projection along a predefined flow direction (being kept constant during this process), which is repeated by updating the predefined value with the resulting one until they match each other, see Fig. 3.13(left). However, while this method allows to back-project all trial stress states onto the phase-specific

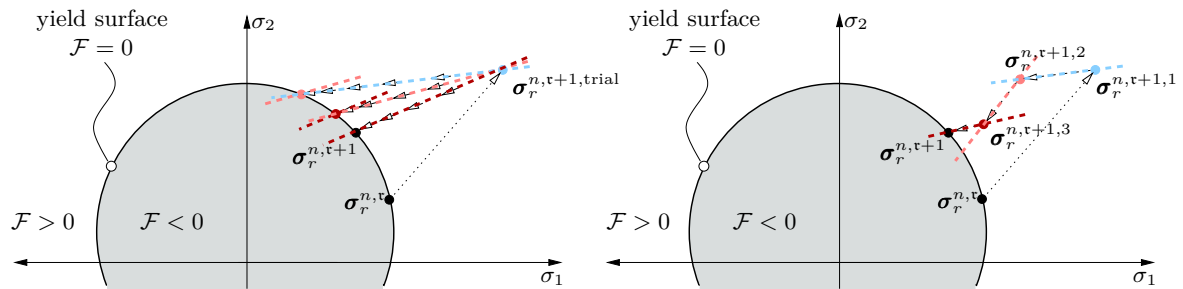


Fig. 3.13: Comparison of iterative return-mapping principles; (left) as proposed by Morin et al. (2017) (right) as proposed in the present work

yield surfaces in between one and ten iteration steps for the single-scale transition investigated by Morin et al. (2017), it reaches its limits when applied in a multiscale scheme. Depending on the macroscopic loading condition, the local stress state which arrives at the mineral level may be much more random and deviating from uniaxial due the downscaling over multiple scales, making it impossible to reach a convergence in the flow directions. To this end we developed a novel, adapted iterative return map algorithm, in which we consider a series of stress states and their corresponding flow directions converging towards the actual one. This series of stress states is developed by a sequential one-step linearized back projection process. The biggest advantage of this method is that each stress member of this series is getting closer and closer to the yield surface until the error that arises from assuming a wrong flow direction is negligibly small.

3.5.4 Sequence of plastic events

The multiscale bone model presented in this paper comprises only one source of elastoplasticity, namely the mutual sliding between the mineral needles, which are situated in both, the extrafibrillar and intermolecular space. These plastic events lead to a non-linear macroscopic stress-strain curve being associated to the propagation of plasticity throughout the differently oriented solid needle phases. The needle phases can take 120 different orientations, defined through the angles θ and φ , see Section 3.4.3. Increasing the loading leads to an increasing fraction of needles which are plasticizing. Introducing a degree of utilization u , with $u = 0$ representing the completely unloaded bone $\Sigma = 0$ and $u = 1$ representing the case that the bone has reached its strength and thus failed $\Sigma = \Sigma^{\text{ult}}$, it is instructive to study in which sequence the needles actually fail upon increasing the macroscopic loading, see Figure 3.14 for uniaxial compression and Figure 3.15 for uniaxial tension. For uniaxial compression, the needles orthogonal to the load direction are the first to plasticize, afterwards a second region

of plasticity emerges in the needles oriented in load direction and finally the plastic events propagate to the inclined needles in between these two regions. For uniaxial tension, on the other hand, plasticity first emerges in the needles oriented in load direction and spreads towards the orthogonal oriented ones. For both load cases, thus tension and compression, plastic events first occur in the extrafibrillar space, followed by the same sequence in the intermolecular space.

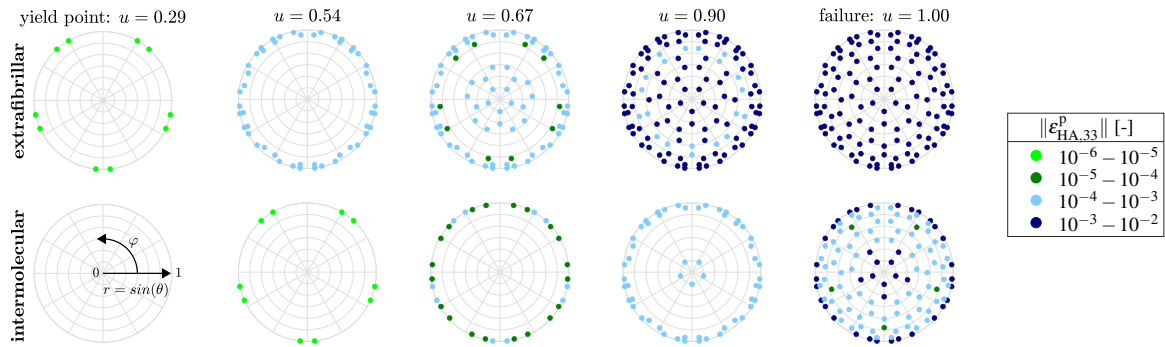


Fig. 3.14: Distribution of the norm of the plastic strains in the mineral $\varepsilon_{HA,33}^p$ over the needle orientations in the extrafibrillar and intermolecular space at selected macroscopic stress levels under uniaxial compression (specified by the degree of utilization u)

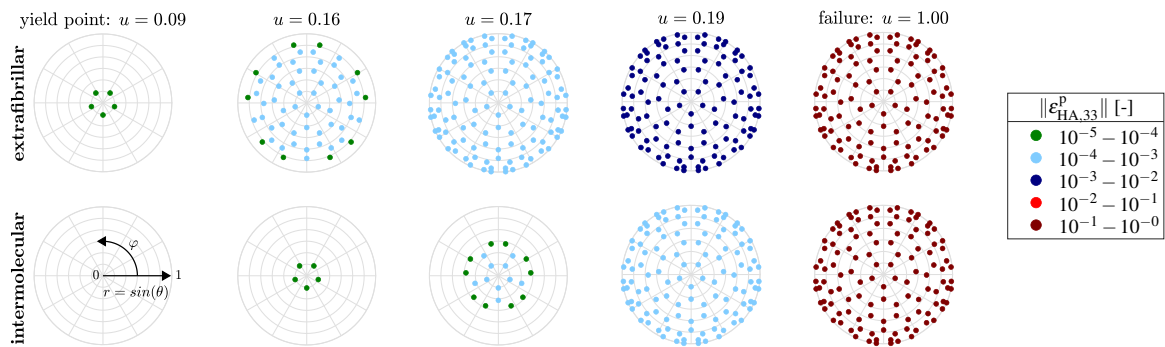


Fig. 3.15: Distribution of the norm of the plastic strains in the mineral $\varepsilon_{HA,33}^p$ over the needle orientations in the extrafibrillar and intermolecular space at selected macroscopic stress levels under uniaxial tension (specified by the degree of utilization u)

3.5.5 Concluding remarks

In this paper, we have presented a novel multiscale elastoplastic micromechanics model for cortical bone, based on previous contributions (Fritsch, Hellmich & Dormieux 2009, Morin et al. 2017), but revising and improving some key aspects, as described above. While the model offers a number of conceptual advantages and potentials, it has turned out to allow for computing strength estimates for bone on two hierarchical levels which fit reasonably well to corresponding experimental values. In particular, this agreement is remarkably good for compressive loading, whereas some deviations between model predictions and experimental data was observed for tensile loading. Hence, future research directions may include focusing on this particular aspect, probably involving the consideration of additional hardening effects in the collagen.

Furthermore, it should be stressed that the computational costs for computing the bone strength estimates is no insignificant. Obviously, this time adds up when considering, for example, large-scale Finite Element simulations of bone organs, involving probably millions of elements to which specific strength properties need to be assigned. Clearly, our model could be of great help in such case, by providing pre-computed lookup plots and/or tables (see Figures 3.16 and 3.17) serving as input data base for large-scale simulations.

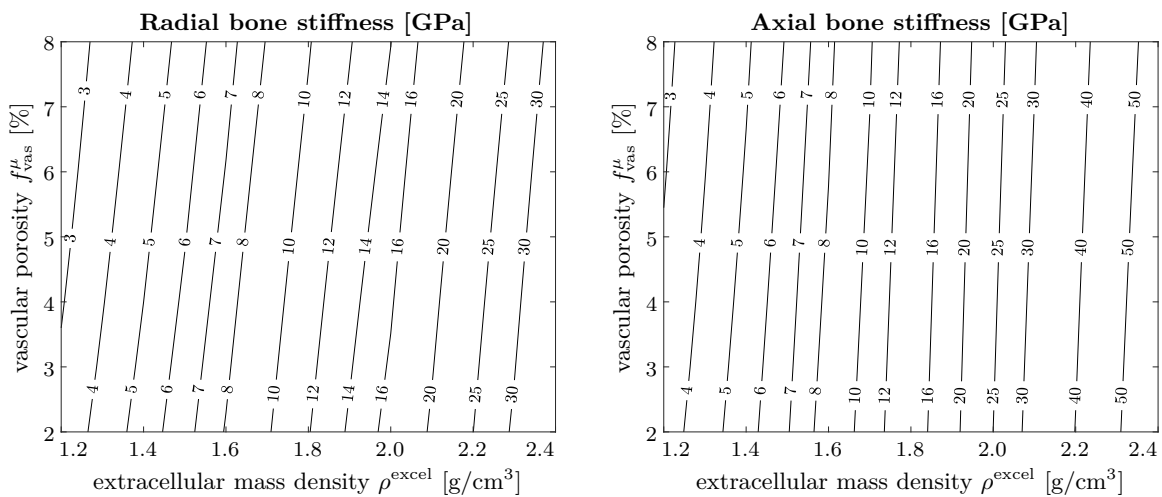


Fig. 3.16: Contourplot of axial (left) and radial (right) cortical bone stiffness as a function of extracellular mass density and vascular porosity (evaluated for $f_{lac+can}^{\mu} = 0.02$)

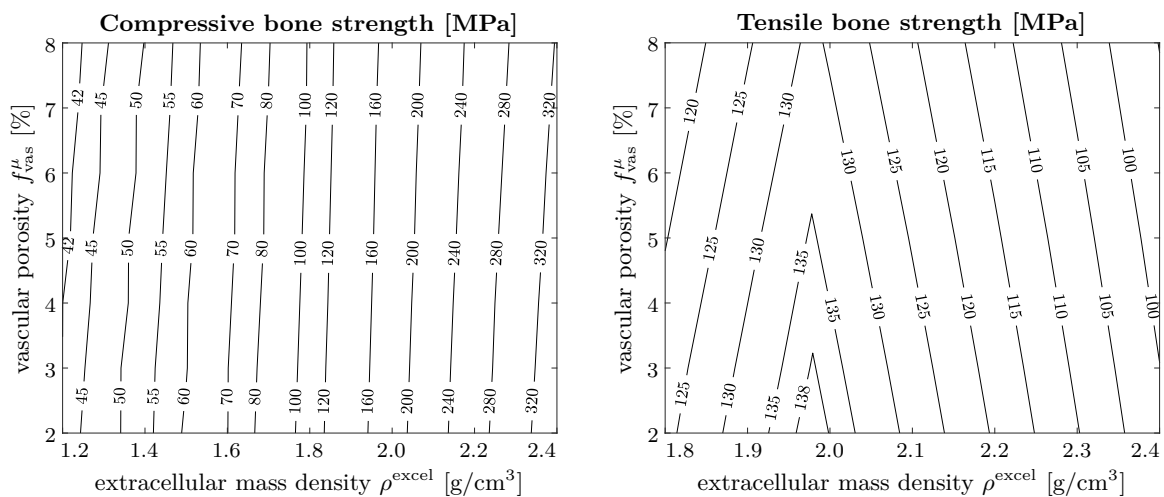


Fig. 3.17: Contourplot of compressive (left) and tensile (right) cortical bone strength as a function of extracellular mass density and vascular porosity (evaluated for $f_{lac+can}^{\mu} = 0.02$)

A Appendix

A.1 Hill tensors

The Hill tensor for the intercrystalline phase within the extrafibrillar or intermolecular space, which is represented by a spherical inclusion in an isotropic matrix reads as

$$\mathbb{P}_{\text{sph}}^{\text{im}} = \mathbb{P}_{\text{sph}}^{\text{ef}} = \mathbb{P}_{\text{sph}}^{\text{iso}} = (\mathbb{C}_{\text{ef}})^{-1} : \mathbb{S}_{\text{sph}}^{\text{esh,iso}} \quad (3.90)$$

$$\mathbb{S}_{\text{sph}}^{\text{esh,iso}} = \alpha_{\text{ef}} \mathbb{I}^{\text{vol}} + \beta_{\text{ef}} \mathbb{I}^{\text{dev}} \quad (3.91)$$

with

$$\alpha_{\text{ef}} = \frac{3k_{\text{ef}}}{3k_{\text{ef}} + 4\mu_{\text{ef}}} \quad \text{und} \quad \beta_{\text{ef}} = \frac{6(k_{\text{ef}} + 2\mu_{\text{ef}})}{5(3k_{\text{ef}} + 4\mu_{\text{ef}})} \quad (3.92)$$

with \mathbb{I}^{vol} as the volumetric part of the identity tensor \mathbb{I} with the components $I_{ijkl}^{\text{vol}} = \frac{1}{3}\delta_{ij}\delta_{kl}$ and \mathbb{I}^{dev} as the deviatoric part defined by $\mathbb{I}^{\text{dev}} = \mathbb{I} - \mathbb{I}^{\text{vol}}$.

The Hill tensor for a mineral needle within the extrafibrillar or intermolecular space, which is represented by a cylindrical inclusion with the orientation angles $\{\theta_i, \varphi_i\}_{i \in \mathcal{G}}$ in an isotropic matrix reads as

$$\mathbb{P}_{\text{cyl}}^{\text{im}} = \mathbb{P}_{\text{cyl}}^{\text{ef}} = \mathbb{P}_{\text{cyl}}^{\text{iso}} = (\mathbb{C}_{\text{ef}})^{-1} : \mathbb{S}_{\text{cyl}}^{\text{esh,iso}} \quad (3.93)$$

The non-zero components of the Eshelby tensor thereby read as

$$\begin{aligned} S_{\text{cyl},\theta\theta\theta\theta}^{\text{esh,iso}} &= S_{\text{cyl},\varphi\varphi\varphi\varphi}^{\text{esh,iso}} = \frac{5 - 4\nu^0}{8(1 - \nu^0)} \\ S_{\text{cyl},\theta\theta\varphi\varphi}^{\text{esh,iso}} &= S_{\text{cyl},\varphi\varphi\theta\theta}^{\text{esh,iso}} = \frac{-1 + 4\nu^0}{8(1 - \nu^0)} \\ S_{\text{cyl},\theta\theta rr}^{\text{esh,iso}} &= S_{\text{cyl},\varphi\varphi rr}^{\text{esh,iso}} = \frac{\nu^0}{2(1 - \nu^0)} \\ S_{\text{cyl},\varphi r\varphi r}^{\text{esh,iso}} &= S_{\text{cyl},r\varphi r\varphi}^{\text{esh,iso}} = S_{\text{zyl},r\varphi\varphi r}^{\text{esh,iso}} = S_{\text{cyl},\varphi rr\varphi}^{\text{esh,iso}} = \\ &= S_{\text{cyl},r\theta r\theta}^{\text{esh,iso}} = S_{\text{cyl},\theta r\theta r}^{\text{esh,iso}} = S_{\text{cyl},\theta rr\theta}^{\text{esh,iso}} = S_{\text{cyl},r\theta\theta r}^{\text{esh,iso}} = \frac{1}{4} \\ S_{\text{cyl},\theta\varphi\theta\varphi}^{\text{esh,iso}} &= S_{\text{cyl},\varphi\theta\varphi\theta}^{\text{esh,iso}} = S_{\text{cyl},\varphi\theta\theta\varphi}^{\text{esh,iso}} = S_{\text{cyl},\theta\varphi\varphi\theta}^{\text{esh,iso}} = \frac{3 - 4\nu^0}{8(1 - \nu^0)} \end{aligned} \quad (3.94)$$

with ν_{ef} as the Poisson's ratio of the matrix material

$$\nu_{\text{ef}} = \frac{3k_{\text{ef}} - 2\mu_{\text{ef}}}{6k_{\text{ef}} + 2\mu_{\text{ef}}} \quad (3.95)$$

The non-zero components of the Hill tensors for the collagen phase within the mineralized fibril ($\mathbb{P}_{\text{cyl}}^{\text{fib}}$), the fibrillar and extrafibrillar phase within the extracellular bone matrix ($\mathbb{P}_{\text{cyl}}^{\text{excel}}$), and the vascular pore phase within the microstructure ($\mathbb{P}_{\text{cyl}}^{\mu}$), which are all represented by cylindrical inclusions in an transversely isotropic matrix with stiffness $\mathbb{C}^0 \in \{\mathbb{C}_{\text{fib}}, \mathbb{C}_{\text{excel}}, \mathbb{C}_{\mu}\}$ read as

$$\begin{aligned}
P_{\text{cyl},1111}^{\text{trans}} &= P_{\text{cyl},2222}^{\text{trans}} = \frac{5C_{1111}^0 - 3C_{1122}^0}{8C_{1111}^0(C_{1111}^0 - C_{1122}^0)} \\
P_{\text{cyl},1122}^{\text{trans}} &= P_{\text{cyl},2211}^{\text{trans}} = \frac{-C_{1111}^0 - C_{1122}^0}{8C_{1111}^0(C_{1111}^0 - C_{1122}^0)} \\
P_{\text{cyl},2323}^{\text{trans}} &= P_{\text{cyl},1313}^{\text{trans}} = \frac{1}{8C_{2323}^0} \\
P_{\text{cyl},1212}^{\text{trans}} &= \frac{3C_{1111}^0 - C_{1122}^0}{8C_{1111}^0(C_{1111}^0 - C_{1122}^0)}
\end{aligned} \tag{3.96}$$

The non-zero components of the Hill tensors for the mineral foam phase within the mineralized fibril ($\mathbb{P}_{\text{sph}}^{\text{fib}}$) and lacunae pore phase within the extravascular bone matrix ($\mathbb{P}_{\text{sph}}^{\text{exvas}}$), which are both represented by spherical inclusions in an transversely isotropic matrix with stiffness $\mathbb{C}^0 \in \{\mathbb{C}_{\text{fib}}, \mathbb{C}_{\text{exvas}}\}$ read as

$$\begin{aligned}
P_{\text{sph},1111}^{\text{trans}} &= \frac{1}{16} \int_{-1}^1 -\frac{1}{D_1} (-5C_{1111}^0 x^4 C_{3333}^0 - 3C_{1122}^0 x^2 C_{3333}^0 - 3C_{1122}^0 x^4 C_{2323}^0 \\
&\quad + 3C_{1122}^0 x^4 C_{3333}^0 + 5C_{1111}^0 x^4 C_{2323}^0 - 10C_{1111}^0 C_{2323}^0 x^2 + 2x^4 (C_{1133}^0)^2 \\
&\quad + 8C_{2323}^0 x^4 C_{3333}^0 - 6(C_{2323}^0)^2 x^4 + 4C_{2323}^0 x^4 C_{1133}^0 + 6C_{1122}^0 C_{2323}^0 x^2 \\
&\quad + 5C_{1111}^0 C_{2323}^0 + 5C_{1111}^0 x^2 C_{3333}^0 - 4C_{2323}^0 x^2 C_{1133}^0 + 6(C_{2323}^0)^2 x^2 \\
&\quad - 2x^2 (C_{1133}^0)^2 - 3C_{1122}^0 C_{2323}^0) (-1 + x^2) dx
\end{aligned} \tag{3.97}$$

$$\begin{aligned}
P_{\text{sph},1122}^{\text{trans}} &= P_{\text{sph},2211}^{\text{trans}} \\
&= \frac{1}{16} \int_{-1}^1 \frac{1}{D_1} (C_{1111}^0 C_{2323}^0 - 2C_{1111}^0 C_{2323}^0 x^2 + C_{1111}^0 x^2 C_{3333}^0 \\
&\quad + C_{1122}^0 C_{2323}^0 - 2C_{1122}^0 C_{2323}^0 x^2 + C_{1122}^0 x^2 C_{3333}^0 + C_{1111}^0 x^4 C_{2323}^0 \\
&\quad - C_{1111}^0 x^4 C_{3333}^0 + C_{1122}^0 x^4 C_{2323}^0 - C_{1122}^0 x^4 C_{3333}^0 - 2(C_{2323}^0)^2 x^2 + 2(C_{2323}^0)^2 x^4 \\
&\quad - 4C_{2323}^0 x^2 C_{1133}^0 + 4C_{2323}^0 x^4 C_{1133}^0 - 2x^2 (C_{1133}^0)^2 + 2x^4 (C_{1133}^0)^2) (-1 + x^2) dx
\end{aligned} \tag{3.98}$$

$$P_{\text{sph},1133}^{\text{trans}} = P_{\text{sph},3311}^{\text{trans}} = \frac{1}{4} \int_{-1}^1 \frac{1}{D_2} (-1 + x^2) x^2 (C_{2323}^0 + C_{1133}^0) dx \tag{3.99}$$

$$P_{\text{sph},3333}^{\text{trans}} = \frac{1}{2} \int_{-1}^1 \frac{x^2}{D_2} (x^2 C_{2323}^0 - C_{1111}^0 x^2 + C_{1111}^0) dx \tag{3.100}$$

$$\begin{aligned}
P_{\text{sph},2323}^{\text{trans}} = & \frac{1}{16} \int_{-1}^1 \frac{1}{D_1} (4C_{1111}^0 C_{2323}^0 x^2 - 8C_{2323}^0 x^4 C_{1133}^0 - 2x^4 (C_{1133}^0)^2 \\
& - C_{1122}^0 x^4 C_{3333}^0 - 8C_{1111}^0 x^4 C_{2323}^0 + 3C_{1111}^0 x^4 C_{3333}^0 + 4C_{1111}^0 x^4 C_{1133}^0 \\
& - 4C_{1122}^0 x^4 C_{1133}^0 + 2C_{1122}^0 x^6 C_{1133}^0 - 2C_{1111}^0 x^6 C_{1133}^0 + C_{1122}^0 x^6 C_{1111}^0 \\
& - 3C_{1122}^0 x^4 C_{1111}^0 + 3C_{1122}^0 C_{1111}^0 x^2 - 2C_{1111}^0 x^2 C_{1133}^0 + 2C_{1122}^0 x^2 C_{1133}^0 \\
& + 8x^6 C_{2323}^0 C_{1133}^0 - 3x^6 C_{1111}^0 C_{3333}^0 + 4x^6 C_{2323}^0 C_{3333}^0 + 4C_{1111}^0 x^6 C_{2323}^0 \\
& + C_{1122}^0 x^6 C_{3333}^0 + 3(C_{1111}^0)^2 x^4 - (C_{1111}^0)^2 x^6 + 2(C_{1133}^0)^2 x^6 - 3(C_{1111}^0)^2 x^2 \\
& + (C_{1111}^0)^2 - C_{1122}^0 C_{1111}^0) dx
\end{aligned} \tag{3.101}$$

with

$$\begin{aligned}
D_2 = & 2C_{2323}^0 x^4 C_{1133}^0 + C_{2323}^0 x^4 C_{3333}^0 + C_{1111}^0 x^4 C_{2323}^0 - 2C_{2323}^0 x^2 C_{1133}^0 \\
& - 2C_{1111}^0 C_{2323}^0 x^2 + C_{1111}^0 C_{2323}^0 + x^4 (C_{1133}^0)^2 - C_{1111}^0 x^4 C_{3333}^0 \\
& - x^2 (C_{1133}^0)^2 + C_{1111}^0 x^2 C_{3333}^0
\end{aligned} \tag{3.102}$$

and

$$\begin{aligned}
D_1 = & -2(C_{1111}^0)^2 x^4 C_{3333}^0 + 2(C_{2323}^0)^2 x^6 C_{3333}^0 - 4C_{1111}^0 (C_{2323}^0)^2 x^4 - 3(C_{1111}^0)^2 C_{2323}^0 x^2 \\
& + (C_{1111}^0)^2 x^2 C_{3333}^0 + 2C_{1111}^0 (C_{2323}^0)^2 x^2 - 2C_{2323}^0 x^4 (C_{1133}^0)^2 - C_{1111}^0 (C_{1133}^0)^2 x^6 \\
& + 2C_{1111}^0 (C_{1133}^0)^2 x^4 + 4(C_{2323}^0)^2 x^6 C_{1133}^0 - 2C_{1122}^0 (C_{1133}^0)^2 x^4 + 2C_{2323}^0 x^6 (C_{1133}^0)^2 \\
& + 3(C_{1111}^0)^2 x^4 C_{2323}^0 + C_{1122}^0 (C_{1133}^0)^2 x^6 - (C_{1111}^0)^2 x^6 C_{2323}^0 + 2C_{1111}^0 x^6 (C_{2323}^0)^2 \\
& + (C_{1111}^0)^2 x^6 C_{3333}^0 - C_{1111}^0 (C_{1133}^0)^2 x^2 - 4(C_{2323}^0)^2 x^4 C_{1133}^0 + C_{1122}^0 (C_{1133}^0)^2 x^2 \\
& + (C_{1111}^0)^2 C_{2323}^0 - C_{1122}^0 C_{1111}^0 C_{2323}^0 - C_{1122}^0 x^6 C_{1111}^0 C_{3333}^0 \\
& + 4C_{1111}^0 x^4 C_{2323}^0 C_{1133}^0 - 2C_{1111}^0 x^2 C_{2323}^0 C_{1133}^0 - 4C_{1122}^0 x^4 C_{2323}^0 C_{1133}^0 \\
& + 2C_{1122}^0 x^2 C_{2323}^0 C_{1133}^0 + 2C_{1122}^0 x^6 C_{2323}^0 C_{1133}^0 - 2C_{1111}^0 x^6 C_{2323}^0 C_{1133}^0 \\
& - 3C_{1111}^0 x^6 C_{2323}^0 C_{3333}^0 + 2C_{1122}^0 C_{1111}^0 x^4 C_{3333}^0 - C_{1122}^0 C_{2323}^0 x^4 C_{3333}^0 \\
& - 3C_{1122}^0 C_{1111}^0 x^4 C_{2323}^0 - C_{1122}^0 C_{1111}^0 x^2 C_{3333}^0 + 3C_{1122}^0 C_{1111}^0 C_{2323}^0 x^2 \\
& + 3C_{1111}^0 C_{2323}^0 x^4 C_{3333}^0 + C_{1122}^0 x^6 C_{1111}^0 C_{2323}^0 + C_{1122}^0 x^6 C_{2323}^0 C_{3333}^0
\end{aligned} \tag{3.103}$$

A.2 Concentration tensors

The concentration tensors of the intermolecular and extrafibrillar space are equal since they have the same volume fractions ($f_{ic}^{im} = f_{ic}^{ef}$ and $f_{HA}^{im} = f_{HA}^{ef}$) and the same composition ($\mathbb{P}_{sph}^{ef} = \mathbb{P}_{sph}^{im}$ and $\mathbb{P}_{cyl}^{ef} = \mathbb{P}_{cyl}^{im}$); they read according to (3.6) as

$$\begin{aligned}
\mathbb{A}_{HA,i} &= \mathbb{A}_{HA,i}^{\infty} : \{f_{ic}^{im} \mathbb{A}_{ic}^{\infty} + f_{HA}^{im} \sum_{j \in \mathcal{G}} \omega_j \mathbb{A}_{HA,j}^{\infty}\}^{-1} = \mathbb{A}_{HA,i}^{\infty} : \{f_{ic}^{ef} \mathbb{A}_{ic}^{\infty} + f_{HA}^{ef} \sum_{j \in \mathcal{G}} \omega_j \mathbb{A}_{HA,j}^{\infty}\}^{-1} \\
\mathbb{A}_{ic} &= \mathbb{A}_{ic}^{\infty} : \{f_{ic}^{im} \mathbb{A}_{ic}^{\infty} + f_{HA}^{im} \sum_{j \in \mathcal{G}} \omega_j \mathbb{A}_{HA,j}^{\infty}\}^{-1} = \mathbb{A}_{ic}^{\infty} : \{f_{ic}^{ef} \mathbb{A}_{ic}^{\infty} + f_{HA}^{ef} \sum_{j \in \mathcal{G}} \omega_j \mathbb{A}_{HA,j}^{\infty}\}^{-1} \\
\mathbb{A}_{HA,i}^{\infty} &= [\mathbb{I} + \mathbb{P}_{cyl}^{im}(\theta_i, \varphi_i) : (\mathbb{C}_{HA} - \mathbb{C}_{im})]^{-1} = [\mathbb{I} + \mathbb{P}_{cyl}^{ef}(\theta_i, \varphi_i) : (\mathbb{C}_{HA} - \mathbb{C}_{ef})]^{-1} \\
\mathbb{A}_{ic}^{\infty} &= [\mathbb{I} + \mathbb{P}_{sph}^{im} : (\mathbb{C}_{ic} - \mathbb{C}_{im})]^{-1} = [\mathbb{I} + \mathbb{P}_{sph}^{ef} : (\mathbb{C}_{ic} - \mathbb{C}_{ef})]^{-1}
\end{aligned} \tag{3.104}$$

The concentration tensors of the mineralized collagen fibril read according to (3.6) as

$$\begin{aligned}
\mathbb{A}_{im} &= \mathbb{A}_{im}^{\infty} : \{f_{im}^{fib} \mathbb{A}_{im}^{\infty} + f_{col}^{fib} \mathbb{A}_{col}^{\infty}\}^{-1} \\
\mathbb{A}_{col} &= \mathbb{A}_{col}^{\infty} : \{f_{im}^{fib} \mathbb{A}_{im}^{\infty} + f_{col}^{fib} \mathbb{A}_{col}^{\infty}\}^{-1} \\
\mathbb{A}_{im}^{\infty} &= [\mathbb{I} + \mathbb{P}_{sph}^{fib} : (\mathbb{C}_{im} - \mathbb{C}_{fib})]^{-1} \\
\mathbb{A}_{col}^{\infty} &= [\mathbb{I} + \mathbb{P}_{cyl}^{fib} : (\mathbb{C}_{col} - \mathbb{C}_{fib})]^{-1}
\end{aligned} \tag{3.105}$$

The concentration tensors of the extracellular bone matrix read according to (3.6) as

$$\begin{aligned}
\mathbb{A}_{ef} &= \mathbb{A}_{ef}^{\infty} : \{f_{ef}^{excel} \mathbb{A}_{ef}^{\infty} + f_{fib}^{excel} \mathbb{A}_{fib}^{\infty}\}^{-1} \\
\mathbb{A}_{fib} &= \mathbb{A}_{fib}^{\infty} : \{f_{ef}^{excel} \mathbb{A}_{ef}^{\infty} + f_{fib}^{excel} \mathbb{A}_{fib}^{\infty}\}^{-1} \\
\mathbb{A}_{ef}^{\infty} &= [\mathbb{I} + \mathbb{P}_{cyl}^{excel} : (\mathbb{C}_{ef} - \mathbb{C}_{excel})]^{-1} \\
\mathbb{A}_{fib}^{\infty} &= [\mathbb{I} + \mathbb{P}_{cyl}^{excel} : (\mathbb{C}_{fib} - \mathbb{C}_{excel})]^{-1}
\end{aligned} \tag{3.106}$$

The concentration tensors of the extravascular bone material read according to (3.6) as

$$\begin{aligned}
\mathbb{A}_{excel} &= \mathbb{A}_{excel}^{\infty} : \{f_{excel}^{exvas} \mathbb{A}_{excel}^{\infty} + f_{lac+can}^{exvas} \mathbb{A}_{lac}^{\infty}\}^{-1} \\
\mathbb{A}_{lac} &= \mathbb{A}_{lac}^{\infty} : \{f_{excel}^{exvas} \mathbb{A}_{excel}^{\infty} + f_{lac+can}^{exvas} \mathbb{A}_{lac}^{\infty}\}^{-1} \\
\mathbb{A}_{excel}^{\infty} &= \mathbb{I} \\
\mathbb{A}_{lac}^{\infty} &= [\mathbb{I} + \mathbb{P}_{sph}^{exvas} : (\mathbb{C}_{lac} - \mathbb{C}_{exvas})]^{-1}
\end{aligned} \tag{3.107}$$

The concentration tensors of the bone microstructure read according to (3.6) as

$$\begin{aligned}
\mathbb{A}_{exvas} &= \mathbb{A}_{exvas}^{\infty} : \{f_{exvas}^{\mu} \mathbb{A}_{exvas}^{\infty} + f_{vas}^{\mu} \mathbb{A}_{vas}^{\infty}\}^{-1} \\
\mathbb{A}_{vas} &= \mathbb{A}_{vas}^{\infty} : \{f_{exvas}^{\mu} \mathbb{A}_{exvas}^{\infty} + f_{vas}^{\mu} \mathbb{A}_{vas}^{\infty}\}^{-1} \\
\mathbb{A}_{exvas}^{\infty} &= \mathbb{I} \\
\mathbb{A}_{vas}^{\infty} &= [\mathbb{I} + \mathbb{P}_{cyl}^{\mu} : (\mathbb{C}_{vas} - \mathbb{C}_{\mu})]^{-1}
\end{aligned} \tag{3.108}$$

A.3 Influence tensors

The influence tensors of the RVE of the intermolecular and extrafibrillar space are equal since they have the same volume fractions ($f_{ic}^{im} = f_{ic}^{ef}$ and $f_{HA}^{im} = f_{HA}^{ef}$) and the same composition ($\mathbb{P}_{sph}^{ef} = \mathbb{P}_{sph}^{im}$ and $\mathbb{P}_{cyl}^{ef} = \mathbb{P}_{cyl}^{im}$); they read according to Morin et al. (2017) as

$$\begin{aligned}
\mathbb{D}_{HA,ij} = & \left\{ -\mathbb{A}_{HA,i} : f_{HA}^{im} \mathbb{A}_{HA,j}^{\infty} : \mathbb{P}_{cyl}^{im}(\theta_j, \varphi_j) + \right. \\
& \left[f_{ic}^{im} \mathbb{A}_{HA,i} : \mathbb{A}_{ic}^{\infty} : \mathbb{P}_{sph}^{im} + f_{HA}^{im} \mathbb{A}_{HA,i} : \sum_{k \in \mathcal{G}} \omega_k \mathbb{A}_{HA,k}^{\infty} : \mathbb{P}_{cyl}^{im}(\theta_k, \varphi_k) - \mathbb{A}_{HA,i}^{\infty} : \mathbb{P}_{cyl}^{im}(\theta_i, \varphi_i) \right] : \\
& \left[f_{ic}^{im} (\mathbb{C}_{im} - \mathbb{C}_{ic}) : \mathbb{A}_{ic}^{\infty} : \mathbb{P}_{sph}^{ic} + f_{HA}^{im} (\mathbb{C}_{im} - \mathbb{C}_{HA}) : \sum_{k \in \mathcal{G}} \omega_k \mathbb{A}_{HA,k}^{\infty} : \mathbb{P}_{cyl}^{im}(\theta_k, \varphi_k) \right]^{-1} : \\
& \left. f_{HA}^{im} \left[(\mathbb{I} - \mathbb{A}_{HA,j})^T + (\mathbb{C}_{im} - \mathbb{C}_{HA}) : \mathbb{A}_{HA,j}^{\infty} : \mathbb{P}_{cyl}^{im}(\theta_j, \varphi_j) \right] \right\} : \mathbb{C}_{HA} \\
\\
\mathbb{D}_{HA,ii} = & \left\{ \left[\omega_i^{-1} \mathbb{I} - \mathbb{A}_{HA,i} : f_{HA}^{im} \right] : \mathbb{A}_{HA,i}^{\infty} : \mathbb{P}_{cyl}^{im}(\theta_i, \varphi_i) + \right. \\
& \left[f_{ic}^{im} \mathbb{A}_{HA,i} : \mathbb{A}_{ic}^{\infty} : \mathbb{P}_{sph}^{im} + f_{HA}^{im} \mathbb{A}_{HA,i} : \sum_{k \in \mathcal{G}} \omega_k \mathbb{A}_{HA,k}^{\infty} : \mathbb{P}_{cyl}^{im}(\theta_k, \varphi_k) - \mathbb{A}_{HA,i}^{\infty} : \mathbb{P}_{cyl}^{im}(\theta_i, \varphi_i) \right] : \\
& \left[f_{ic}^{im} (\mathbb{C}_{im} - \mathbb{C}_{ic}) : \mathbb{A}_{ic}^{\infty} : \mathbb{P}_{sph}^{ic} + f_{HA}^{im} (\mathbb{C}_{im} - \mathbb{C}_{HA}) : \sum_{k \in \mathcal{G}} \omega_k \mathbb{A}_{HA,k}^{\infty} : \mathbb{P}_{cyl}^{im}(\theta_k, \varphi_k) \right]^{-1} : \\
& \left. f_{HA}^{im} \left[(\mathbb{I} - \mathbb{A}_{HA,i})^T + (\mathbb{C}_{im} - \mathbb{C}_{HA}) : \mathbb{A}_{HA,i}^{\infty} : \mathbb{P}_{cyl}^{im}(\theta_i, \varphi_i) \right] \right\} : \mathbb{C}_{HA} \\
\\
\mathbb{D}_{ic,j} = & \left\{ -\mathbb{A}_{ic} : f_{HA}^{im} \mathbb{A}_{HA,j}^{\infty} : \mathbb{P}_{cyl}^{im}(\theta_j, \varphi_j) + \right. \\
& \left[f_{ic}^{im} \mathbb{A}_{ic} : \mathbb{A}_{ic}^{\infty} : \mathbb{P}_{sph}^{im} + f_{HA}^{im} \mathbb{A}_{ic} : \sum_{k \in \mathcal{G}} \omega_k \mathbb{A}_{HA,k}^{\infty} : \mathbb{P}_{cyl}^{im}(\theta_k, \varphi_k) - \mathbb{A}_{ic}^{\infty} : \mathbb{P}_{sph}^{im} \right] : \\
& \left[f_{ic}^{im} (\mathbb{C}_{im} - \mathbb{C}_{ic}) : \mathbb{A}_{ic}^{\infty} : \mathbb{P}_{sph}^{im} + f_{HA}^{im} (\mathbb{C}_{im} - \mathbb{C}_{HA}) : \sum_{k \in \mathcal{G}} \omega_k \mathbb{A}_{HA,k}^{\infty} : \mathbb{P}_{cyl}^{im}(\theta_k, \varphi_k) \right]^{-1} : \\
& \left. f_{HA}^{im} \left[(\mathbb{I} - \mathbb{A}_{HA,j})^T + (\mathbb{C}_{im} - \mathbb{C}_{HA}) : \mathbb{A}_{HA,j}^{\infty} : \mathbb{P}_{cyl}^{im}(\theta_j, \varphi_j) \right] \right\} : \mathbb{C}_{HA}
\end{aligned} \tag{3.109}$$

Following the derivation in Pichler & Hellmich (2010) for an extended matrix-inclusion problem and considering that, in the present case, the eigenstrain of the auxiliary matrix is equal to the

eigenstrain of the matrix phase, delivers the influence tensors of the RVE of the mineralized collagen fibril as

$$\begin{aligned} \mathbb{D}_{\text{im}} = & \left\{ [\mathbb{I} - f_{\text{im}}^{\text{fib}} \mathbb{A}_{\text{im}}] : \mathbb{A}_{\text{im}}^{\infty} : \mathbb{P}_{\text{sph}}^{\text{fib}} + \right. \\ & \left[\mathbb{A}_{\text{im}} : (f_{\text{im}}^{\text{fib}} \mathbb{A}_{\text{im}}^{\infty} : \mathbb{P}_{\text{sph}}^{\text{fib}} + f_{\text{col}}^{\text{fib}} \mathbb{A}_{\text{col}}^{\infty} : \mathbb{P}_{\text{cyl}}^{\text{fib}}) - \mathbb{A}_{\text{im}}^{\infty} : \mathbb{P}_{\text{sph}}^{\text{fib}} \right] : \\ & \left[f_{\text{im}} (\mathbb{C}_{\text{fib}} - \mathbb{C}_{\text{im}}) : \mathbb{A}_{\text{im}}^{\infty} : \mathbb{P}_{\text{sph}}^{\text{fib}} + f_{\text{col}} (\mathbb{C}_{\text{fib}} - \mathbb{C}_{\text{col}}) : \mathbb{A}_{\text{col}}^{\infty} : \mathbb{P}_{\text{cyl}}^{\text{fib}} \right]^{-1} : \\ & \left. f_{\text{im}} \left[(\mathbb{I} - \mathbb{A}_{\text{im}})^{\text{T}} + (\mathbb{C}_{\text{fib}} - \mathbb{C}_{\text{im}}) : \mathbb{A}_{\text{im}}^{\infty} : \mathbb{P}_{\text{sph}}^{\text{fib}} \right] \right\} : \mathbb{C}_{\text{im}} \end{aligned} \quad (3.110)$$

$$\begin{aligned} \mathbb{D}_{\text{col}} = & \left\{ -\mathbb{A}_{\text{col}} : f_{\text{im}}^{\text{fib}} \mathbb{A}_{\text{im}}^{\infty} : \mathbb{P}_{\text{sph}}^{\text{fib}} \right. \\ & \left. + \left[\mathbb{A}_{\text{col}} : (f_{\text{im}}^{\text{fib}} \mathbb{A}_{\text{im}}^{\infty} : \mathbb{P}_{\text{sph}}^{\text{fib}} + f_{\text{col}}^{\text{fib}} \mathbb{A}_{\text{col}}^{\infty} : \mathbb{P}_{\text{cyl}}^{\text{fib}}) - \mathbb{A}_{\text{col}}^{\infty} : \mathbb{P}_{\text{cyl}}^{\text{fib}} \right] : \right. \\ & \left. \left[f_{\text{im}} (\mathbb{C}_{\text{fib}} - \mathbb{C}_{\text{im}}) : \mathbb{A}_{\text{im}}^{\infty} : \mathbb{P}_{\text{sph}}^{\text{fib}} + f_{\text{col}} (\mathbb{C}_{\text{fib}} - \mathbb{C}_{\text{col}}) : \mathbb{A}_{\text{col}}^{\infty} : \mathbb{P}_{\text{cyl}}^{\text{fib}} \right]^{-1} : \right. \\ & \left. f_{\text{im}}^{\text{fib}} \left[(\mathbb{I} - \mathbb{A}_{\text{im}})^{\text{T}} + (\mathbb{C}_{\text{fib}} - \mathbb{C}_{\text{im}}) : \mathbb{A}_{\text{im}}^{\infty} : \mathbb{P}_{\text{sph}}^{\text{fib}} \right] \right\} : \mathbb{C}_{\text{im}} \end{aligned}$$

the influence tensors of the RVE of the extracellular bone matrix as

$$\begin{aligned} \mathbb{D}_{\text{ef,ef}} &= [\mathbb{I} - f_{\text{ef}}^{\text{excel}} \mathbb{A}_{\text{ef}}] : \mathbb{A}_{\text{ef}}^{\infty} : \mathbb{P}_{\text{cyl}}^{\text{excel}} : \mathbb{C}_{\text{ef}} \\ \mathbb{D}_{\text{ef,fib}} &= -\mathbb{A}_{\text{ef}} : f_{\text{fib}}^{\text{excel}} \mathbb{A}_{\text{fib}}^{\infty} : \mathbb{P}_{\text{cyl}}^{\text{excel}} : \mathbb{C}_{\text{fib}} \\ \mathbb{D}_{\text{fib,fib}} &= [\mathbb{I} - f_{\text{fib}}^{\text{excel}} \mathbb{A}_{\text{fib}}] : \mathbb{A}_{\text{fib}}^{\infty} : \mathbb{P}_{\text{cyl}}^{\text{excel}} : \mathbb{C}_{\text{fib}} \\ \mathbb{D}_{\text{fib,ef}} &= -\mathbb{A}_{\text{fib}} : f_{\text{ef}}^{\text{excel}} \mathbb{A}_{\text{ef}}^{\infty} : \mathbb{P}_{\text{cyl}}^{\text{excel}} : \mathbb{C}_{\text{ef}} \end{aligned} \quad (3.111)$$

the influence tensors of the RVE of the extravascular bone material as

$$\begin{aligned} \mathbb{D}_{\text{excel}} &= f_{\text{lac+can}}^{\text{exvas}} \mathbb{A}_{\text{excel}} : \mathbb{A}_{\text{lac}}^{\infty} : \mathbb{P}_{\text{sph}}^{\text{exvas}} : \mathbb{C}_{\text{excel}} \\ \mathbb{D}_{\text{lac}} &= [f_{\text{lac+can}}^{\text{exvas}} \mathbb{A}_{\text{lac}} - \mathbb{I}] : \mathbb{A}_{\text{lac}}^{\infty} : \mathbb{P}_{\text{sph}}^{\text{exvas}} : \mathbb{C}_{\text{excel}} \end{aligned} \quad (3.112)$$

and the influence tensors of the RVE of the bone microstructure as

$$\begin{aligned} \mathbb{D}_{\text{exvas}} &= f_{\text{vas}}^{\mu} \mathbb{A}_{\text{exvas}} : \mathbb{A}_{\text{vas}}^{\infty} : \mathbb{P}_{\text{cyl}}^{\mu} : \mathbb{C}_{\text{exvas}} \\ \mathbb{D}_{\text{vas}} &= [f_{\text{vas}}^{\text{exvas}} \mathbb{A}_{\text{vas}} - \mathbb{I}] : \mathbb{A}_{\text{vas}}^{\infty} : \mathbb{P}_{\text{cyl}}^{\mu} : \mathbb{C}_{\text{exvas}} \end{aligned} \quad (3.113)$$

A.4 Derivation of the multiscale influence tensors

Extrafibrillar space

Inserting Eq. (3.59) in (3.55), the resulting expression in (3.51), and this result subsequently in (3.43) yields

$$\begin{aligned}
\boldsymbol{\varepsilon}_{\text{efHA},i} &= \mathbb{A}_{\text{HA},i} : \mathbb{A}_{\text{ef}} : \mathbb{A}_{\text{excel}} : \mathbb{A}_{\text{exvas}} : \mathbf{E} \\
&\quad + \mathbb{A}_{\text{HA},i} : \mathbb{A}_{\text{ef}} : \mathbb{A}_{\text{excel}} : \mathbb{D}_{\text{exvas}} : \boldsymbol{\varepsilon}_{\text{exvas}}^{\text{P}} \\
&\quad + \mathbb{A}_{\text{HA},i} : \mathbb{A}_{\text{ef}} : \mathbb{D}_{\text{excel}} : \boldsymbol{\varepsilon}_{\text{excel}}^{\text{P}} \\
&\quad + \mathbb{A}_{\text{HA},i} : \mathbb{D}_{\text{ef,ef}} : \boldsymbol{\varepsilon}_{\text{ef}}^{\text{P}} \\
&\quad + \mathbb{A}_{\text{HA},i} : \mathbb{D}_{\text{ef,fb}} : \boldsymbol{\varepsilon}_{\text{fb}}^{\text{P}} \\
&\quad + \sum_j \omega_j \mathbb{D}_{\text{HA},ij} : \boldsymbol{\varepsilon}_{\text{efHA},j}^{\text{P}}
\end{aligned} \tag{3.114}$$

The next step is to express all the plastic strains in (3.114) as a function of the plasticity-inducing strains $\boldsymbol{\varepsilon}_{\text{efHA},i}^{\text{P}}$ and $\boldsymbol{\varepsilon}_{\text{imHA},i}^{\text{P}}$ only by inserting (3.41) into (3.49), yielding

$$\boldsymbol{\varepsilon}_{\text{fb}}^{\text{P}} = f_{\text{im}}^{\text{fib}} : \mathbb{C}_{\text{fb}}^{-1} : A_{\text{im}}^{\text{T}} : f_{\text{HA}}^{\text{im}} : \sum_j \omega_j A_{\text{HA},j}^{\text{T}} : \mathbb{C}_{\text{HA}} : \boldsymbol{\varepsilon}_{\text{imHA},j}^{\text{P}} \tag{3.115}$$

inserting (3.45) and (3.115) into (3.53), yielding

$$\begin{aligned}
\boldsymbol{\varepsilon}_{\text{excel}}^{\text{P}} &= f_{\text{ef}}^{\text{excel}} : \mathbb{C}_{\text{excel}}^{-1} : A_{\text{ef}}^{\text{T}} : f_{\text{HA}}^{\text{ef}} : \sum_j \omega_j A_{\text{HA},j}^{\text{T}} : \mathbb{C}_{\text{HA}} : \boldsymbol{\varepsilon}_{\text{efHA},j}^{\text{P}} \\
&\quad + f_{\text{fb}}^{\text{excel}} : \mathbb{C}_{\text{excel}}^{-1} : A_{\text{fb}}^{\text{T}} : f_{\text{im}}^{\text{fb}} : A_{\text{im}}^{\text{T}} : f_{\text{HA}}^{\text{im}} : \sum_j \omega_j A_{\text{HA},j}^{\text{T}} : \mathbb{C}_{\text{HA}} : \boldsymbol{\varepsilon}_{\text{imHA},j}^{\text{P}}
\end{aligned} \tag{3.116}$$

and inserting (3.116) into (3.57), yielding

$$\begin{aligned}
\boldsymbol{\varepsilon}_{\text{exvas}}^{\text{P}} &= f_{\text{excel}}^{\text{exvas}} : \mathbb{C}_{\text{exvas}}^{-1} : A_{\text{excel}}^{\text{T}} : f_{\text{ef}}^{\text{excel}} : A_{\text{ef}}^{\text{T}} : f_{\text{HA}}^{\text{ef}} : \sum_j \omega_j A_{\text{HA},j}^{\text{T}} : \mathbb{C}_{\text{HA}} : \boldsymbol{\varepsilon}_{\text{efHA},j}^{\text{P}} \\
&\quad + f_{\text{excel}}^{\text{exvas}} : \mathbb{C}_{\text{exvas}}^{-1} : A_{\text{excel}}^{\text{T}} : f_{\text{fb}}^{\text{excel}} : A_{\text{fb}}^{\text{T}} : f_{\text{im}}^{\text{fb}} : A_{\text{im}}^{\text{T}} : f_{\text{HA}}^{\text{im}} : \sum_j \omega_j A_{\text{HA},j}^{\text{T}} : \mathbb{C}_{\text{HA}} : \boldsymbol{\varepsilon}_{\text{imHA},j}^{\text{P}}
\end{aligned} \tag{3.117}$$

Next, inserting (3.45), (3.115), (3.116) and (3.117) into (3.114) allows to express the microscopic strain in the extrafibrillar mineral needle i as function of the applied macroscopic strain \mathbf{E} and the plastic strains in the mineral only

$$\begin{aligned}
\boldsymbol{\varepsilon}_{\text{efHA},i} = & \mathbb{A}_{\text{HA},i} : \mathbb{A}_{\text{ef}} : \mathbb{A}_{\text{excel}} : \mathbb{A}_{\text{exvas}} : \mathbf{E} \\
& + \sum_{j \in \mathcal{G}} \left\{ \mathbb{A}_{\text{HA},i} : \mathbb{A}_{\text{ef}} : \mathbb{A}_{\text{excel}} : \mathbb{D}_{\text{exvas}} : f_{\text{excel}}^{\text{exvas}} \mathbb{C}_{\text{exvas}}^{-1} : \mathbb{A}_{\text{excel}}^{\text{T}} \right. \\
& : f_{\text{ef}}^{\text{excel}} \mathbb{A}_{\text{ef}}^{\text{T}} : f_{\text{HA}}^{\text{ef}} \omega_j \mathbb{A}_{\text{HA},j}^{\text{T}} : \mathbb{C}_{\text{HA}} \\
& + \mathbb{A}_{\text{HA},i} : \mathbb{A}_{\text{ef}} : \mathbb{D}_{\text{excel}} : f_{\text{ef}}^{\text{excel}} \mathbb{C}_{\text{excel}}^{-1} : \mathbb{A}_{\text{ef}}^{\text{T}} : f_{\text{HA}}^{\text{ef}} \omega_j \mathbb{A}_{\text{HA},j}^{\text{T}} : \mathbb{C}_{\text{HA}} \\
& + \mathbb{A}_{\text{HA},i} : \mathbb{D}_{\text{ef,ef}} : f_{\text{HA}}^{\text{ef}} \mathbb{C}_{\text{ef}}^{-1} : \omega_j \mathbb{A}_{\text{HA},j}^{\text{T}} : \mathbb{C}_{\text{HA}} \\
& \left. + \omega_j \mathbb{D}_{\text{HA},ij} \right\} : \boldsymbol{\varepsilon}_{\text{efHA},j}^{\text{P}} \\
& + \sum_{j \in \mathcal{G}} \left\{ \mathbb{A}_{\text{HA},i} : \mathbb{A}_{\text{ef}} : \mathbb{A}_{\text{excel}} : \mathbb{D}_{\text{exvas}} : f_{\text{excel}}^{\text{exvas}} \mathbb{C}_{\text{exvas}}^{-1} : \mathbb{A}_{\text{excel}}^{\text{T}} \right. \\
& : f_{\text{fib}}^{\text{excel}} \mathbb{A}_{\text{fib}}^{\text{T}} : f_{\text{im}}^{\text{fib}} \mathbb{A}_{\text{im}}^{\text{T}} : f_{\text{HA}}^{\text{im}} \omega_j \mathbb{A}_{\text{HA},j}^{\text{T}} : \mathbb{C}_{\text{HA}} \\
& + \mathbb{A}_{\text{HA},i} : \mathbb{A}_{\text{ef}} : \mathbb{D}_{\text{excel}} : f_{\text{fib}}^{\text{excel}} \mathbb{C}_{\text{excel}}^{-1} : \mathbb{A}_{\text{fib}}^{\text{T}} : f_{\text{im}}^{\text{fib}} \mathbb{A}_{\text{im}}^{\text{T}} : f_{\text{HA}}^{\text{im}} \omega_j \mathbb{A}_{\text{HA},j}^{\text{T}} : \mathbb{C}_{\text{HA}} \\
& \left. + \mathbb{A}_{\text{HA},i} : \mathbb{D}_{\text{ef,fib}} : f_{\text{im}}^{\text{fib}} \mathbb{C}_{\text{fib}}^{-1} : \mathbb{A}_{\text{im}}^{\text{T}} : f_{\text{HA}}^{\text{im}} \omega_j \mathbb{A}_{\text{HA},j}^{\text{T}} : \mathbb{C}_{\text{HA}} \right\} : \boldsymbol{\varepsilon}_{\text{imHA},j}^{\text{P}}.
\end{aligned} \tag{3.118}$$

Comparing (3.118) to (3.62) finally allows to identify the multiscale influence tensors as given in (3.64) and (3.66)

Intermolecular space

Inserting Eq. (3.59) in (3.55), the resulting expression in (3.52), an this result subsequently in (3.47) and finally in (3.39) yields

$$\begin{aligned}
\boldsymbol{\varepsilon}_{\text{imHA},i} = & A_{\text{HA},i} : A_{\text{im}} : A_{\text{fib}} : A_{\text{excel}} : A_{\text{exvas}} : \mathbf{E} \\
& + A_{\text{HA},i} : A_{\text{im}} : A_{\text{fib}} : A_{\text{excel}} : \mathbb{D}_{\text{exvas}} : \boldsymbol{\varepsilon}_{\text{exvas}}^{\text{P}} \\
& + A_{\text{HA},i} : A_{\text{im}} : A_{\text{fib}} : \mathbb{D}_{\text{excel}} : \boldsymbol{\varepsilon}_{\text{excel}}^{\text{P}} \\
& + A_{\text{HA},i} : A_{\text{im}} : \mathbb{D}_{\text{fib,ef}} : \boldsymbol{\varepsilon}_{\text{ef}}^{\text{P}} \\
& + A_{\text{HA},i} : A_{\text{im}} : \mathbb{D}_{\text{fib,fib}} : \boldsymbol{\varepsilon}_{\text{fib}}^{\text{P}} \\
& + A_{\text{HA},i} : \mathbb{D}_{\text{im}} : \boldsymbol{\varepsilon}_{\text{im}}^{\text{P}} \\
& + \sum_j \omega_j \mathbb{D}_{\text{HA},ij} : \boldsymbol{\varepsilon}_{\text{imHA},j}^{\text{P}}
\end{aligned} \tag{3.119}$$

In the next step, inserting (3.41), (3.45), (3.115), (3.116) and (3.117) into (3.119) allows to express the microscopic strain in the intermolecular mineral needle i as function of the applied macroscopic strain \mathbf{E} and the plastic strains in the mineral only

$$\begin{aligned}
\boldsymbol{\sigma}_{\text{imHA},i} &= \mathbb{A}_{\text{HA},i} : \mathbb{A}_{\text{im}} : \mathbb{A}_{\text{fib}} : \mathbb{A}_{\text{excel}} : \mathbb{A}_{\text{exvas}} : \mathbf{E} \\
&+ \sum_{j \in \mathcal{G}} \left\{ \mathbb{A}_{\text{HA},i} : \mathbb{A}_{\text{im}} : \mathbb{A}_{\text{fib}} : \mathbb{A}_{\text{excel}} : \mathbb{D}_{\text{exvas}} : f_{\text{excel}}^{\text{exvas}} \mathbb{C}_{\text{exvas}}^{-1} : \mathbb{A}_{\text{excel}}^{\text{T}} : \right. \\
&f_{\text{ef}}^{\text{excel}} \mathbb{A}_{\text{ef}}^{\text{T}} : f_{\text{HA}}^{\text{ef}} \omega_j \mathbb{A}_{\text{HA},j}^{\text{T}} : \mathbb{C}_{\text{HA}} \\
&+ \mathbb{A}_{\text{HA},i} : \mathbb{A}_{\text{im}} : \mathbb{A}_{\text{fib}} : \mathbb{D}_{\text{excel}} : f_{\text{ef}}^{\text{excel}} \mathbb{C}_{\text{excel}}^{-1} : \mathbb{A}_{\text{ef}}^{\text{T}} : f_{\text{HA}}^{\text{ef}} \omega_j \mathbb{A}_{\text{HA},j}^{\text{T}} : \mathbb{C}_{\text{HA}} \\
&\left. + \mathbb{A}_{\text{HA},i} : \mathbb{A}_{\text{im}} : \mathbb{D}_{\text{fib,ef}} : f_{\text{HA}}^{\text{ef}} \mathbb{C}_{\text{ef}}^{-1} : \omega_j \mathbb{A}_{\text{HA},j}^{\text{T}} : \mathbb{C}_{\text{HA}} \right\} : \boldsymbol{\varepsilon}_{\text{efHA},j}^{\text{P}} \\
&+ \sum_{j \in \mathcal{G}} \left\{ \mathbb{A}_{\text{HA},i} : \mathbb{A}_{\text{im}} : \mathbb{A}_{\text{fib}} : \mathbb{A}_{\text{excel}} : \mathbb{D}_{\text{exvas}} : f_{\text{excel}}^{\text{exvas}} \mathbb{C}_{\text{exvas}}^{-1} : \mathbb{A}_{\text{excel}}^{\text{T}} : \right. \\
&f_{\text{fib}}^{\text{excel}} \mathbb{A}_{\text{fib}}^{\text{T}} : f_{\text{im}}^{\text{fib}} \mathbb{A}_{\text{im}}^{\text{T}} : f_{\text{HA}}^{\text{im}} \omega_j \mathbb{A}_{\text{HA},j}^{\text{T}} : \mathbb{C}_{\text{HA}} \\
&+ \mathbb{A}_{\text{HA},i} : \mathbb{A}_{\text{im}} : \mathbb{A}_{\text{fib}} : \mathbb{D}_{\text{excel}} : f_{\text{fib}}^{\text{excel}} \mathbb{C}_{\text{excel}}^{-1} : \mathbb{A}_{\text{fib}}^{\text{T}} : f_{\text{im}}^{\text{fib}} \mathbb{A}_{\text{im}}^{\text{T}} : f_{\text{HA}}^{\text{im}} \omega_j \mathbb{A}_{\text{HA},j}^{\text{T}} : \mathbb{C}_{\text{HA}} \\
&+ \mathbb{A}_{\text{HA},i} : \mathbb{A}_{\text{im}} : \mathbb{D}_{\text{fib,fib}} f_{\text{im}}^{\text{fib}} : \mathbb{C}_{\text{fib}}^{-1} : \mathbb{A}_{\text{im}}^{\text{T}} : f_{\text{HA}}^{\text{im}} \omega_j \mathbb{A}_{\text{HA},j}^{\text{T}} : \mathbb{C}_{\text{HA}} \\
&+ \mathbb{A}_{\text{HA},i} : \mathbb{D}_{\text{im}} : f_{\text{HA}}^{\text{im}} \mathbb{C}_{\text{im}}^{-1} : \omega_j \mathbb{A}_{\text{HA},j}^{\text{T}} : \mathbb{C}_{\text{HA}} \\
&\left. + \omega_j \mathbb{D}_{\text{HA},ij} \right\} : \boldsymbol{\varepsilon}_{\text{imHA},j}^{\text{P}}.
\end{aligned} \tag{3.120}$$

Comparing (3.120) to (3.63) finally allows to identify the multiscale influence tensors as given in (3.65) and (3.67).

A.5 Volume fractions of the extracellular space

The volume fraction of the phases within the extracellular space can be accessed through the so-called *universal composition rules* of bone (Vass et al. 2018) based on the extracellular mass density ρ^{excel} , and known vascular, lacunar and canalicular porosities of a bone sample, f_{vas}^{μ} and $f_{\text{lac+can}}^{\mu}$.

The extracellular mass density can either serve as input value itself, or the macroscopic mass density of a millimeter-sized bone sample ρ^{μ} is transformed to the extravascular and extracellular level, yielding the corresponding mass densities at the two lower scales as

$$\begin{aligned}
\rho^{\text{exvas}} &= \frac{\rho^{\mu} - \rho_{\text{H}_2\text{O}} \cdot f_{\text{vas}}^{\mu}}{1 - f_{\text{vas}}^{\mu}} \\
\rho^{\text{excel}} &= \frac{\rho^{\text{exvas}} - \rho_{\text{H}_2\text{O}} \cdot f_{\text{lac+can}}^{\text{exvas}}}{1 - f_{\text{lac+can}}^{\text{exvas}}}
\end{aligned} \tag{3.121}$$

with

$$f_{\text{lac+can}}^{\text{exvas}} = \frac{f_{\text{lac+can}}^{\mu}}{f_{\text{exvas}}^{\mu}} \quad \text{and} \quad f_{\text{exvas}}^{\mu} = 1 - f_{\text{vas}}^{\mu}. \tag{3.122}$$

Based on the extracellular mass density, the universal composition rule for mineral and collagen dosages in extracellular bone (Vass et al. 2018) gives access to the volume fractions of the constituents in the extracellular RVE, namely mineral, organic and water content

$$\text{if } \rho^{excel} \leq 1.978 \text{ g/cm}^3 \begin{cases} f_{HA}^{excel} = \frac{1}{\rho_{HA}} \left(1.3275\rho^{excel} - 1.3938 \right) \\ f_{org}^{excel} = \frac{1}{\rho_{org}} \left(0.3888\rho^{excel} - 0.2393 \right) \\ f_{H_2O}^{excel} = 1 - f_{HA}^{excel} - f_{org}^{excel} \end{cases} \quad (3.123)$$

$$\text{if } \rho^{excel} \geq 1.978 \text{ g/cm}^3 \begin{cases} f_{HA}^{excel} = \frac{1}{\rho_{HA}} \left(1.7298\rho^{excel} - 2.1895 \right) \\ f_{org}^{excel} = \frac{1}{\rho_{org}} \left(-0.5180\rho^{excel} + 1.5541 \right) \\ f_{H_2O}^{excel} = 1 - f_{HA}^{excel} - f_{org}^{excel} \end{cases} \quad (3.124)$$

whereby $\rho_{org} = 1.42 \text{ g/cm}^3$, $\rho_{HA} = 3 \text{ g/cm}^3$ and $\rho_{H_2O} = 1 \text{ g/cm}^3$ are the real mass densities of the constituents (Gong et al. 1964, Lees 1987, Hellmich & Ulm 2005). The collagen is assumed to make up 90% of the organic content

$$f_{col}^{excel} = 0.9 \cdot f_{org}^{excel} . \quad (3.125)$$

The universal composition rule for tissue evolution during mineralization (Morin & Hellmich 2013) allows to transform these constituents volume fractions into phase volume fractions of the extracellular RVE, reading as

$$f_{ef}^{excel} = \frac{f_{ef,0}^{excel}}{\frac{1}{1 + \left(\frac{\rho_{HA}}{\rho_{H_2O}} - 1 \right) \cdot f_{HA}^{excel}}} + \frac{f_{ef,0}^{excel}}{1 - f_{col,0}^{excel}} \cdot \left(1 - \frac{\rho_{HA}}{\rho_{H_2O}} \right) \cdot f_{HA}^{excel} \quad (3.126)$$

$$f_{fib}^{excel} = 1 - f_{ef}^{excel} \quad (3.127)$$

with subscript 0 marking the beginning of the mineralization process and

$$f_{ef,0}^{excel} = 1 - \frac{1}{0.88} \left(\frac{d_{max}}{d_{dry}} \right)^2 \frac{f_{col}^{excel}}{\frac{\rho_{HA} \cdot f_{HA}^{excel}}{\rho_{H_2O}} + f_{H_2O}^{excel} + f_{col}^{excel}} \quad (3.128)$$

$$f_{col,0}^{excel} = \frac{f_{col}^{excel}}{\frac{\rho_{HA} \cdot f_{HA}^{excel}}{\rho_{H_2O}} + f_{H_2O}^{excel} + f_{col}^{excel}} \quad (3.129)$$

d_{dry} represents the lateral diffraction spacing in dry tissues and d_{max} the maximum value of diffraction spacing.

A.6 Experimental stiffness data from literature

Tab. 3.5: *Experimental characterization of various cortical bone samples by Lees et al. (1979)^a, Lees et al. (1983)^b, and Lees et al. (1996)^c; Macroscopic and extracellular bone mass densities ρ^μ and ρ^{excel} , and experimental and predicted normal stiffness values at the extracellular scale in radial direction, C_{1111}^{exp} and C_{1111}^{pred} with their relative error $E = (C^{\text{exp}} - C^{\text{pred}})/C^{\text{exp}}$*

Tissue	ρ^μ (g/cm ³)	ρ^{excel} (g/cm ³)	C_{1111}^{exp} (GPa)	C_{1111}^{pred} (GPa)	E (%)
Bovine tibia ^a	2.02	2.07	20.97	21.35	1.83
Bovine tibia ^a	1.99	2.04	20.65	20.06	-2.87
Bovine tibia ^a	1.95	2.00	20.22	18.45	-8.76
Bovine tibia ^a	2.01	2.06	20.60	20.91	1.51
Bovine tibia ^a	2.04	2.09	22.40	22.27	-0.59
Bovine tibia ^a	2.05	2.11	22.37	22.74	1.63
Bovine tibia ^b	2.07	2.13	23.44	23.71	1.18
Dugong rib ^b	2.02	2.07	18.66	21.35	14.42
Elephant radius ^b	1.94	1.99	18.51	18.07	-2.35
Human femur ^b	1.93	1.98	19.39	17.70	-8.71
Deer antler ^b	1.78	1.82	10.32	13.62	32.03
Deer antler ^b	1.74	1.78	10.25	12.57	22.69
Whale malleus ^c	2.49	2.49	58.57	51.19	-12.60
Whale malleus ^c	2.53	2.53	60.50	55.92	-7.57
Whale malleus ^c	2.51	2.51	51.96	53.50	2.96
Whale malleus ^c	2.45	2.45	52.07	46.87	-9.98
Whale incus ^c	2.50	2.50	57.36	52.34	-8.76
Whale incus ^c	2.46	2.46	54.34	47.92	-11.82
Whale periotic ^c	2.40	2.40	41.33	42.01	1.63
Whale periotic ^c	2.48	2.48	52.48	50.08	-4.57
Whale periotic ^c	2.50	2.50	51.30	52.34	2.01
Whale periotic ^c	2.52	2.52	54.49	54.70	0.38
Whale periotic ^c	2.58	2.58	60.44	62.41	3.26
Whale typamic bulla ^c	2.54	2.54	53.75	57.16	6.35
Whale typamic bulla ^c	2.50	2.50	51.30	52.34	2.01
Whale typamic bulla ^c	2.53	2.53	51.92	55.92	7.70
Whale typamic bulla ^c	2.54	2.54	52.35	57.16	9.18
Whale typamic bulla ^c	2.49	2.49	49.98	51.19	2.44

Tab. 3.6: *Experimental characterization of various cortical bone samples by Lees et al. (1979)^a and Lees et al. (1983)^b; Macroscopic and extracellular bone mass densities ρ^μ and ρ^{excel} , and experimental and predicted normal stiffness values at the extracellular scale in axial direction, C_{3333}^{exp} and C_{3333}^{pred} with their relative error $E = (C^{\text{exp}} - C^{\text{pred}})/C^{\text{exp}}$*

Tissue	ρ^μ (g/cm ³)	ρ^{excel} (g/cm ³)	C_{3333}^{exp} (GPa)	C_{3333}^{pred} (GPa)	E %
Bovine tibia ^a	2.06	2.12	32.51	35.64	9.61
Bovine tibia ^a	2.05	2.11	32.35	34.77	7.47
Bovine tibia ^a	2.02	2.07	30.10	32.23	7.07
Bovine tibia ^a	2.02	2.07	30.90	32.23	4.32
Bovine tibia ^a	2.00	2.05	31.22	30.60	-1.99
Bovine tibia ^a	2.05	2.11	31.69	34.77	9.70
Bovine tibia ^a	2.10	2.16	32.49	39.21	20.71
Bovine tibia ^a	2.08	2.14	32.84	37.40	13.91
Bovine tibia ^b	2.06	2.12	36.97	35.64	-3.60
Elephant radius ^b	1.93	1.98	29.95	25.27	-15.62
Human femur ^b	1.96	2.01	28.42	27.48	-3.34
Deer antler ^b	1.74	1.78	16.88	14.18	-15.97
Deer antler ^b	1.73	1.77	17.55	13.78	-21.44

Tab. 3.7: *Experimental characterization of equine cortical bone samples by McCarthy et al. (1990); Macroscopic and extravascular bone mass densities ρ^μ and ρ^{exas} , experimental and predicted normal stiffness values at the extravascular scale in radial and axial direction, C_{1111}^{exp} , C_{1111}^{pred} and C_{3333}^{exp} , C_{3333}^{pred} with their relative error $E = (C^{exp} - C^{pred})/C^{exp}$*

ρ^μ (g/cm ³)	ρ^{exas} (g/cm ³)	C_{1111}^{exp} (GPa)	C_{3333}^{exp} (GPa)	C_{1111}^{pred} (GPa)	C_{3333}^{pred} (GPa)	E_{1111} %	E_{3333} %
2.03	2.14	27.8	39.7	24.9	38.5	-10.4	-2.9
2.02	2.11	26.6	37.2	23.2	35.5	-12.9	-4.5
2.01	2.13	25.4	35.9	24.4	37.7	-3.9	5.0
2.01	2.09	27.8	40.4	22.1	33.7	-20.4	-16.6
2.00	2.10	26.5	37.0	22.7	34.7	-14.2	-6.3
2.00	2.08	24.0	36.6	21.6	32.8	-9.8	-10.4
2.00	2.06	26.5	38.2	21.1	31.9	-20.1	-16.4
1.98	2.11	24.7	35.5	23.4	35.9	-5.4	1.1
1.98	2.11	23.7	36.4	23.4	35.9	-1.4	-1.3
1.98	2.09	25.6	36.0	22.2	33.9	-13.1	-5.8
1.98	2.09	27.1	38.6	22.2	33.9	-17.8	-12.2
1.97	2.08	25.5	33.7	21.8	33.0	-14.5	-2.2
1.97	2.10	23.6	37.1	22.9	35.0	-3.1	-5.7
1.96	2.08	25.5	33.8	21.8	33.1	-14.4	-2.0
1.96	2.07	26.8	36.5	21.3	32.1	-20.6	-11.9
1.95	2.10	26.1	32.8	23.0	35.2	-11.9	7.1
1.95	2.04	23.6	33.2	20.3	30.4	-14.0	-8.5
1.95	2.08	23.3	35.0	21.8	33.1	-6.5	-5.2
1.95	2.16	25.2	36.3	25.6	39.7	1.6	9.5
1.95	2.07	24.6	35.6	21.3	32.2	-13.4	-9.6
1.95	2.10	26.5	36.2	23.0	35.2	-13.4	-3.0
1.93	2.06	23.1	33.4	20.9	31.4	-9.7	-6.1
1.93	2.02	22.0	34.0	19.4	28.7	-11.7	-15.5
1.93	2.07	25.1	37.4	21.4	32.3	-14.7	-13.5
1.92	2.05	23.0	32.7	20.4	30.5	-11.2	-6.8
1.92	2.02	23.4	32.8	19.4	28.8	-16.8	-12.5
1.92	2.05	23.0	36.1	20.4	30.5	-11.2	-15.5
1.92	2.03	23.5	35.9	19.9	29.6	-15.3	-17.5
1.91	2.03	22.8	34.7	19.9	29.6	-12.7	-14.6
1.91	2.17	26.2	37.7	26.1	40.4	-0.6	7.4
1.91	2.11	25.1	39.9	23.2	35.6	-7.6	-10.8
1.9	2.20	21.6	34.3	28.0	43.4	29.7	26.5
1.9	2.02	23.4	32.4	19.5	28.8	-16.7	-11.0
1.82	1.90	20.7	30.4	15.7	20.5	-24.2	-32.6
1.76	2.09	21.4	30.9	22.1	33.6	3.5	8.8

Chapter 4

Finite Element-based periodic homogenization of cage-like microcaffolds for tissue engineering

Authored by Valentina Kumbolder, Aleksandr Ovsianikov & Christian Hellmich

Prepared for submission

Abstract: Tissue engineering is a rapidly expanding interdisciplinary field of biotechnology, where two main strategies have emerged in the last two decades. However, in recent years, a new strategy has arisen, which is building on a synergy of the two classic scaffold-based and scaffold-free approaches. The so-called third strategy in tissue engineering proposes the fabrication of tissue spheroids, which are capable of tissue fusion, directly within cage-like microcaffolds with appropriate material properties.

The implementation of the new synergetic strategy is envisioned in bone tissue engineering: Using minimally invasive procedures, the scaffold-spheroid conglomerate serves as filling for bone defects and subsequently regenerates the defective tissue. For successful clinical application, the mechanical properties of the conglomerate have to match those of the bone it replaces. In order to facilitate the design process of the scaffolds targeting this challenge, this work investigates the effects of varying scaffold-materials and dimensions on the overall effective stiffness properties of different complex scaffold-packings. We use the unit cell method based on periodic homogenization by means of the Finite Element Method to predict the stiffness of the different periodic scaffold packings with varying individual properties. The resulting correlations between the single scaffold and the overall complex construct allow for a much faster scaffold-design process in order to achieve a final construct with desired properties for the target clinical application.

Contribution: This paper results from a collaboration in the course of the interdisciplinary doctoral program BioInterface. Aleksandr Ovsianikov brought in the research question and the framework of investigation. Christian Hellmich set up the overall research strategy and supervised the research progress. Valentina Kumbolder conducted the derivation of the mathematical framework, developed the detailed geometries, performed extensive computations in Abaqus, documented the results and wrote the manuscript.

Keywords: tissue engineering, microcaffolds, homogenization of discrete structure, unit cell method, periodic homogenization

4.1 Introduction

Three decades ago a first conceptual framework for artificial development of three-dimensional living human tissue has been published (Vacanti & Langer 1999, Lanza et al. 2011). Since then, tissue engineering is a rapidly expanding interdisciplinary field of biotechnology where two main strategies have emerged.

The first strategy - the so-called scaffold-based approach - relies on the use of a biodegradable structure (scaffold) which is seeded with cells and is acting as temporal support for the growing tissue in order to obtain its desired shape while being provided with protection from external loads. However, the use of scaffolds does present some challenges, like a inhomogeneous cell distribution or low initial cell density.

Consequently, a distinct approach emerged, the so-called scaffold-free method, which is a bottom-up strategy using cell sheets, spheroids, or tissue strands as building blocks for an additive layer-by-layer fabrication of 3D constructs. In contrast to the scaffold-based approach, the proliferation and migration of cells are not decisive factors due to the high initial cell density and dramatically reduce the time necessary for tissue formation. However, despite this advantage the lack of desirable material properties leading to possible cell damage is the main problem of this method.

Therefore, in recent years a third strategy has arisen, building on a synergy of the two classic approaches: Tissue spheroids, capable of tissue fusion are fabricated directly within cage-like microscaffolds with appropriate material properties and thereby combine the advantages of the two classic approaches (Ovsianikov et al. 2018). The implementation of this new synergetic strategy is envisioned in bone tissue engineering: Using minimally invasive procedures, the scaffold-spheroid conglomerate serves as filling for bone defects and subsequently regenerates the defective tissue (Rezende et al. 2012). For successful clinical application, the mechanical properties of the conglomerate have to match those of the bone it replaces (Gómez et al. 2016). However, producing scaffolds with appropriate mechanical properties is one of the great challenges in bone tissue engineering (O'Brien 2011, O'Keefe & Mao 2011, Liu et al. 2013). In order to facilitate the scaffold-design process, there is a need to predict the overall stiffness of the scaffold-spheroid material in a fast and easy way. We here propose a method based on periodic homogenization of a discrete beam structure in combination with the unit cell method to compute the effective stiffness of the different scaffold packings based on its microstructure and the properties of its constituents.

To this end, the remainder of the present chapter is organized as follows: We first introduce the microscaffolds in Section 4.2 by defining their geometry and different considered packings. In Section 4.3 the discrete microstructures of the unit cells are identified and a meaningful homogenization relation for the transition from locally changing beam quantities to a fictitious homogenized continuum is proposed. Furthermore the prescribed effective strains as well as the boundary conditions are defined and the implementation into the commercial FE software Abaqus is explained. Section 4.4 includes the results of the FE simulations carried out based on different scaffold configurations. The effects of the individual scaffold properties are investigated and interpreted. Finally a dimensional analysis of the simulation input values and results gives access to a power-law function describing the effective behavior of a scaffold-packing in a very fast and easy way. The conclusion and an assessment of clinical relevance of the microscaffolds in bone tissue engineering is given in Section 4.5.

4.2 Microscaffolds

In the original tissue engineering sense, a scaffold is a temporary 3D construct made out of a variety of biomaterials, which acts as template for tissue regeneration. The scaffold is seeded with cells and provides a biomimetic environment and initial support for the cells to attach, proliferate and differentiate. During the last decades, many different materials from natural to synthetic, and biodegradable to permanent have been investigated to find suitable scaffold materials (O'Brien 2011, Drury & Mooney 2003, Hollister 2005). There are three main groups of biomaterials used in the fabrication of scaffolds for tissue engineering: (i) ceramic scaffolds, such as hydroxyapatite and tricalcium phosphate (ii) synthetic polymers such as polystyrene and (iii) natural polymers such as collagen or various proteoglycans. However, since the scaffold is ideally not intended as permanent implant, the biomaterial should have a degradation profile matching to the formation of new tissue, which thereby allows the cells to produce their own extracellular matrix.

In contrast to the conventional seeded scaffolds, the scaffolds proposed in the third strategy of tissue engineering have a cage-like shape produced by means of two-photon polymerization technique (Stampfl et al. 2016). Since the scaffolds are produced by localized polymerization of a material induced by nonlinear absorption of laser light, the used biomaterial has to be photosensitive (e.g. cross-linkable gelatin as proposed by Van Hoorick et al. (2017)). In the further course, these scaffolds are not seeded with cells but tissue spheroids are produced directly within them as described by Silva et al. (2016) (see Figure 4.1). Spheroids are ball-shaped cell aggregates consisting of living cells with maximal initial cell density and have the ability to fuse into larger constructs. The task of the scaffold is to protect the spheroids from mechanical damage without hindering the tissue fusion process. Therefore the scaffold has to be designed in a way to provide high mechanical stiffness while maximizing porosity. Within this work, the microscaffolds are considered to correspond to the edges of a truncated icosahedron (see Figure 4.1 and Appendix B.1) and are assumed to be arranged in different periodic lattice packings.

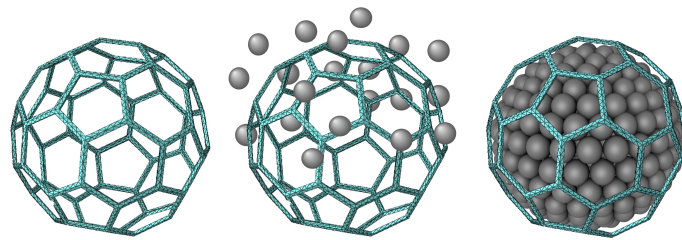


Fig. 4.1: *Truncated icosahedron shaped microscaffold encapsulating a tissue spheroid*

4.2.1 Lattice packing

An arrangement of copies of a convex body B in the d -dimensional Euclidean space is called a “packing” P if there is no overlap between any of the bodies. Furthermore, if all convex bodies are oriented in the same direction and it needs only d vectors \mathbf{w}_i , $i \in (1, d)$, which are connecting the centers of two adjacent convex bodies, for the packing to be uniquely described, the arrangement is referred to as “lattice packing” P_L . Each lattice packing is periodic and is build up by identical basic repetitive units, so-called “unit cells” (UC). Generally, unit cells are non-unique, leading to a wide range of possible shapes for one packing. However, for a lattice packing a unit cell can be found which contains the center of just one body. Within this

work we define the unit cell in three-dimensional space as the parallelepiped being spanned by the lattice vectors \mathbf{w}_i ($i = 1, 2, 3$). The packing density ρ as the fraction of three-dimensional space covered by the bodies, is for a lattice packing given by the volume of one body per volume of the unit cell of the respective packing

$$\rho^{PL} = \frac{V_B}{V_{UC}} = \frac{V_B}{\det(\mathbf{w}_1^{PL}, \mathbf{w}_2^{PL}, \mathbf{w}_3^{PL})}. \quad (4.1)$$

Within this paper, three exemplary lattice packings of truncated icosahedra (trunc) are considered (see Figure 4.2), each of which is described by its lattice vectors \mathbf{w}_i^{PL} ($i = 1, 2, 3$) and its packing density ρ^{PL} (see Table 4.1 and Appendix B.2).

Tab. 4.1: Three lattice packings of truncated icosahedra with edge length ℓ ($\phi = \frac{1+\sqrt{5}}{2}$ is the golden ratio)

	P_L^{xyz} xyz-packing	P_L^{xz} xz-packing	P_L^{opt} densest packing
V_{trunc}	$(125 + 43\sqrt{5})/4 \cdot \ell^3 = 55.288 \cdot \ell^3$		
V_{UC}^{PL}	$(3\ell\phi)^3 = 114.374 \cdot \ell^3$	$(3\ell\phi)^2(\frac{3}{2}\ell\phi + \frac{5\ell\phi}{2(1+\phi)}) = 93.593 \cdot \ell^3$	$70.431 \cdot \ell^3$
ρ^{PL}	0.483395	0.590727	0.784988

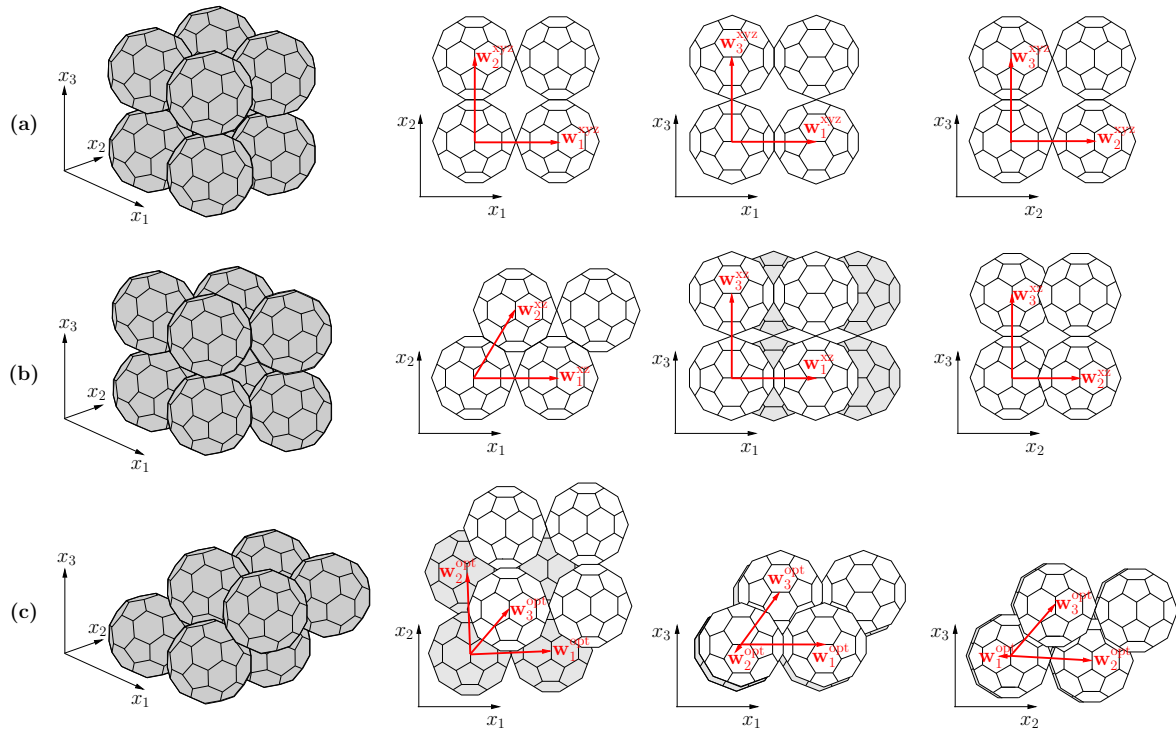


Fig. 4.2: Three different lattice packings of truncated icosahedra: (a) xyz-packing; (b) xz-packing; (c) densest packing

4.3 Homogenization: Unit Cell method

4.3.1 Discrete beam problem

We consider a scaffold-spheroid packing fulfilling the separation of scales: While the microscopic scale is small enough to clearly identify the complex, discrete arrangement of beam elements of the scaffold, the macroscopic scale is large enough to allow - with sufficient accuracy - the replacement of the discrete structure with a fictitious homogeneous material with smeared-out heterogeneities (Michel et al. 1999). The effective properties of such a material can be derived by homogenization of the properties of the individual constituents (phases) and their distribution (microstructure). However, since the spheroids have inferior mechanical properties during their proliferation process (Ovsianikov et al. 2018), the properties of the scaffold-spheroid material are initially determined almost exclusively by the design and the properties of the scaffold and its packing. We therefore disregard the spheroids in the further course of this paper and focus on the prediction of the homogenized, effective properties of different periodic scaffold packings with varying individual scaffold properties. Due to the periodic packing, the microstructure is completely defined by a basic repetitive unit, a so-called “unit cell”, which is consisting of a discrete arrangement of beam elements in empty air space (see Figure 4.3).

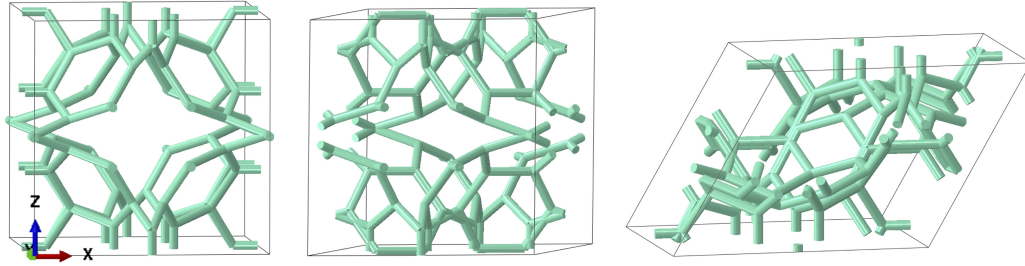


Fig. 4.3: Unit cells of three different lattice packings P_L^{xyz} , P_L^{xz} and P_L^{opt}

4.3.2 Principle of Virtual Power based homogenization

To determine the effective properties of a scaffold packing, it is sufficient to evaluate the effective properties of a single unit cell, a principle referred to as *unit cell method*. To this end a displacement controlled model may be chosen, where the unit cell is subjected to predefined effective strain states \mathbf{E} at the macroscopic scale, which provoke a locally changing response at the microscopic scale of the beam structure. For the transition from the locally changing beam quantities to a fictitious homogenized continuum, a physically meaningful criterion of equivalence is found based on the Principle of Virtual Power, reading as

$$\mathcal{P}_{\text{int}} + \mathcal{P}_{\text{ext}} = 0. \quad (4.2)$$

While the virtual power of the internal forces is defined at the macroscopic scale of the homogeneous continuum with the macroscopic stress $\mathbf{\Sigma}$ and the macroscopic virtual velocity gradient $\hat{\mathbf{D}}$

$$\mathcal{P}_{\text{int}} = - \int_{V_{\text{UC}}} \mathbf{\Sigma} : \hat{\mathbf{D}} \, dV, \quad (4.3)$$

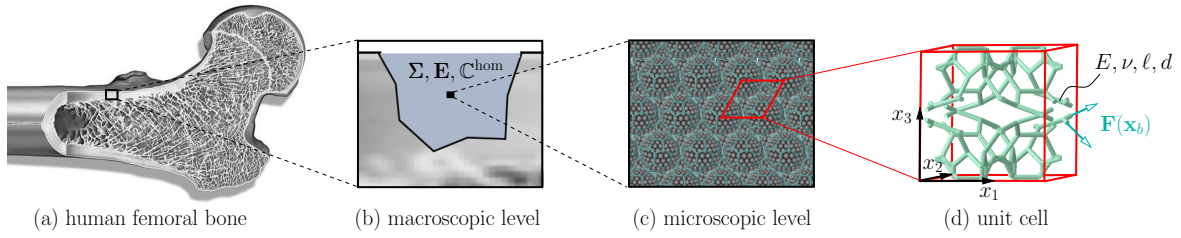


Fig. 4.4: (a) human femoral bone; (b) macroscopic scale: defect in cortical bone filled with quasi-homogeneous scaffold spheroid material; (c) microscopic scale: discrete beam scaffold-structure filled with tissue spheroids; (d) unit cell representing the scaffold packing with forces acting at all beam-ends on the surface of the unit cell

the virtual power of the external forces is defined at the microscopic level as the power produced by the system of microscopic forces $\mathbf{F}(\mathbf{x})$ in virtual motion acting on the cross-sectional ends of all beams b , which are cut by the boundaries of the unit cell in point \mathbf{x}_b , see Figure 4.4

$$\mathcal{P}_{\text{ext}} = \sum_b \hat{\mathbf{v}}(\mathbf{x}_b) \cdot \mathbf{F}(\mathbf{x}_b). \quad (4.4)$$

The microscopic external forces $\mathbf{F}(\mathbf{x}_b)$ are derived based on the so-called beam related stress resultants, the axial force $\mathbf{N}(\mathbf{x}_b)$ and the transverse forces $\mathbf{Q}_{y^*}(\mathbf{x}_b)$ and $\mathbf{Q}_{z^*}(\mathbf{x}_b)$, acting in y^* - and z^* -direction perpendicular to the beam axis. These stress resultants are provoked due to the macroscopic deformation of the unit cell.

$$\mathbf{F}(\mathbf{x}_b) = \mathbf{N}(\mathbf{x}_b) + \mathbf{Q}_{y^*}(\mathbf{x}_b) + \mathbf{Q}_{z^*}(\mathbf{x}_b) \quad (4.5)$$

Finally, homogenization is performed by requiring the microscopic virtual velocity field $\hat{\mathbf{v}}$ to be fully captured through the macroscopic virtual strain rate $\hat{\mathbf{D}}$, which does not depend on the microscopic location vector \mathbf{x}

$$\hat{\mathbf{v}}(\mathbf{x}) = \hat{\mathbf{D}} \cdot \mathbf{x}. \quad (4.6)$$

Combining equations (4.2)-(4.6) gives access to the homogenization relation for the macroscopic, effective stress Σ based on the microscopic forces acting on all cross-sectional ends of the beams on the surface of the unit cell

$$\Sigma = \sum_b \frac{\mathbf{x}_b \otimes \mathbf{F}(\mathbf{x}_b)}{V_{\text{UC}}}. \quad (4.7)$$

Relating the predefined macroscopic strain to the resulting associated macroscopic stress, finally gives access to the homogenized, effective stiffness of the composite \mathbb{C}^{hom}

$$\Sigma = \mathbb{C}^{\text{hom}} : \mathbf{E}, \quad (4.8)$$

reading in Kelvin-Mandel vector-matrix notation (see e.g. eq. (2a) in Cowin (2003)) as

$$\begin{pmatrix} \Sigma_{11} \\ \Sigma_{22} \\ \Sigma_{33} \\ \sqrt{2}\Sigma_{23} \\ \sqrt{2}\Sigma_{13} \\ \sqrt{2}\Sigma_{12} \end{pmatrix} = \begin{pmatrix} C_{1111} & C_{1122} & C_{1133} & \sqrt{2}C_{1123} & \sqrt{2}C_{1113} & \sqrt{2}C_{1112} \\ C_{2211} & C_{2222} & C_{2233} & \sqrt{2}C_{2223} & \sqrt{2}C_{2213} & \sqrt{2}C_{2212} \\ C_{3311} & C_{3322} & C_{3333} & \sqrt{2}C_{3323} & \sqrt{2}C_{3313} & \sqrt{2}C_{3312} \\ \sqrt{2}C_{2311} & \sqrt{2}C_{2322} & \sqrt{2}C_{2333} & 2C_{2323} & 2C_{2313} & 2C_{2312} \\ \sqrt{2}C_{1311} & \sqrt{2}C_{1322} & \sqrt{2}C_{1333} & 2C_{1323} & 2C_{1313} & 2C_{1312} \\ \sqrt{2}C_{1211} & \sqrt{2}C_{1222} & \sqrt{2}C_{1233} & 2C_{1223} & 2C_{1213} & 2C_{1212} \end{pmatrix} \cdot \begin{pmatrix} E_{11} \\ E_{22} \\ E_{33} \\ \sqrt{2}E_{23} \\ \sqrt{2}E_{13} \\ \sqrt{2}E_{12} \end{pmatrix} \quad (4.9)$$

4.3.3 Unit effective strain

The effective strain states \mathbf{E} which are applied to the unit cell to determine the effective stiffness, are chosen such that only one of the six independent components of the macroscopic strain tensor is not equal to zero. This approach leads to six independent unit strain states \mathbf{E}^{kl} ($k, l \in \{1, 2, 3\}$) with components

$$E_{ij}^{kl} = \frac{1}{2}(\delta_{ik}\delta_{jl} + \delta_{il}\delta_{jk}) = \begin{cases} i = k, j = l, k \neq l & 1/2 \\ i = l, j = k, k \neq l & 1/2 \\ i = k, j = l, k = l & 1 \\ else & 0 \end{cases} \quad i, j, k, l \in \{1, 2, 3\} \quad (4.10)$$

Applying the unit strain states according to (4.10) to the constitutive relation (4.8), shows that the components of the effective stiffness tensor \mathbb{C}^{hom} are equal to the components of the six macroscopic stress states Σ^{kl} corresponding to the six strain configurations \mathbf{E}^{kl} . Each of the six unit strain states (see Figure 4.5) gives access to one column of the stiffness tensor \mathbb{C}^{hom}

$$\Sigma_{ij}^{kl} = C_{ijmn}^{\text{hom}} E_{mn}^{kl} = C_{ijmn}^{\text{hom}} \frac{1}{2}(\delta_{mk}\delta_{nl} + \delta_{ml}\delta_{nk}) = C_{ijkl}^{\text{hom}}. \quad (4.11)$$

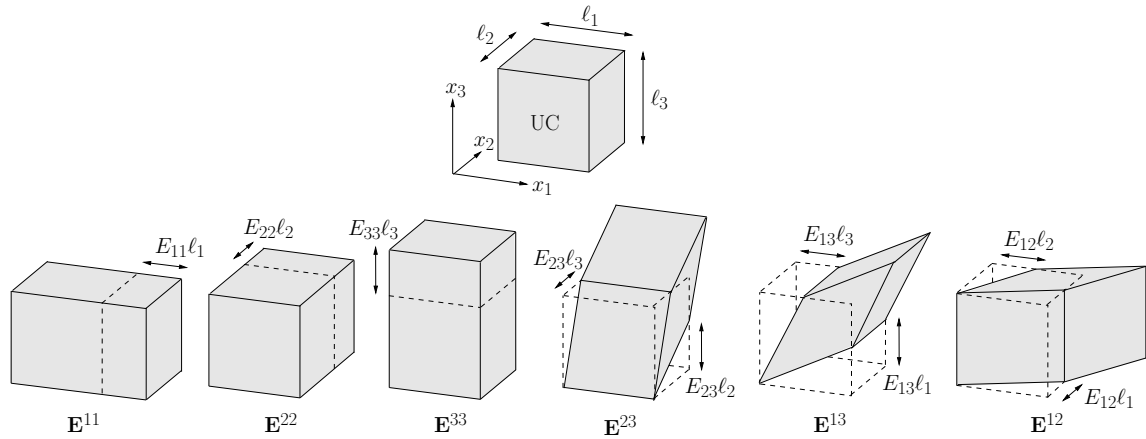


Fig. 4.5: Effective strain states applied to a unit cell: three axial strain configurations (\mathbf{E}^{11} , \mathbf{E}^{22} , \mathbf{E}^{33}) and three shear strain configurations (\mathbf{E}^{12} , \mathbf{E}^{13} , \mathbf{E}^{23})

4.3.4 Periodic boundary conditions

If a periodic material is subjected to a macroscopic, effective strain state \mathbf{E}^{kl} , the resulting microscopic deformation field conforms to the periodicity of the microstructure (Suquet 1985). The boundary conditions which have to be applied to the unit cell of the considered packing to reproduce this state of periodicity and ensure equilibrium as well as a seamless tiling of space with the unit cell in both its undeformed and deformed configuration, read as

$$\left. \begin{aligned} \mathbf{u}(\mathbf{x}) &= \mathbf{E}^{kl} \cdot \mathbf{x} + \mathbf{u}^*(\mathbf{x}) \\ \mathbf{u}^*(\mathbf{x}^{i+}) &= \mathbf{u}^*(\mathbf{x}^{i-}) \\ \mathbf{F}(\mathbf{x}^{i+}) &= -\mathbf{F}(\mathbf{x}^{i-}) \end{aligned} \right\} \forall \mathbf{x} \in S_{UC} \quad (4.12)$$

The displacement field $\mathbf{u}(\mathbf{x})$ is thereby split into the overall (average) displacement field $\mathbf{E}^{kl} \cdot \mathbf{x}$ and an additional (fluctuation) field $\mathbf{u}^*(\mathbf{x})$, which accounts for the heterogeneities within the material and can be proved to be periodic up to a rigid body motion (Michel et al. 1999). To ensure periodicity, the boundary of the unit cell S_{UC} is divided into two parts, a positive part S_{UC}^{i+} and a negative part S_{UC}^{i-} with corresponding nodes $\mathbf{x}^{i+} \in S_{UC}^{i+}$ and $\mathbf{x}^{i-} \in S_{UC}^{i-}$. These two points reside on opposite surfaces of the unit cell and are hence connected by the lattice vector \mathbf{w}_i^{PL} of the considered packing (see Figure 4.6)

$$\mathbf{x}^{i+} - \mathbf{x}^{i-} = \mathbf{w}_i^{PL} \quad i \in \{1, 2, 3\} \quad (4.13)$$

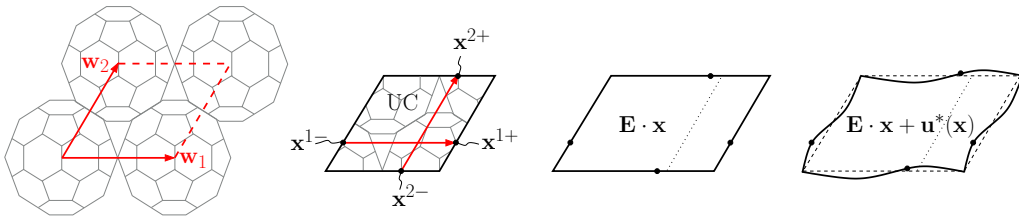


Fig. 4.6: Periodic displacement boundary conditions

Periodicity implies identical values for the displacement fluctuation field $\mathbf{u}^*(\mathbf{x}^{i+})$ and anti-periodic forces $\mathbf{F}(\mathbf{x}^{i+})$ acting at the cross-sectional ends of the beams in two periodically corresponding points \mathbf{x}^{i+} and \mathbf{x}^{i-} of the microstructure.

4.3.4.1 Implementing the boundary conditions in Abaqus

An effective way to implement the periodic boundary conditions in a FE analysis is the introduction of additional arbitrarily chosen master nodes M_i , $i \in \{1, 2, 3\}$ (one for each surface pair) that are not attached to the unit cell. As described by Kästner et al. (2011), these master nodes are used to control the relative displacement of two opposite surfaces and are connected to the unit cell by enforcing constraint equations

$$\mathbf{u}(\mathbf{x}^{i+}) - \mathbf{u}(\mathbf{x}^{i-}) = \mathbf{E}^{kl} \cdot (\mathbf{x}^{i+} - \mathbf{x}^{i-}) = \mathbf{E}^{kl} \cdot \mathbf{w}_i^{PL} = \mathbf{u}(M_i) \quad (4.14)$$

for each degree of freedom (translational and rotational) of each node representing a beam-end at each surface, see Figure 4.7.

In the commercial FE software Abaqus, these constraint conditions may be written in terms

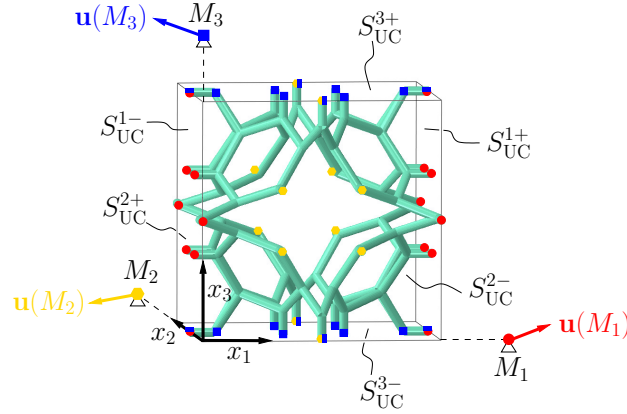


Fig. 4.7: Master nodes for implementation of periodic boundary conditions

of so-called linear equations. The displacement that has to be described to the master node M_i is defined by the effective strain state \mathbf{E}^{kl} and the rotational degrees of freedom at the master nodes are set to zero to avoid relative rotation of the opposite surfaces and thereby ensure geometric compatibility. The linear constraints generate constraint forces acting at all degrees of freedom involved in the equations. Due to the kinematic coupling, the reaction force \mathbf{F}_{M_i} generated at the master node M_i is in equilibrium with the constraint forces acting at the cross-sectional ends of the beams b on the associated surface S_{UC}^{i+}

$$\mathbf{F}_{M_i} = \sum_b \mathbf{F}(\mathbf{x}_b^{i+}) = - \sum_b \mathbf{F}(\mathbf{x}_b^{i-}) \quad (4.15)$$

Expanding equation (4.7) for the six surfaces of the unit cell while considering equation (4.13) and (4.15), delivers a relation between the macroscopic stress and the reaction forces acting on the master nodes as ¹

$$\boldsymbol{\Sigma}^{kl} = \sum_{i=1}^3 \frac{\mathbf{w}_i^{P_L} \otimes \mathbf{F}_{M_i}^{kl}}{V_{UC}} \quad (4.16)$$

Considering equation (4.11) finally relates the reaction forces to the components of the effective stiffness tensor of the scaffold packing as

$$C_{ijkl}^{P_L} = \Sigma_{ij}^{kl} = \sum_{r=1}^3 \frac{w_{r,i}^{P_L} F_{M_r,j}^{kl}}{V_{UC}}. \quad (4.17)$$

¹see Appendix B.3 for a detailed derivation

4.4 Results

The effective elastic properties of the different scaffold packings were obtained by investigating the unit cell models in the commercial FE software Abaqus 2018. To that end, the discrete beam arrangements of the three different unit cells were modeled as wire structures, to which linear Timoshenko beam elements (B31), a circular cross section and linear elastic material behavior were assigned. After the constraint equations were defined for all nodes on the boundary of the unit cell according to equation (4.14), the six effective strain states \mathbf{E}^{kl} according to equation (4.10) were successively applied by adjusting the boundary conditions of the three master nodes. Finally, the resulting effective stiffness tensor was determined for varying individual scaffold properties using equation (4.17).

4.4.1 Densest packing: Effects of varying scaffold properties

The properties governing the scaffold design are the edge length ℓ of the truncated icosehdon and the diameter d of the circular beam cross section. The size of the microscaffold is governed by the diameter of the encaged spheroid, typically ranging between 100 and 300 μm (Ovsianikov et al. 2018, Mehesz et al. 2011). Assuming the spheroid to have the size of the inscribed sphere, the edge length ℓ of the truncated icosahedron ranges consequently between 22 and 66 μm . The diameter d of the circular beam cross section is restricted on the one hand by means of porosity and on the other hand by means of stability, resulting in a meaningful range for the slenderness ratio of the beam elements of $d/\ell = 1/10 - 1/2$. The material properties of the scaffold are assumed to be in the order of magnitude of the properties of a cross-linkable gelatin (Van Hoorick et al. 2017) that could be suitable for the fabrication of microscaffolds ($\nu = 0.5$, $E = 441$ kPa).

These properties were varied within their respective ranges to produce 33 different configurations of the densest packing (see Table 4.2), which were used as input for finite element simulations. The effects of a variation of the individual scaffold properties on the effective stiffness of the densest scaffold packing are shown in Figure 4.8. The detailed results can be found in in Appendix B.4 in Table 4.5-4.7 .

Tab. 4.2: *Varying scaffold configurations used as input for finite element simulations of the densest packing*

	E [kPa]	ν [-]	ℓ [μm]	d [μm]		E [kPa]	ν [-]	ℓ [μm]	d [μm]		E [kPa]	ν [-]	ℓ [μm]	d [μm]
1	441	0.5	22	2	12	441	0.15	22	6	23	441	0.5	26	6
2	441	0.5	22	3	13	441	0.2	22	6	24	441	0.5	30	6
3	441	0.5	22	4	14	441	0.25	22	6	25	441	0.5	33	6
4	441	0.5	22	5	15	441	0.3	22	6	26	441	0.5	38	6
5	441	0.5	22	6	16	441	0.35	22	6	27	441	0.5	44	6
6	441	0.5	22	7	17	441	0.4	22	6	28	441	0.5	55	6
7	441	0.5	22	8	18	441	0.45	22	6	29	441	0.5	66	6
8	441	0.5	22	9	19	100	0.5	22	6	30	441	0.5	33	9
9	441	0.5	22	10	20	600	0.5	22	6	31	441	0.5	44	12
10	441	0.5	22	11	21	1000	0.5	22	6	32	441	0.5	55	14
11	441	0.1	22	6	22	441	0.5	24	6	33	441	0.5	66	18

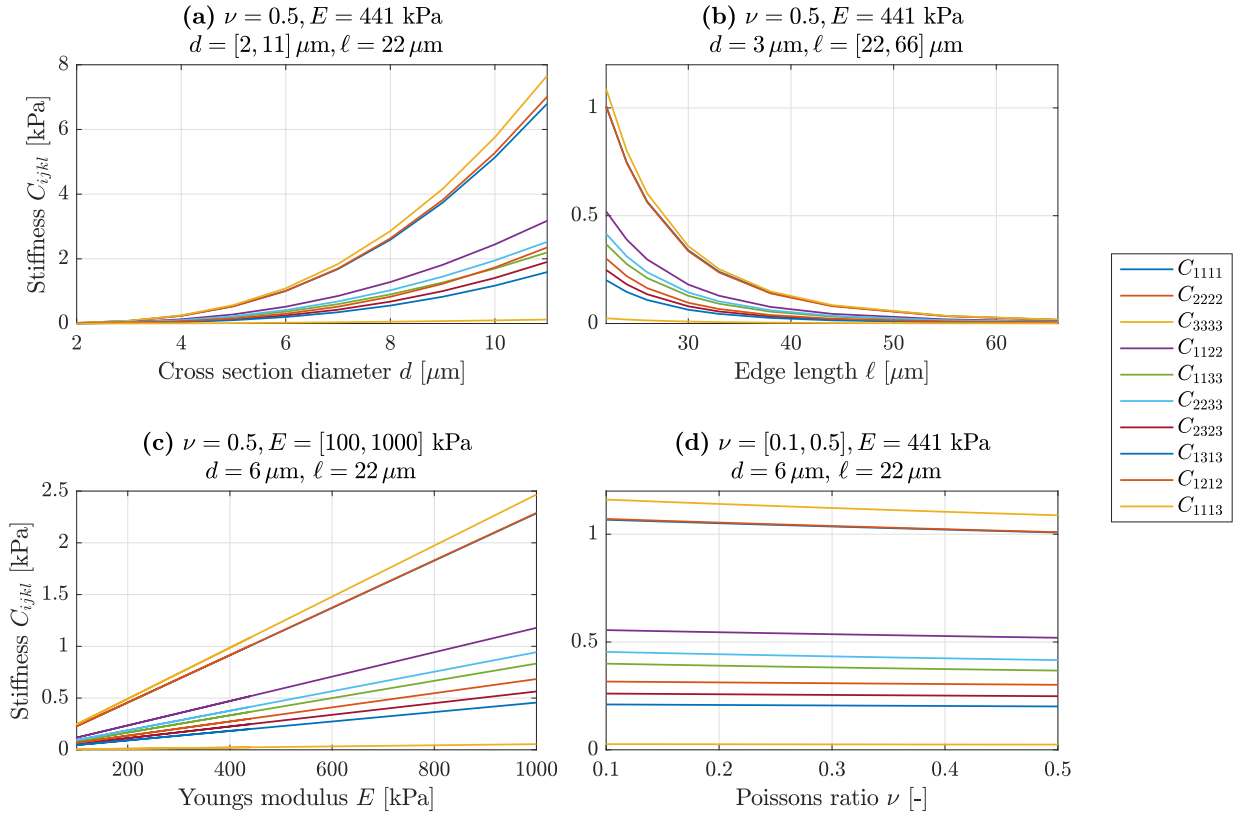


Fig. 4.8: Effects of varying scaffold properties on the effective stiffness components of the densest scaffold packing: (a) varying cross section diameter; (b) varying edge length; (c) varying Young's modulus; (d) varying Poisson's ratio

Figure 4.8 shows, that while the homogenized stiffness scales linear with the material properties E and ν , variations in the cross section diameter d or the edge length ℓ cause higher-order changes. In detail, both the increase of the homogenized stiffness due to an increase of d and the decrease of the same due to an increase of ℓ occurs in a cubic extent and hence causes a constant stiffness for a constant d/ℓ -ratio.

4.4.2 Effects of varying packing configurations

Scaffolds with the same individual properties can be arranged in different lattice packings, differing in terms of their packing density. We consider three exemplary lattice packings which are also varying in terms of symmetries in their microstructure. While the densest packing does not exhibit any symmetries, the xyz- and the xz-packing have some symmetry planes in their microstructure, resulting in different effective material behaviors: (i) The symmetric microstructure of the xyz-packing is reflected by a cubic symmetry of the stiffness tensor \mathbb{C}^{xyz} , thus described by three independent elastic constants E^{xyz} , ν^{xyz} and G^{xyz} (ii) The xz-packing exhibits orthotropic material behavior and the stiffness tensor \mathbb{C}^{xz} is therefore defined by nine non-vanishing independent components if it is represented in a base orthogonal to the aforementioned symmetry planes (iii) The densest packing exhibits anisotropic material behavior being described by a stiffness tensor \mathbb{C}^{opt} with 21 independent components. Figure 4.9 and Table 4.3 show the change of the homogenized stiffness components when the packing of scaffolds with equal properties is varied. The individual components always depend on the

actual geometry of the packing in the corresponding direction, but in general, it can be stated that, the higher the packing density, the higher the homogenized stiffness. Only the stiffness component C_{1313}^{PL} reaches its maximum value in the xz-packing.

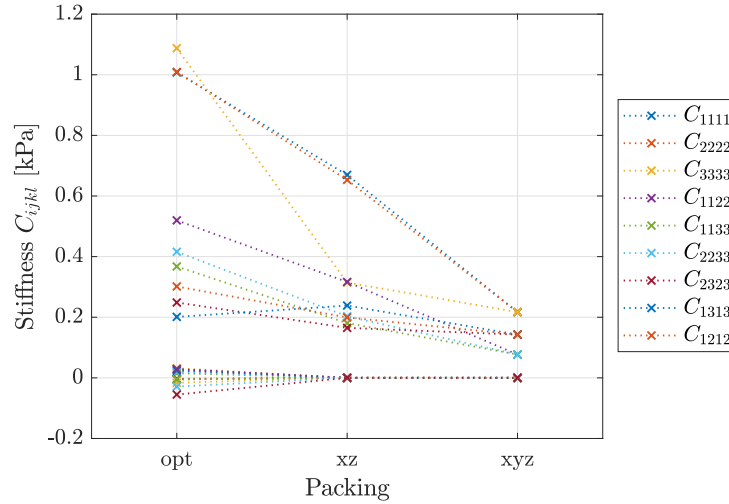


Fig. 4.9: Effective stiffness components of varying scaffold packings with equal individual scaffold properties ($E = 441 \text{ kPa}$, $d/\ell = 6/22$, $\nu = 0.5$)

Tab. 4.3: Effective stiffness components of varying scaffold packings with equal individual scaffold properties ($E = 441 \text{ kPa}$, $d/\ell = 6/22$, $\nu = 0.5$)

	C_{1111}^{PL} [kPa]	C_{1122}^{PL} [kPa]	C_{1133}^{PL} [kPa]	C_{1123}^{PL} [kPa]	C_{1113}^{PL} [kPa]	C_{1112}^{PL} [kPa]	C_{2222}^{PL} [kPa]	C_{2233}^{PL} [kPa]	C_{2223}^{PL} [kPa]	C_{2213}^{PL} [kPa]	C_{2212}^{PL} [kPa]
xyz	1.008	0.520	0.367	-0.055	0.024	0.029	1.009	0.416	-0.029	0.032	0.028
xz	0.669	0.316	0.181	0	0	0	0.653	0.203	0	0	0
opt	0.217	0.077	0.077	0	0	0	0.217	0.077	0	0	0
	C_{3333}^{PL} [kPa]	C_{3323}^{PL} [kPa]	C_{3313}^{PL} [kPa]	C_{3312}^{PL} [kPa]	C_{2323}^{PL} [kPa]	C_{2313}^{PL} [kPa]	C_{2312}^{PL} [kPa]	C_{1313}^{PL} [kPa]	C_{1312}^{PL} [kPa]	C_{1212}^{PL} [kPa]	
xyz	1.088	0.015	0.020	-0.003	0.249	-0.005	-0.016	0.201	-0.005	0.302	
xz	0.314	0	0	0	0.165	0	0	0.239	0	0.199	
opt	0.217	0	0	0	0.143	0	0	0.143	0	0.143	

4.4.3 Dimensional analysis

In order to simplify and speed up the prediction process for the effective material behavior, we want to derive equations describing the effective stiffness as a function of the scaffold properties. To this end, the homogenized stiffness tensor \mathbb{C}^{P_L} of the scaffold packing P_L , and hence its components $C_{ijkl}^{P_L}$, are assumed to be governed by the elastic Young's modulus E and the Poisson's ratio ν of the scaffold-material, as well as by the edge length ℓ and the beam cross section diameter d of the scaffold-design

$$C_{ijkl}^{P_L} = f(E, \nu, \ell, d). \quad (4.18)$$

Based on dimensional analysis and the Buckingham-Pi theorem (Barenblatt 1996) the relationship (4.18) can be written in dimensionless form as

$$\pi_C = \frac{C_{ijkl}^{P_L}}{E} = \mathcal{F}\left(\pi_1 = \nu, \pi_2 = \frac{d}{\ell}\right), \quad (4.19)$$

whereby the number of arguments in the function is reduced from four to two. The dimensionless function \mathcal{F} is assumed to have a power-law form reading as

$$\frac{C_{ijkl}^{P_L}}{E} = \phi_1 \cdot \nu^{\phi_2} \cdot \left(\frac{d}{\ell}\right)^{\phi_3} \quad (4.20)$$

where the coefficient ϕ_1 and the exponents ϕ_2 and ϕ_3 are used to fit the function to the 21 independent stiffness components. To this end, the 33 finite element simulations of the densest packing with varying scaffold configurations (see Table 4.2) were used. By randomly combining the data obtained in three out of 33 different simulations, $\binom{33}{3} = 5456$ solutions for the three fitting parameters ϕ_1 , ϕ_2 and ϕ_3 were determined. Table 4.4 lists the fitting parameters which provide the least fitting error $F = \|(C_{ijkl}^{\mathcal{F}} - C_{ijkl}^{\text{FEA}})\| / \max\|C_{ijkl}^{\text{FEA}}\|$ for all the 33 varying scaffold configurations. Figure 4.10 and 4.11 shows the thereby achieved perfect agreement between the FEA-results and the power-law prediction and underlines the accuracy of the power-law function.

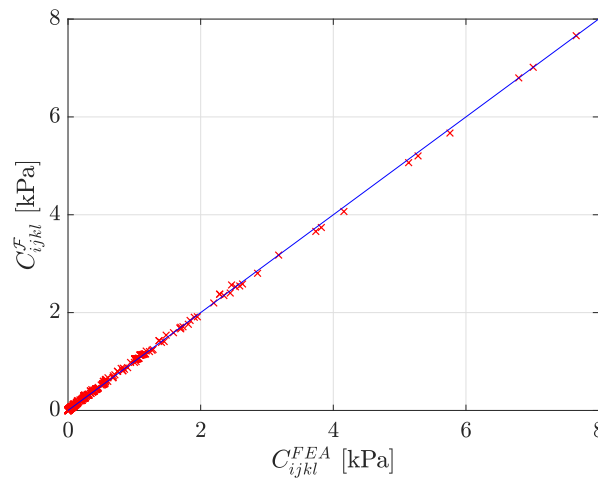


Fig. 4.10: Comparison of all 21 independent FE-based and power-law-predicted stiffness components for the 33 varying scaffold configurations of the densest packing

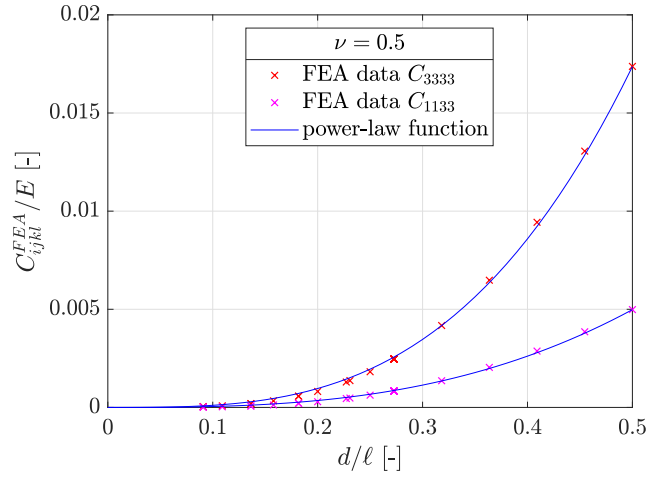


Fig. 4.11: FE-based results of the radial and axial stiffness of the densest packing (C_{1111}^{opt} and C_{1133}^{opt}) based on a constant Poisson's ratio $\nu = 0.5$ and varying E, ℓ and d in dimensionless form fitted with power-law functions

Tab. 4.4: Power-law function fitting parameters ϕ_1, ϕ_2 and ϕ_3 for the 21 independent components of the homogenized stiffness tensor of the densest scaffold packing

	ϕ_1 [-]	ϕ_2 [-]	ϕ_3 [-]
C_{1111}^{opt}	0.1298	-0.0117	3.0857
C_{1122}^{opt}	0.0543	-0.0227	2.9374
C_{1133}^{opt}	0.0362	-0.0294	2.8908
C_{1123}^{opt}	-0.0033	-0.0226	2.5066
C_{1113}^{opt}	0.0016	-0.0298	2.5979
C_{1112}^{opt}	0.0007	-0.0303	1.8089
C_{2222}^{opt}	0.1387	-0.0106	3.1349
C_{2233}^{opt}	0.0422	-0.0308	2.9116
C_{2223}^{opt}	-0.0010	-0.0216	2.1138
C_{2213}^{opt}	0.0017	-0.0285	2.4223
C_{2212}^{opt}	0.0012	-0.0230	2.2458
C_{3333}^{opt}	0.1534	-0.0157	3.1556
C_{3323}^{opt}	0.0038	-0.0289	3.5553
C_{3313}^{opt}	0.0008	-0.0315	2.2335
C_{3312}^{opt}	-0.0010	-0.0095	3.6471
C_{2323}^{opt}	0.0424	-0.0058	3.3007
C_{2313}^{opt}	-0.0005	-0.0295	2.9783
C_{2312}^{opt}	-0.0016	-0.0066	2.8557
C_{1313}^{opt}	0.0371	0.0080	3.3562
C_{1312}^{opt}	-0.0006	-0.0627	3.0883
C_{1212}^{opt}	0.0533	-0.0093	3.3318

4.5 Conclusion and perspectives

By employing the most fundamental element of continuum mechanics, the Principle of Virtual Power, a homogenization relation for the transition of a complex, discrete beam structure to a homogeneous continuum has been derived. To determine the local response of the discrete structure, finite element simulations using the commercial FE software Abaqus were carried out. The postprocessing comprises the application of the proposed homogenization relation to the FE results in order to compute the effective material behavior of different scaffold packings. Further investigation shows, that the results for the effective stiffness gained by FE simulations followed by periodic homogenization can be predicted with almost perfect agreement by a power-law function derived through dimensional analysis. The resulting correlations between the single scaffold and the overall scaffold packing construct, allow for a fast and easy way to predict the effective properties of the final scaffold packing.

However, regarding the aim to achieve a construct with properties desired for the clinical application in bone tissue engineering, it has to be stated that the porous scaffold structure, consisting of slender beam elements, leads to effective properties which are significantly lower than those of the scaffold-material itself. Furthermore, since the properties of the gelatin material used for the fabrication are per se inferior to those of cortical bone, the scaffold-structure leads to an even bigger deviation from the desired bone properties. In detail, while bone stiffness in axial direction is around 25 GPa in human cortical bone (see Figure 3.4), the maximum effective stiffness achieved with the densest scaffold packing is around 8 kPa and thus not even close to the target value. As a result, the clinical relevance of microscaffolds in bone tissue engineering, is currently certainly limited due the lack of appropriate mechanical properties of the available scaffold materials.

B Appendix

B.1 Truncated icosahedron

A truncated icosahedron (trunc) is constructed by cutting off the 12 vertices of a regular icosahedron. Instead of this 12 truncated vertices there are now 12 regular pentagons and the 20 triangles of the icosahedron become regular hexagons. The truncated icosahedron is thus composed of a total of 32 faces and has 60 vertices and 90 edges, all having the same length ℓ . The volume V and the area A of the truncated icosahedron are given by

$$V_{\text{trunc}} = \frac{125 + 43\sqrt{5}}{4} \ell^3 \quad \text{and} \quad A_{\text{trunc}} = \left(20 \cdot \frac{3}{2}\sqrt{3} + 12 \cdot \frac{5}{4}\sqrt{1 + \frac{2}{\sqrt{5}}} \right) \ell^2 \quad (4.21)$$

The Cartesian coordinates of the 60 vertices of a truncated icosahedron with edge length ℓ centered at the origin are given by all even permutations of

$$\begin{aligned} & \left(0, \pm \frac{\ell}{2}, \pm \frac{3\ell}{2}\phi \right) \\ & \left(\pm \frac{\ell}{2}, \pm \frac{\ell}{2}(2 + \phi), \pm \ell\phi \right) \\ & \left(\pm \frac{\ell}{2}\phi, \pm \ell, \pm \frac{\ell}{2}\phi^3 \right) \end{aligned} \quad (4.22)$$

whereby $\phi = \frac{1+\sqrt{5}}{2}$ is the golden ratio. The resulting representation of the truncated icosahedron is standing on an edge, being shared between two hexagonal faces and oriented in x_2 -direction, see Figure 4.12. The height h and width b of the truncated icosahedron are equal to $h = b = 3\ell\phi$.

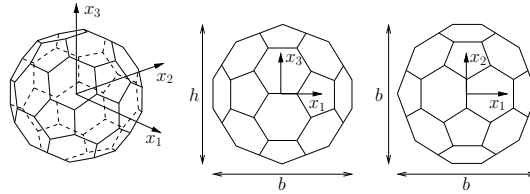


Fig. 4.12: Orientation of the truncated icosahedron in the x, y, z -coordinate system

B.2 Lattice packings

B.2.1 Densest packing

The lattice vectors of the densest packing (opt) of truncated icosahedra with egde length ℓ and orientation according to (4.22) are derived by integer linear combinations of the basis vectors given by Betke & Henk (2000) and Conway & Torquato (2006) and read as

$$\mathbf{w}_1^{\text{opt}} = 3\ell \cdot \begin{pmatrix} \bar{x} \\ \left(-\frac{3}{2} - \frac{1}{2}\sqrt{5}\right)\bar{x} + 2 + \sqrt{5} \\ 0 \end{pmatrix} \quad (4.23)$$

$$\mathbf{w}_2^{\text{opt}} = 3\ell \cdot \begin{pmatrix} \left(\frac{3}{2} + \frac{1}{2}\sqrt{5}\right)\bar{x} - 2 - \sqrt{5} \\ \left(\frac{3}{4} - \frac{81}{20}\sqrt{5}\right)\bar{x}^2 + \left(1 + \frac{31}{5}\sqrt{5}\right)\bar{x} - \frac{1}{4} - \frac{7}{20}\sqrt{5} \\ \left(-9 - \frac{57}{10}\sqrt{5}\right)\bar{x}^2 + \left(17 + \frac{49}{5}\sqrt{5}\right)\bar{x} - \frac{13}{4} - \frac{33}{20}\sqrt{5} \end{pmatrix} \quad (4.24)$$

$$\mathbf{w}_3^{\text{opt}} = 3\ell \cdot \begin{pmatrix} \left(\frac{5}{4} + \frac{1}{4}\sqrt{5}\right)\bar{x} - 1 - \frac{1}{2}\sqrt{5} \\ \left(\frac{39}{8} + \frac{33}{40}\sqrt{5}\right)\bar{x}^2 - \left(\frac{35}{4} + \frac{41}{20}\sqrt{5}\right)\bar{x} + \frac{5}{2} + \frac{23}{20}\sqrt{5} \\ \left(-\frac{39}{8} - \frac{33}{40}\sqrt{5}\right)\bar{x}^2 + \left(\frac{15}{2} + \frac{9}{5}\sqrt{5}\right)\bar{x} - \frac{3}{20}\sqrt{5} \end{pmatrix} \quad (4.25)$$

whereby $\bar{x} \in (1, 2)$ is the unique root of the polynomial $1.086x^3 - (1.603 + 113\sqrt{5})x^2 + (15\sqrt{5} + 43)x + 102 + 44\sqrt{5}$, which is found to be $\bar{x} = 1.59160301$ and therefore

$$\mathbf{w}_1^{\text{opt}} = 3\ell \cdot \begin{pmatrix} 1.59160301 \\ 0.06919719 \\ 0 \end{pmatrix} \quad (4.26)$$

$$\mathbf{w}_2^{\text{opt}} = 3\ell \cdot \begin{pmatrix} -0.06919719 \\ 1.58340967 \\ -0.09064763 \end{pmatrix} \quad (4.27)$$

$$\mathbf{w}_3^{\text{opt}} = 3\ell \cdot \begin{pmatrix} 0.761202911 \\ 0.871627249 \\ 0.985203828 \end{pmatrix} \quad (4.28)$$

B.2.2 Packing along the x_1, x_2, x_3 -axes

The lattice vectors for a packing achieved by arranging the truncated icosahedra with egde length ℓ and orientation according to (4.22) adjacent along the x_1, x_2, x_3 -axes (xyz) are determined by the maximum dimension of the polyhedron in the respective direction and read as

$$\mathbf{w}_1^{\text{xyz}} = \begin{pmatrix} 3\ell\phi \\ 0 \\ 0 \end{pmatrix} \quad (4.29)$$

$$\mathbf{w}_2^{\text{xyz}} = \begin{pmatrix} 0 \\ 3\ell\phi \\ 0 \end{pmatrix} \quad (4.30)$$

$$\mathbf{w}_3^{\text{xyz}} = \begin{pmatrix} 0 \\ 0 \\ 3\ell\phi \end{pmatrix} \quad (4.31)$$

B.2.3 Packing along the x_1 - and x_3 -axis

The third lattice packing is achieved by arranging the truncated icosahedra with egde length ℓ and orientation according to (4.22) adjacent along the x_1 - and x_3 -axis (xz). However, every second row in x_2 -direction is offset by half of the bodies maximum dimension in x_1 -direction, while minimizing the distance in x_2 -direction. The lattice vectors are given by

$$\mathbf{w}_1^{\text{xz}} = \begin{pmatrix} 3\ell\phi \\ 0 \\ 0 \end{pmatrix} \quad (4.32)$$

$$\mathbf{w}_2^{\text{xz}} = \begin{pmatrix} \frac{3}{2}\ell\phi \\ \frac{3}{2}\ell\phi + \frac{5\ell\phi}{2(1+\phi)} \\ 0 \end{pmatrix} \quad (4.33)$$

$$\mathbf{w}_3^{\text{xz}} = \begin{pmatrix} 0 \\ 0 \\ 3\ell\phi \end{pmatrix} \quad (4.34)$$

B.3 Derivations

The detailed derivation of equation (4.17) reads as

$$\begin{aligned} \Sigma^{kl} &= \sum_b \frac{\mathbf{x}_b \otimes \mathbf{F}(\mathbf{x}_b)}{V_{\text{UC}}} = \sum_{i=1}^3 \frac{1}{V_{\text{UC}}} \left(\sum_b \mathbf{x}_b^{i+} \otimes \mathbf{F}(\mathbf{x}_b^{i+}) + \sum_b \mathbf{x}_b^{i-} \otimes \mathbf{F}(\mathbf{x}_b^{i-}) \right) \\ &= \sum_{i=1}^3 \frac{1}{V_{\text{UC}}} \left(\sum_b \mathbf{x}_b^{i+} \otimes \mathbf{F}(\mathbf{x}_b^{i+}) - \sum_b \mathbf{x}_b^{i-} \otimes \mathbf{F}(\mathbf{x}_b^{i+}) \right) \\ &= \sum_{i=1}^3 \frac{1}{V_{\text{UC}}} \left(\sum_b (\mathbf{x}_b^{i+} - \mathbf{x}_b^{i-}) \otimes \mathbf{F}_b^{i+} \right) \\ &= \sum_{i=1}^3 \frac{1}{V_{\text{UC}}} \left(\mathbf{w}_i^{PL} \otimes \sum_b \mathbf{F}_b^{i+} \right) = \sum_{i=1}^3 \frac{\mathbf{w}_i^{PL} \otimes \mathbf{F}_{M_i}}{V_{\text{UC}}} \end{aligned} \quad (4.35)$$

B.4 FE-simulation results

Tab. 4.5: Results of the finite element simulations for the 33 different densest packing configurations - Part 1

	E	ν	ℓ	d	C_{1111}	C_{1122}	C_{1133}	C_{1123}	C_{1113}	C_{1112}	C_{2222}
1	441	0.5	22	1	0.017	0.010	0.007	-0.001	0.001	0.001	0.017
2	441	0.5	22	1.5	0.082	0.045	0.032	-0.005	0.002	0.003	0.080
3	441	0.5	22	2	0.240	0.129	0.092	-0.015	0.006	0.009	0.237
4	441	0.5	22	2.5	0.536	0.282	0.200	-0.031	0.014	0.018	0.533
5	441	0.5	22	3	1.008	0.520	0.367	-0.055	0.024	0.029	1.009
6	441	0.5	22	3.5	1.685	0.852	0.600	-0.086	0.038	0.041	1.701
7	441	0.5	22	4	2.589	1.282	0.899	-0.123	0.055	0.054	2.631
8	441	0.5	22	4.5	3.736	1.814	1.266	-0.165	0.075	0.066	3.820
9	441	0.5	22	5	5.136	2.446	1.700	-0.211	0.097	0.076	5.278
10	441	0.5	22	5.5	6.796	3.176	2.198	-0.261	0.122	0.084	7.014
11	441	0.1	22	3	1.067	0.555	0.400	-0.059	0.026	0.032	1.071
12	441	0.15	22	3	1.059	0.550	0.395	-0.059	0.026	0.031	1.062
13	441	0.2	22	3	1.051	0.545	0.390	-0.058	0.026	0.031	1.054
14	441	0.25	22	3	1.043	0.541	0.386	-0.058	0.026	0.031	1.046
15	441	0.3	22	3	1.036	0.536	0.382	-0.057	0.025	0.030	1.038
16	441	0.35	22	3	1.028	0.532	0.378	-0.057	0.025	0.030	1.031
17	441	0.4	22	3	1.021	0.528	0.374	-0.056	0.025	0.029	1.023
18	441	0.45	22	3	1.014	0.524	0.371	-0.056	0.024	0.029	1.016
19	100	0.5	22	3	0.229	0.118	0.083	-0.013	0.005	0.007	0.229
20	600	0.5	22	3	1.371	0.707	0.500	-0.075	0.033	0.039	1.373
21	1000	0.5	22	3	2.285	1.178	0.833	-0.125	0.055	0.065	2.289
22	441	0.5	24	3	0.748	0.389	0.276	-0.042	0.018	0.023	0.746
23	441	0.5	26	3	0.566	0.297	0.211	-0.033	0.014	0.018	0.562
24	441	0.5	30	3	0.340	0.181	0.128	-0.021	0.009	0.012	0.336
25	441	0.5	33	3	0.240	0.129	0.092	-0.015	0.006	0.009	0.237
26	441	0.5	38	3	0.143	0.077	0.055	-0.009	0.004	0.006	0.140
27	441	0.5	44	3	0.082	0.045	0.032	-0.005	0.002	0.003	0.080
28	441	0.5	55	3	0.035	0.019	0.014	-0.002	0.001	0.002	0.034
29	441	0.5	66	3	0.017	0.009	0.007	-0.001	0.001	0.001	0.017
30	441	0.5	33	4.5	1.007	0.520	0.367	-0.055	0.024	0.029	1.009
31	441	0.5	44	6	1.008	0.520	0.367	-0.055	0.024	0.029	1.009
32	441	0.5	55	7.5	1.008	0.520	0.367	-0.055	0.024	0.029	1.009
33	441	0.5	66	9	1.008	0.520	0.367	-0.055	0.024	0.029	1.009

Tab. 4.6: Results of the finite element simulations for the 33 different densest packing configurations - Part 2

	E	ν	ℓ	d	C_{2233}	C_{2223}	C_{2313}	C_{2212}	C_{3333}	C_{3323}	C_{3313}
1	441	0.5	22	1	0.008	-0.001	0.001	0.001	0.018	0.000	0.000
2	441	0.5	22	1.5	0.036	-0.003	0.003	0.003	0.085	0.001	0.002
3	441	0.5	22	2	0.103	-0.008	0.009	0.008	0.252	0.003	0.006
4	441	0.5	22	2.5	0.225	-0.017	0.018	0.017	0.571	0.007	0.011
5	441	0.5	22	3	0.416	-0.029	0.032	0.028	1.088	0.015	0.020
6	441	0.5	22	3.5	0.682	-0.043	0.049	0.043	1.841	0.028	0.030
7	441	0.5	22	4	1.027	-0.059	0.070	0.059	2.858	0.047	0.042
8	441	0.5	22	4.5	1.450	-0.075	0.093	0.077	4.160	0.072	0.054
9	441	0.5	22	5	1.950	-0.092	0.118	0.096	5.759	0.103	0.067
10	441	0.5	22	5.5	2.525	-0.108	0.143	0.114	7.662	0.141	0.080
11	441	0.1	22	3	0.454	-0.031	0.035	0.030	1.161	0.016	0.022
12	441	0.15	22	3	0.449	-0.031	0.034	0.030	1.150	0.016	0.022
13	441	0.2	22	3	0.443	-0.030	0.034	0.030	1.140	0.015	0.021
14	441	0.25	22	3	0.438	-0.030	0.033	0.030	1.131	0.015	0.021
15	441	0.3	22	3	0.433	-0.030	0.033	0.029	1.122	0.015	0.021
16	441	0.35	22	3	0.429	-0.030	0.033	0.029	1.113	0.015	0.021
17	441	0.4	22	3	0.424	-0.029	0.032	0.029	1.104	0.015	0.020
18	441	0.45	22	3	0.420	-0.029	0.032	0.029	1.096	0.015	0.020
19	100	0.5	22	3	0.094	-0.007	0.007	0.006	0.247	0.003	0.004
20	600	0.5	22	3	0.566	-0.039	0.043	0.038	1.480	0.021	0.027
21	1000	0.5	22	3	0.943	-0.065	0.072	0.064	2.466	0.034	0.045
22	441	0.5	24	3	0.312	-0.023	0.024	0.022	0.802	0.011	0.015
23	441	0.5	26	3	0.237	-0.018	0.019	0.017	0.603	0.008	0.012
24	441	0.5	30	3	0.144	-0.011	0.012	0.011	0.359	0.004	0.008
25	441	0.5	33	3	0.103	-0.008	0.009	0.008	0.252	0.003	0.006
26	441	0.5	38	3	0.061	-0.005	0.005	0.005	0.149	0.001	0.003
27	441	0.5	44	3	0.036	-0.003	0.003	0.003	0.085	0.001	0.002
28	441	0.5	55	3	0.015	-0.001	0.001	0.001	0.036	0.000	0.001
29	441	0.5	66	3	0.008	-0.001	0.001	0.001	0.018	0.000	0.000
30	441	0.5	33	4.5	0.416	-0.029	0.032	0.028	1.088	0.015	0.020
31	441	0.5	44	6	0.416	-0.029	0.032	0.028	1.088	0.015	0.020
32	441	0.5	55	7.5	0.416	-0.029	0.032	0.028	1.088	0.015	0.020
33	441	0.5	66	9	0.416	-0.029	0.032	0.028	1.088	0.015	0.020

Tab. 4.7: Results of the finite element simulations for the 33 different densest packing configurations - Part 3

	E	ν	ℓ	d	C_{3312}	C_{2323}	C_{2313}	C_{2312}	C_{1313}	C_{1312}	C_{1212}
1	441	0.5	22	1	0.000	0.004	0.000	0.000	0.003	0.000	0.005
2	441	0.5	22	1.5	0.000	0.019	0.000	-0.001	0.015	0.000	0.022
3	441	0.5	22	2	0.000	0.056	-0.001	-0.004	0.045	-0.001	0.067
4	441	0.5	22	2.5	-0.001	0.128	-0.003	-0.009	0.103	-0.003	0.155
5	441	0.5	22	3	-0.003	0.249	-0.005	-0.016	0.201	-0.005	0.302
6	441	0.5	22	3.5	-0.007	0.428	-0.008	-0.026	0.349	-0.008	0.521
7	441	0.5	22	4	-0.012	0.677	-0.012	-0.040	0.555	-0.013	0.827
8	441	0.5	22	4.5	-0.019	1.001	-0.017	-0.056	0.827	-0.019	1.228
9	441	0.5	22	5	-0.027	1.409	-0.023	-0.075	1.170	-0.026	1.734
10	441	0.5	22	5.5	-0.036	1.903	-0.030	-0.096	1.590	-0.034	2.350
11	441	0.1	22	3	-0.004	0.261	-0.005	-0.017	0.210	-0.006	0.317
12	441	0.15	22	3	-0.004	0.259	-0.005	-0.017	0.209	-0.006	0.315
13	441	0.2	22	3	-0.004	0.258	-0.005	-0.017	0.208	-0.006	0.313
14	441	0.25	22	3	-0.004	0.256	-0.005	-0.017	0.207	-0.005	0.311
15	441	0.3	22	3	-0.004	0.254	-0.005	-0.017	0.206	-0.005	0.309
16	441	0.35	22	3	-0.004	0.253	-0.005	-0.017	0.204	-0.005	0.307
17	441	0.4	22	3	-0.003	0.251	-0.005	-0.016	0.203	-0.005	0.305
18	441	0.45	22	3	-0.003	0.250	-0.005	-0.016	0.202	-0.005	0.303
19	100	0.5	22	3	-0.001	0.056	-0.001	-0.004	0.046	-0.001	0.068
20	600	0.5	22	3	-0.005	0.338	-0.007	-0.022	0.274	-0.007	0.410
21	1000	0.5	22	3	-0.008	0.564	-0.011	-0.037	0.456	-0.011	0.684
22	441	0.5	24	3	-0.002	0.182	-0.004	-0.012	0.146	-0.004	0.220
23	441	0.5	26	3	-0.001	0.136	-0.003	-0.009	0.109	-0.003	0.164
24	441	0.5	30	3	-0.001	0.080	-0.002	-0.006	0.064	-0.002	0.096
25	441	0.5	33	3	0.000	0.056	-0.001	-0.004	0.045	-0.001	0.067
26	441	0.5	38	3	0.000	0.033	-0.001	-0.002	0.026	-0.001	0.039
27	441	0.5	44	3	0.000	0.019	0.000	-0.001	0.015	0.000	0.022
28	441	0.5	55	3	0.000	0.008	0.000	-0.001	0.006	0.000	0.009
29	441	0.5	66	3	0.000	0.004	0.000	0.000	0.003	0.000	0.005
30	441	0.5	33	4.5	-0.003	0.249	-0.005	-0.016	0.201	-0.005	0.302
31	441	0.5	44	6	-0.003	0.249	-0.005	-0.016	0.201	-0.005	0.301
32	441	0.5	55	7.5	-0.003	0.249	-0.005	-0.016	0.201	-0.005	0.301
33	441	0.5	66	9	-0.003	0.249	-0.005	-0.016	0.201	-0.005	0.301

Chapter 5

Conclusion

The key objective of the present work is to demonstrate and apply the power of homogenization as a tool to determine, explain and predict the mechanical behavior of various complex biomedical materials. This thesis is built upon the philosophy that understanding and modeling the mechanical behavior of (bio)materials at the macroscopic scale requires the knowledge of their basic constituents and mechanisms at the underlying microscales. Accordingly, throughout the whole thesis, the concept of homogenization and localization with particular emphasis on the Principle of Virtual Power is used to link the characteristic features of different length scales which are describing or building up a material. While Chapter 2 and 4 deal with two-scale-transitions, Chapter 3 links multiple successive levels to each other and is thereby generating a so-called multiscale homogenization scheme. To ensure a meaningful homogenization process, a realistic representation of the materials' microstructures in agreement with the separation of scales requirement is necessary. Within the present work, two different methods are used to describe the microstructure of a material:

- On the one hand, the framework of **continuum micromechanics** is employed, which resolves the complex microstructure in an averaged sense into material phases with distinct mechanical and morphological characteristics.
- On the other hand, a **discrete** approximation of the microstructure is taken into account and studied in terms of a **unit cell** for periodic arrangements.

The individual levels which are investigated in this work, have characteristic lengths from the nano- up to the millimeter-scale and cover diverse structures, ranging from polycrystals, over porous networks up to discrete beam arrangements and thus prove the versatile applicability of the homogenization concept.

Furthermore, this thesis provides different theoretical concepts and numerical models and algorithms which allow the computational realization of such homogenization processes - even beyond elasticity. The main objective thereby is the assessment of the elastic behavior in terms of material stiffness and structural stability in terms of material strength.

- The **elastic stiffness** is determined by using a bottom-up approach, in which the effective mechanical properties on the macroscale are predicted based on homogenization of the properties and physical laws defined on the microscale(s). To this end, Chapter 2 and 3 are based on homogenization relations arising from transformation field analysis and Chapter 4 uses a homogenization relation derived for the transition of a discrete beam structure to a homogeneous continuum by employing the most fundamental element of continuum mechanics, the Principle of Virtual Power.

- To determine the **material strength**, two different methods are presented in this work in the framework of computational elastoplasticity:
 - * The first method proposed to assess the structural stability of a material, i.e. plastic collapse related limit loads, is a novel **yield design** approach based on Dvorak's transformation field analysis (Dvorak 1992, Dvorak et al. 1994, Dvorak & Benveniste 1992, Pichler & Hellmich 2010, Morin et al. 2017) and the Principle of Virtual Power. Therein the classical concept of yield design is extended towards microstructures exhibiting non-localized plastic fields, such as plastic porous polycrystals. At the limit state, the elastic portion of the overall strain rate vanishes, so that the concentration-influence relations of transformation field analysis, after setting equal the total and the plastic microscopic strain rates, give direct access to plastic collapse load-related macro-to-micro concentration relations. This new concept allows for reducing the computational cost needed for the determination of plastic collapse loads by a factor of one hundred, when compared to state-of-the-art elastoplastic homogenization approaches.
 - * The second method for assessing the structural stability is a **full elastoplastic analysis** based on an incremental load apposition. The computation of the elastoplastic behavior is therein enabled by a novel adaptation of the well-known return map algorithm (Simo & Hughes 1998). Within this updated method, the micromechanical concentration-influence relations arising from transformation field analysis give access to the plastic behavior. While the used non-associated, multi-surface Mohr-Coulomb plasticity appears as linear in the principal stress state, the corresponding principal stress directions do change during the loading and back-projection steps, which renders the problem as fully non-linear. The back projection of the stress states onto the plastic yield surfaces is therefore realized iteratively by considering a series of stress states and their corresponding flow directions, which are converging towards the actual ones. This series of stress states is developed by a novel sequential one-step linearized backprojection process. Thereby each new member of the stress series is getting closer to the yield surface until the error that arises from assuming a wrong flow direction is negligibly small. This contribution has advanced the state of the art concerning full elastoplastic micromechanics. While it is computationally more expansive compared to the yield design approach, the full elastoplastic analysis provides additional information, such as the heterogeneous distribution of microstress states, or the macroscopic stress-strain relations.

In both approaches, the unknown macroscopic failure processes are traced back to failure criteria that are defined for the individual constituents at the microscopic scale. By linking the different scales to each other, the homogenization approach integrates the microscopic failure criteria into a multiscale model and thereby allows to identify the overall material strength once the load bearing constituents and mechanisms fail.

Besides the novel yield design approach and the new iterative return-mapping algorithm, the main theoretical contributions and innovations in the present thesis are (i) the utilization of the **Principle of Virtual Power** as a key tool to adapt and further develop different homogenization approaches, for the assessment of both strength and stiffness of continuous and discrete microstructures; and (ii) the development of a theoretical framework for continuum micromechanics-based **multiscale elastoplasticity**, which allows to *directly link all*

independent plastic strains arising within a multiscale scheme to each other by means of novel multiscale influence tensors.

The developed theoretical concepts and models arising from the field of civil engineering, are used to assess and predict the mechanical behavior of three fundamentally different biological or biomedical materials, which are, nevertheless, strongly linked to each other: **porous polycrystals, cortical bone and cage-like microcaffolds**. We are able to accurately predict and validate (i) the strength of porous polycrystal-type microstructures on the example of cement lines in osteonal bone; and (ii) sample-specific stiffness and strength values of cortical bone of different species and anatomical locations. Furthermore, the generated models allow for a better mechanobiological understanding, e.g. (i) the proposed bone model and algorithm explain the great variety in the mechanical properties of bone; and (ii) the discovered correlations between the single microcaffolds and the overall scaffold packing construct, enable a very fast and easy way to assess the clinical relevance of the microcaffolds. Beyond these applications in the biological/biomedical field, the developed concepts and algorithms are also applicable or extendable for many other (non-biological) materials and thereby provide an advanced theoretical framework of the concept of homogenization.

Nomenclature

Symbol	Description
\mathbb{A}	fourth order strain concentration tensor
\mathbb{A}_p	fourth order strain concentration tensor associated with the pore phase
\mathbb{A}_r	fourth order strain concentration tensor of phase r
$\mathbb{A}_{s,i}$	fourth order strain concentration tensor associated with the i -th solid phase
\mathbb{A}_r^∞	auxiliary strain concentration tensor of phase r
$\mathbb{A}_{r\pi,i+1}^{\pi,i}$	strain concentration tensor used to downscale the macroscopic strain imposed on RVE i of path π to its phase $r_{\pi,i+1}$, which hosts RVE $i + 1$
\mathbb{A}^{PC}	plastic collapse-related strain rate downscaling tensor
$\mathbb{A}_{s,i}^{\text{PC}}$	plastic collapse-related strain rate downscaling tensor associated with the i -th solid phase
\mathbf{A}	compilation of several $\mathcal{M}_{\mathbb{A}}$ -matrices into one big matrix
A	area
\mathbb{C}_p	stiffness tensor of the pore phase
\mathbb{C}_r	stiffness tensor of phase r
\mathbb{C}_s	stiffness tensor of the solid needle phase
\mathbb{C}_{hom}	homogenized stiffness tensor
\mathbb{C}^0	auxiliary elastic stiffness tensor of the matrix
C_{ijkl}	component of the stiffness tensor
can	suffix labeling canalicular pores
col	suffix labeling the collagen phase
cyl	suffix labeling a cylindrical shaped inclusion
\mathbb{D}	fourth order influence tensor
\mathbb{D}_{ij}	fourth order influence tensor quantifying the effect of plastic strains in solid phase j on the total strains in solid phase i
\mathbb{D}_{pj}	fourth order influence tensor quantifying the effect of plastic strains in solid phase j on the total strains in the pore phase
\mathbb{D}_{rs}	fourth-order strain influence tensor linking eigenstrains in phase s to total strains in phase r
$\mathbb{D}_{r\pi,i+1}^{\pi,i}$	fourth-order strain influence tensor of RVE i of path π linking eigenstrains in phase s to total strains in phase $r_{\pi,i+1}$, which hosts RVE $i + 1$
\mathbf{D}	compilation of several $\mathcal{M}_{\mathbb{D}}$ -matrices into one big matrix
$\hat{\mathbf{D}}$	macroscopic virtual Eulerian strain rate tensor
$\hat{\mathbf{d}}$	virtual Eulerian strain rate tensor
d	characteristic length of inhomogeneities within an RVE
$d_{\pi,i}$	or cross-section diameter characteristic length of inhomogeneities within RVE i of the up-/downscaling path π

Symbol	Description
d_{dry}	lateral diffraction spacing in dry tissues
d_{max}	maximum value of diffraction spacing
\mathcal{E}	compilation of several \mathcal{V}_ε -vectors into one big vector
\mathbf{E}	macroscopic strain
\mathbf{E}^n	macroscopic strain at the end of load step n
$\mathbf{E}^{n,r}$	macroscopic strain at the end of iteration step r during load step n
\mathbf{E}^p	macroscopic plastic strain
$\mathbf{E}^{p,n,r}$	macroscopic plastic strain at the end of iteration step r during load step n
\mathbf{E}^0	auxiliary macroscopic strain
\mathbf{E}^{kl}	effective unit strain state
$\dot{\mathbf{E}}$	macroscopic strain rate
$\Delta\mathbf{E}$	macroscopic strain increment
E	Young's modulus
$\mathbf{e}_1, \mathbf{e}_2, \mathbf{e}_3$	unit base vectors of Cartesian reference base frame
$\mathbf{e}_\varphi, \mathbf{e}_\theta, \mathbf{e}_r$	unit base vectors of spherical base frame attached to the solid (needle-shaped) phase
ef	suffix labeling the extrafibrillar space
efHA	suffix labeling a hydroxyapatite phase in the extrafibrillar space
excel	suffix labeling the extracellular space
exvas	suffix labeling the extravascular space
exp	suffix labeling the experimentally determined data
\mathfrak{F}	yield (failure) criterion
$\mathfrak{F}_r^{(\alpha)}$	α -th yield function of the multisurface yield criterion of phase r
$\mathfrak{F}_{s,i}^{(\alpha),n,r,k}$	α -th yield function evaluated for the k -th member of the microscopic stress series in the i -th solid phase during iteration step r and load step n
\mathbf{F}	force vector
	<i>or</i> macroscopic volume force
\mathbf{F}_{M_i}	reaction force generated at the master node M_i
\mathcal{F}	dimensionless function
\mathbf{f}	volume force vector
f_p	volume fraction of the pore phase
f_r	volume fraction of phase r
f_s	volume fraction of the solid phase
f_r^R	volume fraction of phase r within RVE R
fib	suffix labeling the mineralized collagen fibril
\mathcal{G}	domain of admissible microstress states
$\mathcal{G}_{s,i}$	domain of admissible microstresses in the i -th solid phase
\mathfrak{G}	plastic potential function
$\mathfrak{G}_r^{(\alpha)}$	α -th plastic potential function of the multisurface yield criterion of phase r
\mathcal{G}	set of Gaussian points chosen for evaluation of integrals over the unit sphere
$\mathcal{G}_{\text{plast}}^{n,r}$	set of plasticizing phases during load step n and iteration step r
\mathbb{I}	fourth-order identity tensor
\mathbb{I}^{dev}	deviatoric part of the identity tensor
\mathbb{I}^{vol}	volumetric part of the identity tensor

Symbol	Description
i	index for an inclusion phase <i>or</i> index labeling the integration points chosen for evaluation of intergrals over the unit sphere and thereby describing the differently orientated (needle-shaped) solid phases
ic	suffix labeling the intercrystalline pores
im	suffix labeling the intermolecular space
imHA	suffix labeling a hydroxyapatite phase in the intermolecular space
k	index numbering the steps within the return-mapping iteration
k_p	bulk modulus of the pore phase
k_r	bulk modulus of phase r
k_s	bulk modulus of the solid phase
\mathcal{L}	characteristic length of the structure represented by an RVE
ℓ	characteristic length of an RVE <i>or</i> edge length
$\ell_{\pi,i}$	characteristic length of RVE i of the up-/downscaling path π
lac	suffix labeling the lacunar pores
$\mathbb{M}_{r\rho}^{\pi,v-\tau,u}$	multiscale influence tensors uniting the multiscale effect of the plastic strain in (needle-shaped) ρ situated within RVE v of path π on the stress in (needle-shaped) r situated within RVE u of path τ
$\mathcal{M}_{\mathbb{T}}$	Kelvin-Mandel matrix representation of the fourth-order tensor \mathbb{T}
\mathcal{M}	auxiliary matrix
M	index labeling the macroscopic scale
M_i	master node
m	index for a matrix phase <i>or</i> number of rows of a matrix
\mathbf{N}	axial force acting in direction of the beam axis
N_i	number of Gaussian points
N_k	number of back-projection steps k during iteration step r
N_n	number of load steps n
N_r	number of iteration steps r during load step n
$N_{\text{Fact},i}^{n,r}$	number active yield surfaces of solid phase i at load step n and iteration step r
$N_{\text{plast}}^{n,r}$	number of plasticizing solid phases during load step n and iteration step r
\mathbf{n}	normal vector
n	index numbering the load steps <i>or</i> number of columns of a matrix
opt	suffix labeling the densest packing of truncated icosahedra
org	suffix labeling organic content
\mathbb{P}_r	Hill tensor associated with phase r
$\mathbb{P}_{s,i}$	fourth-order Hill tensor associated with the i -th solid phase
\mathcal{P}	characteristic length of the loading acting onto a structure
\mathcal{P}_{ext}	power of the external forces
\mathcal{P}_{int}	power of the internal forces
P_{ijkl}	component of the Hill tensor
P_L	suffix labeling a lattice packing
p	index for a pore phase

Symbol	Description
p_{ext}	power density of the external forces
p_{int}	power density of the internal forces
pore	suffix labeling a pore phase
pred	suffix labeling data predicted by a model
\mathbf{Q}_{y^*}	transverse forces acting perpendicular to the beam axis
\mathbf{Q}_{z^*}	transverse forces acting perpendicular to the beam axis
$\mathbf{R}^{n,r}$	residual stress increment of iteration step r during load step n
RVE	Representative Volume Element
\mathbf{t}	index numbering the steps within the residual iteration
r	index labeling a phase <i>or</i> index numbering the iteration steps within the modified Newton-Raphson scheme
$r_{\pi,i}$	index labeling a phase which is hosting RVE i of up-/downscaling path π
\mathbb{S}^{esh}	Eshelby tensor
S^{esh}	component of the Eshelby tensor
S	surface
S_{UC}	surface of a unit cell
s	index labeling a solid phase <i>or</i> aspect ratio
sph	suffix labeling a spherical shaped inclusion
\mathbf{T}	traction vector
t	time
trial	suffix labeling a trial state
trunc	suffix labeling a truncated icosahedron
UC	unit cell
\mathbf{u}	displacement vector
\mathbf{u}^*	displacement fluctuation vector
$\mathbf{V}_{\mathbf{T}}$	Kelvin-Mandel vector representation of the second-order tensor \mathbf{T}
$\hat{\mathbf{V}}$	macroscopic virtual velocity vector
V	Volume
V_r	Volume of phase r
V_{RVE}	Volume of an RVE
V_{UC}	volume of a unit cell
\mathbf{v}	velocity vector
$\hat{\mathbf{v}}$	virtual velocity vector
vas	suffix labeling the vascular pores
\mathbf{w}_i	vector of translational invariance of a periodic microstructure
w	slenderness ratio
\mathbf{X}	macroscopic location vector
\mathbf{x}	microscopic location vector
\mathbf{x}'	microscopic location vector
\mathbf{x}_b	vector describing the position of an end of a beam element b
$\mathbf{x}^{i+}, \mathbf{x}^{i-}$	periodically corresponding nodes on the surface of a unit cell
xyz	suffix labeling a lattice packing of truncated icosahedra
xz	suffix labeling a lattice packing of truncated icosahedra
α	index numbering the yield criterion

Symbol	Description
β	friction parameter
δ	Dirac delta distribution
δ_{ij}	Kronecker delta
$\delta_{V_{RVE}}$	boundary of an RVE
$\boldsymbol{\varepsilon}$	microscopic strain
$\boldsymbol{\varepsilon}_p$	average microscopic strain in the pore phase
$\boldsymbol{\varepsilon}_r$	average microscopic strain in phase r
$\boldsymbol{\varepsilon}_{s,i}$	average microscopic strain in the i -th solid phase
$\boldsymbol{\varepsilon}_r^{\pi,i} = \boldsymbol{\varepsilon}_{r\pi,i}$	average microscopic strain of phase r within RVE i of path π
$\boldsymbol{\varepsilon}^p$	microscopic plastic strain
$\boldsymbol{\varepsilon}_r^p$	average microscopic plastic strain in phase r
$\boldsymbol{\varepsilon}_{s,i}^p$	average microscopic plastic strain in the i -th solid phase
$\boldsymbol{\varepsilon}_{s,i}^{p,n,r}$	average microscopic plastic strain in the i -th solid phase at the end of iteration step r during load step n
$\boldsymbol{\varepsilon}^*$	microscopic strain fluctuation
$\dot{\boldsymbol{\varepsilon}}$	microscopic strain rate
$\dot{\boldsymbol{\varepsilon}}^p$	microscopic plastic strain rate
$\Delta\boldsymbol{\varepsilon}_{s,i}^{p,n}$	plastic strain increment of the i -th solid phase during load step n
$\Delta\boldsymbol{\varepsilon}_{s,i}^{p,n,r}$	plastic strain increment of the i -th solid phase at the end of iteration step r during load step n
η	index numbering the levels of a multiscale scheme
θ	angle
$\dot{\lambda}_i^{(\alpha)}$	plastic multiplier related to the α -th yield surface associated to the i -th solid phase
$\Delta\lambda_i^{(\alpha),n,r,k}$	plastic multiplier associated to the α -th yield surface of the i -th solid phase and corresponding to the k -th member of the stress series during iteration step r and load step n
μ	index labeling the microscopic scale
$\mu_{\eta\pi}$	index labeling the η -th microscopic scale of a downscaling path π
μ_r	shear modulus of phase r
ν_r	Poisson's ratio of phase r
ξ	microscopic displacement
$\boldsymbol{\pi}$	supremum function
π	index labeling a certain up-/downscaling path within a multiscale homogenization scheme
π, i	index labeling RVE i within up-/downscaling path π
ρ	mass density
	<i>or</i> index labeling a plasticity-inducing phase
ρ^{PL}	packing density
$\boldsymbol{\Sigma}$	macroscopic stress
$\boldsymbol{\Sigma}^n$	macroscopic stress at the end of load step n
$\boldsymbol{\Sigma}^{n,r}$	macroscopic stress at the end of iteration step r during load step n
$\Delta\boldsymbol{\Sigma}$	macroscopic stress increment
$\boldsymbol{\Sigma}^{\text{plastic}}$	macroscopic stress at which all solid phases exhibit plastic behavior
$\boldsymbol{\Sigma}^{\text{ult}}$	macroscopic uniaxial ultimate stress

Symbol	Description
Σ^{yield}	yield point, macroscopic stress at which the first solid phase exhibit plastic behavior
σ	microscopic stress
σ_p	average microscopic stress in the pore phase
σ_r	average microscopic stress in phase r
$\sigma_{s,i}$	average microscopic stress in the i -th solid phase
$\sigma_r^{\pi,i} = \sigma_{r\pi,i}$	average microscopic stress of phase r within RVE i of path π
$\sigma_{s,i}^{n,r}$	average microscopic stress in the i -th solid phase at the end of iteration step r during load step n
$\sigma_{s,i}^{n,r,k}$	k -th member of the stress series in the i -th solid phase during iteration step r and load step n
σ^{ult}	microscopic extreme load (strength)
$\Delta\sigma$	microscopic stress increment
σ_r^{yield}	yield strength of phase r
$\sigma_{\text{I}}, \sigma_{\text{II}}, \sigma_{\text{III}}$	principle values of the stress tensor σ
τ	index labeling a downscaling path within a multiscale homogenization scheme
φ	angle
ϕ	golden ratio
ϕ_1, ϕ_2, ϕ_3	fitting parameters
ω_i	Gaussian weight

Bibliography

- Alexander, B., Daulton, T. L., Genin, G. M., Lipner, J., Pasteris, J. D., Wopenka, B. & Thomopoulos, S. (2012), 'The nanometre-scale physiology of bone: steric modelling and scanning transmission electron microscopy of collagen–mineral structure', *Journal of the Royal Society Interface* 9(73), 1774–1786.
- Anoukou, K., Pastor, F., Dufrenoy, P. & Kondo, D. (2016), 'Limit analysis and homogenization of porous materials with Mohr–Coulomb matrix. Part I: Theoretical formulation', *Journal of the Mechanics and Physics of Solids* 91, 145–171.
- Auriault, J.-L., Boutin, C. & Geindreau, C. (2009), *Homogenization of Coupled Phenomena in Heterogenous Media*, John Wiley & Sons.
- Badel, P.-B. & Leblond, J.-B. (2004), 'A note on integration schemes for the microplane model of the mechanical behaviour of concrete', *International Journal for Numerical Methods in Biomedical Engineering* 20(1), 75–81.
- Barenblatt, G. I. (1996), *Scaling, self-similarity, and intermediate asymptotics*, Cambridge University Press.
- Barthélémy, J.-F. & Dormieux, L. (2004), 'A micromechanical approach to the strength criterion of Drucker-Prager materials reinforced by rigid inclusions', *International Journal for Numerical and Analytical Methods in Geomechanics* 28(7-8), 565–582.
- Bekaert, A. & Maghous, S. (1996), 'Three-dimensional yield strength properties of jointed rock mass as a homogenized medium', *Mechanics of Cohesive-frictional Materials: An International Journal on Experiments, Modelling and Computation of Materials and Structures* 1(1), 1–24.
- Bensoussan, A., Lions, J.-L. & Papanicolaou, G. (1978), *Asymptotic analysis for periodic structures*.
- Benzerga, A. A. & Besson, J. (2001), 'Plastic potentials for anisotropic porous solids', *European Journal of Mechanics-A/Solids* 20(3), 397–434.
- Betke, U. & Henk, M. (2000), 'Densest lattice packings of 3-polytopes', *Computational Geometry* 16(3), 157–186.
- Bhowmik, R., Katti, K. S. & Katti, D. R. (2007), 'Mechanics of molecular collagen is influenced by hydroxyapatite in natural bone', *Journal of Materials Science* 42(21), 8795–8803.
- Bhowmik, R., Katti, K. S. & Katti, D. R. (2009), 'Mechanisms of load-deformation behavior of molecular collagen in hydroxyapatite-tropocollagen molecular system: steered molecular dynamics study', *Journal of Engineering Mechanics* 135(5), 413–421.

- Bigley, R. F., Griffin, L. V., Christensen, L. & Vandenbosch, R. (2006), ‘Osteon interfacial strength and histomorphometry of equine cortical bone’, *Journal of Biomechanics* 39(9), 1629–1640.
- Bignonnet, F., Dormieux, L. & Kondo, D. (2016), ‘A micro-mechanical model for the plasticity of porous granular media and link with the Cam clay model’, *International Journal of Plasticity* 79, 259–274.
- Borja, R. I. (2013), *Plasticity: modeling & computation*, Springer Science & Business Media.
- Brach, S., Anoukou, K., Kondo, D. & Vairo, G. (2018), ‘Limit analysis and homogenization of nanoporous materials with a general isotropic plastic matrix’, *International Journal of Plasticity* 105, 24–61.
- Brach, S., Dormieux, L., Kondo, D. & Vairo, G. (2017), ‘Nanoporous materials with a general isotropic plastic matrix: exact limit state under isotropic loadings’, *International Journal of Plasticity* 89, 1–28.
- Buckwalter, J., Glimcher, M., Cooper, R., Recker, R. et al. (1995), ‘Bone biology’, *The Journal of Bone & Joint Surgery* 77(8), 1256–1275.
- Burstein, A. H., Reilly, D. T. & Martens, M. (1976), ‘Aging of bone tissue: mechanical properties.’, *The Journal of Bone and Joint Surgery. American volume* 58(1), 82–86.
- Capsoni, A., Corradi, L. & Vena, P. (2001), ‘Limit analysis of anisotropic structures based on the kinematic theorem’, *International Journal of Plasticity* 17(11), 1531–1549.
- Castaneda, P. P. & Suquet, P. (1997), Nonlinear composites, in ‘Advances in applied mechanics’, Vol. 34, Elsevier, pp. 171–302.
- Cazacu, O., Revil-Baudard, B., Lebensohn, R. A. & Găărăjeu, M. (2013), ‘On the combined effect of pressure and third invariant on yielding of porous solids with von Mises matrix’, *Journal of Applied Mechanics* 80(6).
- Cezayirlioglu, H., Bahniuk, E., Davy, D. & Heiple, K. (1985), ‘Anisotropic yield behavior of bone under combined axial force and torque’, *Journal of Biomechanics* 18(1), 61–69.
- Conway, J. H. & Torquato, S. (2006), ‘Packing, tiling, and covering with tetrahedra’, *Proceedings of the National Academy of Sciences* 103(28), 10612–10617.
- Corradi, L. & Vena, P. (2003), ‘Limit analysis of orthotropic plates’, *International Journal of Plasticity* 19(10), 1543–1566.
- Coulomb, C. A. (1773), ‘Essai sur une application des règles de maximis et minimis à quelques problèmes de statique relatifs à l’architecture (essay on maximums and minimums of rules to some static problems relating to architecture)’, *Académie Royale des Sciences, Mémoires de Mathématique et de Physique* 7(1), 343–382.
- Cowin, S. C. (2003), ‘A recasting of anisotropic poroelasticity in matrices of tensor components’, *Transport in Porous Media* 50(1-2), 35–56.
- Currey, J. (1959), ‘Differences in the tensile strength of bone of different histological types’, *Journal of Anatomy* 93(Pt 1), 87.

- Currey, J. (1975), 'The effects of strain rate, reconstruction and mineral content on some mechanical properties of bovine bone', *Journal of Biomechanics* 8(1), 83–86.
- De Buhan, P. & De Felice, G. (1997), 'A homogenization approach to the ultimate strength of brick masonry', *Journal of the Mechanics and Physics of Solids* 45(7), 1085–1104.
- de Souza Neto, E. A., Peric, D. & Owen, D. R. (2011), *Computational methods for plasticity: theory and applications*, John Wiley & Sons.
- Dormieux, L. & Kondo, D. (2010), 'An extension of Gurson model incorporating interface stresses effects', *International Journal of Engineering Science* 48(6), 575–581.
- Dormieux, L. & Ulm, F.-J. (2007), *Applied micromechanics of porous materials*, Springer Science & Business Media.
- Drucker, D. C. & Prager, W. (1952), 'Soil mechanics and plastic analysis or limit design', *Quarterly of Applied Mathematics* 10(2), 157–165.
- Drugan, W. & Willis, J. (1996), 'A micromechanics-based nonlocal constitutive equation and estimates of representative volume element size for elastic composites', *Journal of the Mechanics and Physics of Solids* 44(4), 497–524.
- Drury, J. L. & Mooney, D. J. (2003), 'Hydrogels for tissue engineering: scaffold design variables and applications', *Biomaterials* 24(24), 4337–4351.
- Dvorak, G. (1992), 'Transformation field analysis of inelastic composite materials', *Proceedings of the Royal Society of London. Series A: Mathematical and Physical Sciences* 437(1900), 311–327.
- Dvorak, G. (2013), *Micromechanics of Composite Materials*, Springer Netherlands.
- Dvorak, G. J. & Benveniste, Y. (1992), 'On transformation strains and uniform fields in multiphase elastic media', *Proceedings of the Royal Society of London A: Mathematical, Physical and Engineering Sciences* 437, 291–310.
- Dvorak, G., Wafa, A. & Bahei-El-Din, Y. (1994), 'Implementation of the transformation field analysis for inelastic composite materials', *Computational Mechanics* 14(3), 201–228.
- Einhorn, T. (2003), 'The structural properties of normal and osteoporotic bone.', *Instructional Course Lectures* 52, 533–539.
- Eshelby, J. D. (1957), 'The determination of the elastic field of an ellipsoidal inclusion, and related problems', *Proceedings of the Royal Society of London A: Mathematical Physical and Engineering Sciences* 241, 1226, 376–396.
- Fritsch, A., Dormieux, L. & Hellmich, C. (2006), 'Porous polycrystals built up by uniformly and axisymmetrically oriented needles: homogenization of elastic properties', *Comptes Rendus Mécanique* 334(3), 151–157.
- Fritsch, A., Dormieux, L., Hellmich, C. & Sanahuja, J. (2009), 'Mechanical behavior of hydroxyapatite biomaterials: an experimentally validated micromechanical model for elasticity and strength', *Journal of Biomedical Materials Research Part A* 88(1), 149–161.

- Fritsch, A. & Hellmich, C. (2007), “Universal’microstructural patterns in cortical and trabecular, extracellular and extravascular bone materials: micromechanics-based prediction of anisotropic elasticity’, *Journal of Theoretical Biology* 244(4), 597–620.
- Fritsch, A., Hellmich, C. & Dormieux, L. (2009), ‘Ductile sliding between mineral crystals followed by rupture of collagen crosslinks: experimentally supported micromechanical explanation of bone strength’, *Journal of Theoretical Biology* 260(2), 230–252.
- Fritzen, F., Forest, S., Böhlke, T., Kondo, D. & Kanit, T. (2012), ‘Computational homogenization of elasto-plastic porous metals’, *International Journal of Plasticity* 29, 102–119.
- Füssl, J., Li, M., Lukacevic, M., Eberhardsteiner, J. & Martin, C. (2017), ‘Comparison of unit cell-based computational methods for predicting the strength of wood’, *Engineering Structures* 141, 427–443.
- Gentleman, E., Lay, A. N., Dickerson, D. A., Nauman, E. A., Livesay, G. A. & Dee, K. C. (2003), ‘Mechanical characterization of collagen fibers and scaffolds for tissue engineering’, *Biomaterials* 24(21), 3805–3813.
- Germain, P. (1973), ‘The method of virtual power in continuum mechanics. Part 2: Microstructure’, *SIAM Journal on Applied Mathematics* 25(3), 556–575.
- Germain, P., Suquet, P. & Nguyen, Q. S. (1983), ‘Continuum thermodynamics’, *Journal of Applied Mechanics* 50(4b), 1010–1020.
- Ghosh, S., Lee, K. & Moorthy, S. (1996), ‘Two scale analysis of heterogeneous elastic-plastic materials with asymptotic homogenization and Voronoi cell finite element model’, *Computer Methods in Applied Mechanics and Engineering* 132(1-2), 63–116.
- Gómez, S., Vlad, M., López, J. & Fernández, E. (2016), ‘Design and properties of 3D scaffolds for bone tissue engineering’, *Acta Biomaterialia* 42, 341–350.
- Gong, J., Arnold, J. & Cohn, S. (1964), ‘Composition of trabecular and cortical bone’, *The Anatomical Record* 149(3), 325–331.
- Guo, T., Faleskog, J. & Shih, C. (2008), ‘Continuum modeling of a porous solid with pressure-sensitive dilatant matrix’, *Journal of the Mechanics and Physics of Solids* 56(6), 2188–2212.
- Gurson, A. L. (1977), ‘Continuum theory of ductile rupture by void nucleation and growth: Part I - yield criteria and flow rules for porous ductile media’, *Journal of Engineering Materials and Technology* 99(1), 2–15.
- Hammett, F. S. (1925), ‘A biochemical study of bone growth I. changes in the ash, organic matter, and water during growth (mus norvegicus albinus)’, *Journal of Biological Chemistry* 64(2), 409–428.
- Hang, F. & Barber, A. H. (2011), ‘Nano-mechanical properties of individual mineralized collagen fibrils from bone tissue’, *Journal of the Royal Society Interface* 8(57), 500–505.
- Hashin, Z. (1983), ‘Analysis of composite materials - a survey’, *Journal of Applied Mechanics* 50(3), 481–505.

- He, Z., Dormieux, L., Lemarchand, E. & Kondo, D. (2013), 'Cohesive Mohr–Coulomb interface effects on the strength criterion of materials with granular-based microstructure', *European Journal of Mechanics-A/Solids* 42, 430–440.
- Hellmich, C. & Ulm, F.-J. (2003), 'Average hydroxyapatite concentration is uniform in the extracollagenous ultrastructure of mineralized tissues: evidence at the 1–10- μm scale', *Biomechanics and Modeling in Mechanobiology* 2(1), 21–36.
- Hellmich, C. & Ulm, F.-J. (2005), 'Drained and undrained poroelastic properties of healthy and pathological bone: a poro-micromechanical investigation', *Transport in Porous Media* 58(3), 243–268.
- Hill, R. (1963), 'Elastic properties of reinforced solids: some theoretical principles', *Journal of the Mechanics and Physics of Solids* 11(5), 357–372.
- Hill, R. (1965), 'Continuum micro-mechanics of elastoplastic polycrystals', *Journal of the Mechanics and Physics of Solids* 13(2), 89–101.
- Hodge, A. & Petruska, J. (1963), 'Aspects of protein structure', *Academic* pp. 289–300.
- Hofstetter, K., Hellmich, C., Eberhardsteiner, J. & Mang, H. A. (2008), 'Micromechanical estimates for elastic limit states in wood materials, revealing nanostructural failure mechanisms', *Mechanics of Advanced Materials and Structures* 15(6-7), 474–484.
- Hollister, S. J. (2005), 'Porous scaffold design for tissue engineering', *Nature Materials* 4(7), 518–524.
- Kalamkarov, A. L., Andrianov, I. V. & Danishevs'kyy, V. V. (2009), 'Asymptotic homogenization of composite materials and structures', *Applied Mechanics Reviews* 62(3).
- Kästner, M., Haasemann, G. & Ulbricht, V. (2011), 'Multiscale XFEM-modelling and simulation of the inelastic material behaviour of textile-reinforced polymers', *International Journal for Numerical Methods in Engineering* 86(4-5), 477–498.
- Katz, J. L., Yoon, H. S., Lipson, S., Maharidge, R., Meunier, A. & Christel, P. (1984), 'The effects of remodeling on the elastic properties of bone', *Calcified Tissue International* 36(1), S31–S36.
- Katz, J. & Ukraincik, K. (1971), 'On the anisotropic elastic properties of hydroxyapatite', *Journal of Biomechanics* 4(3), 221–227.
- Keralavarma, S. & Benzerga, A. (2010), 'A constitutive model for plastically anisotropic solids with non-spherical voids', *Journal of the Mechanics and Physics of Solids* 58(6), 874–901.
- Keulen, P. (2015), 'Osteoporose - Prophylaxe und Rehabilitation', *MTC Pieter Keulen AG*.
- Kohlhauser, C. & Hellmich, C. (2013), 'Ultrasonic contact pulse transmission for elastic wave velocity and stiffness determination: influence of specimen geometry and porosity', *Engineering Structures* 47, 115–133.
- Koiter, W. T. (1953), 'Stress-strain relations, uniqueness and variational theorems for elastic-plastic materials with a singular yield surface', *Quarterly of Applied Mathematics* 11(3), 350–354.

- Königsberger, M., Pichler, B. & Hellmich, C. (2020), 'Multiscale poro-elasticity of densifying calcium-silicate hydrates in cement paste: An experimentally validated continuum micromechanics approach', *International Journal of Engineering Science* 147, 103196.
- Kotha, S. P. & Guzelsu, N. (2002), 'Modeling the tensile mechanical behavior of bone along the longitudinal direction', *Journal of Theoretical Biology* 219(2), 269–279.
- Landis, W. J. & Jacquet, R. (2013), 'Association of calcium and phosphate ions with collagen in the mineralization of vertebrate tissues', *Calcified Tissue International* 93(4), 329–337.
- Landis, W., Song, M., Leith, A., McEwen, L. & McEwen, B. (1993), 'Mineral and organic matrix interaction in normally calcifying tendon visualized in three dimensions by high-voltage electron microscopic tomography and graphic image reconstruction', *Journal of Structural Biology* 110(1), 39–54.
- Lanza, R., Langer, R. & Vacanti, J. P. (2011), *Principles of tissue engineering*, Academic press.
- Laws, N. (1977), 'The determination of stress and strain concentrations at an ellipsoidal inclusion in an anisotropic material', *Journal of Elasticity* 7(1), 91–97.
- Lees, S. (1987), 'Possible effect between the molecular packing of collagen and the composition of bony tissues', *International Journal of Biological Macromolecules* 9(6), 321–326.
- Lees, S., Ahern, J. & Leonard, M. (1983), 'Parameters influencing the sonic velocity in compact calcified tissues of various species', *The Journal of the Acoustical Society of America* 74(1), 28–33.
- Lees, S., Cleary, P. F., Heeley, J. D. & Gariepy, E. L. (1979), 'Distribution of sonic plesio-velocity in a compact bone sample', *The Journal of the Acoustical Society of America* 66(3), 641–646.
- Lees, S., Hanson, D. B. & Page, E. A. (1996), 'Some acoustical properties of the otic bones of a fin whale', *The Journal of the Acoustical Society of America* 99(4), 2421–2427.
- Lees, S. & Heeley, J. D. (1981), 'Density of a sample bovine cortical bone matrix and its solid constituent in various media', *Calcified Tissue International* 33(1), 499–504.
- Levin, V. (1967), 'Thermal expansion coefficient of heterogeneous materials', *Mechanics of Solids* 2, 58–61.
- Liu, X. S., Stein, E. M., Zhou, B., Zhang, C. A., Nickolas, T. L., Cohen, A., Thomas, V., McMahan, D. J., Cosman, F., Nieves, J. et al. (2012), 'Individual trabecula segmentation (ITS)-based morphological analyses and microfinite element analysis of HR-pQCT images discriminate postmenopausal fragility fractures independent of DXA measurements', *Journal of Bone and Mineral Research* 27(2), 263–272.
- Liu, Y., Lim, J. & Teoh, S.-H. (2013), 'Development of clinically relevant scaffolds for vascularised bone tissue engineering', *Biotechnology Advances* 31(5), 688–705.
- Lubarda, V. A. (2001), *Elastoplasticity Theory*, CRC press.

- Maghous, S., De Buhan, P. & Bekaert, A. (1998), 'Failure design of jointed rock structures by means of a homogenization approach', *Mechanics of Cohesive-frictional Materials: An International Journal on Experiments, Modelling and Computation of Materials and Structures* 3(3), 207–228.
- Mandel, J. (1965), 'Généralisation de la théorie de plasticité de WT Koiter', *International Journal of Solids and Structures* 1(3), 273–295.
- Martin, R. & Ishida, J. (1989), 'The relative effects of collagen fiber orientation, porosity, density, and mineralization on bone strength', *Journal of Biomechanics* 22(5), 419–426.
- Matsui, K., Terada, K. & Yuge, K. (2004), 'Two-scale finite element analysis of heterogeneous solids with periodic microstructures', *Computers & Structures* 82(7-8), 593–606.
- McCarthy, R., Jeffcott, L. & McCartney, R. (1990), 'Ultrasound speed in equine cortical bone: effects of orientation, density, porosity and temperature', *Journal of Biomechanics* 23(11), 1139–1143.
- Meek, K., Fullwood, N., Cooke, P., Elliott, G., Maurice, D., Quantock, A., Wall, R. & Worthington, C. (1991), 'Synchrotron x-ray diffraction studies of the cornea, with implications for stromal hydration', *Biophysical Journal* 60(2), 467–474.
- Mehesz, A. N., Brown, J., Hajdu, Z., Beaver, W., Da Silva, J., Visconti, R., Markwald, R. & Mironov, V. (2011), 'Scalable robotic biofabrication of tissue spheroids', *Biofabrication* 3(2), 025002.
- Melan, E. (1938), 'Zur Plastizität des räumlichen Kontinuums', *Ingenieur-Archiv* 9(2), 116–126.
- Michel, J.-C. & Suquet, P. (2003), 'Nonuniform transformation field analysis', *International journal of solids and structures* 40(25), 6937–6955.
- Michel, J., Moulinec, H. & Suquet, P. (1999), 'Effective properties of composite materials with periodic microstructure: a computational approach', *Computer Methods in Applied Mechanics and Engineering* 172, 1, 109–143.
- Milani, G., Lourenço, P. B. & Tralli, A. (2006), 'Homogenised limit analysis of masonry walls, Part I: Failure surfaces', *Computers & Structures* 84(3-4), 166–180.
- Milani, G., Shehu, R. & Valente, M. (2018), 'A kinematic limit analysis approach for seismic retrofitting of masonry towers through steel tie-rods', *Engineering Structures* 160, 212–228.
- Morin, C. & Hellmich, C. (2013), 'Mineralization-driven bone tissue evolution follows from fluid-to-solid phase transformations in closed thermodynamic systems', *Journal of Theoretical Biology* 335, 185–197.
- Morin, C., Hellmich, C. & Henits, P. (2013), 'Fibrillar structure and elasticity of hydrating collagen: a quantitative multiscale approach', *Journal of Theoretical Biology* 317, 384–393.
- Morin, C., Vass, V. & Hellmich, C. (2017), 'Micromechanics of elastoplastic porous polycrystals: Theory, algorithm, and application to osteonal bone', *International Journal of Plasticity* 91, 238–267.
- Nahshon, K. & Hutchinson, J. (2008), 'Modification of the Gurson model for shear failure', *European Journal of Mechanics-A/Solids* 27(1), 1.

- O'Brien, F. J. (2011), 'Biomaterials & scaffolds for tissue engineering', *Materials Today* 14(3), 88–95.
- O'Keefe, R. J. & Mao, J. (2011), 'Bone tissue engineering and regeneration: from discovery to the clinic - an overview', *Tissue Engineering Part B: Reviews* 17(6), 389–392.
- Orgel, J. P., Irving, T. C., Miller, A. & Wess, T. J. (2006), 'Microfibrillar structure of type I collagen in situ', *Proceedings of the National Academy of Sciences* 103(24), 9001–9005.
- Ortiz, M. & Popov, E. P. (1985), 'Accuracy and stability of integration algorithms for elastoplastic constitutive relations', *International Journal for Numerical Methods in Engineering* 21(9), 1561–1576.
- Ortiz, M. & Simo, J. (1986), 'An analysis of a new class of integration algorithms for elastoplastic constitutive relations', *International Journal for Numerical Methods in Engineering* 23(3), 353–366.
- Ovsianikov, A., Khademhosseini, A. & Mironov, V. (2018), 'The synergy of scaffold-based and scaffold-free tissue engineering strategies', *Trends in Biotechnology* .
- Parker, G. (2001), 'Encyclopedia of materials: science and technology'.
- Pichler, B. & Hellmich, C. (2010), 'Estimation of influence tensors for eigenstressed multiphase elastic media with nonaligned inclusion phases of arbitrary ellipsoidal shape', *Journal of Engineering Mechanics* 136(8), 1043–1053.
- Prostak, K. & Lees, S. (1996), 'Visualization of crystal-matrix structure. in situ demineralization of mineralized turkey leg tendon and bone', *Calcified Tissue International* 59(6), 474–479.
- Rajagopal, K. (2013), 'Particle-free bodies and point-free spaces', *International Journal of Engineering Science* 72, 155–176.
- Reilly, D. T., Burstein, A. H. & Frankel, V. H. (1974), 'The elastic modulus for bone', *Journal of Biomechanics* 7(3), 271–275.
- Rezende, R. A., Pereira, F. D., Kasyanov, V., Ovsianikov, A., Torgensen, J., Gruber, P., Stampfl, J., Brakke, K., Nogueira, J. A., Mironov, V. et al. (2012), 'Design, physical prototyping and initial characterisation of "lockyballs"', *Virtual and Physical Prototyping* 7(4), 287–301.
- Runesson, K., Sture, S. & Willam, K. (1988), Integration in computational plasticity, in 'Computational Structural Mechanics & Fluid Dynamics', Elsevier, pp. 119–130.
- Salençon, J. (1990), 'Introduction to the yield design theory and its applications to soil mechanics', *European Journal of Mechanics-A/Solids* 9(5), 477–500.
- Salençon, J. (2012), *Handbook of continuum mechanics: General concepts thermoelasticity*, Springer Science & Business Media.
- Sasaki, N. & Odajima, S. (1996), 'Stress-strain curve and young's modulus of a collagen molecule as determined by the x-ray diffraction technique', *Journal of Biomechanics* 29(5), 655–658.

- Scalet, G. & Auricchio, F. (2018), 'Computational methods for elastoplasticity: an overview of conventional and less-conventional approaches', *Archives of Computational Methods in Engineering* 25(3), 545–589.
- Schneider, P., Meier, M., Wepf, R. & Müller, R. (2011), 'Serial FIB/SEM imaging for quantitative 3D assessment of the osteocyte lacuno-canalicular network', *Bone* 49(2), 304–311.
- Schneider, P., Stauber, M., Voide, R., Stampanoni, M., Donahue, L. R. & Müller, R. (2007), 'Ultrastructural properties in cortical bone vary greatly in two inbred strains of mice as assessed by synchrotron light based micro-and nano-CT', *Journal of Bone and Mineral Research* 22(10), 1557–1570.
- Schwiedrzik, J., Raghavan, R., Bürki, A., LeNader, V., Wolfram, U., Michler, J. & Zysset, P. (2014), 'In situ micropillar compression reveals superior strength and ductility but an absence of damage in lamellar bone', *Nature Materials* 13(7), 740.
- Schwiedrzik, J., Taylor, A., Casari, D., Wolfram, U., Zysset, P. & Michler, J. (2017), 'Nanoscale deformation mechanisms and yield properties of hydrated bone extracellular matrix', *Acta Biomaterialia* 60, 302–314.
- Seifert, A. C., Li, C., Wehrli, S. L. & Wehrli, F. W. (2015), 'A surrogate measure of cortical bone matrix density by long T2-suppressed MRI', *Journal of Bone and Mineral Research* 30(12), 2229–2238.
- Shen, W., Cao, Y., Liu, Z. & Shao, J.-F. (2020), 'A multiscale elastoplastic constitutive model for geomaterials with a porous matrix-inclusion microstructure', *Computers and Geotechnics* 126, 103683.
- Shen, W., Kondo, D., Dormieux, L. & Shao, J.-F. (2013), 'A closed-form three scale model for ductile rocks with a plastically compressible porous matrix', *Mechanics of Materials* 59, 73–86.
- Shen, W., Shao, J.-F., Dormieux, L. & Kondo, D. (2012), 'Approximate criteria for ductile porous materials having a green type matrix: Application to double porous media', *Computational Materials Science* 62, 189–194.
- Silva, K. R., Rezende, R. A., Pereira, F. D., Gruber, P., Stuart, M. P., Ovsianikov, A., Brakke, K., Kasyanov, V., da Silva, J. V., Granjeiro, J. M. et al. (2016), 'Delivery of human adipose stem cells spheroids into lockyballs', *PloS one* 11(11), e0166073.
- Simo, J. C. & Taylor, R. L. (1985), 'Consistent tangent operators for rate-independent elastoplasticity', *Computer Methods in Applied Mechanics and Engineering* 48(1), 101–118.
- Simo, J. & Hughes, T. (1998), *Computational Inelasticity*, Springer, New York.
- Stampfl, J., Liska, R. & Ovsianikov, A. (2016), *Multiphoton lithography: Techniques, materials, and applications*, John Wiley & Sons.
- Suquet, P. (1997), Effective properties of nonlinear composites, in 'Continuum micromechanics', Springer, pp. 197–264.

- Suquet, P. M. (1985), ‘Elements of homogenization for inelastic solid mechanics, homogenization techniques for composite media’, *Lecture Notes in Physics* 272, 193.
- Tiberti, S. & Milani, G. (2020), ‘Fast brick-based homogenized limit analysis for in-and out-of-plane loaded periodic masonry panels’, *Computers & Structures* 231, 106206.
- Vacanti, J. P. & Langer, R. (1999), ‘Tissue engineering: the design and fabrication of living replacement devices for surgical reconstruction and transplantation’, *The Lancet* 354, S32–S34.
- Van Hoorick, J., Gruber, P., Markovic, M., Tromayer, M., Van Erps, J., Thienpont, H., Liska, R., Ovsianikov, A., Dubruel, P. & Van Vlierberghe, S. (2017), ‘Cross-linkable gelatins with superior mechanical properties through carboxylic acid modification: increasing the two-photon polymerization potential’, *Biomacromolecules* 18(10), 3260–3272.
- Vass, V., Morin, C., Scheiner, S. & Hellmich, C. (2018), Review of “universal” rules governing bone composition, organization, and elasticity across organizational hierarchies, in ‘Multiscale Mechanobiology of Bone Remodeling and Adaptation’, Springer, pp. 175–229.
- Vena, P., Gastaldi, D. & Contro, R. (2008), ‘Determination of the effective elastic–plastic response of metal–ceramic composites’, *International Journal of Plasticity* 24(3), 483–508.
- Walpole, L. (1984), ‘Fourth-rank tensors of the thirty-two crystal classes: multiplication tables’, *Proceedings of the Royal Society of London. A. Mathematical and Physical Sciences* 391(1800), 149–179.
- Walsh, W. & Guzelsu, N. (1994), ‘Compressive properties of cortical bone: mineral-organic interfacial bonding’, *Biomaterials* 15(2), 137–145.
- Weiner, S. & Wagner, H. D. (1998), ‘The material bone: structure-mechanical function relations’, *Annual Review of Materials Science* 28(1), 271–298.
- Wilson, E. E., Awonusi, A., Morris, M. D., Kohn, D. H., Tecklenburg, M. M. & Beck, L. W. (2006), ‘Three structural roles for water in bone observed by solid-state NMR’, *Biophysical Journal* 90(10), 3722–3731.
- Yang, S., Yu, S., Ryu, J., Cho, J.-M., Kyoung, W., Han, D.-S. & Cho, M. (2013), ‘Nonlinear multiscale modeling approach to characterize elastoplastic behavior of CNT/polymer nanocomposites considering the interphase and interfacial imperfection’, *International Journal of Plasticity* 41, 124–146.
- Zahn, D. & Hochrein, O. (2003), ‘Computational study of interfaces between hydroxyapatite and water’, *Physical Chemistry Chemical Physics* 5(18), 4004–4007.
- Zahn, D., Hochrein, O., Kawska, A., Brickmann, J. & Kniep, R. (2007), ‘Towards an atomistic understanding of apatite–collagen biomaterials: linking molecular simulation studies of complex-, crystal-and composite-formation to experimental findings’, *Journal of Materials Science* 42(21), 8966–8973.
- Zaoui, A. (2002), ‘Continuum micromechanics: survey’, *Journal of Engineering Mechanics* 128(8), 808–816.

- Zelaya-Lainez, L. (2016), Allocation of bone fluid throughout the hierarchical structure of bone: multi-technique analysis on bovine femur, Master's thesis, Vienna University of Technology.
- Zeng, T., Shao, J.-F. & Xu, W. (2014), 'Multiscale modeling of cohesive geomaterials with a polycrystalline approach', *Mechanics of Materials* 69(1), 132–145.
- Zhang, H., Wu, J. & Fu, Z. (2010), 'Extended multiscale finite element method for elasto-plastic analysis of 2D periodic lattice truss materials', *Computational Mechanics* 45(6), 623–635.
- Zhang, W., Wang, T. & Chen, X. (2010), 'Effect of surface/interface stress on the plastic deformation of nanoporous materials and nanocomposites', *International Journal of Plasticity* 26(7), 957–975.

Curriculum Vitae

Personal Data

Name	Valentina Kumbolder (formerly Wittner)
Date of Birth	10.01.1992
Place of Birth	Korneuburg, Austria
Nationality	Austrian
Current address	Heldenplatz 23, 2440 Reisenberg, Austria

Education

2016 - 2020	Doctoral programme in Engineering Sciences in the field of civil engineering within the Doctoral School Biointerface TU Wien, Austria
2014 - 2016	Master's programme of Civil Engineering (Dipl.-Ing.) TU Wien, Austria
2010 - 2014	Bachelor's programme of Civil Engineering and Management of Infrastructure (BSc) TU Wien, Austria
2002 - 2010	High School Don Bosco Gymnasium, Unterwaltersdorf, Austria
1998 - 2002	Primary School , Götzensdorf, Austria

Awards

2016	Graduation with distinction (master's degree)
2016	Award for excellent performance as a student (master's degree) granted by the Department of Civil Engineering
2015	Award for excellent performance as a student (master's degree) granted by the Department of Civil Engineering
2011	Award for excellent performance as a student (bachelor's degree) granted by the Department of Civil Engineering
2010	Graduation with distinction (high school)

Work experience

11/2016 - 08/2020	University Assistant at the Institute for Mechanics of Materials and Structures, TU Wien, Austria
03/2016 - 10/2016	Technical drafter at Brandschutz Kubick, Austria
03/2015 - 07/2016	Tutor in Structural Analysis at the Institute for Mechanics of Materials and Structures, TU Wien, Austria
03/2014 - 07/2016	Tutor in Mathematics at the Institute of Building Construction and Technology, TU Wien, Austria
10/2012 - 07/2016	Tutor in Mechanics at the Institute of Building Construction and Technology, TU Wien, Austria
05/2011 - 01/2012	Self employed for MK-ZT Kolar & Partner Ziviltechniker GmbH, Vienna, Austria

Conference Contributions

09/2019	<i>Hierarchical Elastoplasticity of Bone</i> , Presentation at the XV. International Conference on Computational Plasticity - Fundamentals and Applications (COMPLAS 2019), Barcelona, Spain
06/2019	<i>Finite Element-Based Periodic Homogenization of Cage-Like Microscaffolds for Tissue Engineering</i> , Presentation at the VIII International Conference on Coupled Problems in Science and Engineering (Coupled 2019), Stiges (Barcelona), Spain
02/2019	<i>Hierarchical Elastoplasticity of Bone</i> , Presentation at 90th Annual Meeting of the International Association of Applied Mathematics and Mechanics (GAMM 2019), Vienna, Austria
12/2018	<i>Hierarchische Elastoplastizität des Knochens</i> , Presentation at the annual meeting of the Austrian National Committee for Theoretical and Applied Mechanics, Austrian Academy of Science, Vienna, Austria
11/2018	<i>Hierarchical Elastoplasticity of Bone</i> , Presentation at the Austrian Bone Conference (ABC 2018), Vienna, Austria
10/2018	<i>Hierarchical Elastoplasticity of Bone</i> , Presentation at the 8th KMM-VIN Industrial Workshop (IW8): Modelling of Composite Materials and Composite Coatings, Freiburg, Germany
07/2018	<i>Hierarchical Elastoplasticity of Bone: Theory, Algorithm, and Experimental Validation</i> , Presentation at the 13th World Congress in Computational Mechanics (WCCM 2018), New York, USA
07/2018	<i>Hierarchical Elastoplasticity of Bone: Theory, Algorithm, and Experimental Validation</i> ", Presentation at the 8th World Congress of Biomechanics (WCB 2018), Dublin, Ireland